Turbulent drag reduction by anisotropic permeable substrates

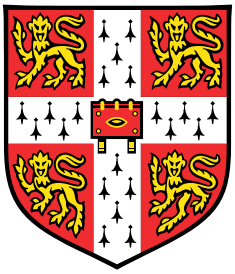

Garazi Gómez de Segura Solay

Department of Engineering
University of Cambridge

This dissertation is submitted for the degree of
Doctor of Philosophy

Newnham College

April 2019

Declaration

I hereby declare that except where specific reference is made to the work of others, the contents of this dissertation are original and have not been submitted in whole or in part for consideration for any other degree or qualification in this, or any other university. This dissertation is my own work and contains nothing which is the outcome of work done in collaboration with others, except as specified in the text and Acknowledgements. This dissertation contains fewer than 65,000 words including appendices, footnotes, tables and equations and has fewer than 150 figures.

Garazi Gómez de Segura Solay
April 2019

Acknowledgements

In the first place, I would like to express my deepest gratitude to my supervisor, Ricardo García Mayoral, for his guidance and support throughout the last four years. He showed me what research driven by enthusiasm, motivation and curiosity should look like, and most importantly, he has taught me an invaluable skill, to *think*. I am very grateful for being part of his 'research family'.

I would also like to thank everyone in the Fluid Dynamics office for fruitful discussions and for making the long hours in the office enjoyable, especially Andrea, Antoine, Francesco, Kshitij and those in Ricardo's group, Nabil, Chris, Akshath, Joe and Wenxiong. A special mention goes to Akshath. We started this PhD adventure together three and half years ago and during this time his support both academically and emotionally has been invaluable. I am deeply grateful that I got to share this experience with him.

I would also like to thank my family, my parents, Belén and Jesús María, and my sisters, Maider and Saioa, for their unconditional support in every goal I pursue. I would not be here without them.

Finally, I would like to thank the person who has been the most important to me these years, Francisco. He has been by my side every day, even during the emotional rollercoaster of the last couple of years. I am deeply indebted to him for his love, advice, support and encouragement. I could not have finished this thesis without him.

Publications

At the time of submission, most of the content of this thesis can be found in the following articles:

- *Flow, Turbulence and Combustion*, **100** (4), 995 – 1014, with Akshath Sharma and Ricardo García-Mayoral as co-authors (parts of the content of chapters 2 and 5).
- *Journal of Physics: Conference Series*, **1001**, 012011, with Christopher Fairhall, Michael MacDonald, Daniel Chung and Ricardo García-Mayoral as co-authors (parts of the content of chapter 3).
- *Fluid Dynamics Research*, **51**, 011410, with Ricardo García-Mayoral and Christopher Fairhall as co-authors (parts of the content of chapter 3).
- *Proceedings of 2018 CTR Summer Program*, 277 – 286, with Akshath Sharma and Ricardo García-Mayoral as co-authors (parts of the content of chapter 4).
- *Journal of Fluid Mechanics*, **875**, 124 – 172, with Ricardo García-Mayoral as co-author (parts of the content of chapters 2, 6 and 7).

Abstract

The objective of the present thesis is to answer the question: 'can anisotropic permeable substrates reduce turbulent skin-friction drag?'

The first part of the thesis aims to extend the existing understanding on how complex surfaces of small texture size can reduce drag. We show that the effect of these surfaces can be reduced to an offset between the apparent, virtual smooth wall perceived by the mean flow and that perceived by the overlying turbulence, but turbulence remains otherwise smooth-wall-like. The drag reduction produced by these surfaces is therefore proportional to the difference between the two virtual origins.

In the second part of the thesis, we study the influence that anisotropic permeable substrates have on the overlying turbulence and show the potential of these substrates to reduce drag. For this, we conduct direct numerical simulations of channel flows bounded by permeable substrates. For small permeabilities, we observe a linear regime, where drag reduction is proportional to the aforementioned offset between the virtual origin perceived by the mean flow and that perceived by turbulence. For the substrates under study, the former is governed by the streamwise permeability and the latter by the spanwise permeability. This linear regime breaks down as spanwise-coherent structures begin to appear, which increase the turbulent mixing and consequently increase the drag. These structures are attributed to a Kelvin-Helmholtz-like instability of the mean flow, a common feature to a variety of obstructed flows, and their onset can be predicted using a linear stability analysis. This analysis shows, and the simulations corroborate, that the governing parameter for the breakdown is the wall-normal permeability. As this permeability increases, the drag-increasing, spanwise-coherent structures become prevalent in the flow, outweighing the drag-reducing effect of the virtual origins and eventually leading to an increase of drag. Based on the virtual-origin theory and the linear stability analysis, we build a predictive model for the behaviour of drag-reducing substrates, which estimates, with good accuracy, the drag reduction observed in the simulations. The present results and the models we subsequently developed provide guidelines for the design of drag-reducing permeable substrates. For the substrate configurations considered, the largest drag reduction observed is $\approx 20 - 25\%$ at a friction Reynolds number $\delta^+ = 180$, which is at least twice that obtained for riblets.

Table of contents

Nomenclature

Roman Symbols

A	Implicit operator of momentum equation in the fractional step method	–
A	Near-wall intercept and wake component of the mean velocity profile	–
c_f	Skin-friction coefficient, $2/U_\delta^{+2}$	–
$\mathcal{C}_{Darcy}$	Coefficients from Darcy's equation	$m^{-1}\,s$
$\mathcal{C}_{ij}$	Coefficients from Brinkman's equation, $i = \{\hat{u}, \hat{w}, \hat{v}\}$ $j = \{\frac{d\hat{u}}{dy}, \frac{d\hat{w}}{dy}, \hat{p}\}$	$m^{-1}\,s$ or m^{-1}
$\mathcal{C}_{Sij}$	Coefficients from Stokes equation, $i = \{\hat{u}, \hat{w}, \hat{v}\}$ $j = \{\frac{d\hat{u}}{dy}, \frac{d\hat{w}}{dy}, \hat{p}\}$	$m^{-1}\,s$ or m^{-1}
DR	Drag reduction, $-\Delta c_f/c_{f0}$	–
E_{uu}	Spectral density of u^2	$m\,s^{-1}$
E_{vv}	Spectral density of v^2	$m\,s^{-1}$
E_{ww}	Spectral density of w^2	$m\,s^{-1}$
E_{uv}	Spectral density of uv	$m\,s^{-1}$
D	Discretised divergence operator	–
G	Discretised gradient operator	–
I	Identity matrix	–
L	Discretised Laplacian operator	–
$k_x k_z E_{uu}$	Premultiplied spectral density of u^2	$m\,s^{-1}$
$k_x k_z E_{vv}$	Premultiplied spectral density of v^2	$m\,s^{-1}$
$k_x k_z E_{ww}$	Premultiplied spectral density of w^2	$m\,s^{-1}$
$k_x k_z E_{uv}$	Premultiplied spectral density of uv	$m\,s^{-1}$

f	An arbitrary function	–
h	Substrate thickness	m
i	Imaginary unit, $\sqrt{-1}$	–
$\boldsymbol{K}$	Permeability tensor	m^2
K_x	Streamwise permeability	m^2
K_y	Wall-normal permeability	m^2
K_z	Spanwise permeability	m^2
K_{Br}	Brinkman's parameter	m^2
K_{Darcy}	Darcy's parameter	m^2
L_p	Penetration depth of the permeable substrate	m
N	Number of grid points	–
$\mathcal{O}$	Order of magnitude	–
p	Kinematic pressure	$m^2\,s^{-2}$
P_x	Mean pressure gradient in the streamwise direction	$Kg\,m^{-2}\,s^{-2}$
$\boldsymbol{r}$	Right-hand side of momentum equation in the fractional step method	–
$\tilde{\boldsymbol{r}}$	Right-hand side of momentum equation in the modified fractional step method	–
Re	Bulk Reynolds number, $U_b\delta/\nu$	–
t	Time	s
U	Mean velocity (it is a function of y)	$m\,s^{-1}$
U_b	Bulk velocity, $= \frac{1}{2\delta}\int_0^{2\delta} U(y)dy$	$m\,s^{-1}$
U_δ	Reference velocity, the centreline velocity of the channel	ms^{-1}
U_{Darcy}	Darcy's velocity within a permeable medium	$m\,s^{-1}$
U_{slip}	Mean slip velocity at $y = 0$	$m\,s^{-1}$
$\boldsymbol{u}$	Velocity vector, (u, v, w)	$m\,s^{-1}$
$\boldsymbol{u}^*$	Intermediate non-solenoidal velocity vector in the fractional step method	–

u_τ	Friction velocity	$m\,s^{-1}$
u	Streamwise velocity component	$m\,s^{-1}$
v	Wall-normal velocity component	$m\,s^{-1}$
w	Spanwise velocity component	$m\,s^{-1}$
x	Streamwise coordinate	m
y	Wall-normal coordinate	m
y_c	Location of the peak of d^2U/dy^2	m
z	Spanwise coordinate	m

Greek Symbols

α	Wavenumber	m^{-1}
α_x	Streamwise wavenumber	m^{-1}
α_z	Spanwise wavenumber	m^{-1}
β	Impedance coefficient between $\hat{v}$ and $\hat{p}$	$m^{-1}\,s$
α_k	Runge-Kutta coefficient of the explicit viscous term	$-$
β_k	Runge-Kutta coefficient of the implicit viscous term	$-$
γ_k	Runge-Kutta coefficient of the advective term	$-$
ζ_k	Runge-Kutta coefficient of the advective term	$-$
Δ	Increment	$-$
Δt	Timestep	s
ΔU	Shift of the logarithmic region of the mean velocity profile	$m\,s^{-1}$
Δy	Grid spacing in the wall-normal direction	m
δ	Flow thickness, half-channel height	m
δ'	Effective half-channel height, $\delta + \ell_T$	m
δ_w	Location of zero total stress	m
δ_i	Thickness of the interfacial region between free-flow and permeable substrate	m

ϵ	Porosity, ratio between void volume and the total volume of the substrate	$-$
κ	Kármán constant	$-$
λ	Wavelength	m
λ_x	Streamwise wavelength	m
λ_z	Spanwise wavelength	m
μ	Viscosity of the fluid	$Kg\,m^{-1}\,s^{-1}$
ν	Kinematic viscosity of the fluid	$m^2\,s^{-1}$
ν_T	Total viscosity, molecular plus eddy viscosity from Cess (1958)	$m^2\,s^{-1}$
$\tilde{\nu}$	Effective viscosity of the permeable substrate	$m^2\,s^{-1}$
ω	Angular frequency of a wave	s^{-1}
ω_i	Growth rate of a wave, imaginary part of ω	s^{-1}
ω_r	Phase velocity of a wave, real part of ω	s^{-1}
ω_x	Vorticity in the streamwise direction	s^{-1}
ρ	Density, $= 1$ throughout	$Kg\,m^{-3}$
τ_w	Wall shear stress	$Kg\,m^{-1}\,s^{-2}$

Superscripts

$(.)^+$	Wall units or viscous units, variable normalised using u_τ and ν
$(.)'$	Fluctuations
$(.)^k$	Runge-Kutta substep index
$\hat{(.)}$	Variable in Fourier space

Subscripts

$(.)_0$	Variable of the reference smooth channel
$(.)_c$	Characteristic value
$(.)_{ch}$	Chebyshev discretisation
$(.)_i$	Imaginary part

$(.)_{max}$	Maximum value	
$(.)_{opt}$	Optimum value	
$(.)_P$	Variable from permeable-channel simulation	
$(.)_r$	Real part	
$(.)_S$	Variable from smooth-channel simulation at same δ^+ as $(.)_P$	
$(.)_{S0}$	Variable from smooth-channel simulation	
$(.)_T$	Turbulent component	

Other Symbols

ℓ	Depth of the virtual wall	m
ℓ_x	Streamwise slip length	m
ℓ_y	Wall-normal slip length	m
ℓ_z	Spanwise slip length	m
$\ell_{z,eff}$	Effective spanwise slip length	m
ℓ_u	Depth of the virtual origin of the streamwise velocity	m
ℓ_v	Depth of the virtual origin of the wall-normal velocity	m
ℓ_w	Depth of the virtual origin of the spanwise velocity	m
ℓ_U	Depth of the virtual origin of the mean flow	m
ℓ_T	Depth of the virtual origin of the overlying turbulence	m

Acronyms / Abbreviations

CUED	Cambridge University Engineering Department
DNS	Direct Numerical Simulation
ODE	Ordinary Differential Equation
PDE	Partial Differential Equation
rms	Root Mean Square
VANS	Volume Averaged Navier-Stokes Equations

Chapter 1

Introduction and theoretical background

On November 2018, the EU announced their plan of becoming the world's first 'climate neutral' economy by 2050. 'Climate neutrality' is defined as achieving net-zero greenhouse gas emissions, which means that the emissions are balanced by the gases removed from the atmosphere. However, fulfilling this ambitious target demands a large reduction in current emissions. Currently, transportation is responsible for approximately 25% of the total European emissions and its contribution keeps increasing every year as traffic volume continues to grow (Eurostat statistics, 2018; IATA, 2016). This problem motivates researchers to find innovative technologies to lower the environmental impact of transportation. One possible strategy is to reduce skin-friction drag, which translates into fuel savings, thereby reducing the carbon emissions and the environmental impact of the transport sector. Other direct consequences of a lower friction drag include cost and noise reductions. This can be achieved by certain surface textures that manipulate the overlying turbulent flow (Luchini, 1996).

In commercial aviation, riblets are the current state of the art for drag reduction technology (Airbus, 2018; Air & Cosmos International, 2017). Riblets are small surface protrusions aligned with the direction of the flow that mimic the skin of sharks, as shown in figure 1.1. This surface, which will be introduced from the beginning of 2020 in the next generation of Airbus A350 XWB airliners, is expected to have a great impact, reducing the overall drag by around $1 - 2\%$. To provide some numbers, for Lufthansa's fleet alone, a 1% of total drag reduction results in yearly savings of €55M worth of kerosene and over $200,000$ tones of CO_2 every year (Air & Cosmos International, 2017). However, this percentage alone is not enough to meet the aforementioned low emission target. The need is therefore to develop new technologies that can give a performance benefit significantly better than riblets. In this thesis, we explore in depth the potential of a novel passive technology, anisotropic

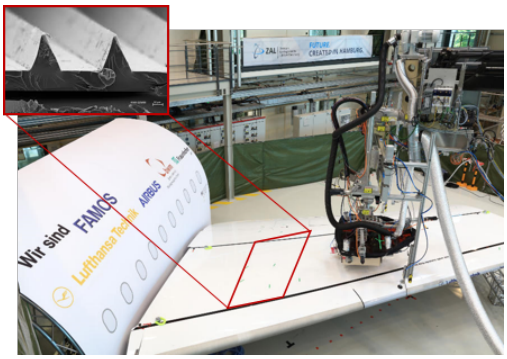

FIGURE 1.1 A robotic arm coating the surface of the wing of an Airbus aeroplane with riblets, providing the wings with a 'shark skin' texture. On the top left corner is an inset of what these riblets look like. Figures extracted from Air & Cosmos International (2017).

permeable substrates, to reduce turbulent skin friction, as has recently been proposed by Abderrahaman-Elena & García-Mayoral (2017).

This idea is motivated by the work of Itoh *et al.* (2006). The authors performed a series of experiments of turbulent flow over a seal fur, achieving a significant drag reduction with respect to a smooth surface. The seal fur studied by Itoh *et al.* (2006) is essentially an anisotropic permeable material, since it is a carpet of hairs preferentially aligned in the direction of the flow. Recently, Abderrahaman-Elena & García-Mayoral (2017) suggested that fibrous coatings, as those of Itoh *et al.* (2006), and possibly other anisotropic permeable coatings, could behave similarly to riblets, as evidenced by the data shown in figure 1.2. For small hair spacings there is a linear regime, where drag reduction increases linearly with the spacing of the hairs in wall units, although more data is required to confirm this. As the spacing increases, the effect of the hairs eventually saturates. A minimum drag is reached for an optimum spacing, beyond which the performance begins to degrade. From the data in figure 1.2, the seal fur not only achieves a greater drag reduction than riblets, but appears to have a wider 'drag reduction bucket', meaning that the range of hair spacings for which the drag reduction is close to maximum is wider. Questions such as how fibrous coatings reduce drag and what the mechanisms behind the drag reducing behaviour are will be answered in this thesis.

Besides the study of anisotropic permeable substrates for drag reduction, this thesis also includes a study on the effect that surface textures in general have on the overlying turbulent flow, which started as a side project for the Turbulence Summer Workshop in Madrid and the CTR Summer Program at Stanford University. However, the insight gained from it completes the study on permeable substrates. Specifically, this research allowed us to fully understand the mechanism by which permeable substrates produce a drag-reducing effect.

Throughout this thesis, we denote the streamwise, wall-normal and spanwise coordinates by x, y and z, respectively, and u, v and w are the corresponding velocity components in each direction. We will use the superscript '+' to indicate scaling in viscous units, defined in

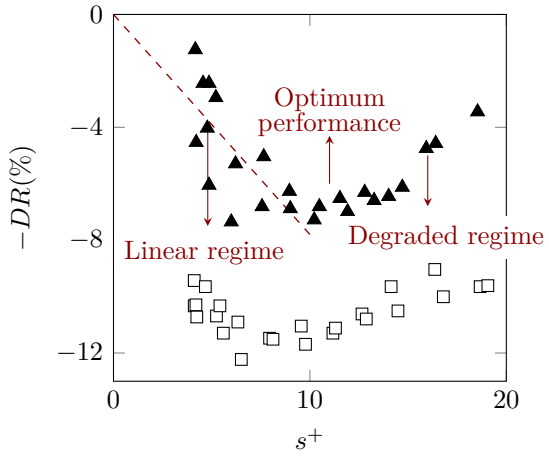

FIGURE 1.2 Drag reduction (DR), as defined later in equation (1.3), as a function of the dimensionless texture size s^+, which corresponds to either the riblet spacing or hair spacing, as plotted in García-Mayoral (2011). Data obtained from Itoh *et al.* (2006). □, seal fur; ▲, trapezoidal riblets.

terms of the kinematic viscosity ν and the friction velocity $u_\tau = \sqrt{\tau_w/\rho}$, which is derived from the shear stress at the wall, τ_w, and the fluid density, ρ. We will always assume that the fluid density is constant and equal to unity for convenience, so that we can drop it from the equations.

In this first chapter, we provide the relevant theoretical background for the understanding of the current work. In section 1.1, we present a general overview of wall-bounded turbulent flows, with emphasis on the near-wall layer. In section 1.2, we discuss the effect that surface textures have on the flow away from the surface, which can be reduced to a shift of the mean velocity profile in the logarithmic region. How surface textures produce this effect is explained in section 1.3. Both these sections apply to any surface manipulation, not only anisotropic permeable substrates. The subsequent sections, sections 1.4 and 1.5, focus on permeable substrates, where we give an overview of the relevant studies and provide a starting point to our work. In section 1.6, we discuss the validity of linear stability analysis to capture certain features of turbulent flows, particularly Kelvin-Helmholtz-like instabilities. Finally, the objectives and the structure of the thesis are summarised in the last section of the chapter.

1.1 Wall-bounded turbulence

Before focusing on how certain textured surfaces cause a reduction in drag, in this section we offer a brief overview of wall-bounded turbulence and its dynamics. A more detailed description can be found in Jiménez (2013*b*). We restrict ourselves to flows in channels, pipes and boundary layers with mild or zero mean streamwise pressure gradient. These flows are characterised by being anisotropic and inhomogeneous due to the presence of the wall, as the size of the eddies is limited by their distance to the wall.

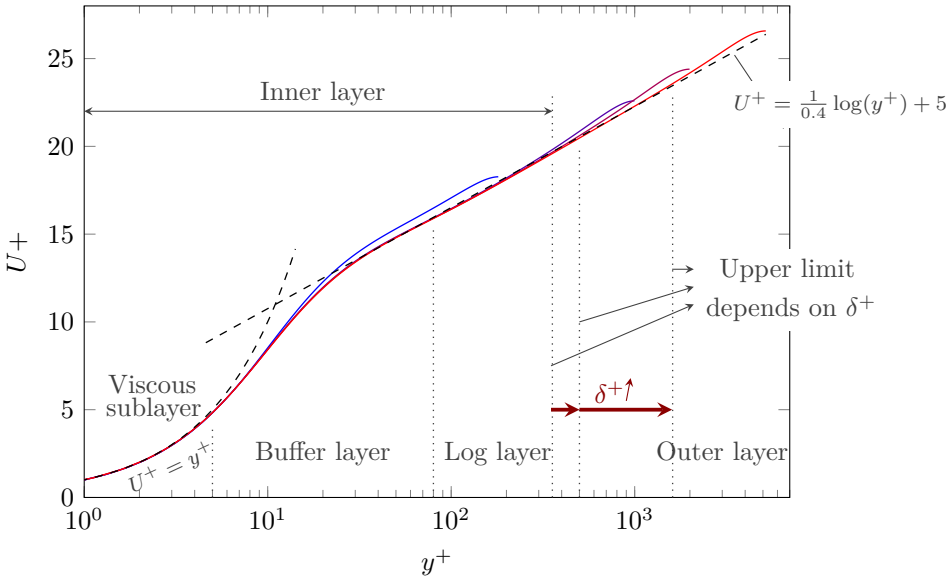

FIGURE 1.3 The different layers in wall-bounded turbulence. From blue to red, mean velocity profiles in a channel flow for different friction Reynolds numbers $\delta^+ = 180$, 1000, 2000 and 5200. The dashed lines correspond to $U^+ = y^+$ and $U^+ = 0.4^{-1}\log(y^+) + 5$. Data from Lee & Moser (2015).

According to the classic theory of turbulence, wall-bounded flows over a smooth wall can be divided in three distinct regions, each of which described by a different scaling (Tennekes & Lumley, 1972). These regions can be distinguished in figure 1.3. In the region closest to the wall, viscous effects are dominant and magnitudes scale in 'wall units' (also referred to as 'viscous units'), where velocities scale with the friction velocity u_τ and lengths with the viscous length ν/u_τ. This near-wall region, in turn, consists of two sublayers: the viscous sublayer, $y^+ < 5$, where the viscous stress dominates; and the buffer layer, between $5 \lesssim y^+ \lesssim 50 - 100$, where both the viscous and Reynolds stresses are relevant. In figure 1.3, the upper limit of the buffer layer has been drawn at $y^+ = 80$.

Far from the wall, there is the so-called outer layer. In this region, velocities also scale with u_τ, but the lengthscale is now set by the flow thickness δ, which refers to the half-height of the channel, the radius of the pipe or the thickness of the boundary layer.

Between the buffer and the outer layer, i.e. $y^+ \gg 1$ and $y \ll \delta$, there is an intermediate region, where the relevant lengthscale is neither ν/u_τ nor δ. The only applicable lengthscale is the distance from the wall, y. This region is generally referred to as 'logarithmic layer' and it receives the name from the form of the mean velocity profile,

$$U^+ = \frac{1}{\kappa}\log y^+ + A, \tag{1.1}$$

where κ is the universal Kármán constant, typically taken as $\kappa \approx 0.41$, and A is the near-wall intercept, whose value depends on the viscous sublayer. For a smooth wall, it is typically $A \approx 5$. The limit to which this logarithmic region extends depends on the flow, but it is

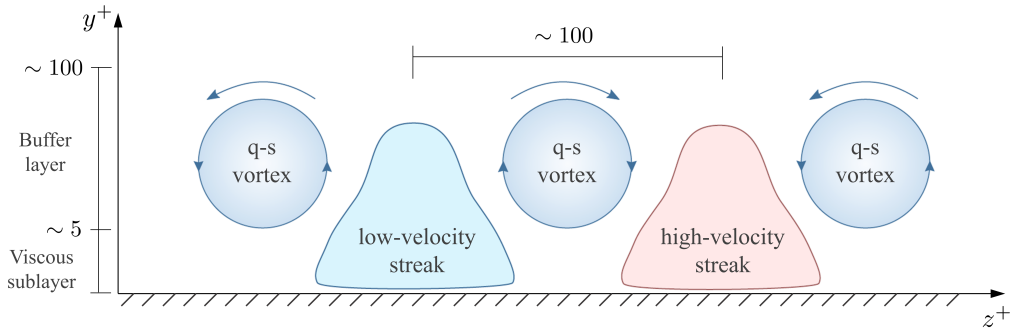

FIGURE 1.4 Sketch of the near-wall cycle across the span with quasi-streamwise vortices (q-s vortex) and low- and high-velocity streaks.

generally set at approximately $\approx 0.2\delta$. In essence, the regions of wall-bounded turbulent flows are characterised by a uniform velocity, u_τ, and a variant lengthscale, where the ratio between the outer and viscous lengthscales is the friction Reynolds number, $\delta^+ = \delta/(\nu/u_\tau) = u_\tau\delta/\nu$. This varies from ~ 150 for marginally turbulent flows to $\sim 10^6$ for atmospheric flows or large pipelines (Jiménez, 2013*b*). Notice that, in figure 1.3, the mean velocity profile in the logarithmic region for $\delta^+ \approx 180$ deviates from those at higher Reynolds numbers. This is because for such a low Reynolds number, the logarithmic layer barely exists and some low Reynolds number effects exist (Spalart, 1988; Moser *et al.*, 1999). The effect of textured surfaces, however, is confined to the near-wall region and, as shown by García-Mayoral & Jiménez (2012) for riblets, simulations at low Reynolds number (i.e. $\delta^+ \approx 180$) are valid to study the physics of flows over these surfaces. Therefore, in this thesis, simulations are run at a friction Reynolds number $\delta^+ \approx 180$, which reduces the computational cost significantly, allowing us to perform a parametric study for permeable substrates.

We are primarily interested in the near-wall region, that is, the viscous and buffer layers. The structures and flow dynamics within these layers are fairly well understood and a thorough description can be found in Jiménez & Pinelli (1999), Schoppa & Hussain (2002), Kawahara *et al.* (2012) or Jiménez (2013*b*). In this region, which extends up to $y^+ \approx 100$, the dominant structures are streaks and quasi-streamwise vortices, as sketched in figure 1.4 and illustrated in figure 1.5. The former are long ($x^+ \approx 1000$) streamwise jets superimposed to the mean shear, forming alternating spanwise regions of high and low streamwise velocity with an average spanwise spacing of $z^+ \approx 100$ (Smith & Metzler, 1983). They contain most of the kinetic energy and were first identified by Kline *et al.* (1967). Quasi-streamwise vortices, on the other hand, are vortical structures with a predominantly streamwise orientation, although they might be slightly tilted away from the wall, hence their name. These are shorter than streaks, with a typical length of $x^+ \approx 200$, and a radius of the order of $r^+ \approx 10 - 15$ (Blackwelder & Eckelmann, 1979). The longitudinal spacing between two adjacent vortices is $x^+ \approx 300$ and several vortices are typically associated to a single streak (Jiménez & Moin, 1991; Jeong *et al.*, 1997). These quasi-streamwise vortices organise the dissipation and Reynolds stresses, and in

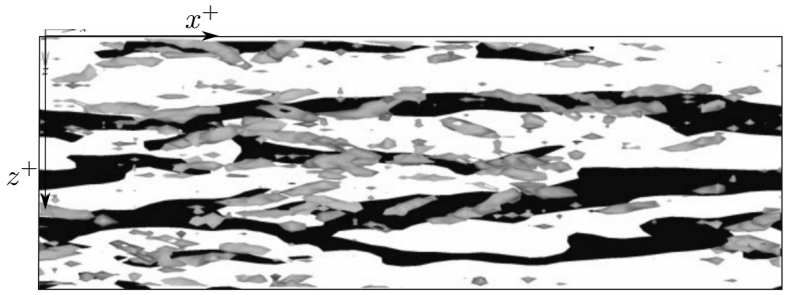

FIGURE 1.5 Top view of the near-wall region, where $(x^+, z^+) = (1400, 450)$. Black, low-velocity streaks ($u' < 0$) at $y^+ = 20$; grey-shaded, streamwise vortices, indicated by the λ_2 vortex definition from Jeong & Hussain (1995) in the region $0 < y^+ < 60$. Figure from Schoppa & Hussain (2002).

general, vortices of different signs are arranged on opposite sides of a streak, as illustrated in figure 1.4. The distribution of these dominant structures in the buffer layer is also illustrated in figure 1.5, which shows a representative snapshot of the buffer layer obtained by Schoppa & Hussain (2002). This figure shows how vortices, represented by the grey-shaded regions, are distributed along both sides of the low- and high-velocity streaks. These streaks are represented by the elongated black and white lines, respectively.

These structures are involved in a self-sustaining cycle, commonly referred to as the 'near-wall cycle', where the streaks and vortices regenerate each other, as sketched in figure 1.4. Quasi-streamwise vortices advect the streamwise velocity in the wall-normal direction forming the streaks. Quasi-streamwise vortices displace low-speed fluid away from the wall, forming a low-velocity streak, and high-speed fluid towards the wall, forming a high-velocity streak. This near-wall turbulent mixing of streamwise momentum gives rise to the high local shear encountered in turbulent flows. This process, driven by quasi-streamwise vortices, is therefore primarily responsible for the high-skin friction in turbulent flows compared to laminar ones (Orlandi & Jiménez, 1994). The quasi-streamwise vortices, in turn, are generated by an instability of the streaks (Swearingen & Blackwelder, 1987). The source of energy for the instability is, however, still unclear and different explanations have been proposed. The main ones are the inflectional-instability model from Swearingen & Blackwelder (1987) and the streak transient growth mechanism from Schoppa & Hussain (2002). The former states that the wall-normal vorticity layers that are formed between low- and high-velocity streaks are unstable to inflectional instabilities. These layers, which are initially oriented in the wall-normal direction, are then tilted forward and intensified by the mean shear, forming the quasi-streamwise vortices. Schoppa & Hussain (2002), on the other hand, suggested that a transient growth of structures in a shear flow could also generate these vortices. Jiménez & Pinelli (1999) showed that this near-wall cycle is located between $y^+ \approx 20 - 60$ and is essentially independent of the rest of the flow.

The structure of the flow becomes more complex in the logarithmic layer, mainly due to the presence of multiple scales. The streamwise velocity remains organised in streaks,

although with a much larger size than those in the buffer layer, but the organisation of the Reynolds stress is now taken over by turbulent eddies, with sizes proportional to their height, $\mathcal{O}(y)$. The structure of the flow in this layer is beyond the scope of this thesis, and the reader is referred to Jiménez (2012), Lozano-Durán *et al.* (2012) Jiménez (2013*b*) or Jiménez (2018) for a detailed description.

1.2 Drag reduction from surface manipulations

Many flow control techniques to reduce drag have targeted the near-wall cycle, particularly the quasi-streamwise vortices, due to their key role in the production of skin friction. This is for instance the case with the opposition control technique from Choi *et al.* (1994) or with certain surfaces of small texture size that are intentionally designed to manipulate the near-wall cycle, which we will refer to as complex surfaces. Examples of complex surfaces include riblets (Walsh & Lindemann, 1984), superhydrophobic surfaces (Rothstein, 2010), or the permeable substrates here studied.

The friction coefficient, c_f, can be defined as

$$c_f = 2\frac{\tau_w}{U_\delta^2} = 2\frac{1}{U_\delta^{+2}}, \tag{1.2}$$

where τ_w is the total shear stress at the wall and U_δ is the reference velocity used to normalise it. The choice of the reference velocity U_δ depends on the type of flow studied. In external flows, the free stream velocity is typically used, while in internal flows the bulk velocity is more common. Most of the complex surfaces for drag reduction, as well as the permeable substrates studied here, are mainly aimed at external flow applications, for instance as coatings in the surfaces of vehicles. The simulations discussed in the present thesis, however, are conducted in channels for simplicity, since unlike in boundary layers, the flow does not evolve in the streamwise direction. In this framework, García-Mayoral & Jiménez (2011) argued that choosing the centreline velocity as the reference for c_f allows a closer comparison with external-flow friction coefficients.

As previously mentioned, in the case of small surface textures, where the texture is smaller than the overlying turbulent structures, their effect on the flow is confined to the near-wall region. According to the classic theory of wall turbulence, sufficiently far away from the wall, the only effect of any surface manipulation is to modify the intercept of the logarithmic law, while Kármán's constant and the wake function remain unaltered (Clauser, 1956). The centreline velocity is then $U_\delta^+ = U_{\delta 0}^+ + \Delta U^+$, where the subscript '0' indicates values for a reference smooth channel, with $U_{\delta_0}^+$ satisfying equation (1.1), and ΔU^+ is the shift of the velocity profile in the logarithmic region and above with respect to the smooth wall. The drag reduction (DR), defined as the reduction in c_f with respect to a smooth wall, can then

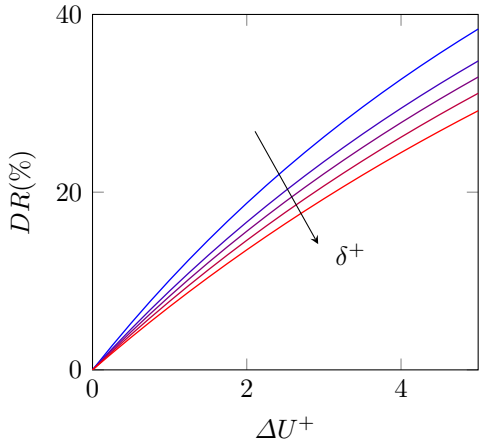

FIGURE 1.6 Drag reduction, DR, as a function of ΔU^+, as given by equation (1.3), for different friction Reynolds numbers. DR has been calculated using the centreline velocities of the smooth channels, $U_{\delta 0}$, from Lee & Moser (2015), Hoyas & Jiménez (2006) and Lozano-Durán & Jiménez (2014). Blue to red, $\delta^+ \approx 180$, 540, 1000, 1990 and 5180. The arrow indicates increasing friction Reynolds number.

be expressed in terms of ΔU^+,

$$DR = -\frac{c_f - c_{f0}}{c_{f0}} = 1 - \frac{1}{\left(1 + \Delta U^+ / U^+_{\delta 0}\right)^2}. \tag{1.3}$$

If $\Delta U^+ > 0$, the logarithmic region is shifted upwards and drag is reduced. Conversely, if $\Delta U^+ < 0$, the logarithmic region is shifted downwards and drag is increased. Note that DR depends on the friction Reynolds number, δ^+, through $U^+_{\delta 0}$, while ΔU^+ does not and hence a fixed surface texture size in wall units would result in the same ΔU^+ regardless of δ^+. The shift ΔU^+ provides therefore a more universal measure, as it can be extrapolated to higher δ^+ (García-Mayoral & Jiménez, 2011; Spalart & McLean, 2011; Gatti & Quadrio, 2016; García-Mayoral *et al.*, 2019). The relation between DR and ΔU^+ given by equation (1.3) is depicted in figure 1.6. The figure shows how DR varies with the friction Reynolds number δ^+. For a given ΔU^+, DR decreases with the Reynolds number, due to larger values of $U^+_{\delta 0}$. This can be expected to lead to discrepancies in DR between simulations or experiments at low Reynolds numbers, and industrial applications at high Reynolds numbers. To circumvent this, in the present thesis we quantify drag reduction in terms of ΔU^+. Note, however, that obtaining ΔU^+ requires measuring the difference in U^+ between the textured surface and the reference smooth case far from the wall, which poses the question of where to set the height origin for the textured case. This question will be addressed in chapter 3.

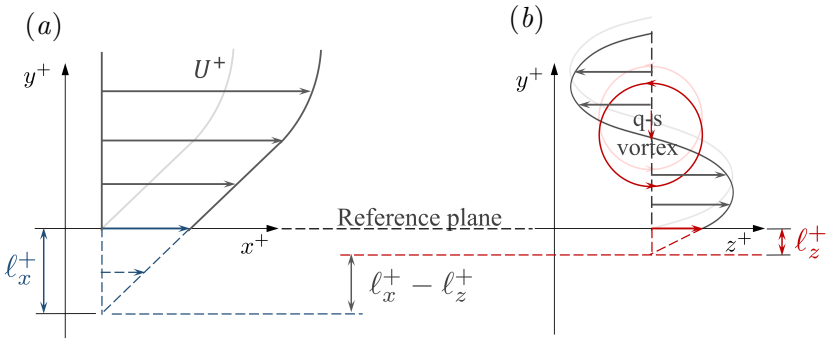

FIGURE 1.7 Sketch of the (a) streamwise and (b) spanwise slip lengths, ℓ_x^+ and ℓ_z^+, and the corresponding virtual origins at $y^+ = -\ell_x^+$ and $y^+ = -\ell_z^+$. A quasi-streamwise vortex (q-s vortex), inducing cross-flow w^+, is sketched in (b).

1.3 Physics underlying the drag reduction mechanism

Studies on how complex surfaces reduce drag date back to the 1990s (Luchini *et al.*, 1991). The first studies were on riblets, but the same drag reduction mechanism is also applicable to permeable substrates, superhydrophobic surfaces or any other complex surface (Jiménez, 1994).

When the surface texture is vanishingly small compared to the near-wall turbulent structures, the overlying flow does not perceive the detail of the texture, but a homogenised effect of it. Bechert & Bartenwerfer (1989) noticed that riblets produce on average a slip velocity, U_{slip}, at the plane of the riblet tips. Taking this plane as reference, where we set $y = 0$, Bechert & Bartenwerfer (1989) suggested that the mean streamwise flow perceived a virtual origin at $y = -\ell_x$, i.e. the mean flow experienced a non-slipping wall at that height, and the depth ℓ_x below the reference plane is what they called protrusion height. Given that for small surface textures the velocity profile near the surface is essentially linear, the concept of the virtual origin for the mean flow can be represented by a Navier slip condition at the reference plane $y = 0$,

$$u|_{y=0} = \ell_x \left.\frac{\partial u}{\partial y}\right|_{y=0}, \tag{1.4}$$

where the streamwise protrusion height, ℓ_x, is the proportionality coefficient between the velocity and the shear. The concept of 'protrusion height' takes different names in the literature, such as 'slip length' in the superhydrophobic community. 'Slip length' is the term that is employed in the present thesis, so that hereafter ℓ_x will be referred to as the streamwise slip length and the height $y = -\ell_x$ as the streamwise virtual origin. Additionally, in viscous units, the mean streamwise shear is $dU^+/dy^+|_{y^+=0} \approx 1$ and, as a result, the slip length, ℓ_x^+, is interchangeable with the slip velocity, U_{slip}^+.

Luchini *et al.* (1991) realised that the streamwise virtual origin is not sufficient to characterise the effect of riblets in turbulent flows, since the overlying turbulence, particularly

the quasi-streamwise vortices of the near-wall cycle, also affects the change in drag. On average, the non-slipping wall perceived by the quasi-streamwise vortices is not at the riblet tips, but at some distance below. Luchini *et al.* (1991) introduced the concept of a virtual origin of turbulence. Given that near the surface these vortices induce mainly a transverse shear in the spanwise direction, Luchini *et al.* (1991) proposed that the virtual origin of turbulence is given by that of the spanwise velocity, $y^+ = -\ell_z^+$. Note that this value is the same in the whole domain. Drag reduction over riblets and by extension over any non-smooth, passive surface can then be viewed as a virtual-origin effect, where the reduction of drag is caused by an offset between the positions of the virtual, equivalent smooth walls perceived by the mean flow and the overlying turbulent flow, as depicted in figure 1.7, but turbulence remains otherwise smooth wall-like (Jiménez, 1994; Luchini, 1996; Gómez-de-Segura *et al.*, 2018*a*; García-Mayoral *et al.*, 2019). The shift of the mean velocity profile is therefore

$$\Delta U^+ = \ell_x^+ - \ell_z^+. \tag{1.5}$$

If $\ell_z^+ < \ell_x^+$, the surface texture impedes the penetration of turbulence as deep as the mean flow and quasi-streamwise vortices are, compared to a smooth wall, 'pushed' away from the origin of the mean flow, $y^+ = -\ell_x^+$. As a result, the local turbulence mixing close to the surface decreases, thereby reducing the shear and the skin friction (Orlandi & Jiménez, 1994). Conversely, if $\ell_x^+ < \ell_z^+$, the vortices perceive a deeper origin than the mean flow and friction drag increases. The effect of complex surfaces on the overlying flow can then be characterised by streamwise and spanwise Navier slip conditions at the reference plane $y = 0$,

$$u^+\Big|_{y^+=0} = \ell_x^+ \left.\frac{\partial u}{\partial y}^+\right|_{y^+=0}, \tag{1.6a}$$

$$w^+\Big|_{y^+=0} = \ell_z^+ \left.\frac{\partial w}{\partial y}^+\right|_{y^+=0}. \tag{1.6b}$$

The reference plane is generally taken at the top plane of the surface geometry, such as at the riblet tips (Luchini *et al.*, 1991) or at the substrate-fluid interface plane for permeable substrates (Abderrahaman-Elena & García-Mayoral, 2017).

The equivalent, homogeneous conditions (1.6) and the linear law (1.5) implicitly assume that the surface texture is small enough for the overlying flow to only perceive an averaged effect of it. This theory would therefore only be valid as long as the texture size is vanishingly small compared to the characteristic lengthscales of near-wall turbulence (Bechert *et al.*, 1997; García-Mayoral & Jiménez, 2011; Seo & Mani, 2016). For a given complex surface, the size of the texture in viscous units increases with the Reynolds number, and so do ℓ_x^+, ℓ_z^+ and their difference. The shift ΔU^+ depends on this difference and hence it increases with the Reynolds number, or alternatively, with the texture size in wall units. This linear increase, however, would eventually break down, either due to turbulence perceiving the granular

nature of the surface or due to additional effects. These effects are dependent on the type of complex surface considered and will be discussed in chapter 7 for permeable substrates and in chapter 4 for a variety of complex surfaces. In chapter 3 we will see that there is a subtle difference between the depths of the virtual origins and the slip lengths, and the two are only equivalent in the vanishingly small limit. A more general expression of Luchini's theory (1.5) will be proposed in chapter 3.

1.4 The flow over permeable substrates

This thesis focuses mainly on turbulent flows over anisotropic permeable substrates. The related literature, however, has focused on isotropic substrates, observing a substantial increase in drag with respect to a smooth wall, both in experiments (Zagni & Smith, 1976; Kong & Schetz, 1982; Wilkinson, 1983; Suga *et al.*, 2010; Manes *et al.*, 2011; Efstathiou & Luhar, 2018) and in numerical simulations (Breugem & Boersma, 2005; Breugem *et al.*, 2006; Rosti *et al.*, 2015; Kuwata & Suga, 2016), independently of the substrate topology considered. This increase has often been attributed to the onset of large spanwise-coherent structures, resembling Kelvin-Helmholtz rollers, which increase the momentum transfer and thus the Reynolds stresses near the permeable surface. In this thesis, we study the effect of anisotropy and provide physical insight into the behaviour of anisotropic permeable substrates in turbulent flows, with special emphasis on drag-reducing substrates, where the permeability is preferential in the streamwise direction.

Previous studies have shown that streamwise-preferential complex surfaces can reduce drag in turbulent flows (Luchini *et al.*, 1991; Jiménez, 1994; Bechert *et al.*, 1997). By streamwise preferential we refer to surface textures that offer less resistance to the streamwise mean flow than to the cross flow. This is indeed the case for some of the most common passive technologies for drag reduction, such as riblets, where the drag reduction mechanism is given by equation (1.5). Recently, Abderrahaman-Elena & García-Mayoral (2017) suggested that the drag reduction ability of anisotropic permeable substrates relies on the same mechanism. This behaviour was, for instance, observed by Hahn *et al.* (2002), who performed simulations of turbulent flows over idealised substrates that were permeable in the streamwise and/or spanwise directions only. They observed that the streamwise slip is beneficial for drag reduction, while the spanwise slip is deleterious. Their substrates, however, were ideal in the sense that they were impermeable in the wall-normal direction. Hence, the work by Hahn *et al.* (2002) is more connected to slip-only simulations, such as those carried out by Min & Kim (2004) and Busse & Sandham (2012), where only tangential slips as given by boundary conditions (1.6) were allowed, than to realistic permeable substrates, where any significant tangential slip at the surface would be accompanied by some degree of wall-normal transpiration (i.e. wall-normal velocity).

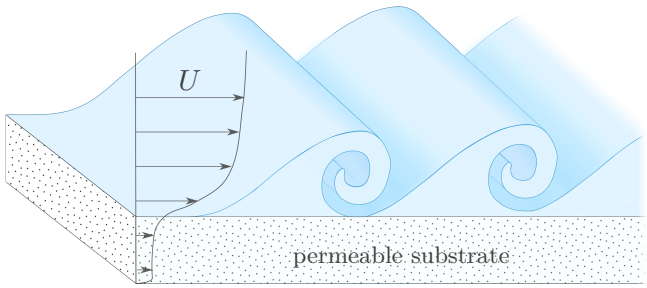

FIGURE 1.8 Sketch of spanwise-coherent, Kelvin-Helmholtz rollers over a complex surface, in this case, a permeable substrate.

As mentioned in section 1.3, the linear theory of Luchini *et al.* (1991) is valid only as long as the texture lengthscales are small compared to the characteristic lengthscales of near-wall turbulence. As the texture size increases, additional deleterious effects to drag reduction set in, breaking down the drag-reducing performance and eventually leading to an increase of drag. The mechanisms behind these deleterious effects vary from one technology to another. In riblets, for instance, the degradation of performance is due to the appearance of spanwise-coherent rollers, as those sketched in figure 1.8, which arise from a Kelvin-Helmholtz instability (García-Mayoral & Jiménez, 2011). These structures are in fact a prevalent feature to a variety of obstructed flows (Ghisalberti, 2009) and they have also been observed to form over permeable substrates (Raupach *et al.*, 1996; Finnigan, 2000; Breugem *et al.*, 2006; Py *et al.*, 2006; Kuwata & Suga, 2016; Suga *et al.*, 2017). In these studies, the large increase of the Reynolds stress and the subsequent increase in drag that these substrates experienced was associated to the presence of Kelvin-Helmholtz rollers. A relevant work in this area is that by Jiménez *et al.* (2001), who observed the formation of Kelvin-Helmholtz rollers over substrates that were permeable in the wall-normal direction only and inferred that the relaxation of the impermeability condition at the wall is sufficient to elicit the rollers. Following these results, Abderrahaman-Elena & García-Mayoral (2017) suggested the formation of these rollers as a possible drag-degrading mechanism for anisotropic permeable substrates. They proposed a model to bound the maximum achievable drag reduction based on the onset of the Kelvin-Helmholtz-like instability.

The combination of the works by Hahn *et al.* (2002) and Jiménez *et al.* (2001) therefore suggest a competition between the beneficial, drag-reducing effect of the tangential slips and the detrimental, drag-increasing effect of the appearance of Kelvin-Helmholtz rollers, driven by the wall-normal transpiration. This recalls the drag-reducing behaviour of riblets and other drag-reducing surfaces, which show a linear regime, where the drag reduction increases linearly with a certain characteristic length of the texture, followed by a saturation and an eventual increase of drag (García-Mayoral & Jiménez, 2011). Although the same has not been shown for anisotropic permeable substrates, the similarities between the drag reduction

curves of riblets and those of seal fur by Itoh *et al.* (2006) shown in figure 1.6 suggest a similar behaviour (Abderrahaman-Elena & García-Mayoral, 2017).

Recently, anisotropic permeable substrates have received some attention. Kuwata & Suga (2017) and Suga *et al.* (2018) examined the effect of different directional permeabilities on the overlying turbulence by starting from substrates with wall-normal permeability alone and adding a combination of the other two directional permeabilities. However, they did not contemplate cases with low wall-normal permeability, and hence all these configurations resulted in an increase of drag. Rosti *et al.* (2018), on the other hand, explored substrates with equal tangential permeabilities and a different wall-normal permeability. For very small wall-normal permeabilities, they observed some drag reduction. However, such substrates, as it will be shown later in this thesis, do not exploit the full potential of the anisotropy, as they effectively rely on a near-zero transpiration to saturate the adverse effect of the spanwise slip, as has already been reported in Gómez-de-Segura *et al.* (2018*b*). This effect will be discussed in detail in chapter 3.

In this thesis, we investigate the drag reduction ability of anisotropic permeable substrates. The aim of this work is to understand how the overlying turbulent flow is modified by the presence of such substrates and build predictive models to estimate their drag-reducing behaviour.

1.5 Characterisation of the flow within permeable substrates

The flow within a permeable substrate can be studied with a microscopic or macroscopic approach. The microscopic approach involves representing the geometry of the substrate in detail and explicitly resolving the flow within (Breugem & Boersma, 2005; Zhang & Prosperetti, 2009; Liu & Prosperetti, 2011; Matsumura & Jackson, 2014; Kuwata & Suga, 2016). The macroscopic approach, in contrast, involves modelling the permeable medium as a continuum and obtaining an average solution of the flow within (Darcy, 1856; Brinkman, 1947; Whitaker, 1996). In the present work, we focus on permeable materials where the pores are much smaller than any near-wall turbulent lengthscale. We therefore opt for a macroscopic, continuum approach to model the flow within the permeable substrate, due to the high resolution otherwise required to explicitly solve the flow within the pores.

A classic approach to characterise the homogenised flow within a permeable medium is Darcy's equation (Darcy, 1856),

$$\nabla p = -\nu \boldsymbol{K}^{-1} \boldsymbol{u}, \tag{1.7}$$

where $\boldsymbol{u}$ is the velocity vector, p the kinematic pressure, ν the molecular viscosity of the fluid and $\boldsymbol{K}$ is the permeability tensor, which measures the ability of the fluid to flow through the permeable medium. Darcy's equation (1.7) is a balance between the pressure gradient across the permeable medium and the viscous drag of the solid matrix caused by the pressure. This

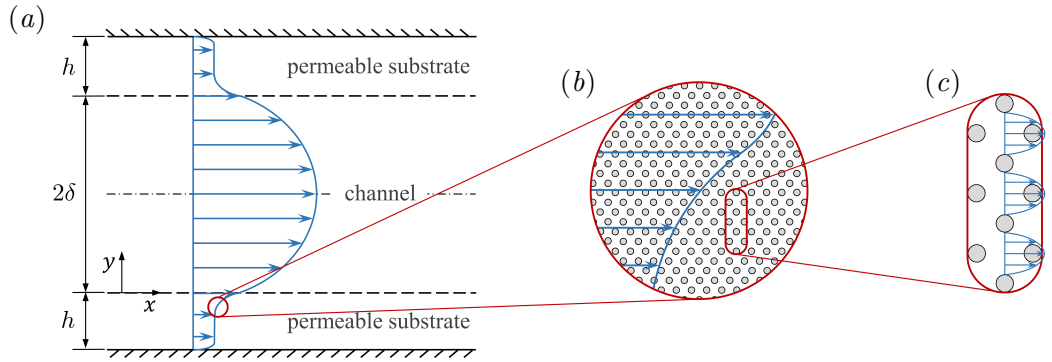

FIGURE 1.9 (*a*) General layout, channel flow delimited by permeable substrates, used in chapters 5, 6 and 7 (view in elevation). (*b*) Detail of the macroscale flow within the substrate. (*c*) Detail of the microscale flow within the substrate.

is the simplest model amongst the continuum approaches, and although it was originally empirical, it results from a volume average of the Stokes equation over many pores/particulate obstacles. Note that under the assumption of vanishingly small pore size, such averages could still be conducted in small volumes compared to the scales of the overlying flow.

More sophisticated continuum approaches used in the literature include the homogenisation techniques, where the macroscopic equations are derived from the microscopic description of the substrate. Among the most commonly used homogenisation techniques is the Volume Averaged Navier-Stokes equations (VANS), where the governing equations are obtained by averaging the microscale equations in space (Ochoa-Tapia & Whitaker, 1995*b*,*a*; Whitaker, 1996). This approach has been extensively used to model the flow within permeable substrates (Breugem *et al.*, 2006; Tilton & Cortelezzi, 2008; Rosti *et al.*, 2015). Another strategy is the multiscale homogenisation, where the governing continuum equations are obtained by a matched asymptotic expansion method (Zampogna & Bottaro, 2016; Lācis & Bagheri, 2017). A recent review on particular aspects of this multiscale homogenisation technique to model permeable and poroelastic substrates is provided by Bottaro (2019). Additionally, Davit *et al.* (2013) offers a detailed comparison between the multiscale asymptotic homogenisation and the volume averaging. These two homogenisation techniques have been used to theoretically derive Darcy's empirical equation and its modifications discussed below (Whitaker, 1986, 1996; Zampogna & Bottaro, 2016). Note that the inherent assumption in any continuum approach, including these, is that the characteristic lengthscales of the microstructure of the permeable substrate are smaller than any lengthscales relevant for the overlying turbulent flow.

The volume average, implicit in Darcy's equation, accounts for the viscous stresses caused by velocity gradients over lengths smaller than the averaging one. This effectively filters out diffusive effects acting over larger lengthscales. If the latter are relevant, they can be accounted for by including a macroscopic diffusive term, yielding Brinkman's equation

(Brinkman, 1947),

$$\nabla p = -\nu \boldsymbol{K}^{-1}\boldsymbol{u} + \tilde{\nu}\nabla^2\boldsymbol{u}. \tag{1.8}$$

The first two terms in equation (1.8) constitute Darcy's equation, and the last term, $\tilde{\nu}\nabla^2\boldsymbol{u}$, is the Brinkman term, with $\tilde{\nu}$ the effective macroscopic viscosity, which depends on the microstructure of the substrate. The homogenised flow within the permeable substrate and the different lengthscales accounted for by the various terms in equation (1.8) are illustrated in figure 1.9. Panel (c) portrays the flow between the obstacles, which results in Darcy's equation when averaged, while panel (b) portrays the large scale diffusion missed by the volume averaging and captured by the Brinkman term. Although originally empirical, Brinkman's equation (1.8) has been theoretically derived by several authors (Tam, 1969; Lundgren, 1972; Whitaker, 1986). The choice of which continuum approach to use depends on the microstructure of the permeable substrate. Materials with different degrees of pore connectivity may require different models. Brinkman's model, for instance, is suitable for substrates made up of open matrices of obstacles, such as that sketched in figure 1.10(a), where fluid regions are significantly interconnected and diffusion can act efficiently over large scales (Sangani & Behl, 1989). However, it does not represent correctly substrates made up of microducts essentially isolated from each other, as that portrayed in figure 1.10(b), where diffusion cannot act over scales larger than the pores (Lévy, 1983; Auriault, 2009). Based on this, Abderrahaman-Elena & García-Mayoral (2017) drew a distinction between 'highly-connected' and 'poorly-connected' substrates, and argued that highly-connected substrates offered better properties for drag reduction, as we will show in chapter 6.

In poorly-connected substrates, Darcy's equation provides a reasonable model for the flow within (Lévy, 1983; Auriault, 2009), but it cannot capture the interfacial layer that forms immediately below the substrate-fluid interface, where the velocity transitions from Darcy's velocity deep inside the substrate to a certain slip velocity at the interface plane. To this end, the 'jump condition' proposed by Beavers & Joseph (1967) is generally used. This imposes a slip velocity proportional to the external shear at the substrate-fluid interface,

$$u|_{y=0} = u_{Darcy} + \frac{\sqrt{K}}{\alpha_{BJ}} \left.\frac{\partial u}{\partial y}\right|_{y=0}, \tag{1.9}$$

where $u_{Darcy} = -(K/\nu)\, dP/dx$ is Darcy's velocity deep inside the substrate obtained from equation (1.7). The constant of proportionality, α_{BJ}, accounts for the microstructure of the permeable material and is determined empirically. Even though this empirical boundary condition results in a discontinuous velocity profile across the interface, Saffman (1971) and later, Jäger & Mikelić (2000) have provided mathematical justification for it and the combination of Darcy's equation with Beaver & Joseph's condition is widely used in the literature (Hahn *et al.*, 2002; Chang, 2006; Deepu *et al.*, 2015).

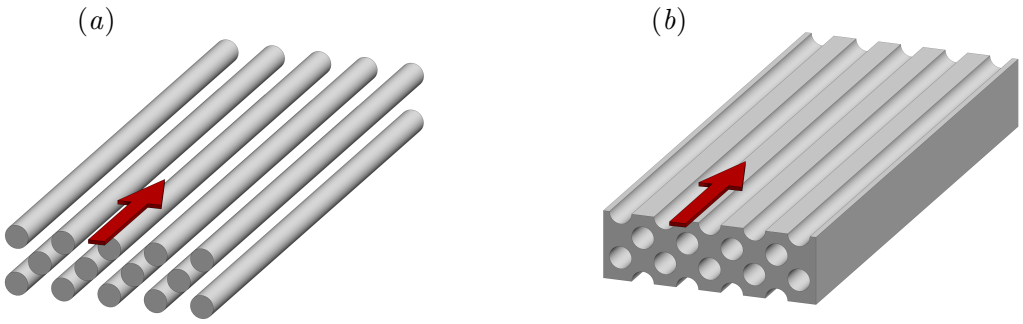

FIGURE 1.10 Conceptual sketches of (a) a highly-connected material, where the interstitial flow is well interconnected and macroscale diffusive effects can propagate throughout, and (b) a poorly-connected permeable material, where no diffusive effects connect different pores. The red arrow represents the direction of the overlying flow.

By contrast, in highly-connected substrates, Brinkman's model allows to capture the interfacial region, under certain assumptions. This equation is also a volume averaging model, so it implicitly assumes that any small volume within the substrate contains a large number of obstacles. However, as the averaging volume approaches the interface with the free flow, this assumption would eventually cease to hold. The specialised literature shows no general agreement regarding the treatment of the substrate-fluid interface (Ochoa-Tapia & Whitaker, 1995*a*; Le Bars & Worster, 2006; Zampogna & Bottaro, 2016; Lācis & Bagheri, 2017). Some studies impose jump conditions, although these can be of different types, such as a jump in velocity (Beavers & Joseph, 1967; Jäger & Mikelić, 2000; Valdés-Parada *et al.*, 2013), a jump in shear stress but not in velocity (Ochoa-Tapia & Whitaker, 1995*a*; Hill & Straughan, 2009; Minale, 2014), or continuity of both velocity and shear stress (Neale & Nader, 1974; Vafai & Kim, 1990; Le Bars & Worster, 2006; Battiato, 2012, 2014). Furthermore, Taylor (1971) and Neale & Nader (1974) have mathematically deduced the equivalency between Brinkman's equation and Beavers & Joseph's boundary condition at the substrate-fluid interface, provided that $\alpha_{BJ} = \sqrt{\tilde{\nu}/\nu}$. The studies mentioned above use different governing equations for the flow within the permeable substrate and the free-fluid region. In the literature, this is referred to as the multi-domain approach. To avoid the computational problem of having a sharp interface where the governing equations change, other studies opt for a single-domain approach instead. This consists of using the same governing equations in the whole domain, with spatially variable permeability. In other words, there is an adaptation region of certain thickness between the free-fluid region and the substrate where the permeability transitions smoothly from its value within the substrate to infinity in the free flow, such as in the work by Le Bars & Worster (2006). This is also the case of Breugem *et al.* (2006), where they use the more general VANS approach with an adaptation region of thickness δ_i. For substrates

where the inertial terms are negligible, the latter approach would be analogous to using Brinkman's model and 'blurring' the solution with a moving average of thickness δ_i.

As mentioned before, the analysis of Abderrahaman-Elena & García-Mayoral (2017) suggested that highly-connected materials would yield greater drag reduction. For simplicity, we assume that pores are infinitely small, so that the continuum hypothesis would hold for any vanishingly small volume, and fluid variables are continuous across the interface (Vafai & Kim, 1990). In this limit, the flow within the permeable substrate would be dominantly viscous, so the advective effects are negligible. In this scenario, Brinkman's model provides a simple but reasonable approximation. For larger pores, where the advective terms begin to be noticeable, they could be considered by an additional Forchheimer term (Joseph *et al.*, 1982; Forchheimer, 1901; Whitaker, 1996).

1.6 Linear stability analysis about the mean flow in a channel

As previously mentioned, the formation of spanwise-coherent rollers in turbulent flows over permeable substrates is a common phenomenon, with several studies reporting their appearance. These structures develop in the flow as a result of the relaxation of the impermeability condition at the wall and their onset has been typically attributed to a Kelvin-Helmholtz-like instability. Recently, Abderrahaman-Elena & García-Mayoral (2017) conducted a linear stability analysis about a mean flow to capture the onset of this instability over poorly-connected, anisotropic permeable substrates, based on a Darcy model for the substrate. In chapter 3, we will extend the analysis to highly-connected permeable substrates, which are more suitable for drag-reducing purposes.

The applicability of a mean flow stability analysis to predict coherent structures or unsteady features in turbulent flows, when turbulence is nonlinear and unsteady, can be questionable. Notwithstanding, this approach has been used for many years and for a variety of problems, obtaining surprisingly satisfactory results (Barkley, 2006; del Álamo & Jiménez, 2006; Mittal, 2008; Pujals *et al.*, 2009; Gudmundsson & Colonius, 2011; García-Mayoral & Jiménez, 2011; Jiménez, 2013*a*), which raises the question of how such a crude approach can lead to such accurate predictions. It can be argued that, although turbulence is nonlinear, some phases of turbulence are dominated by linear processes (Jiménez, 2013*a*). In shear flows, for instance, the mean velocity gradient is identified as the energy source, and energy is fed into turbulence through the interaction of that gradient with the transverse velocity fluctuations (Tennekes & Lumley, 1972), a mechanism that is also present in the linearised Navier-Stokes equations. But a formal mathematical justification for the validity of this approach is yet to be derived. There have been a few studies in the literature devoted to address this question (Barkley, 2006; Sipp & Lebedev, 2007; Turton *et al.*, 2015). Progress towards a formal justification has been made by Beneddine *et al.* (2016), who, using a resolvent analysis, concluded that a mean flow stability analysis can be used to capture

spatio-temporal features in a flow as long as the instability is convective and there is a clear scale separation between the turbulent fluctuations and the instability. In any event, previous studies have already demonstrated the ability of a mean flow stability analysis to predict the appearance of Kelvin-Helmholtz instabilities in turbulent flows over complex surfaces (Jiménez *et al.*, 2001; Dupont *et al.*, 2010; García-Mayoral & Jiménez, 2011; Abderrahaman-Elena & García-Mayoral, 2017). In chapter 5, we follow the above works and use the same approach to capture the Kelvin-Helmholtz-like instabilities over anisotropic permeable substrates.

1.7 Objectives and organisation of the thesis

The aim of the present thesis is to understand how the overlying turbulent flow is affected by the presence of anisotropic permeable substrates and investigate whether these substrates can reduce skin friction. To that end, in chapters 3 and 4 we explore the drag-reducing mechanism for complex surfaces and extend the existing virtual-origin theory, which can also be applied to permeable substrates. In chapter 7 we perform a series of DNSs of channel flows bounded by permeable substrates, which are selected using the information obtained from a linear stability theory and the virtual-origin theory for drag reduction previously developed, detailed in chapters 5 and 6. In more detail, the objectives of the remaining seven chapters are the following:

Chapter 2 outlines the numerical methods used. It provides the analytical solution of the flow within the permeable substrate and describes code used for the the direct numerical simulation of the channel flow, with a special emphasis on the implementation of complex boundary conditions.

Chapter 3 extends the existing understanding of the virtual-origin theory for drag reduction presented in section 1.3. This chapter explores several techniques to define and implement different virtual origins for the three velocity components, with the ultimate goal of developing simplified models that mimic the effect of complex surfaces on the overlying flow. By accounting also for the effect of the wall-normal transpiration, this chapter provides a generalisation of Luchini's expression (1.5) to predict the change in drag. In essence, the chapter offers a general perspective into the effect that complex surfaces have on the overlying flow and the drag, without focusing on any particular complex surface.

Chapter 4 reviews a variety of surface textures, namely riblets, superhydrophobic surfaces, permeable substrates and canopies. Using the virtual-origin model from chapter 3, this chapter intends to provide a unified framework to explain the effect that these surfaces have on the overlying flow and the change in drag.

Chapters 5-7 are devoted to turbulent flows over anisotropic permeable substrates and aim to understand the effect that such substrates have on the overlying flow, focusing on their drag reduction ability.

Chapter 5 studies, using linear stability analysis, the formation of Kelvin-Helmholtz-like instabilities over anisotropic permeable substrates, which is a potential breakdown mechanism for drag-reducing substrates, and proposes a predictive model to characterise their onset.

Chapter 6 provides theoretical models to estimate the drag-reducing behaviour of anisotropic permeable substrates, based on the virtual-origin theory from chapter 3 and the model for the onset of Kelvin-Helmholtz-like instabilities from chapter 5. It bounds the permeability range of interest for the subsequent campaign of DNSs.

Chapter 7 presents and discusses the results from DNSs of channel flows bounded by identical permeable substrates and reassesses the validity of the previous theoretical models. In addition, based on the drag-reduction curves obtained for different anisotropic permeable substrates, this chapter provides design guidelines for optimal configurations.

Finally, **Chapter 8** summarises the main conclusions obtained in this thesis and includes some recommendations for future work.

Chapter 2

Models and numerical methods*

This chapter presents the numerical methods used in this thesis. Section 2.1 details the analytical solution of the flow within the permeable substrate, which is used in chapters 5, 6 and 7 for the linear stability analysis and Direct Numerical Simulations (DNSs) of turbulent channel flows bounded by permeable substrates. The DNS code of a fully-turbulent, three dimensional channel flow is outlined in section 2.2. This code is used in chapter 7 to simulate the flow over permeable substrates, as well as in chapter 3 to model the effect of virtual origins on the overlying flow. The code is adapted from García-Mayoral & Jiménez (2011) and Fairhall & García-Mayoral (2018), which was originally developed to study turbulent flows over riblets and superhydrophobic surfaces. The modifications introduced allow the implementation of complex boundary conditions, with a fully implicit coupling between the velocities and the pressure at the boundaries. This will allow us to couple the solution within the permeable substrate to that within the channel on one hand, and to explore different techniques to impose virtual origins on the other. Finally, the validation for Brinkman's model for the substrate is presented in section 2.4, followed by a study to understand the effect of the different terms that appear in the solution of Brinkman's equation in section 2.5.

2.1 Analytical solution of Brinkman's equation

To study the flow over permeable substrates, we consider channels of height 2δ delimited by two identical anisotropic permeable substrates of thickness h, as sketched in figure 1.9. The substrate-channel interfaces are located at $y = 0$ and $y = 2\delta$, and the substrates are bounded by impermeable walls at $y = -h$ and $y = 2\delta + h$. Henceforth, we will refer to the free-flow region between $y = 0$ and $y = 2\delta$ as 'channel' and to the permeable region below $y = 0$ (or above $y = 2\delta$) as 'substrate'. As mentioned before, the flow within the permeable substrates

*Parts of the content of this chapter have been published in *Flow, Turbulence and Combustion*, 100 (4), 995 – 1014, with Akshath Sharma and Ricardo García-Mayoral as co-authors, and in *Journal of Fluid Mechanics*, 875, 124 – 172, with Ricardo García-Mayoral as co-author.

is modelled using a homogenised equation – Brinkman's equation, given by equation (2.1). For reference, we rewrite below Brinkman's equation from chapter 1,

$$\nabla p = -\nu \boldsymbol{K}^{-1}\boldsymbol{u} + \tilde{\nu}\nabla^2\boldsymbol{u}. \tag{2.1}$$

The simplicity of this equation allows us to solve it analytically, and the particular solution at the substrate-channel interface can be implemented as boundary condition for the overlying channel flow, fully coupling the flow in both regions. The procedure to solve Brinkman's equation is detailed in appendix A. Here only the problem formulation and its solution are presented.

As discussed chapter 1, poorly-connected substrates have negligible macroscale viscous effects, which in equation (2.1) can be interpreted as having $\tilde{\nu} = 0$, recovering Darcy's equation. Highly-connected substrates, in turn, would asymptotically tend to have macroscale diffusion as efficient as a free flow, so $\tilde{\nu} \approx \nu$ (Tam, 1969; Neale & Nader, 1974; Lévy, 1983; James & Davis, 2001; Abderrahaman-Elena & García-Mayoral, 2017). Abderrahaman-Elena & García-Mayoral (2017) suggested that such materials would have a better potential for drag reduction, as it will be later discussed in chapter 6. Here we follow their approach and assume $\tilde{\nu} = \nu$. The permeable substrates are then characterised by the thickness, h, and the permeabilities K_x, K_y and K_z in the streamwise, x, wall-normal, y, and spanwise, z, directions, respectively, which are considered to be the principal directions of the permeability tensor $\boldsymbol{K}$ in equation (2.1). The tensor has dimensions of length squared, and is a measure of the ability of the fluid to flow through a permeable medium. When $\boldsymbol{K} \to \infty$ the medium offers no resistance to the flow, and when $\boldsymbol{K} = 0$ an impermeable medium is recovered.

Let us consider the lower substrate between $y = -h$ and $y = 0$. Since Brinkman's equation is second order in velocity, it can be matched to the second-order Navier-Stokes equations for the overlying flow, allowing us to accommodate a complete set of boundary conditions. To solve equation (2.1), we impose no slip and impermeability at $y = -h$, and continuity of the tangential and normal stresses at the substrate-channel interface, i.e. at $y = 0$. The solution within the substrate will be later coupled to the flow within the channel by imposing the continuity of the three velocity components. The resulting boundary conditions at $y = 0$ are then

$$\nu\left[\frac{\partial u}{\partial y} + \frac{\partial v}{\partial x}\right]_{y=0^+} = \tilde{\nu}\left[\frac{\partial u}{\partial y} + \frac{\partial v}{\partial x}\right]_{y=0^-}, \tag{2.2a}$$

$$\nu\left[\frac{\partial w}{\partial y} + \frac{\partial v}{\partial z}\right]_{y=0^+} = \tilde{\nu}\left[\frac{\partial w}{\partial y} + \frac{\partial v}{\partial z}\right]_{y=0^-}, \tag{2.2b}$$

$$\left[-p + 2\nu\frac{\partial v}{\partial y}\right]_{y=0^+} = \left[-p + 2\tilde{\nu}\frac{\partial v}{\partial y}\right]_{y=0^-}, \tag{2.2c}$$

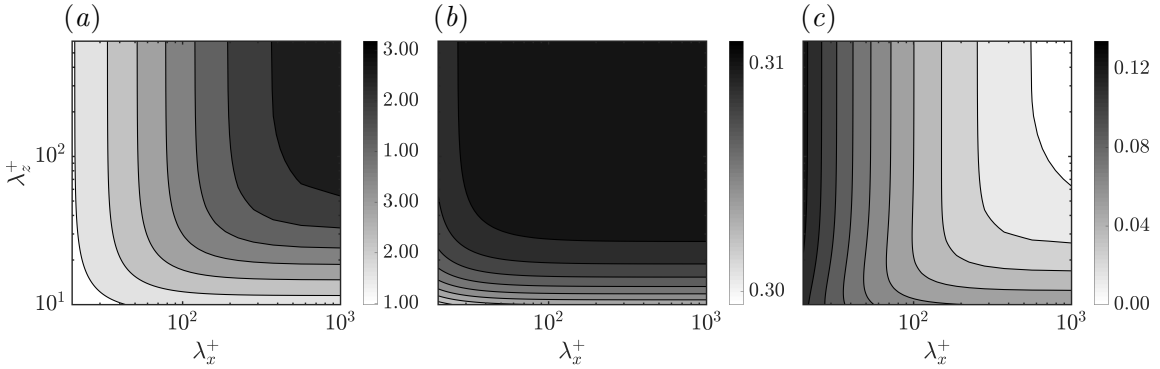

FIGURE 2.1 Maps of (*a*) $\mathcal{C}_{uu}^+$, (*b*) $\mathcal{C}_{ww}^+$ and (*c*) $-\mathcal{C}_{vp}^+$, from equation (2.3), as a function of the wavelengths λ_x^+ and λ_z^+ for substrate C4 in table 7.1, with $K_x^+ = 13$, $K_y^+ = K_z^+ = 0.1$ and $h^+ = 32$.

where $y = 0^+$ and $y = 0^-$ correspond to the channel and the substrate sides of the interface, respectively. Under the above assumptions, the boundary conditions (2.2) can be further simplified. The continuity of tangential stresses becomes that of $\partial u/\partial y$ and $\partial w/\partial y$, and the continuity of normal stresses that of p. Equation (2.1) is then solved by taking Fourier transforms in the tangential directions (x, z). Following the derivations presented in appendix A, the analytical solution at $y = 0$ provides the following expressions for the velocities,

$$\hat{u}|_{y=0^+} = \hat{u}|_{y=0^-} = \mathcal{C}_{uu}\frac{d\hat{u}}{dy}\bigg|_{y=0^+} + \mathcal{C}_{uw}\frac{d\hat{w}}{dy}\bigg|_{y=0^+} + \mathcal{C}_{up}\hat{p}|_{y=0^+}\,, \tag{2.3a}$$

$$\hat{w}|_{y=0^+} = \hat{w}|_{y=0^-} = \mathcal{C}_{wu}\frac{d\hat{u}}{dy}\bigg|_{y=0^+} + \mathcal{C}_{ww}\frac{d\hat{w}}{dy}\bigg|_{y=0^+} + \mathcal{C}_{wp}\hat{p}|_{y=0^+}\,, \tag{2.3b}$$

$$\hat{v}|_{y=0^+} = \hat{v}|_{y=0^-} = \mathcal{C}_{vu}\frac{d\hat{u}}{dy}\bigg|_{y=0^+} + \mathcal{C}_{vw}\frac{d\hat{w}}{dy}\bigg|_{y=0^+} + \mathcal{C}_{vp}\hat{p}|_{y=0^+}\,, \tag{2.3c}$$

where the hat denotes variables in Fourier space. The coefficients $\mathcal{C}_{ij}$ with $i = \{u, w, v\}$ and $j = \{u, w, p\}$ are complex numbers and depend on the structure of the permeable substrate through K_x, K_y, K_z and h, as well as on the overlying flow through the streamwise and spanwise wavenumbers, α_x and α_z, or the corresponding wavelengths, $\lambda_x = 2\pi/\alpha_x$ and $\lambda_z = 2\pi/\alpha_z$. In appendix A we express them as $\mathcal{C}_{ij}(\alpha_x, \alpha_z)$ for completeness. The same procedure can be used to obtain a symmetric solution for the upper substrate, and the resulting expressions for the interface at $y = 2\delta$ are stated in appendix A. The effect of the permeable substrates on the channel flow is therefore introduced through equations (2.3) and the corresponding equations at $y = 2\delta$, which serve as boundary conditions.

To illustrate how the coefficients in equation (2.3) vary with the wavelengths, figure 2.1 shows maps of $\mathcal{C}_{uu}^+$, $\mathcal{C}_{ww}^+$ and $\mathcal{C}_{vp}^+$, which have zero imaginary part, as a function of λ_x^+ and λ_z^+ for a particular substrate. The coefficient $\mathcal{C}_{vp}^+$ represents an impedance relating the wall-

normal velocity and the pressure (Jiménez *et al.*, 2001), and $\mathcal{C}_{uu}^{+}$ and $\mathcal{C}_{ww}^{+}$ relate the streamwise and spanwise velocities with their corresponding wall-normal gradients, respectively. The latter two are equivalent to the slip lengths ℓ_x^+ and ℓ_z^+ introduced in chapter 1, which define the slip boundary conditions typically used in slip-only simulations (Hahn *et al.*, 2002; Min & Kim, 2004; Busse & Sandham, 2012). The slip coefficients $\mathcal{C}_{uu}^{+}$ and $\mathcal{C}_{ww}^{+}$ are purely real, so the tangential velocity is in phase with the tangential shear, whereas the transpiration coefficient $\mathcal{C}_{vp}^{+}$ is also real but negative, so the wall-normal velocity is in anti-phase with the pressure. For the mean flow, i.e. $\alpha_x^+ = 0$ and $\alpha_z^+ = 0$ (or alternatively $\lambda_x^+ \to \infty$ and $\lambda_z^+ \to \infty$), out of the 9 coefficients from equation (2.3) only $\mathcal{C}_{uu}^{+}$ and $\mathcal{C}_{ww}^{+}$ are non-zero and their value decreases as the wavelengths decrease, as shown in figure 2.1. In contrast, the transpiration coefficient $\mathcal{C}_{vp}^{+}$ is zero for the mean flow and becomes increasingly negative as the wavelengths decrease, since smaller eddies penetrate more easily through the substrate.

2.2 Numerical method for the direct numerical simulations of the channel flow

The channel flow between $y \in [0, 2\delta]$ is governed by the incompressible Navier-Stokes equations,

$$\boldsymbol{\nabla} \cdot \boldsymbol{u} = 0, \tag{2.4a}$$

$$\frac{\partial \boldsymbol{u}}{\partial t} + \boldsymbol{u} \cdot \boldsymbol{\nabla} \boldsymbol{u} = -\nabla p + \frac{1}{Re} \nabla^2 \boldsymbol{u}, \tag{2.4b}$$

where p is the kinematic pressure, $\boldsymbol{u} = (u, v, w)$ the velocity vector, ν the viscosity of the fluid and Re the bulk Reynolds number, defined as $Re = U_b \delta / \nu$, with U_b being the bulk velocity in the channel region.

As mentioned before, the DNS code is adapted from García-Mayoral & Jiménez (2011) and Fairhall & García-Mayoral (2018). It solves the incompressible Navier-Stokes equations (2.4) in a doubly-periodic channel of height 2δ, where $\delta = 1$ is the distance between the substrate-channel interface and the centre of the channel. In this section, we outline the main features of the DNS code, with special emphasis on the implementation of complex boundary conditions. A more detailed description of the code can be found in Fairhall (2019).

2.2.1 Spatial discretisation

The spatial discretisation is spectral in the wall-parallel directions x and z, and the code uses second-order centred finite differences on a staggered grid in the wall-normal direction, y. One advantage of using spectral methods is their high accuracy, as the error in the computed derivatives decreases exponentially with increasing the number of grid points, as opposed to algebraically for finite-difference methods (Canuto *et al.*, 1988; Ferziger & Perić, 2002).

This reduces the number of grid points necessary to achieve the same degree of accuracy. For a smooth channel, the spatial resolution is that required to accurately capture all the relevant turbulent scales, which in the wall-parallel directions corresponds to $\Delta x^+ \lesssim 8$ and $\Delta z^+ \lesssim 4$ (Jiménez & Moin, 1991; Moin & Mahesh, 1998). With surface textures, however, the resolution requirement is set by the need to accurately capture the flow near each individual surface texture, which requires generally a higher resolution than that set by turbulence. In this thesis, however, we will not be representing the geometry of the permeable substrate. Instead, the substrate is modelled with the homogenised Brinkman equation and the solution is coupled to the channel through the interface conditions obtained in section 2.1. The resolution required in this thesis is therefore set by the near-wall turbulence, i.e. $\Delta x^+ \lesssim 8$ and $\Delta z^+ \lesssim 4$. The code has a multi-block feature to alleviate the computational cost of resolving flow over textured surfaces, but it is not needed here and therefore not used.

Another benefit of using Fourier series is the simplified form of linear partial differential equations (PDEs), as derivatives become products in Fourier space, i.e. for a certain function $f(x)$, the derivative is $\widehat{df/dx} = i\alpha\hat{f}(\alpha)$, where, as before, the hat denotes variables in Fourier space and α is the wavenumber. As a result, the linear differential equations are decoupled between different modes when expressed in the base of Fourier modes. Given that in our code the nonlinear terms are treated explicitly, as it will be shown in the next subsection, the spectral discretisation allows us to solve the implicit part of the Navier-Stokes equations independently for each streamwise and spanwise mode pair (α_x, α_z), which reduces the computational cost substantially. The discretisation in the wall-normal direction is second order centred finite difference, so the overall discretisation produces tridiagonal linear problems, which can be solved efficiently by an LU decomposition. The code therefore solves a separate set of equation with tridiagonal matrices for each mode pair (α_x, α_z), which is substantially cheaper than solving the large set of equations with sparse matrices otherwise obtained when a finite-difference discretisation is used in the three directions.

On the other hand, the drawback of using Fourier series is that the nonlinear advective terms in equation (2.4) result in a convolution in Fourier space. This convolution would be computationally expensive to compute, as it would require $\mathcal{O}(N^2)$ operations, with N being the number of grid points. To circumvent this, the product is computed in physical space, with a 2/3 rule de-aliasing (Orszag, 1971; Ferziger & Perić, 2002). The overall cost of calculating the nonlinear term in one direction would then be the sum of the costs of transforming the velocities into physical space via a Fast Fourier Transform, $\mathcal{O}(N\log_2 N)$; computing the product, $\mathcal{O}(N)$; and transforming back to Fourier space, $\mathcal{O}(N\log_2 N)$, which is in overall cheaper than computing the convolution.

The inhomogeneity in the wall-normal direction requires higher resolution of the flow near the walls. We therefore use a non-uniform grid in y, where the grid resolution is finest near the wall and it coarsens towards the centre of the channel. The simplest grid would store the three velocity components and the pressure at the same grid points, which is referred to as a

'collocated' grid. This, however, can introduce the so-called 'chequerboard' problem when solving the pressure. The pressure is obtained by solving a Poisson equation to impose the incompressibility condition, which includes second order derivatives (see equation (2.7b)). When using second order centred finite differences, the second order derivatives, treated as the divergence of the gradient, at each grid point do not depend on the adjacent points, but use the values of two grid points apart. That is, the derivative at grid point j depends on the grid points $j+2$, j and $j-2$. This leads to two disconnected pressure fields, those evaluated at even and odd grid points. A staggered arrangement in the wall-normal direction (Ferziger & Perić, 2002), which was implemented in the code by Fairhall *et al.* (2019), solves this problem. The grid points for the wall-normal velocity are then offset from the pressure grid points, so that the adjacent points are used when calculating the second derivatives of the pressure. Only the grid points for the wall-normal velocity are staggered, as the streamwise and spanwise directions are discretised spectrally, and the grid is set so that the wall-normal velocities include the boundary planes. This requires the addition of 'ghost points' immediately below the bottom boundary and above the top one, so that the streamwise and spanwise velocities can be interpolated at the boundaries and appropriate boundary conditions imposed.

2.2.2 Temporal discretisation

A Runge-Kutta discretisation is used for the temporal integration. Every time step is divided into three substeps, each of which uses a semi-implicit scheme for the viscous terms and an explicit scheme for the advective terms. Discretised this way, the Navier-Stokes equations in (2.4) result in

$$\mathrm{D}(\boldsymbol{u}^k) = 0, \tag{2.5a}$$

$$\frac{\boldsymbol{u}^k - \boldsymbol{u}^{k-1}}{\Delta t} = \frac{\alpha_k}{Re}\mathrm{L}(\boldsymbol{u}^{k-1}) + \frac{\beta_k}{Re}\mathrm{L}(\boldsymbol{u}^k) - \gamma_k \mathrm{N}(\boldsymbol{u}^{k-1}) - \zeta_k \mathrm{N}(\boldsymbol{u}^{k-2}) - (\alpha_k + \beta_k)\,\mathrm{G}(p^k), \tag{2.5b}$$

where L, G and D represent the discretised Laplacian, gradient and divergence operators, respectively, and N represents the nonlinear, advective operator. The superscript $k = 1, 2, 3$ denotes the Runge-Kutta substep. Hence, the velocities $\boldsymbol{u}^0$ and $\boldsymbol{u}^3$ correspond to the velocities at time-step n and $n+1$, respectively. Additionally, α_k, β_k, γ_k and ζ_k are the Runge-Kutta coefficients for substep k from Le & Moin (1991), which are listed in table 2.1.

Equation (2.5) can be rearranged as

$$\begin{aligned}\left[I - \Delta t\frac{\beta_k}{Re}\mathrm{L}\right]\boldsymbol{u}^k = \boldsymbol{u}^{k-1} + \Delta t\Big[&\frac{\alpha_k}{Re}\mathrm{L}(\boldsymbol{u}^{k-1}) - \gamma_k \mathrm{N}(\boldsymbol{u}^{k-1}) \\ &- \zeta_k \mathrm{N}(\boldsymbol{u}^{k-2}) - (\alpha_k + \beta_k)\,\mathrm{G}(p^k)\Big],\end{aligned} \tag{2.6a}$$

$$\mathrm{D}(\boldsymbol{u}^k) = 0, \tag{2.6b}$$

	$k=1$	$k=2$	$k=3$
α_k	$4/15$	$1/15$	$1/6$
β_k	$4/15$	$1/15$	$1/6$
γ_k	$8/15$	$5/12$	$3/4$
ζ_k	0	$-17/60$	$-5/12$

TABLE 2.1 Values of the Runge-Kutta coefficients from Le & Moin (1991) used herein.

where the velocity at substep k is expressed in terms of the velocities at the previous substeps, as well as the pressure at that same substep k. To solve equation (2.6), a fractional step method is integrated in each substep (Kim & Moin, 1985; Le & Moin, 1991). This method is essentially a time-splitting scheme, similar to a predictor-corrector scheme. In the predictor step, the velocity is advanced using equation (2.6a), but with the pressure obtained from the previous substep. This velocity, here referred to as intermediate velocity u^*, is non-solenoidal. In the corrector step, the pressure is calculated so that its gradient projects the intermediate velocity into a divergence-free velocity field. The resulting algorithm is,

$$\left[I - \Delta t \frac{\beta_k}{Re}\mathrm{L}\right] \boldsymbol{u}^* = \boldsymbol{u}^{k-1} + \Delta t \left[\frac{\alpha_k}{Re}\mathrm{L}(\boldsymbol{u}^{k-1}) - \gamma_k \mathrm{N}(\boldsymbol{u}^{k-1}) - \zeta_k \mathrm{N}(\boldsymbol{u}^{k-2}) - (\alpha_k + \beta_k)\,\mathrm{G}(p^{k-1})\right] \tag{2.7a}$$

$$\Delta t\,(\alpha_k + \beta_k)\,\mathrm{DG}(\Delta p^k) = \mathrm{D}(\boldsymbol{u}^*), \tag{2.7b}$$

$$\boldsymbol{u}^k = \boldsymbol{u}^* - \Delta t\,(\alpha_k + \beta_k)\,\mathrm{G}(\Delta p^k), \tag{2.7c}$$

$$p^k = p^{k-1} + \Delta p^k. \tag{2.7d}$$

The algorithm is essentially that of Le & Moin (1991), except that the pressure is corrected in every substep.

The presence of permeable substrates is accounted for by the boundary conditions (2.3). Similar boundary conditions are also applied for the virtual-origin models explored in chapter 3. Viewing the fractional step method as a time-splitting scheme as above, the problem arises of how to implement these boundary conditions into the method, as boundary conditions for the intermediate velocity u^* and pressure would be required. This problem can be solved by interpreting the fractional step method as a LU-block decomposition of the Navier-Stokes equations, as proposed by Perot (1993, 1995). The discretised Navier-Stokes equations from (2.6) can be expressed in matrix form,

$$\begin{pmatrix} \mathrm{A} & \Delta t(\alpha_k + \beta_k)\mathrm{G} \\ \mathrm{D} & 0 \end{pmatrix} \begin{pmatrix} \boldsymbol{u}^k \\ p^k \end{pmatrix} = \begin{pmatrix} \boldsymbol{r} \\ 0 \end{pmatrix}, \tag{2.8}$$

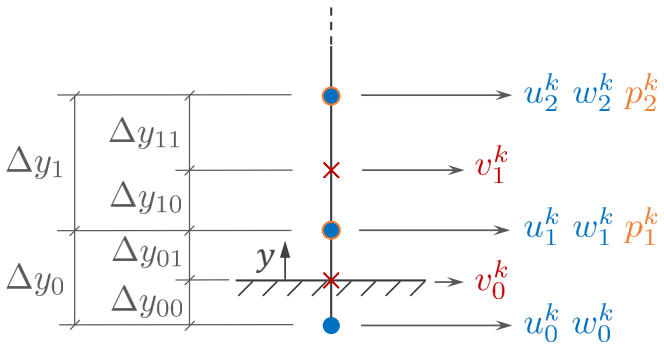

FIGURE 2.2 Schematic of the staggered grid near the bottom boundary. ×, wall-normal velocity grid points; ●, streamwise and spanwise velocity grid points, including the ghost point; ○, pressure grid points.

where $\boldsymbol{u}^k$ and p^k are the discrete velocity and pressure unknowns, respectively. A is the operator containing the implicit terms of the velocity. For the internal points of the domain, from equation (2.6a) they are $\mathrm{A} = [I - \Delta t \frac{\beta_k}{\mathrm{Re}} \mathrm{L}]$. The vector $\boldsymbol{r}$ is the explicit right-hand side, which contains all the quantities from previous time-steps. Note that the operators and the right-hand side vector depend on the spatial and temporal discretisation schemes. Given that in our case the problem is Fourier-transformed in x and z, the linear operators are decoupled for each mode pair (α_x, α_z), and the system of equations (2.8) for each streamwise-spanwise wavenumber pair can be solved independently along the y-direction. This means that the unknown vectors $\boldsymbol{u}^k$ and p^k in equations (2.8) only include the values at the wall-normal grid points.

The boundary conditions given by equations (2.3) are imposed implicitly and are embedded in the block matrices. Note that due to the staggered grid used in this code, only the wall-normal velocity is defined at the boundary points, as shown in figure 2.2. The streamwise and spanwise velocity components at the boundaries are interpolated using the ghost points and their immediate neighbours. The pressure p^k in equation (2.11) is defined only at the internal points of the channel (Kim & Moin, 1985). Hence, to obtain the pressure at the interface, we extrapolate from the first two points into the channel. For instance, discretising equation (2.3a), the boundary condition for the streamwise velocity at the bottom boundary is imposed as

$$u_0^k \frac{\Delta y_{01}}{\Delta y_0} + u_1^k \frac{\Delta y_{00}}{\Delta y_0} = \mathcal{C}_{uu} \frac{u_1^k - u_0^k}{\Delta y_0} + \mathcal{C}_{uw} \frac{w_1^k - w_0^k}{\Delta y_0} + \mathcal{C}_{up} \left(p_1^k \frac{\Delta y_{01} + \Delta y_1}{\Delta y_1} - p_2^k \frac{\Delta y_{01}}{\Delta y_1} \right), \quad (2.9)$$

where u_0^k and w_0^k refer to the velocities at the ghost point, u_1^k and w_1^k to those at the first grid point above the boundary, and p_1^k and p_2^k to the pressure at the first and second grid points above the boundary. We use Δy_i to denote the distances between the grid points, as shown in figure 2.2. Equation (2.9) can be rearranged as

$$\underbrace{\left(\frac{\Delta y_{01}}{\Delta y_0}+\frac{\mathcal{C}_{uu}}{\Delta y_0}\right)}_{A_{11}} u_0^k+\underbrace{\left(\frac{\Delta y_{00}}{\Delta y_0}-\frac{\mathcal{C}_{uu}}{\Delta y_0}\right)}_{A_{12}} u_1^k+$$
$$\underbrace{\frac{\mathcal{C}_{uw}}{\Delta y_0}}_{A_{13}} w_0^k \underbrace{-\frac{\mathcal{C}_{uw}}{\Delta y_0}}_{A_{14}} w_1^k \underbrace{-\mathcal{C}_{up}\frac{\Delta y_{01}+\Delta y_1}{\Delta y_1}}_{G_{11}} p_1^k+\underbrace{\mathcal{C}_{up}\frac{\Delta y_{01}}{\Delta y_1}}_{G_{12}} p_2^k=0. \tag{2.10}$$

Similar expressions are obtained for the other two velocities from equation (2.3a) and their respective equations for the top interface. Implementing these boundary conditions in the system of equations (2.8), the system for a particular mode results in the modification of the following rows,

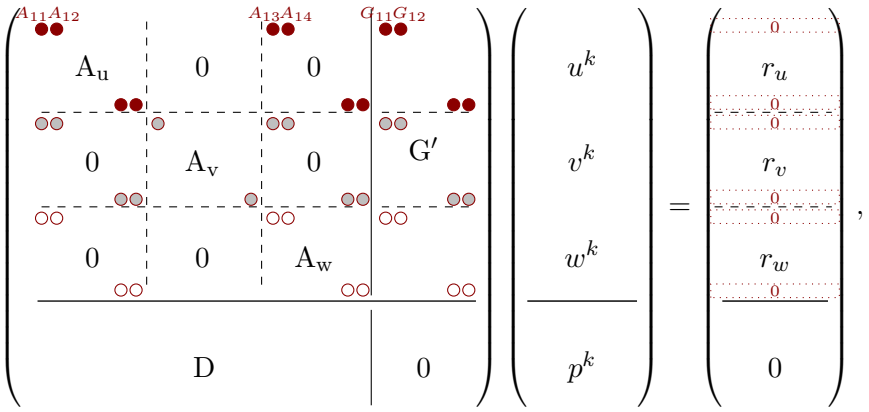

, (2.11)

where the A matrix and the vectors $\boldsymbol{u}^k$ and $\boldsymbol{r}$ from equation (2.8) have been expanded in order to introduce the boundary conditions. We have also redefined the gradient operator as $\mathrm{G}' = \Delta t(\alpha_k + \beta_k)\mathrm{G}$ for clarity, since this matrix also includes terms from the boundary equations, as illustrated by equation (2.10), and the time step $\Delta t(\alpha_k + \beta_k)$ multiplies only the internal points of the domain, excluding the rows containing the boundary conditions. The symbols in equation (2.11) refer to the non-zero matrix elements containing the terms introduced by the boundary conditions (2.3). The first row with full symbols (●), for instance, corresponds to the condition for the streamwise velocity, as given by equation (2.10), and the rows with grey (◉) and empty (○) symbols correspond to the boundary conditions for the wall-normal and spanwise velocities, respectively, as given by the discretisation of equations (2.3b) and (2.3c) and their analogous for the top boundary. Thus, the relationships between the three velocities and the tangential shears $d\hat{u}/dy$ and $d\hat{w}/dy$ are embedded in A, which is no longer tridiagonal, while the coupling between the velocities and pressure is embedded in both A and G.

Once the boundary conditions have been applied, the LU decomposition of the system (2.11) yields

$$\left(\begin{array}{c|c} \mathrm{A} & 0 \\ \hline \mathrm{D} & -\mathrm{D}\mathrm{A}^{-1}\mathrm{G}' \end{array}\right)\left(\begin{array}{c} u^* \\ v^* \\ w^* \\ \hline p^* \end{array}\right) = \left(\begin{array}{c} r_u \\ r_v \\ r_w \\ \hline 0 \end{array}\right), \tag{2.12a}$$

$$\left(\begin{array}{c|c} \mathrm{I} & \mathrm{A}^{-1}\mathrm{G}' \\ \hline 0 & \mathrm{I} \end{array}\right)\left(\begin{array}{c} u^k \\ v^k \\ w^k \\ \hline p^k \end{array}\right) = \left(\begin{array}{c} u^* \\ v^* \\ w^* \\ \hline p^* \end{array}\right), \tag{2.12b}$$

where the superscript $*$ denotes intermediate variables. The resulting algorithm is

$$\mathrm{A}\boldsymbol{u}^* = \boldsymbol{r}, \tag{2.13a}$$

$$\mathrm{D}\mathrm{A}^{-1}\mathrm{G}'p^k = \mathrm{D}\boldsymbol{u}^*, \tag{2.13b}$$

$$\boldsymbol{u}^k = \boldsymbol{u}^* - \mathrm{A}^{-1}\mathrm{G}'p^k. \tag{2.13c}$$

Solving the Poisson equation (2.13b) is computationally expensive, as it requires the inversion of matrix A at every iteration. For efficiency, A^{-1} is generally approximated to its first order term, $\approx \mathrm{I}$, since $\mathrm{A} = \mathrm{I} + \mathcal{O}(\Delta t)$ and hence $\mathrm{A}^{-1} = \mathrm{I} + \mathcal{O}(\Delta t)$ (Kim & Moin, 1985; Le & Moin, 1991). However, this is only applicable for the internal points. In the present work, we approximate the internal points in A by I, while keeping the rows of A that contain the boundary conditions unchanged, and then invert the resulting matrix to obtain A^{-1}. Approximating the internal points in A^{-1} to the first order produces an error $\Delta t\beta_k/\mathrm{ReL}$, which is of order $\mathcal{O}(\Delta t)$, and the accuracy of the method is therefore first order in time.

As proposed by Simens (2008), the accuracy of the velocities can be improved to second order in time by solving for the change of pressure, Δp^k, rather than the pressure, where $p^k = p^{k-1} + \Delta p^k + \mathcal{O}(\Delta t^2)$ with $\Delta p^k \sim \mathcal{O}(\Delta t)$. Expressing the system (2.13) in terms of Δp^k results in

$$\mathrm{A}\boldsymbol{u}^* = \tilde{\boldsymbol{r}}, \tag{2.14a}$$

$$\mathrm{D}\mathrm{A}^{-1}\mathrm{G}'\Delta p^k = \mathrm{D}\boldsymbol{u}^*, \tag{2.14b}$$

$$\boldsymbol{u}^k = \boldsymbol{u}^* - \mathrm{A}^{-1}\mathrm{G}'\Delta p^k, \tag{2.14c}$$

$$p^k = p^{k-1} + \Delta p^k, \tag{2.14d}$$

where the pressure gradient from the previous iteration is now included in the right-hand side, $\tilde{\boldsymbol{r}} = \boldsymbol{r} - \Delta t(\alpha_k + \beta_k)\mathrm{G}p^{k-1}$. When approximating A^{-1} as detailed above, the error is

now $\Delta t/\mathrm{ReL}\Delta p^k \sim \mathcal{O}(\Delta t^2)$ and the method is second order in time for the velocities. The pressure, however, remains first order in time, but it does not affect the order of accuracy of the velocity field, as it is updated at each time-step from the velocities. Notice also that, when approximating A^{-1} and neglecting the viscous part of the operator, we are neglecting terms of order $1/\Delta y^2$, which due to the grid stretching, are greater near the boundaries than away from them.

The system of equations (2.14) obtained by the LU-block decomposition is similar to the traditional fractional step method given by equations (2.7). However, the subtle, but significant, differences in the A and, specially, G′ blocks allow us to implement the boundary conditions with a fully implicit coupling of velocity and pressure. This coupling has been observed to become easily unstable when implemented explicitly (Encinar *et al.*, 2014; Seo *et al.*, 2018).

Implementation of virtual origins using Robin boundary conditions

In chapter 3, one of the techniques to model virtual origins consists of imposing Robin boundary conditions of the form,

$$\hat{u}|_{y=0} = \ell_x \frac{d\hat{u}}{dy}\bigg|_{y=0}, \qquad \hat{v}|_{y=0} = \ell_y \frac{d\hat{v}}{dy}\bigg|_{y=0}, \qquad \hat{w}|_{y=0} = \ell_z \frac{d\hat{w}}{dy}\bigg|_{y=0}. \tag{2.15}$$

Discretising equation (2.15) and rearranging yields

$$\underbrace{\left(\frac{\Delta y_{01}}{\Delta y_0} + \frac{\ell_x}{\Delta y_0}\right)}_{A_{u11}} u_0^k + \underbrace{\left(\frac{\Delta y_{00}}{\Delta y_0} - \frac{\ell_x}{\Delta y_{00}}\right)}_{A_{u12}} u_1^k = 0, \tag{2.16a}$$

$$\underbrace{\left(1 + \frac{\ell_y}{\Delta y_{01} + \Delta y_{10}}\right)}_{A_{v11}} v_0^k \underbrace{- \frac{\ell_y}{\Delta y_{01} + \Delta y_{10}}}_{A_{v12}} v_1^k = 0, \tag{2.16b}$$

$$\underbrace{\left(\frac{\Delta y_{01}}{\Delta y_0} + \frac{\ell_z}{\Delta y_0}\right)}_{A_{w11}} w_0^k + \underbrace{\left(\frac{\Delta y_{00}}{\Delta y_0} - \frac{\ell_z}{\Delta y_0}\right)}_{A_{w12}} w_1^k = 0, \tag{2.16c}$$

where the different velocities and distances Δy_i refer to those illustrated in figure 2.2. To calculate the gradient of $\hat{v}$ at the boundary, the velocities v_0^k and v_1^k are used, which maintains the tridiagonal character of matrix A. Implementing boundary conditions (2.16) and their symmetric for the upper wall, the system of equations to solve is

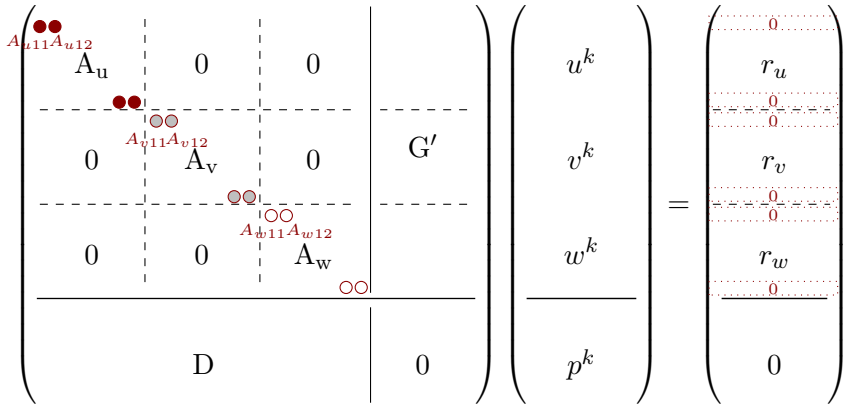

(2.17)

where matrix A is block-diagonal and contains blocks A_u, A_v and A_w with red (●), grey (◉) and empty (○) symbols referring to the non-zero terms of the boundary conditions for the streamwise, wall-normal and spanwise velocities, i.e. equations (2.16a), (2.16b) and (2.16c), respectively. The system of equations (2.17) is solved again by performing an LU-block decomposition, yielding an algorithm analogous to (2.14).

2.3 Simulation set-up for DNSs

For the channel simulations in this thesis, the computational domain is of size $2\pi\delta \times \pi\delta \times 2\delta$ in the streamwise, spanwise and wall-normal directions, respectively, with the half-channel height δ taken as unity in all cases. It was shown by Lozano-Durán & Jiménez (2014) that this domain is sufficiently large to accurately capture the lengthscales active in the logarithmic layer. Unless otherwise stated, the simulations are conducted at a fixed friction Reynolds number $\delta^+ = u_\tau \delta/\nu \approx 180$ by imposing a constant mean pressure gradient in the channel region, $y \in [0, 2]$. The kinematic viscosity is $\nu = 1/2870$ and we use a smooth-wall channel with the same mean pressure gradient as a reference. This is the case for the simulations presented in chapters 3 and 7. For those presented in the next sections, however, a constant mass flow rate is imposed in order to reproduce the results from previous studies.

Traditionally, in channel flows simulations are conducted either at a constant mass flow rate or at a constant pressure gradient, allowing the other to fluctuate in time. At a constant mass flow rate, the bulk velocity, U_b, is fixed and a drag reduction manifests through a reduction of the friction velocity, u_τ, which results in a reduction of the friction Reynolds number δ^+. If the friction Reynolds number of the reference smooth wall is low, this method may, in a drag reduction simulation, lead to a relaminarisation of the flow, which would not occur at the large Reynolds numbers of most applications. At constant pressure gradient, on the other hand, the friction velocity, u_τ, is fixed, and drag reduction results in an increase of flow rate or U_b. The choice of which approach to use depends on the specific application. The implications of using each one of the two approaches were discussed by Frohnapfel *et al.*

Cases	ϵ	$\tilde{\nu}/\nu$	δ^+	K^+	δ_w/δ	δ_i/δ	$c_f(\times 10^{-3})$	$c_{f_0}(\times 10^{-3})$	$\Delta D\,\%$
BB_E80	0.8	-	203	1.14	1.12	0.04	10.41	8.19	27.15
BB_Br	-	1.0	204	1.19	1.11	-	10.34	8.07	28.06

TABLE 2.2 Characteristics of the simulations for VANS approach (BB_E80) and Brinkman's (BB_Br). Porosity, ϵ; viscosity ratio, $\tilde{\nu}/\nu$; friction Reynolds number, $\delta^+ = u_\tau \delta/\nu$; permeability, $K^+ = K u_\tau^2/\nu^2$; location of zero total stress, δ_w; thickness of the interfacial region, δ_i; friction coefficient, $c_f = 2(u_\tau/U_b)^2$; friction coefficient of the corresponding smooth channel, c_{f_0}; and change of drag defined as $\Delta D = 100\,(c_f - c_{f_0})/c_{f_0}$. Viscous units are defined with u_τ measured at the reference plane $y = 0$.

(2012). They also considered a third approach, constant power input, where the product of flow rate and pressure gradient is kept constant in time, while both the pressure gradient and the flow rate fluctuate in time. The statistically steady state of a channel flow, however, is independent of the particular choice, provided that the friction Reynolds number imposed when running at a constant pressure gradient and that obtained at constant mass flow rate and at constant power input are the same (Quadrio *et al.*, 2016). Furthermore, assuming that a given texture size in viscous units (in our case K_x^+, K_y^+ and K_z^+) results in the same ΔU^+ independently of the friction Reynolds number δ^+, results can be extrapolated to higher δ^+, and simulations could be run at either constant pressure gradient, constant power input, or constant mass flow rate, provided that for the latter the flow has not relaminarised (García-Mayoral *et al.*, 2019). Note, however, that the texture size, ΔU^+ and the results in general should be scaled with the friction velocity of the resulting flow, and not with that of the reference smooth wall. For convenience, in the present thesis we have chosen to run at constant pressure gradient, as in this case u_τ remains constant and consequently we can prescribe the permeabilities in wall units accurately in advance. However, we could have also fixed the texture size with constant mass flow rate by adjusting the viscosity of the fluid.

A grid with $192 \times 192 \times 153$ collocation points with grid stretching is used, which in viscous units gives a resolution of $\Delta x^+ \approx 5.9$ and $\Delta z^+ \approx 2.9$, and $\Delta y^+ \simeq 0.3$ near the wall, while the resolution in the wall-normal direction coarsens to $\Delta y^+ \simeq 3$ in the centre of the channel. For the two main set of simulations analysed in chapters 3 and 7, statistics are obtained by averaging over approximately 100 eddy-turnovers, once the statistically steady state has been reached. Such a large number of turnovers was needed to minimise the uncertainty in ΔU^+ (García-Mayoral & Jiménez, 2011). Statistical convergence was verified using the criterion of Hoyas & Jiménez (2008).

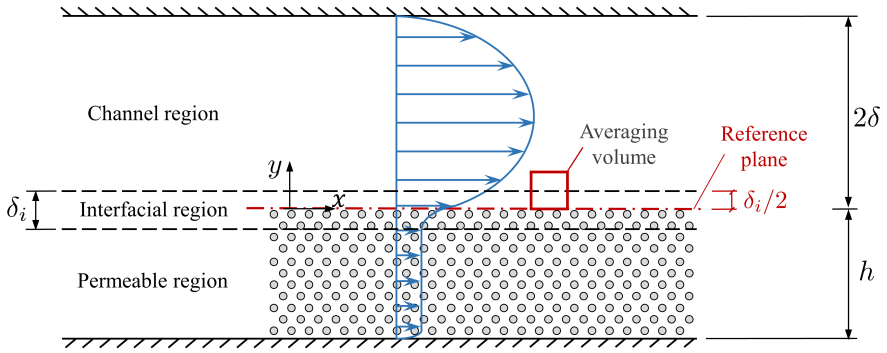

FIGURE 2.3 Sketch of the channel of Breugem *et al.* (2006) used here for validation. The red dashed-dotted line corresponds to the location of the reference plane used in the present analysis for comparison with the analogous Brinkman model, BB_Br.

2.4 Validation of Brinkman's model

We validate the Brinkman model introduced in section 2.1 with one of the cases studied by Breugem *et al.* (2006), where the authors used the VANS equations within the permeable substrate. We consider their case E80, here referred to as BB_E80, with a porosity – the ratio between the void volume and the total volume of the substrate – $\epsilon = 0.8$ and an isotropic permeability $K^+ \approx 1$. This permeability is of the same order of magnitude as our largest permeabilities K_y^+ and K_z^+ in the DNSs presented in chapter 7. The results of BB_E80 is compared to a simulation using our Brinkman model, here referred to as BB_Br, also with $K^+ \approx 1$. To match the validation domain in Breugem *et al.* (2006), we use an asymmetric channel of height 2δ, delimited by an impermeable wall at the top and a permeable substrate at the bottom, as sketched in figure 2.3, where the thickness of the permeable layer is $h = 2\delta$.

In the VANS simulation of Breugem *et al.* (2006), the porosity, and hence the permeability, evolved gradually from the inner value $\epsilon = 0.8$ to the free flow value $\epsilon = 1$ over a thin interfacial layer of thickness δ_i. This corresponded to the averaging volumes in VANS capturing varying proportions of free flow and substrate, so that the volumes centred at the top of the interfacial layer did not contain any substrate, and the volumes centred at its bottom did not contain any free flow, as illustrated in figure 2.3. This can be interpreted as VANS being applied on a set-up with a sharp interface half-way through the interfacial layer. We therefore set our reference plane $y = 0$ for BB_E80 at this height, so results from Breugem *et al.* (2006) are represented in the same frame of reference as those for our Brinkman model. Note that in Breugem *et al.* (2006) the reference plane was at the top of the interfacial region instead. For a consistent comparison, the results from Breugem *et al.* (2006) have been rescaled with the friction velocity measured at the present reference $y = 0$, and with the bulk velocity integrated between that plane and the top, impermeable smooth wall.

Both BB_Br and the original simulation of Breugem *et al.* (2006) were run at a constant mass flow rate starting from a smooth channel, at $Re = 2750$ in the latter case and $Re = 2832$

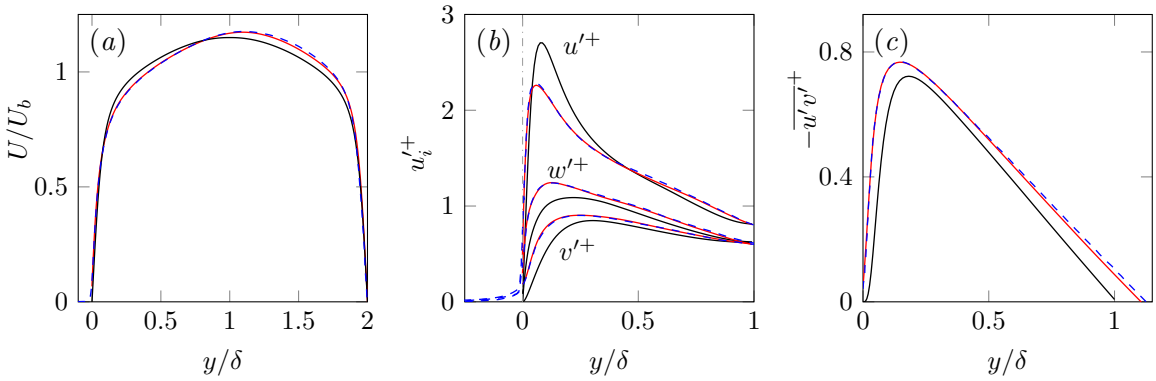

FIGURE 2.4 Comparison of a simulation from Breugem *et al.* (2006) using VANS (BB_E80), – – –, with a corresponding simulation using Brinkman's model (BB_Br), ——. The curves from Breugem *et al.* (2006) are shifted by $\delta_i/2$ to match the substrate-channel interface in both set-ups. Black lines represent smooth-channel data for reference. (*a*) Mean velocity profile, (*b*) rms (root-mean-square) velocity fluctuations, (*c*) Reynolds shear stress.

in ours. Defining viscous units using the friction velocity at $y = 0$, the initial friction Reynolds numbers were $\delta^+ = 176$ and $\delta^+ = 180$, respectively, while in the final statistically-steady state they were $\delta^+ \approx 204$ and $\delta^+ \approx 203$, respectively, and drag increases slightly compared to the smooth case. Results from Breugem & Boersma's VANS approach (BB_E80) and Brinkman's model under study (BB_Br) are compared in table 2.2 and figure 2.4, all showing good agreement.

This agreement between VANS and Brinkman's approach could be expected, given the similarities between the models for the values of the parameters considered. VANS equations can be interpreted as Brinkman's equation with the addition of the advective and temporal terms, with ϵ playing in the former the role that $\nu/\tilde{\nu}$ plays in the latter. For small permeabilities, such as those under consideration, the advective terms can be neglected. In addition, an order of magnitude analysis shows that the temporal term can also be neglected. This term is of the order $\sim \mathcal{O}(u_c/t_c)$, where u_c and t_c denote a characteristic velocity and time, respectively. When the substrate is isotropic and highly-connected (i.e. $\tilde{\nu} \approx \nu$), both the Brinkman and Darcy terms are of the same order of magnitude, as the penetration length in an isotropic substrate is of order $\sim \sqrt{K}$ (Saffman, 1971; Battiato, 2012). Comparing the temporal and Brinkman terms, we obtain

$$\frac{u_c/t_c}{\nu u_c/K} \sim \frac{K}{\nu t_c} = \frac{K^+}{t_c^+}. \tag{2.18}$$

For the temporal term to be negligible, the characteristic time should satisfy $t_c^+ > K^+$. Considering that the fastest-evolving turbulent structures near the wall are typically the quasi-streamwise vortices, with a radius $r^+ \sim 15$ and turnover velocity $\sim u_\tau$, the smallest characteristic timescale would be $t_c^+ \sim 15$, and given that $K^+ \sim 1$, the condition $t_c^+ > K^+$ is

Case	$\hat{u}^+\big\vert_{y^+=0} =$	$\hat{w}^+\big\vert_{y^+=0} =$	$\hat{v}^+\big\vert_{y^+=0} =$	δ^+	ΔD %
MK	$\ell_x^+ \frac{d\hat{u}}{dy}^+$ where $\ell_x^+ = 3.3$	$\ell_z^+ \frac{d\hat{w}}{dy}^+$ where $\ell_z^+ = 3.3$	0	165	-15
MK+J	$\ell_x^+ \frac{d\hat{u}}{dy}^+$ where $\ell_x^+ = 3.6$	$\ell_z^+ \frac{d\hat{w}}{dy}^+$ where $\ell_z^+ = 3.6$	$\beta^+ \hat{p}^+$ where $\beta^+ = -0.043$	184	+5
SES	$\mathcal{C}_{uu}^+(\alpha_x, \alpha_z) \frac{d\hat{u}}{dy}^+$ where $K_x^+ = 11.3$	$\mathcal{C}_{ww}^+(\alpha_x, \alpha_z) \frac{d\hat{w}}{dy}^+$ where $K_z^+ = 11.3$	$\mathcal{C}_{vp}^+(\alpha_x, \alpha_z)\, \hat{p}^+$ where $K_y^+ = 0.09$	168	-12
ES	eq. (2.3a), $f(\alpha_x, \alpha_z)$ where $K_x^+ = 12.9$	eq. (2.3b), $f(\alpha_x, \alpha_z)$ where $K_z^+ = 12.9$	eq. (2.3c), $f(\alpha_x, \alpha_z)$ where $K_y^+ = 0.1$	179	-1

TABLE 2.3 Boundary conditions for u^+, w^+ and v^+ for the four cases studied, including the friction Reynolds number, δ^+, and the change in drag compared to a smooth channel at $\delta_0^+ \simeq 180$, as defined by equation (2.19). The values in viscous units are scaled with the corresponding u_τ at the substrate-channel interface for each case. MK reproduces a case from Min & Kim (2004); MK+J adds a transpiration from Jiménez *et al.* (2001); SES (Simplified Equivalent Substrate) uses coefficients $\mathcal{C}_{uu}^+$, $\mathcal{C}_{ww}^+$ and $\mathcal{C}_{vp}^+$ from equation (2.3); ES (Equivalent Substrate) uses full boundary conditions (2.3).

satisfied. The flow within the permeable medium can then be assumed to be quasisteady. Additionally, for VANS and Brinkman's equation to be equivalent, the value of the porosity ϵ should be equal to the ratio $\nu/\tilde{\nu}$. In the simulations compared here, these values differ slightly, with $\epsilon = 0.8$ in BB_E80 and $\nu/\tilde{\nu} = 1$ in our model. Nonetheless, Rosti *et al.* (2015) reported that, for porosity values $\epsilon \gtrsim 0.6$, a further increase of ϵ had no significant effect on the overlying flow, and the permeability K was the only relevant parameter. This justifies the similarities between the results of the two models, even if the values of ϵ and $\nu/\tilde{\nu}$ are slightly different.

2.5 Influence of Brinkman's interface coefficients

In this section, we present some DNS results to investigate the influence that the different terms in boundary conditions (2.3) have on the near-wall turbulence. For that, we begin with simple boundary conditions, homogeneous slip-only boundary conditions, as those commonly found in the literature (Min & Kim, 2004; Busse & Sandham, 2012) and systematically introduce increasing complexity until reaching the wavelength-dependent boundary conditions (2.3) obtained from resolving the flow within the permeable substrate.

Simulations shown in this section are run at a constant mass flow rate, starting from a smooth-channel flow at a friction Reynolds number $\delta_0^+ \simeq 180$, in order to validate and compare the results with those obtained by Min & Kim (2004) and Jiménez *et al.* (2001). The friction coefficient and the change in drag are also defined as in Min & Kim (2004). The

friction coefficient is defined using the bulk velocity, $c_f = 2\tau_w/(\rho U_b^2) = 2/(U_b^{+2})$, where the density, ρ, is considered to be unity, and the latter is given by the resulting change in the mean pressure gradient $d\bar{p}/dx$,

$$\Delta D = \frac{c_f - c_{f_0}}{c_{f_0}} = \frac{\left(-\dfrac{d\bar{p}}{dx}\right) - \left(-\dfrac{d\bar{p}}{dx}\Big|_0\right)}{\left(-\dfrac{d\bar{p}}{dx}\Big|_0\right)}, \tag{2.19}$$

where the subscript 0 denotes the values for a smooth channel.

To understand how the boundary conditions in equation (2.3) affect the near-wall flow, we consider the following four cases, for which the parameters are summarised in table 2.3:

a) MK reproduces one of the cases of Min & Kim (2004), with homogeneous streamwise and spanwise slip lengths and zero transpiration,

$$\hat{u}^+|_{y=0} = \ell_x^+ \frac{d\hat{u}^+}{dy}\bigg|_{y=0}, \qquad \hat{w}^+|_{y=0} = \ell_z^+ \frac{d\hat{w}^+}{dy}\bigg|_{y=0}, \qquad \hat{v}^+|_{y=0} = 0, \tag{2.20}$$

where the slips in both directions are equal, $\ell_x^+ = \ell_z^+ \approx 3.3$. This case allows us to validate the slip boundary conditions and later study the influence of the transpiration velocity separately from that of the slip.

b) MK+J adds a homogeneous transpiration velocity to the previous case,

$$\hat{u}^+|_{y=0} = \ell_x^+ \frac{d\hat{u}^+}{dy}\bigg|_{y=0}, \qquad \hat{w}^+|_{y=0} = \ell_z^+ \frac{d\hat{w}^+}{dy}\bigg|_{y=0}, \qquad \hat{v}^+|_{y=0} = \beta^+ \hat{p}^+|_{y=0}. \tag{2.21}$$

The transpiration velocity is roughly similar to one of the cases of Jiménez *et al.* (2001), where $\beta^+ = -0.043$ is the impedance coefficient, homogeneous for all wavelengths. By comparing this case to MK, we evaluate the additional effect of a homogeneous transpiration.

c) SES (Simplified Equivalent Substrate) implements wavelength-dependent transpiration and slip lengths obtained from Brinkman's solution of the flow within the substrate. This yields the boundary conditions of equation (2.3) for the overlying flow, but for this case, only the coefficients $\mathcal{C}_{uu}^+$, $\mathcal{C}_{ww}^+$ and $\mathcal{C}_{vp}^+$ are considered: $\mathcal{C}_{uu}^+$ and $\mathcal{C}_{ww}^+$, which represent the slip lengths in the streamwise and spanwise directions, respectively, as ℓ_x^+ and ℓ_z^+ in Min & Kim (2004) and Busse & Sandham (2012); and $\mathcal{C}_{vp}^+$, which relates the wall-normal velocity to the pressure fluctuations, as does the β^+ coefficient in Jiménez *et al.* (2001). The depth and permeabilities of this substrate were selected to match the slip lengths of case MK for the mean shear and to match $\mathcal{C}_{vp}^+$ with the impedance coefficient of case MK+J, β^+, for the lengthscales of Kelvin-Helmholtz rollers that

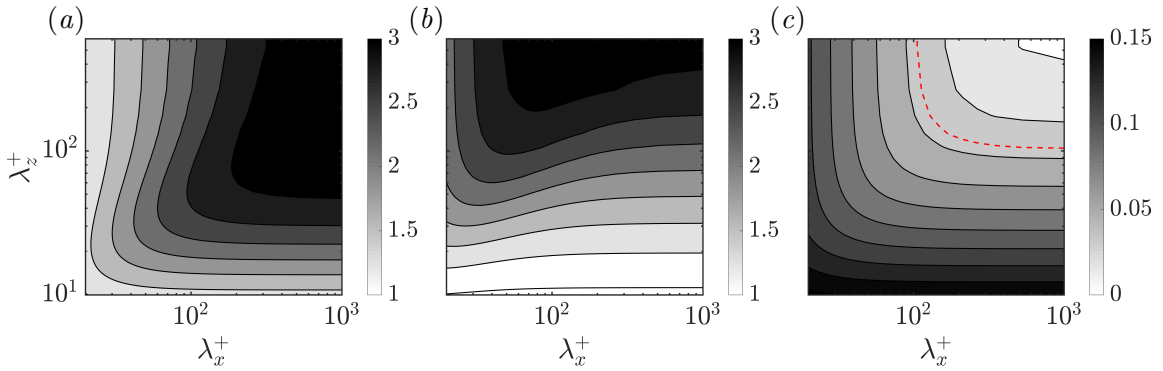

FIGURE 2.5 Boundary condition coefficients used for case SES as a function of λ_x^+ and λ_z^+ in viscous units: (a) $\mathcal{C}_{uu}^+$, (b) $\mathcal{C}_{ww}^+$ and (c) $-\mathcal{C}_{vp}^+$. The red dashed line in (c) is the contour where $\mathcal{C}_{vp}^+$ is equal to the impedance coefficient from Jiménez *et al.* (2001), β^+, used in the present work for case MK+J.

had previously been observed in DNS, $\lambda_x^+ \approx 150$ (García-Mayoral & Jiménez, 2011). This case corresponds to a permeable substrate with $K_x^+ = K_z^+ \approx 11.3$ and $K_y^+ \approx 0.09$. The variation of $\mathcal{C}_{uu}^+$, $\mathcal{C}_{ww}^+$ and $\mathcal{C}_{vp}^+$ with the wall-parallel wavelengths, λ_x^+ and λ_z^+, are portrayed in figure 2.5. Given that the values of the tangential permeabilities for these cases coincide, $K_x^+ = K_z^+$, the equations for the flow within the substrate are invariant to a rotation in the $x - z$ plane. $\mathcal{C}_{ww}^+$ in panel (b) is therefore equal to $\mathcal{C}_{uu}^+$ in panel (a) if λ_x^+ and λ_z^+ are interchanged.

d) ES (Equivalent Substrate) implements the full set of Brinkman's boundary conditions, defined in equation (2.3). The characteristics of the substrate are similar to those defined in the previous case. The small discrepancy between the resulting values of the permeabilities in viscous units for case SES and ES observed in table 2.3 results from the variation in the friction Reynolds number.

For a consistent comparison with Min & Kim (2004) and Jiménez *et al.* (2001), throughout this section the viscous scaling is based on the friction velocity measured at the substrate-channel interface plane, $y = 0$, where the boundary conditions are applied. To assess how these boundary conditions affect the overlying flow, we first focus on the mean velocity profiles and the rms velocity fluctuations. Results for the validation case, MK, as well as for the original simulation from Min & Kim (2004) that it replicates, are depicted in figure 2.6, all showing good agreement.

The change in drag with respect to the smooth case is, as explained in chapter 1, related to the shift of the mean velocity profile in the logarithmic region, ΔU^+. For the cases under study, the latter can be obtained from the velocity profiles portrayed in figure 2.7(a), where the upward and downward shifts of the logarithmic region result in the changes in drag reported in table 2.3.

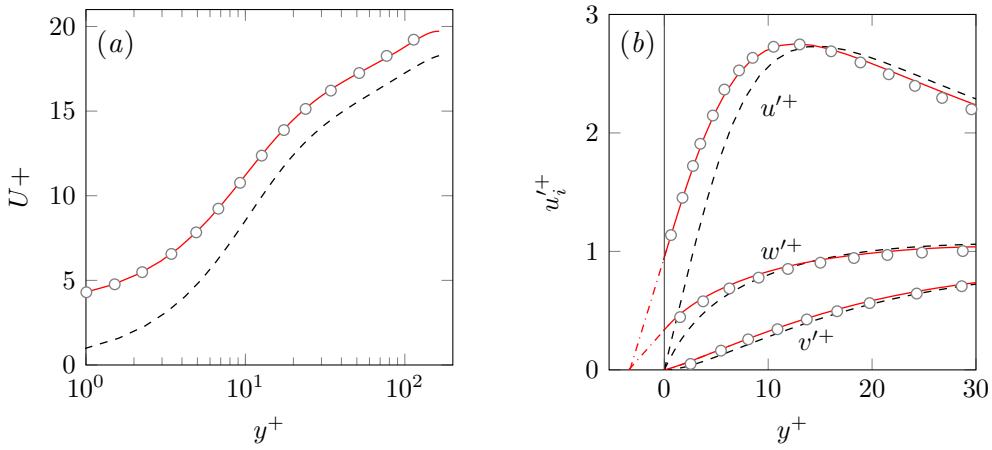

FIGURE 2.6 (a) Mean velocity profiles and (b) rms velocity fluctuations scaled with the corresponding u_τ at the substrate-channel interface. – – –, smooth channel; ○, data from Min & Kim (2004); ——, case MK.

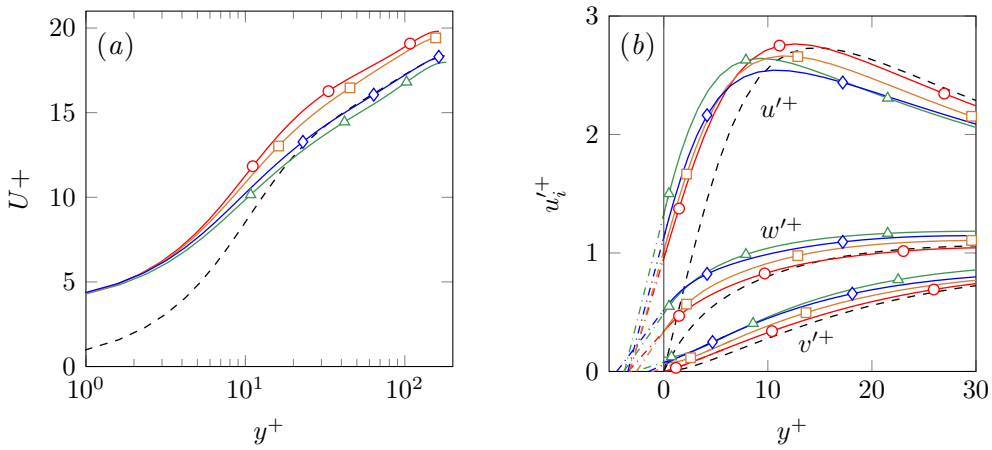

FIGURE 2.7 (a) Mean velocity profiles and (b) rms velocity fluctuations scaled with the corresponding u_τ at the substrate-channel interface. – – –smooth channel; —○—, case MK; —△—, case MK+J; —□—, case SES; —◇—, case ES.

According to Luchini's theory, given by equation (1.5), ΔU^+ varies linearly with $\ell_x^+ - \ell_z^+$ (Luchini *et al.*, 1991). This theory is based on both slip lengths, ℓ_x^+ and ℓ_z^+, being vanishingly small, smaller than the lengthscales of the overlying turbulent flow. Note, however, that in case MK a net drag reduction is obtained in spite of both slip lengths being equal, which results from the saturation effect of the spanwise slip length on ΔU^+ for $\ell_z^+ \gtrsim 1$. This effect will be thoroughly discussed in chapter 3. The general idea is that, for ℓ_z^+ beyond one wall unit, the displacement of the quasi-streamwise vortices towards $y = 0$ saturates if the spanwise slip is not accompanied by a corresponding wall-normal transpiration. Thus, for isotropic slip lengths of $\ell_x^+ = \ell_z^+ \approx 3$ and zero transpiration, this saturation effect leads to a decrease in drag in case MK. This effect has been often observed in the context of

superhydrophobic surfaces (Fukagata *et al.*, 2006; Busse & Sandham, 2012; Seo & Mani, 2016; Fairhall *et al.*, 2019).

When a wall-normal transpiration similar to that of Jiménez *et al.* (2001) is added, as in case MK+J, ΔU^+ is negative, that is, a slight increase in drag is observed, since the drag-decreasing effect of the slip lengths is outweighed by the drag-increasing effect of the wall-normal transpiration. On the other hand, case SES, which considers wavelength-dependent slip and transpiration coefficients, recovers a significant drag decrease. The reason is that the transpiration coefficient in this case, $\mathcal{C}^+_{vp}$, is smaller than that from case MK+J for the largest wavelengths, as shown in figure 2.1(b), which inhibits the formation of drag-increasing, large-scale structures observed in Jiménez *et al.* (2001) and MK+J. However, considering all the nine terms from boundary conditions (2.3), as in case ES, negates the drag reduction obtained in case SES. This is because, although the overlying flow is driven primarily by $\mathcal{C}^+_{uu}$, $\mathcal{C}^+_{ww}$ and $\mathcal{C}^+_{vp}$, the other coefficients modulate the flow. The effect of the three directional permeabilities on the three velocity components is coupled primarily through the additional cross terms, considered in case ES, but neglected in case SES. For low permeabilities the modulation introduced by these terms is negligible, but for the large values of K^+_x and K^+_z considered, the modulation becomes significant. Particularly, K^+_x and K^+_z act, through $\mathcal{C}^+_{vu}$ and $\mathcal{C}^+_{vw}$, on increasing the effective wall-normal transpiration, which is found to govern the appearance of drag-increasing spanwise-coherent rollers (Jiménez *et al.*, 2001; García-Mayoral & Jiménez, 2011). The permeability K^+_y, in turn, also affects the streamwise and spanwise velocities. In any event, the aim of this section is to simply provide an intuition of how the slip and transpiration coefficients affect the overlying turbulence and to show the effect of wavelength-dependent boundary conditions compared to homogeneous ones. The effect that different permeabilities have on the overlying turbulent flow will be discussed in detail in chapter 7.

The variations of the rms velocity fluctuations observed in figure 2.7(b) support the conclusions derived from the analysis of the mean flow profile. The main effect of introducing slips and transpiration at the substrate-channel interface is a shift of the velocity profiles towards the wall. This shift can be quantified by extrapolating the profiles into the substrate, as shown in the figure. The locations where the extrapolated velocity profiles go to zero correspond to different component-wise virtual origins. Note that for u and w, the virtual origins correspond to the streamwise and spanwise slip lengths, ℓ^+_x and ℓ^+_z, respectively, and while these are approximately equal for the four cases studied, the origin of the wall-normal velocity differs. The origin of v is deepest in case MK+J, and consequently the positive effect of tangential slip is more severely negated in this case. In addition to a shift of the velocity profiles, figure 2.7(b) also shows a change in the intensity of the fluctuations, particularly for the cases where the impermeability condition has been relaxed. While for case MK the velocity profiles seem to be essentially those of the smooth channel shifted towards the wall by their virtual origins, for cases MK+J and ES, and to a lesser extent SES, the peak rms

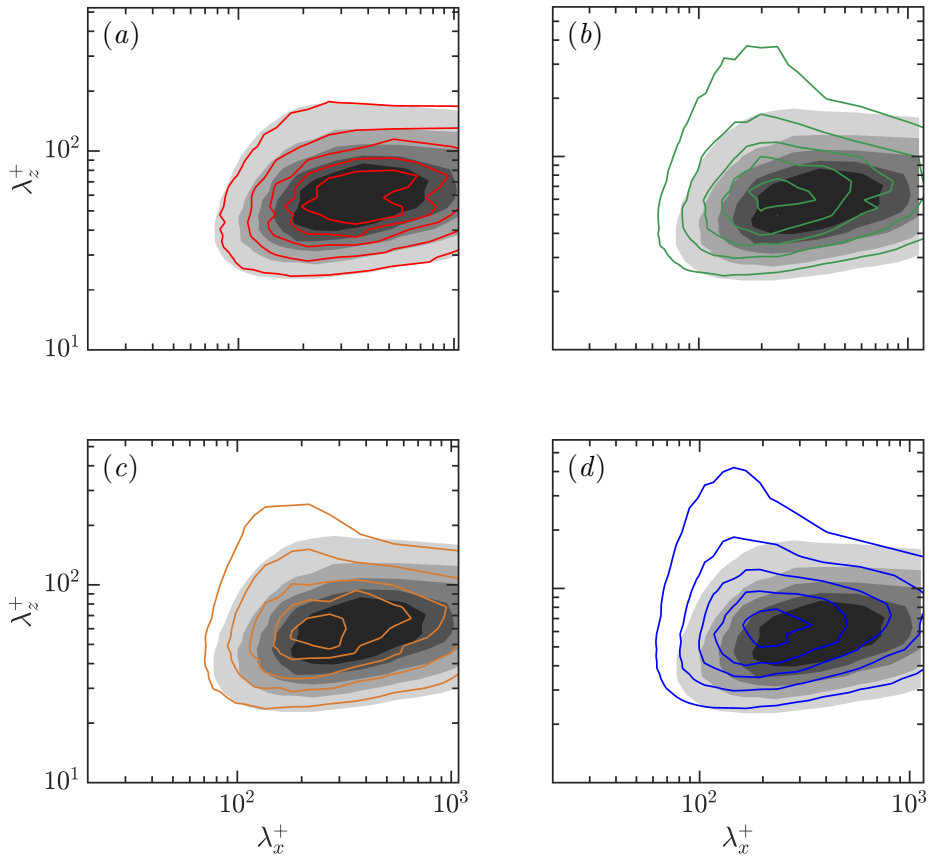

FIGURE 2.8 Premultiplied two-dimensional spectral density of the wall-normal velocity, $k_x k_z E_{vv}$. Shaded, smooth channel at $y^+ = 7$; lines, present DNSs shifted by the virtual origin of the wall-normal velocity. The contour increments in wall units are 0.00145 from clear to dark. (a) MK at $y^+ = 6.6$, (b) MK+J at $y^+ = 3.4$, (c) SES at $y^+ = 4.5$ and (d) ES at $y^+ = 3.6$.

value of the streamwise velocity decreases, whereas v'^+ and w'^+ increase. This suggests that the overlying flow is modified beyond a mere shift in the origin.

To gain further insight on the contribution of different flow lengthscales to the variation of intensities observed, a two-dimensional spectral energy distribution of the wall-normal velocity near the interface is depicted in figure 2.8. This represents how the energy of v in a wall-parallel plane is distributed along in the (λ_x^+,λ_z^+) wavelength space. As observed in figure 2.7(b), the virtual origin of the wall-normal velocity differs from case to case. The relevant wall-normal location for comparison of the v-spectra between the cases should then be at the same height measured from the corresponding virtual origin of v. Therefore, in figure 2.8 the spectrum for the smooth channel at $y^+ \approx 7$ is superimposed to those for the present cases at $y^+ = 7 - \ell_v^+$, where ℓ_v^+ is the virtual origin of v fluctuations. This virtual origin, ℓ_v^+, is defined as the wall-normal displacement of the v'^+ curve in figure 2.7(b) with respect to the smooth channel.

While case MK does not show a significant difference compared to the smooth channel, in case MK+J there is an accumulation of energy at $\lambda_x^+ \approx 200$ and large λ_z^+. Although not shown here, this new energetic region decays at heights above $y^+ \approx 25$, which supports the idea of the presence of large spanwise-coherent structures in the immediate vicinity of the interface. The relaxation of the impermeability condition is therefore, as mentioned before, associated to the formation of spanwise-coherent structures, and these, in turn, are responsible for the large increase of the spanwise and wall-normal fluctuations observed in figure 2.7(b). For case SES, on the other hand, the energetic peak is slightly attenuated and displaced to lower wavelengths, $\lambda_x^+ \approx 150$, which agrees with the wavelengths observed over riblets in García-Mayoral & Jiménez (2011). The weakening of the energetic region can be attributed to the lower effective transpiration values imposed for large lengthscales, caused by the transpiration coefficient, $\mathcal{C}_{vp}^+$, vanishing for large wavelengths, as shown in figure 2.5(b). The energetic region at $\lambda_x^+ \approx 150$, however, amplifies slightly when introducing the full boundary conditions (2.3) for case ES, as observed in panel (d).

The presence of these energetic structures can also be shown in the instantaneous realisations of the streamwise and wall-normal velocities depicted in figure 2.9. For case MK, the u- and v-fields resemble those observed over a smooth wall, as shown in panels (a-b) and (c-d). For case MK+J, panels (e-f) show the footprint of large spanwise-coherence, in agreement with the new energetic region observed in the v-spectrum in figure 2.8(b). The spanwise-coherent structures can be associated with the Kelvin-Helmholtz rollers observed by Jiménez *et al.* (2001). These structures disrupt the strength and coherence of the streaky structures, contributing to a degradation of drag (Jiménez *et al.*, 2001; García-Mayoral & Jiménez, 2011; Kuwata & Suga, 2016). For case SES, the large rollers are inhibited due to a lower wall-normal permeability for the larger scales, and smaller spanwise-coherent structures appear instead. This relates to the smaller new energetic region observed in the v-spectrum in figure 2.8(c) compared to that in figure 2.8(b), which suggests that the effect of these structures is not as significant. When including all the terms from equations (2.3), more spanwise coherence emerges, as shown for case ES in panels (i-j). This coherence, however, is not as strong as in case MK+J and there is still some trace of the near-wall cycle that remains.

Luchini's theory (1.5) is based on the slip lengths being sufficiently small, so that these can be considered homogeneous and the transpiration at the interface can be neglected. However, from the present results we can conclude that, for texture sizes beyond a certain size (or permeabilities in our case), the slip lengths become wavelength-dependent, and the coupling between the three velocity components at the interface plane, accounted by the cross terms considered in case ES, becomes significant. For permeable substrates, the linear drag reduction regime predicted by Luchini's theory will therefore stop holding for permeabilities beyond a certain value. In that case, the wavelength-dependent character of the interface coefficients, as well as the coupling between the velocities, would need to be accounted for to

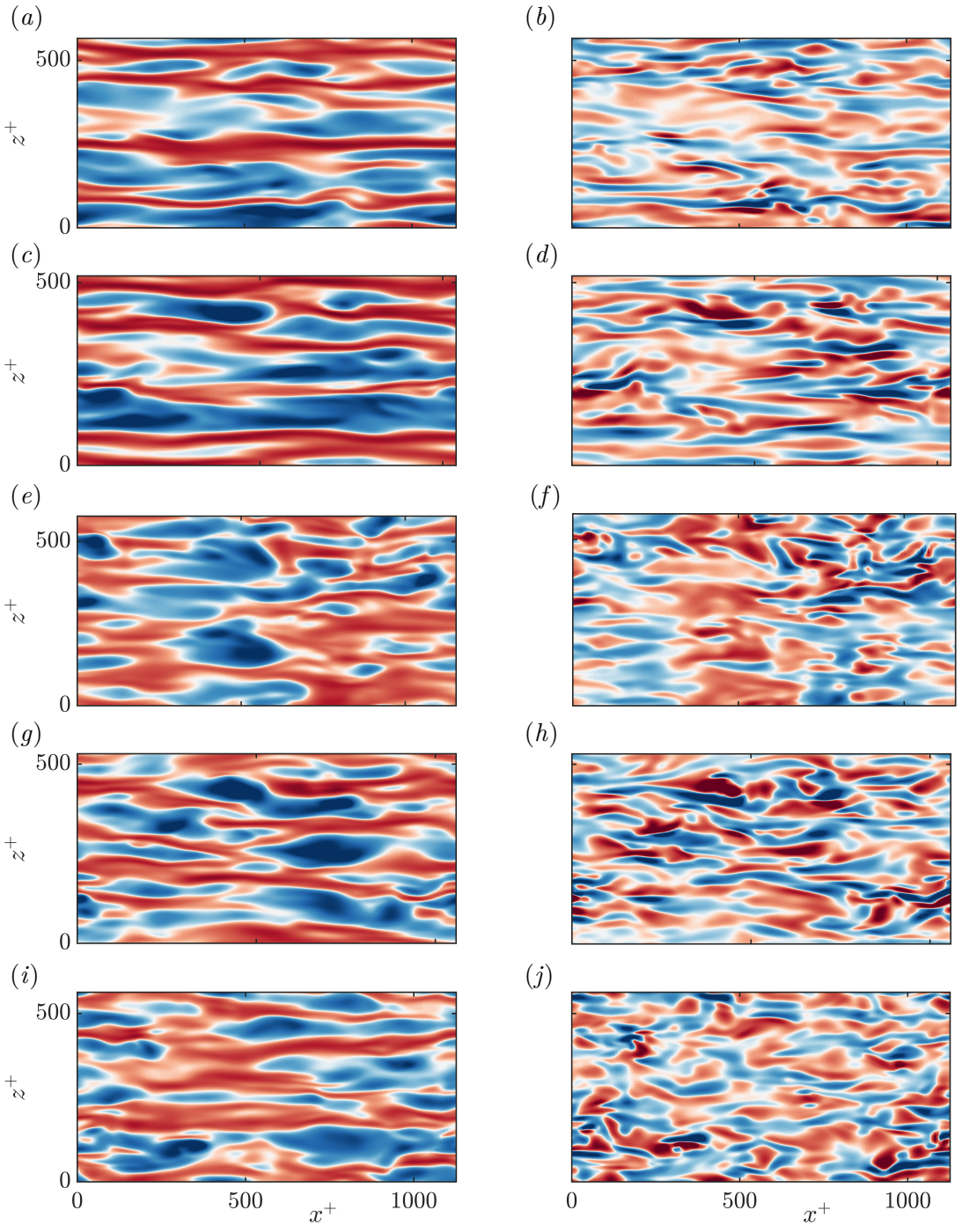

FIGURE 2.9 Instantaneous realisations of streamwise, u'^+, (left) and wall-normal, v^+, (right) velocities at a plane parallel to the wall. (a-b) Smooth channel at $y^+ \approx 7$. (c-d) MK at $y^+ \approx 6$. (e-f) MK+J at $y^+ \approx 3$. (g-h) SES at $y^+ \approx 4$. (i-j) ES at $y^+ \approx 4$. In all cases, red to blue corresponds to $[-5.0, +5.0]$ for u'^+ and $[-0.48, +0.48]$ for v'^+.

properly characterise the effect of the substrate. This will be the approach followed for the DNSs in chapter 7.

Chapter 3

Virtual Origins Part I: extension of Luchini's virtual-origin model for the change in drag*

As mentioned in the introduction, complex surfaces can cause a relative wall-normal displacement of the near-wall turbulence with respect to the mean flow, which produces a change in drag. This effect can be modelled by imposing different virtual origins for the different velocity components. In this chapter, we study the effect that offsetting these origins has on the near-wall turbulence through DNSs of channel flows with different virtual origins for the different velocity components. The aim of this chapter is to extend the existing understanding on how these virtual origins affect the flow. In the literature, the origins for the tangential velocities are typically characterised by slip boundary conditions, while the wall-normal velocity is considered to be zero. Here we explore different techniques to define and implement virtual origins for the three components, with special emphasis on the wall-normal component. Robin boundary conditions for the three velocities turned out to be the most satisfactory technique. These boundary conditions relate the velocity components to their respective wall-normal gradients. Our results confirm that the change in drag, or ΔU^+, is determined by the offset between the origins perceived by the mean flow and that perceived by turbulence. The origin for the latter, however, is not set by the spanwise virtual origin alone, as previously proposed, but by a combination of the spanwise and wall-normal origins. These observations allow us to extend Luchini's virtual-origin theory to predict the change in drag, accounting for the wall-normal transpiration effect when this is not negligible.

*Parts of the content of this chapter have been published in *Journal of Physics: Conference Series*, 1001, 012011, with Christopher Fairhall, Michael MacDonald, Daniel Chung and Ricardo García-Mayoral as co-authors and in *Fluid Dynamics Research*, 51, 011410, with Ricardo García-Mayoral and Christopher Fairhall as co-authors.

3.1 Saturation of the effect of the spanwise slip

Complex surfaces, such as riblets, superhydrophobic surfaces or the permeable substrates that will be studied in the following chapters are made up of small surface textures that interact with the near-wall turbulence and cause a reduction in skin-friction drag. In chapter 1 we mentioned that this change in drag is caused by an offset between the virtual, equivalent smooth wall perceived by the mean flow and that perceived by turbulent fluctuations, particularly the quasi-streamwise vortices of the near-wall cycle. Luchini (1996) and Jiménez (1994) proposed that the change in drag produced by these surfaces can be estimated by equation (1.5). Based on this, the effect of the texture can be reduced to a reference plane with non-zero slip velocities, as portrayed in figure 1.7. In the literature, Robin boundary conditions of the form of equation (1.6) are typically used to model the effect of small surface textures, while the wall-normal velocity is assumed to be zero at the boundary plane (Min & Kim, 2004; Fukagata *et al.*, 2006; Busse & Sandham, 2012).

In the above studies, however, the adverse effect of the spanwise slip length on ΔU^+ is observed to saturate for relatively small values of ℓ_z^+. The linear expression $\Delta U^+ = \ell_x^+ - \ell_z^+$ is valid only for $\ell_z^+ \lesssim 1$ and increasing ℓ_z^+ beyond ≈ 4 has a negligible effect on ΔU^+. Busse & Sandham (2012) carried out a parametric study of channel flows with a wide range of values for ℓ_x^+ and ℓ_z^+. The mean velocity shift ΔU^+ obtained from their simulations is portrayed in figure 3.1(a), where the saturation effect of ℓ_z^+ can be appreciated, as the zero-ΔU^+ line does not correspond to $\ell_x^+ = \ell_z^+$. The figure shows that isotropic textures with equal streamwise and spanwise slip lengths, $\ell_x^+ = \ell_z^+$, can also lead to a decrease of drag, contrary to what the linear theory of slip lengths in equation (1.5) predicts. This is in agreement with the DNS results of Min & Kim (2004), who studied the effect of ℓ_x^+ and ℓ_z^+ independently, as well as combined, and observed a drag reduction when both slip lengths were equal. Analysing the results from Busse & Sandham (2012), Fairhall & García-Mayoral (2018) suggested that ΔU^+ can still be represented by an expression similar to equation (1.5) by introducing an empirical, effective spanwise slip length, $\ell_{z,eff}^+$, to account for the saturation effect of ℓ_z^+,

$$\ell_{z,eff}^+ = \frac{\ell_z^+}{1 + \ell_z^+/4}. \tag{3.1}$$

The shift of the velocity profile is then

$$\Delta U^+ = \ell_x^+ - \ell_{z,eff}^+. \tag{3.2}$$

For $\ell_z^+ \lesssim 1$, $\ell_{z,eff}^+ \approx \ell_z^+$, recovering equation (1.5) for ΔU^+, while for large values of ℓ_z^+, $\ell_{z,eff}^+$ asymptotes to 4. Using equation (3.2), the two-dimensional parametric space (ℓ_x^+, ℓ_z^+) in figure 3.1(a) can be fitted to a single curve, as shown in figure 3.1(b). There is, however, some deviation for simulations at low Reynolds number, $\delta_0^+ \approx 180$, with large spanwise slip

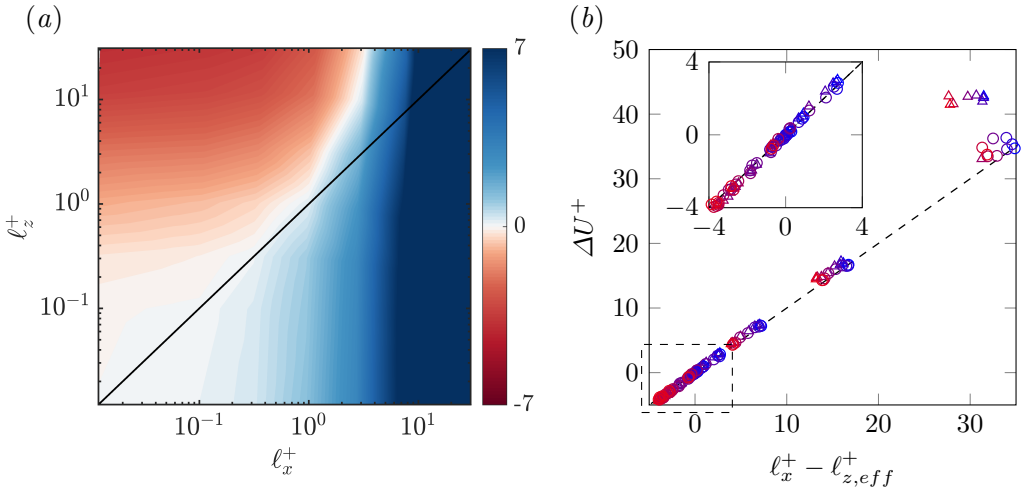

FIGURE 3.1 (*a*) Map of ΔU^+ for different slip lengths, ℓ_x^+ and ℓ_z^+ from Busse & Sandham (2012) starting from a friction Reynolds number of $\delta_0^+ = 180$. The black solid line corresponds to $\ell_x^+ = \ell_z^+$. (*b*) ΔU^+ as a function of $\ell_x^+ - \ell_{z,eff}^+$ using the same data as in (*a*), where $\ell_{z,eff}^+$ is given by equation (3.1). $\triangle$, simulations at $\delta_0^+ = 180$; $\circ$, at $\delta_0^+ = 360$. From blue to red the spanwise slip length increases. The dashed line represents equation (3.2). The inset shows a zoom of the small values, where the dashed line represents equation (3.2).

lengths, $\ell_x^+ \sim 100$. Recall that δ_0^+ refers to the friction Reynolds number of the reference smooth channel. These simulations were conducted at constant mass flow rate, and for such large ℓ_x^+, the actual δ^+ would be significantly lower and the flow may have relaminarised. If this was indeed the case, ℓ_z^+ would no longer affect the flow, which would explain the deviation from equation (3.2) observed in the figure. This is, however, not the case for larger friction Reynolds numbers, and simulations at $\delta_0^+ \approx 360$ agree well with equation (3.2).

To understand the saturation effect of ℓ_z^+ and extend the existing understanding on how virtual origins affect the overlying flow, in this chapter, we study the effect of virtual origins not only for the tangential velocities, u and w, but also for the wall-normal velocity, v. Although imposing a virtual origin for u and w in terms of slip lengths is very intuitive, defining a virtual origin for v is not as simple. To our knowledge, the origin of v has never been included in this framework. Nevertheless, some previous work exists that investigates the effect of v separately from that of u and w. Jiménez *et al.* (2001), for instance, showed that turbulence is highly sensitive to transpiration, and García-Mayoral & Jiménez (2011) observed that transpiration is responsible for the eventual degradation of performance for riblets.

In what follows, we will first explain the saturation of the spanwise slip length, and then present the results for the different methods considered to define virtual origins, followed by a discussion on the effect of virtual origins in section 3.5.

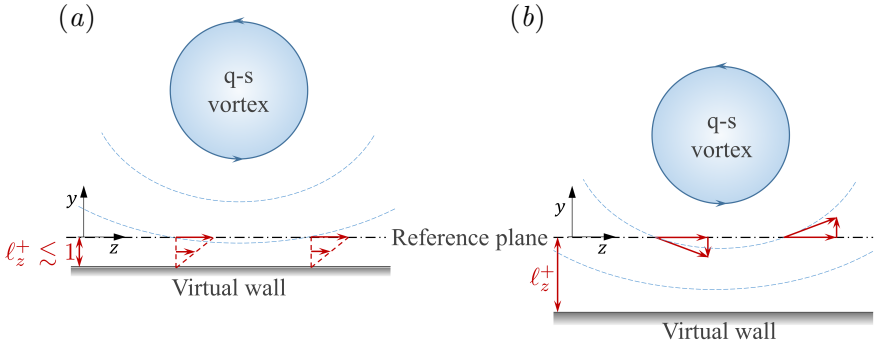

FIGURE 3.2 Schematic of the spanwise and wall-normal velocities induced by quasi-streamwise vortices at the reference plane for (a) virtual origins $\lesssim 1$ wall unit and (b) larger virtual origins. The velocity at the reference plane has a spanwise (horizontal arrow) and a wall-normal (vertical arrow) component.

3.2 Interpretation of the saturation of ℓ_z^+

The simulations of Busse & Sandham (2012) shown in figure 3.2 assume zero wall-normal velocity fluctuations at the reference plane. However, real surfaces that produce non-zero slips, such as riblets (García-Mayoral & Jiménez, 2011), permeable substrates (Breugem & Boersma, 2005) or superhydrophobic surfaces (Seo *et al.*, 2018), can also induce a non-zero wall-normal velocity at the reference plane, which is in our case taken at the top plane of the surface geometry. Here we argue that this absence of transpiration is what leads to the saturation of the effect of ℓ_z^+ observed in figure 3.1.

The inherent assumption in Luchini's theory, given by equation (1.5), is that the quasi-streamwise vortices induce a spanwise velocity at the reference plane, but no wall-normal velocity. In practice, these vortices induce both spanwise and wall-normal velocity and their displacement towards $y^+ = 0$ would eventually saturate if the spanwise velocity at the reference plane is not accompanied by a corresponding wall-normal velocity. This idea is illustrated in the sketches portrayed in figure 3.2. For $\ell_z^+ \lesssim 1$, the wall-normal velocity induced by the vortices at the reference plane is negligible, since, immediately above a wall (in this case a virtual wall), w increases linearly with y, while v increases with the square of y. As a first order approximation, the effect of v can be neglected, and the displacement of the vortices can be effectively represented by a slip boundary condition for w and an impermeability condition for v, as shown in figure 3.2(a). The origin perceived by quasi-streamwise vortices is then at $y^+ = -\ell_z^+$, and the change in drag is properly captured by Luchini's linear law.

On the other hand, if the reference plane is farther away from the wall and closer to the mean height of vortex cores, as in figure 3.2(b), the wall-normal velocity that the vortices would induce at the reference plane is no longer negligible. When impeding v at this plane, such as in the study by Busse & Sandham (2012) and all the classic slip-length or protrusion

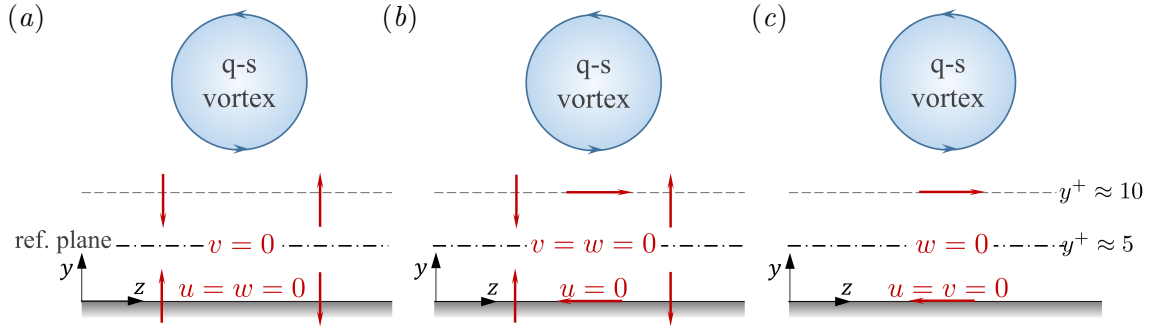

FIGURE 3.3 Schematics of the different control strategies studied by Choi *et al.* (1994). (*a*) *v-control*, (*b*) *v-w-control* and (*c*) *w-control*.

height studies, the proximity of the vortices to the reference plane is restricted. For values of ℓ_z^+ of the order of ~ 4 wall units, for which the saturation is already observed, a further increase of ℓ_z^+ has little or no effect on the overlying turbulence, as the quasi-streamwise vortices cannot approach the reference plane any further. The virtual origin perceived by the vortices in this case would be at an intermediate plane between the origins that would be imposed by the spanwise slip, $y^+ = -\ell_z^+$, and by the zero transpiration, $y^+ = 0$. Some form of transpiration would also need to exist at the reference plane for the vortices to move closer to it. To explore this idea, in addition to the streamwise and spanwise virtual origins traditionally defined, in this chapter, we investigate different methods to impose a virtual origin for the wall-normal velocity.

In retrospect, the opposition control studies of Choi *et al.* (1994) can also be interpreted as an alternative method of imposing virtual origins, which suggests that some active control techniques are based on the same drag-reduction mechanism. Choi *et al.* (1994) explored several active control strategies for the wall-normal and spanwise velocities, including opposition control of the wall-normal velocity alone (*v-control*), opposition control of the spanwise velocity alone (*w-control*), and combined opposition control of v and w (*v-w-control*). In each case, the velocity components imposed at the wall, $y^+ = 0$, were opposite to those measured at $y^+ \approx 10$. The authors concluded that the reduction of skin friction in the three cases was a result of the outward shift of the origin of turbulence with respect to the mean flow, which is essentially the idea introduced by Luchini (1996). Their simulations can be interpreted as setting different origins for the different velocity components, since imposing a velocity at $y^+ = 0$ equal and opposite to that at $y^+ = 10$ is roughly equivalent to imposing a zero velocity at an intermediate plane, $y^+ \approx 5$. Schematics for the three cases considered are shown in figure 3.3, where the intermediate plane, where the controlled velocities roughly vanish, would be the equivalent of the reference plane in a slip-length framework.

The corresponding depths of the virtual origins below the reference plane, at $y^+ \approx 5$, and the drag reduction achieved can be found in table 3.1. Note, however, that these values only allow for qualitative comparison, since the above analogy only produces a rough estimate of

	v-control	*v-w-control*	*w-control*
Depth of VO for u	5	5	5
Depth of VO for w	5	0	0
Depth of VO for v	0	0	5
DR	25%	30%	30%

TABLE 3.1 Different control strategies studied by Choi *et al.* (1994) and the equivalence with the displacement of virtual origins. VO refers to virtual origin. The depths of the virtual origins are measured from the reference plane, taken at the intermediate plane, i.e. the dash-dotted plane at $y^+ \approx 5$ in figure 3.3. Drag reduction (DR) is measured in terms of the change in the mean pressure gradient for a fixed mass flow rate.

the effective virtual origins. In the framework of virtual origins, the *v-control* case would be analogous to setting $v = 0$ at the reference plane and virtual origins for u and w at a depth below of 5 wall units. This corresponds to one of the results from Busse & Sandham (2012) with $\ell_x^+ \approx \ell_z^+ \approx 5$, portrayed in figure 3.1. A similar drag reduction is obtained, agreeing well with the prediction from equation (3.2). The *v-w-control* case would be analogous to imposing $v = w = 0$ at the reference plane and a virtual origin for u at a depth below of 5 wall units, which is also one of the simulations from Busse & Sandham (2012) included in figure 3.1. The last case, *w-control*, is equivalent to imposing a virtual origin for u and v at a depth of 5 wall units, but not for w, which cannot be represented in a slip-length framework. The obtained drag reduction is practically equal to that of the *v-w-control* case. The comparison between cases *w-control* and *v-control* suggests that shifting the origin of w has a greater effect than shifting the origin of v.

Let us assume that the only effect of the virtual origins, in particular those of the spanwise and wall-normal velocities, on the near-wall turbulence is setting its origin at an intermediate plane $y^+ = -\ell_T^+$, here referred to as the origin of turbulence, but the near-wall turbulence and its dynamics remain otherwise smooth-wall-like. It follows from the mean streamwise momentum equation for $U(y)$ that the mean velocity profile is determined by the overlying turbulence through the Reynolds shear stress. If the only effect of the virtual origins on turbulence, and hence on the Reynolds stress, is shifting its origin to $y^+ = -\ell_T^+$, the only change in the mean velocity profile compared to a smooth wall would be a shift by its value at $y^+ = -\ell_T^+$. These hypotheses will be investigated in this chapter.

We will define the depth of the virtual origin perceived by the mean flow as ℓ_U^+ and that perceived by turbulence, embodied by the quasi-streamwise vortices, as ℓ_T^+. These are obtained *a posteriori* from the simulations. The former is obtained from the wall-normal displacement of the mean velocity profile with respect to a smooth channel with the wall at the reference plane, while the latter is obtained from that of the Reynolds stress curve or

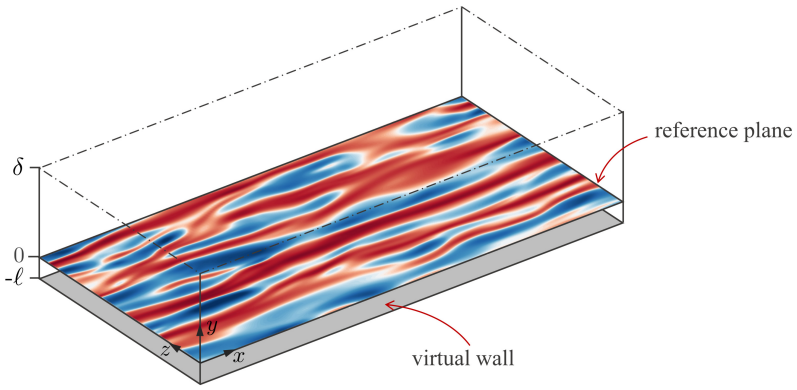

FIGURE 3.4 Channel flow with appropriate boundary conditions at the reference plane, $y = 0$, so that the flow perceives the wall at the virtual wall, $y = -\ell$. The flow field at the reference plane corresponds to an instantaneous realisation of the streamwise velocity for case DHV444 in table 3.2.

the streamwise vorticity $\omega_x'^+$, which, as we will see, are essentially equal. Note that the high values of $\omega_x'^+$ near the wall are caused by the quasi-streamwise vortices, providing a good measure for their displacement (Choi *et al.*, 1994).

In what follows, we explore different techniques to impose virtual origins by conducting DNSs of channel flows with different boundary conditions. All the simulations are conducted in symmetric channels, with the boundary conditions being applied at the bottom and upper boundaries. The DNS code used for this study was presented in chapter 2. Simulations are conducted at constant pressure gradient, starting from a smooth wall flow at $\delta^+ \simeq 180$. Before setting the virtual origins of the three velocities independently, we first explore imposing the presence of a virtual smooth wall at $y^+ = -\ell^+$, equal for all the velocities, as represented in figure 3.4. This will allow us to validate the models, as we should recover a smooth channel flow with a wall at $y^+ = -\ell^+$. In other words, the mean velocity profile and all turbulence statistics should be smooth-wall-like, except shifted in y^+ by ℓ^+ compared to a smooth wall with the wall at the reference plane, $y^+ = 0$. Once we identify a suitable technique, we extend it to impose different virtual origins for different velocity components. The different simulations and their numerical parameters are summarised in tables 3.2 and 3.3, respectively.

3.3 Modelling the presence of a smooth wall at $y^+ = -\ell^+$

We begin by considering off-wall conditions at the simulation boundary, where we set the reference plane, to model the presence of a smooth wall at $y^+ = -\ell^+$. This is a technique used in the literature to model the presence of smooth walls below the simulation boundary (Mizuno & Jiménez, 2013; Encinar *et al.*, 2014; Bae *et al.*, 2018). Four cases will be analysed, $\ell^+ = 1$, 2, 3 and 4.

Case	$\hat{u}^+\big\vert_{y^+=0} =$	$\hat{w}^+\big\vert_{y^+=0} =$	$\hat{v}^+\big\vert_{y^+=0} =$	δ^+
FP222	eq. (3.4a), $f(\alpha_x, \alpha_z)$	eq. (3.4b), $f(\alpha_x, \alpha_z)$	eq. (3.4c), $f(\alpha_x, \alpha_z)$	183
DIP222	$\mathcal{C}^+_{S,uu}(\alpha_x, \alpha_z)\, \frac{d\hat{u}}{dy}^+$	$\mathcal{C}^+_{S,ww}(\alpha_x, \alpha_z)\, \frac{d\hat{w}}{dy}^+$	$\mathcal{C}^+_{S,vp}(\alpha_x, \alpha_z)\, \hat{p}^+$	183
DHP222	$\ell_x^+ \frac{d\hat{u}}{dy}^+$	$\ell_z^+ \frac{d\hat{w}}{dy}^+$	$\mathcal{C}^+_{S,vp}(\alpha_x, \alpha_z)\, \hat{p}^+$	183
DHV222	$\ell_x^+ \frac{d\hat{u}}{dy}^+$	$\ell_z^+ \frac{d\hat{w}}{dy}^+$	$\ell_y^+ \frac{d\hat{v}}{dy}^+$	182
DHV220	$\ell_x^+ \frac{d\hat{u}}{dy}^+$	$\ell_z^+ \frac{d\hat{w}}{dy}^+$	0	182
FP333	eq. (3.4a), $f(\alpha_x, \alpha_z)$	eq. (3.4b), $f(\alpha_x, \alpha_z)$	eq. (3.4c), $f(\alpha_x, \alpha_z)$	184
DIP333	$\mathcal{C}^+_{S,uu}(\alpha_x, \alpha_z)\, \frac{d\hat{u}}{dy}^+$	$\mathcal{C}^+_{S,ww}(\alpha_x, \alpha_z)\, \frac{d\hat{w}}{dy}^+$	$\mathcal{C}^+_{S,vp}(\alpha_x, \alpha_z)\, \hat{p}^+$	185
DHP333	$\ell_x^+ \frac{d\hat{u}}{dy}^+$	$\ell_z^+ \frac{d\hat{w}}{dy}^+$	$\mathcal{C}^+_{S,vp}(\alpha_x, \alpha_z)\, \hat{p}^+$	184
DHV333	$\ell_x^+ \frac{d\hat{u}}{dy}^+$	$\ell_z^+ \frac{d\hat{w}}{dy}^+$	$\ell_y^+ \frac{d\hat{v}}{dy}^+$	183
DHV330	$\ell_x^+ \frac{d\hat{u}}{dy}^+$	$\ell_z^+ \frac{d\hat{w}}{dy}^+$	0	182
FP444	eq. (3.4a), $f(\alpha_x, \alpha_z)$	eq. (3.4b), $f(\alpha_x, \alpha_z)$	eq. (3.4c), $f(\alpha_x, \alpha_z)$	186
DHP444	$\ell_x^+ \frac{d\hat{u}}{dy}^+$	$\ell_z^+ \frac{d\hat{w}}{dy}^+$	$\mathcal{C}^+_{S,vp}(\alpha_x, \alpha_z)\, \hat{p}^+$	185
DHV444	$\ell_x^+ \frac{d\hat{u}}{dy}^+$	$\ell_z^+ \frac{d\hat{w}}{dy}^+$	$\ell_y^+ \frac{d\hat{v}}{dy}^+$	184
DHV440	$\ell_x^+ \frac{d\hat{u}}{dy}^+$	$\ell_z^+ \frac{d\hat{w}}{dy}^+$	0	182

TABLE 3.2 Boundary conditions for the three velocity components for each case simulated, where δ^+ is the friction Reynolds number measured either at the virtual wall, $y^+ = -\ell^+$, when the three virtual origins are equal, or at the origin of turbulence, $y^+ = -\ell_T^+$, otherwise. Each case is labelled with 2 or 3 letters followed by 3 numbers. The letters refer to the equations used as boundary conditions and the numbers correspond to the desired values for the virtual origins for u, w and v, respectively. For the first letter, F(*ull*) means that the full Stokes conditions from equation (3.4) are used, and D(*iagonal*) means that only the three dominant terms, $\mathcal{C}_{S,uu}$, $\mathcal{C}_{S,ww}$ and $\mathcal{C}_{S,vp}$ are used. The second letter denotes the type of boundary condition used for u and w: I(*nhomogeneous*) when wavelength-dependent coefficients from Stokes equation are considered, and H(*omogeneous*) when homogeneous slip lengths are considered. The last letter denotes the type of boundary condition used for v: P when an impedance between v and p is imposed, derived from Stokes model, and V when $v = \ell_y\, dv/dy$ is used instead.

3.3.1 Fully coupled boundary conditions from Stokes model

Assuming that the flow between the simulation boundary, $y^+ = 0$, and the virtual wall, $y^+ = -\ell^+$, is dominantly viscous, the flow can be modelled as a Stokes flow. We therefore solve the Stokes equation,

$$-\nabla p + \nu \nabla^2 \boldsymbol{u} = 0, \tag{3.3}$$

analytically and obtain the off-wall conditions at $y^+ = 0$ for the DNSs. The procedure followed is similar to that used in section 2.1 to solve Brinkman's equation and is detailed in appendix B. We consider the response of the modelled fluid region to the interfacial shear and pressure waves in the spectral space $(\lambda_x^+, \lambda_z^+)$. This yields the following conditions at the

	ℓ_u^+	ℓ_w^+	ℓ_v^+	ℓ_x^+	ℓ_z^+	ℓ_y^+	ℓ_{sm}^+	ℓ_U^+	ℓ_T^+	$\ell_{T,pred}^+$
FP222	2.0	2.0	2.0	–	–	–	–	2.0	2.1	–
DIP222	2.0	2.0	2.0	–	–	–	–	2.0	1.5	–
DHP222	2.0	(1.7)	2.0	2.0	2.0	–	–	2.0	1.5	–
DHV222	2.0	(1.7)	2.0	2.0	2.0	1.2	0.8	2.0	1.7	1.7
DHV220	2.0	(1.7)	0.0	2.0	2.0	0.0	0.0	2.0	1.3	1.3
FP333	3.0	3.0	3.0	–	–	–	–	3.0	$*$	$*$
DIP333	3.0	3.0	3.0	–	–	–	–	3.0	$*$	$*$
DHP333	3.0	(2.3)	3.0	3.0	3.0	–	–	3.0	$*$	$*$
DHV333	3.0	(2.3)	3.0	3.0	3.0	1.9	1.1	3.0	2.4	2.3
DHV330	3.0	(2.3)	0.0	3.0	3.0	0.0	0.0	3.0	1.7	1.6
FP444	4.0	4.0	4.0	–	–	–	–	4.0	$*$	$*$
DHP444	4.0	(2.9)	4.0	4.0	4.0	–	–	3.6	$*$	$*$
DHV444	4.0	(2.9)	4.0	4.0	4.0	2.5	1.5	4.0	3.1	2.9
DHV440	4.0	(2.9)	0.0	4.0	4.0	0.0	0.0	4.0	1.9	1.8

TABLE 3.3 Values of slip lengths and depths of virtual origins. Parameters specified *a priori*: the depths of virtual origins for the three velocities (ℓ_u^+, ℓ_w^+ and ℓ_v^+), the slip lengths (ℓ_x^+, ℓ_z^+ and ℓ_y^+), and ℓ_{sm}^+, as defined in figure 3.9(b). For certain simulations we do not define any slip lengths, as a wavelength-dependent model is used instead. The values between parentheses for ℓ_w^+ correspond to the actual virtual origins that we impose when accounting for the curvature of w. Parameters specified *a posteriori*: depth of the virtual origin for the mean flow, ℓ_U^+, and that for turbulence, ℓ_T^+, measured *a posteriori* from DNSs. $\ell_{T,pred}^+$ corresponds to the origin of turbulence predicted using equation (3.9). The symbol '$*$' indicates that the simulation failed to model the effect of virtual origins, and we could not obtain them.

reference plane $y^+ = 0$,

$$\hat{u}|_{y^+=0}^+ = \mathcal{C}_{S,uu}^+ \frac{d\hat{u}}{dy}\bigg|_{y^+=0}^+ + \mathcal{C}_{S,uw}^+ \frac{d\hat{w}}{dy}\bigg|_{y^+=0}^+ + \mathcal{C}_{S,up}^+ \hat{p}\big|_{y^+=0}^+ , \tag{3.4a}$$

$$\hat{w}|_{y^+=0}^+ = \mathcal{C}_{S,wu}^+ \frac{d\hat{u}}{dy}\bigg|_{y^+=0}^+ + \mathcal{C}_{S,ww}^+ \frac{d\hat{w}}{dy}\bigg|_{y^+=0}^+ + \mathcal{C}_{S,wp}^+ \hat{p}\big|_{y^+=0}^+ , \tag{3.4b}$$

$$\hat{v}|_{y^+=0}^+ = \mathcal{C}_{S,vu}^+ \frac{d\hat{u}}{dy}\bigg|_{y^+=0}^+ + \mathcal{C}_{S,vw}^+ \frac{d\hat{w}}{dy}\bigg|_{y^+=0}^+ + \mathcal{C}_{S,vp}^+ \hat{p}\big|_{y^+=0}^+ . \tag{3.4c}$$

The expressions for the upper wall ($y^+ = 2\delta^+$) can be obtained by symmetry, and together they provide off-wall conditions for the flow within the channel. The constants $\mathcal{C}_{S,ij}^+$ are complex and depend on the virtual origin ℓ^+, as well as on the streamwise and spanwise wavelengths, λ_x^+ and λ_z^+. The dominant terms in equation (3.4) are those in the diagonal, that is $\mathcal{C}_{S,uu}^+$ and $\mathcal{C}_{S,ww}^+$ for u and w, which are equivalent to the slip lengths in the streamwise

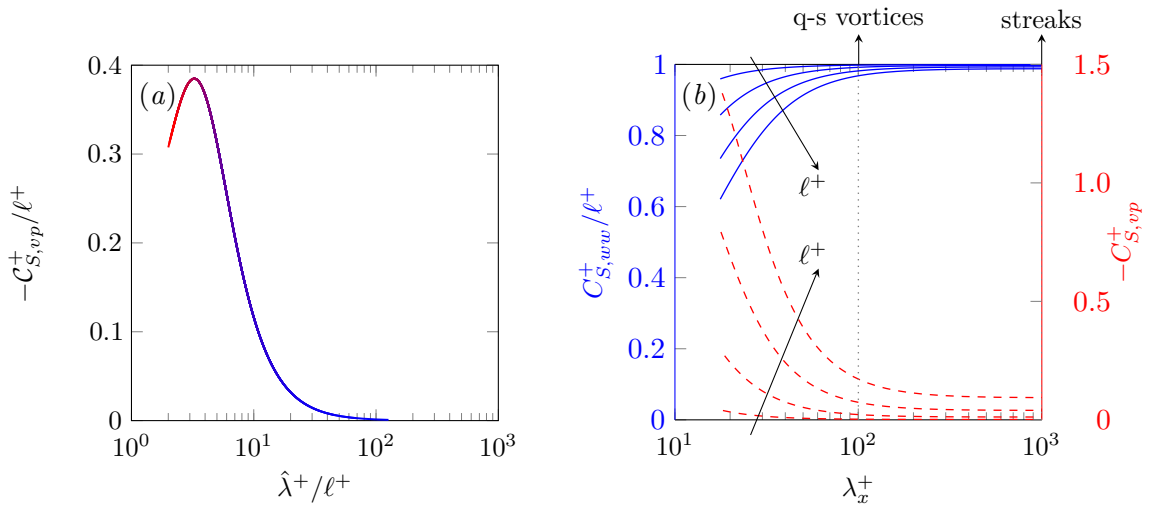

FIGURE 3.5 (a) Dimensionless transpiration coefficient $\mathcal{C}_{S,vp}$ as a function of the spherical wavelength $\hat{\lambda} = 2\pi/\sqrt{\alpha_x^2 + \alpha_z^2}$, both scaled with the depth of the virtual wall, ℓ^+. (b) – – –, transpiration coefficient $\mathcal{C}^+_{S,vp}$; ——, spanwise slip coefficient $\mathcal{C}^+_{S,ww}/\ell^+$, for $\lambda_z^+ \approx 100$ as a function of λ_x^+ for different virtual origins $\ell^+ = 1$, 2, 3 and 4. Arrows indicate increasing ℓ^+ and the vertical dotted lines correspond to lengthscales of the size of streaks and quasi-streamwise vortices.

and spanwise directions, respectively, and $\mathcal{C}^+_{S,vp}$ for v, which is equivalent to the impedance coefficient of Jiménez *et al.* (2001) that relates the wall-normal velocity and the pressure.

To illustrate how the impedance for the wall-normal transpiration varies for different flow lengthscales, the transpiration coefficient $\mathcal{C}^+_{S,vp}$ for different wavelengths is portrayed in figure 3.5(a). Note that the Stokes equation is isotropic in the x and z directions, and therefore $\mathcal{C}^+_{S,vp}$ depends only on the spherical wavelength, $\hat{\lambda} = 2\pi/\sqrt{\alpha_x^2 + \alpha_z^2}$. In figure 3.5($a$), values are scaled with ℓ^+. This figure shows that the reference plane is essentially impermeable to large eddies, while the impermeability relaxes for smaller eddies and these can permeate through more easily. Actual correlations of the pressure with the wall-normal velocity from direct observations of DNSs are discussed by Sanmiguel Vila & Flores (2018) for smooth channels and by Gómez-de-Segura *et al.* (2018*c*) for complex surfaces. The latter will be discussed in chapter 4. Figure 3.5(b) compares the transpiration coefficient, $\mathcal{C}^+_{S,vp}$, and the spanwise slip coefficient, $\mathcal{C}^+_{S,ww}$, experienced by eddies of the size of near-wall streaks, $\lambda_x^+ \approx 1000$ and $\lambda_z^+ \approx 100$, and of quasi-streamwise vortices, $\lambda_x^+ \approx 100$ and $\lambda_z^+ \approx 100$, for different ℓ^+. It shows that both the streaks and quasi-streamwise vortices are subject to essentially the same slip length as the mean, $\mathcal{C}^+_{S,ww} = \ell^+$. This, although not shown, is also the case for the streamwise slip coefficient $\mathcal{C}^+_{S,uu}$. The transpiration $\mathcal{C}^+_{S,vp}$, in contrast, is more sensitive to the wavelengths. Although $\mathcal{C}^+_{S,vp}$ is zero for very large $\hat{\lambda}^+$, its value increases as the wavelengths decrease. This can be observed especially for $\ell^+ = 4$ in figure 3.5(b), where the surface is already quite permeable for $\lambda_z^+ \approx 100$. These observations will allow us to simplify the off-wall conditions (3.4).

From the four virtual origins under study, $\ell^+ = 1$, 2, 3 and 4, the first two exhibit proportionately the same behaviour. Therefore, for clarity only results for $\ell^+ = 2$, 3 and 4 are presented. These are labelled as cases FP222, FP333 and FP444, respectively, where the numbers correspond to the desired values for the virtual origins for u, w and v, respectively, and the letters refer to the model used. The first letter F(ull) means that the full Stokes conditions from equation (3.4) are used, and the second letter, P($ressure$), means that the boundary condition for v uses an implicit coupling between v and the pressure p.

To assess if these cases successfully model a smooth wall at $y^+ = -\ell^+$, figure 3.6 portrays one-point statistics obtained from the DNSs, showing two different representations. In the panels on the left, panels (a.1-a.4), the mean velocity profile and the turbulent fluctuations are represented in the conventional form, with the origin of the wall-normal height at the reference plane, $y^+ = 0$, and scaled with u_τ measured at that height. In this framework, in panel (a.1) the non-zero slip velocity, U^+_{slip}, is observed at the reference plane, $y^+ = 0$, which is essentially the depth of the virtual origin for the mean flow, ℓ^+_U, as discussed in section 1.3, while far from that plane the adverse effect of the boundary conditions can be appreciated. Additionally, the rms velocity profiles, the Reynolds stresses and the streamwise vorticity in panel (a.2-a.4) are displaced towards the reference plane and show a change in magnitude compared to a smooth channel. Since the aim was to model a smooth wall at $y^+ = -\ell^+$, smooth-channel profiles with an origin at $y^+ = -\ell^+$ should be recovered. This origin implies that u_τ should be obtained from the total stress at that height. This cannot be measured directly, but the linear stress profile within the channel can be extrapolated to $y = -\ell$. The friction velocity at that height is then $u_\tau = u_{\tau_{y=0}}(1 + \ell/\delta)^{1/2}$, although for the values of ℓ^+ considered and at a friction Reynolds number $\delta^+ = 180$, the effect of ℓ on u_τ is small. The effective half-channel height, in turn, becomes $\delta' = \delta + \ell$. Defined this way, the only difference between the profiles should be the offset in y by their origin, ℓ, and shifting them in y by ℓ should then give a collapse of all the turbulence profiles. This is how results are represented in panels (b.1-b.4). At a first glance, results suggest that boundary conditions (3.4) provide a good model for $\ell^+ \lesssim 2$, as illustrated by case FP222 in panels (b.1-b.4), where all the curves show an excellent collapse with smooth-wall data. Note that in the panels on the left, the peaks of the fluctuations for case FP222 show a slight increase in magnitude with respect to a smooth wall. This is an artefact of the scaling and all deviations from the smooth-wall data vanish when values are scaled by the friction velocity measured at $y^+ = -2$, as shown in the panels on the right, which demonstrates the relevance of the scaling to simplify the interpretation of the data. For larger ℓ^+, however, the Stokes model fails to mimic a smooth wall at $y^+ = -\ell^+$. This is shown by the deviations of the mean velocity profile and the turbulent intensities for $\ell^+ = 3$ and $\ell^+ = 4$, cases FP333 and FP444, in panels 3.6(b.1-b.4). For these cases, the model does not merely shift the overlying flow by the virtual origin, but it also modifies it.

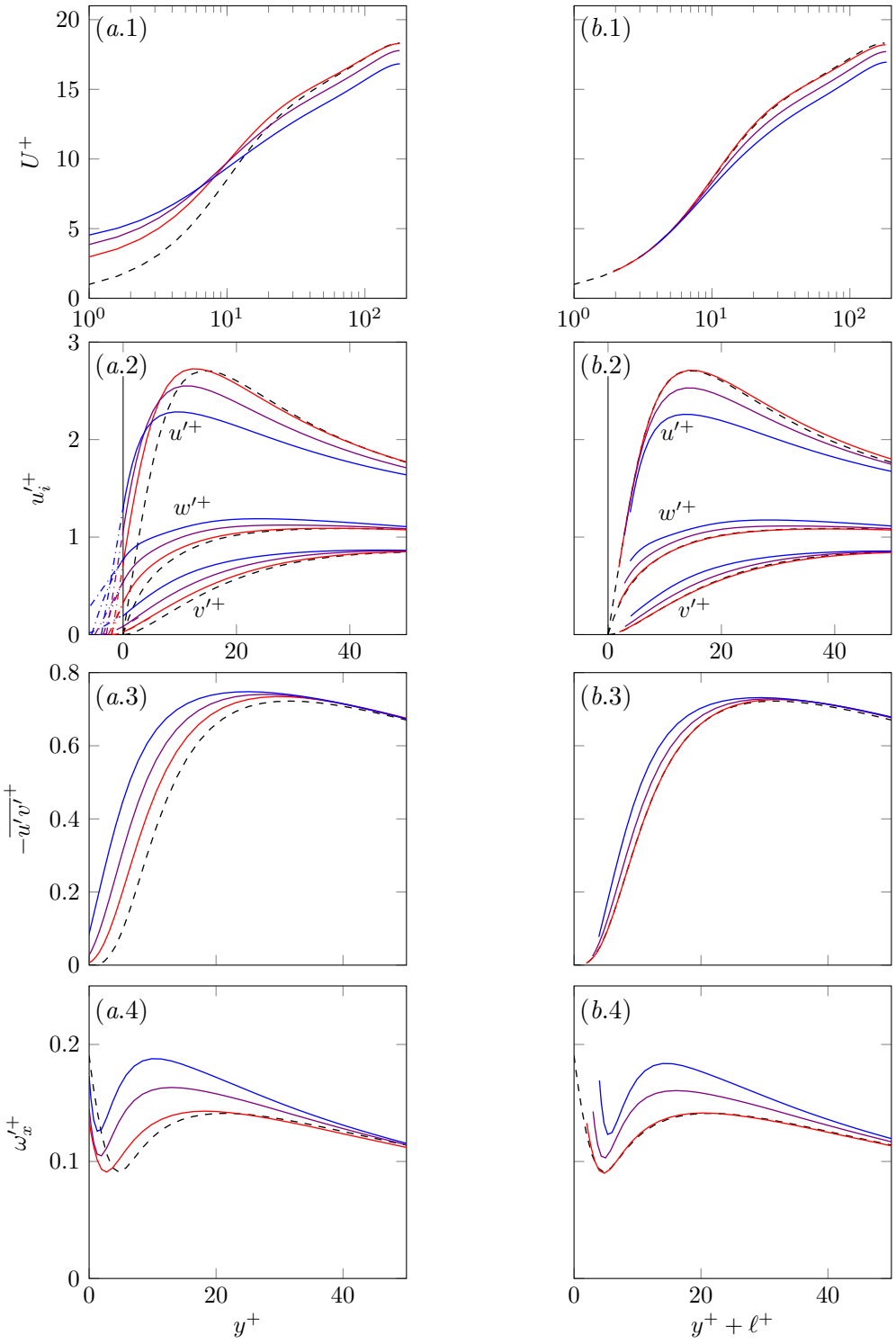

FIGURE 3.6 First column (*a*.1-*a*.4), profiles scaled with u_τ measured at the reference plane where the boundary conditions are imposed, $y^+ = 0$. Second column (*b*.1-*b*.4), profiles scaled with u_τ measured at the virtual wall, $y^+ = -\ell^+$, and shifted by ℓ^+. - - - -, smooth channel; ——, FP222; ——, FP333; ——, FP444. (*a*.1,*b*.1) Mean velocity profiles; (*a*.2,*b*.2) rms velocity fluctuations; (*a*.3,*b*.3) Reynolds shear stress; (*a*.4,*b*.4) streamwise vorticity fluctuations.

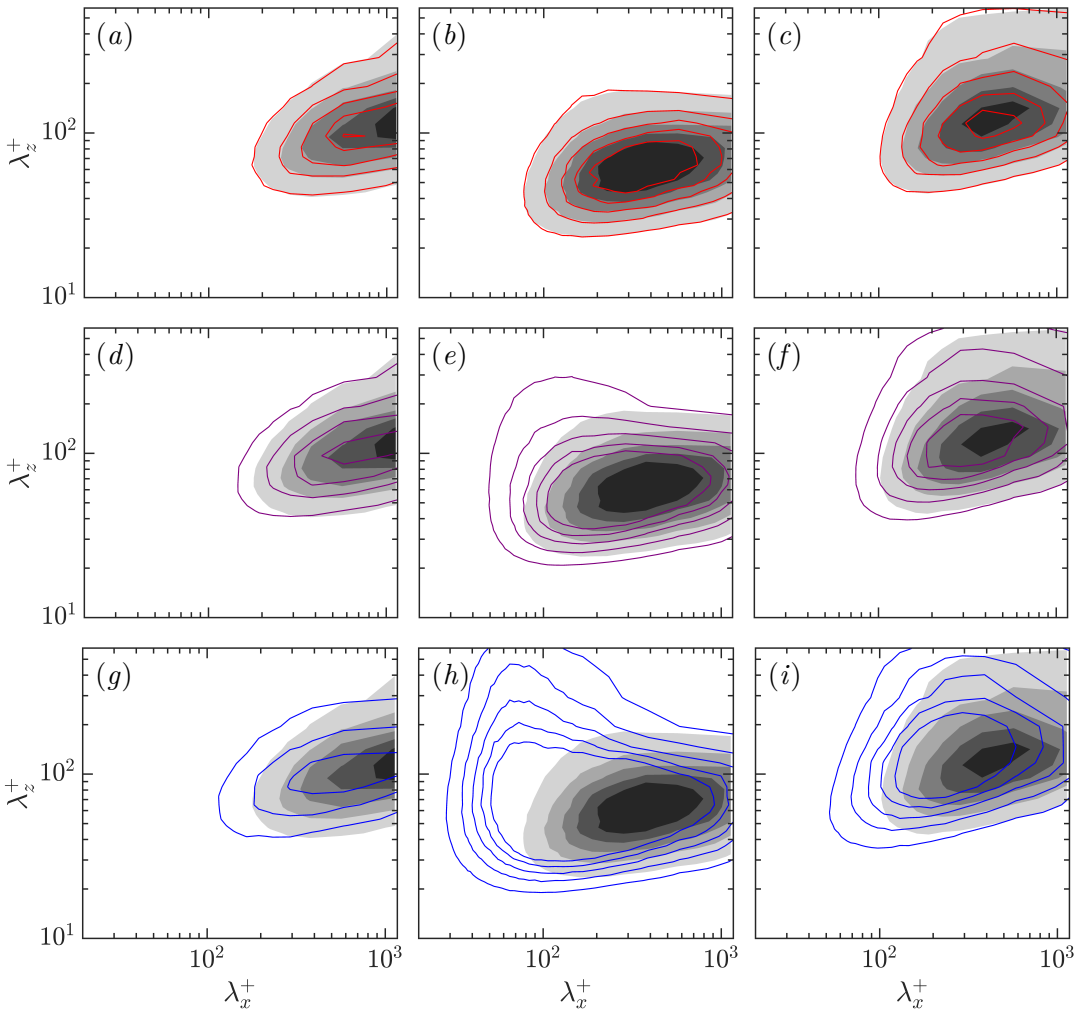

FIGURE 3.7 Premultiplied two-dimensional spectral densities of u^2, v^2 and w^2, referred to as $k_x k_z E_{uu}$, $k_x k_z E_{vv}$ and $k_x k_z E_{ww}$, respectively. Shaded contours correspond to the smooth channel at $y^+ \approx 10$ and the solid lines to the DNSs shifted by their corresponding virtual origin, i.e. at $y^+ \approx 10 - \ell^+$, and scaled with u_τ measured at $y^+ = -\ell^+$. (*a-c*) ——, FP222; (*d-f*) ——, FP333; (*g-i*) ——, FP444. First column, $k_x k_z E_{uu}$; second column $k_x k_z E_{vv}$; third column, $k_x k_z E_{ww}$. The contour increments in wall units are 0.3241, 0.0092 and 0.0404, respectively.

To gain further insight on whether the intensity of the one-point statistics comes from flow lengthscales that are also present in smooth channel, we examine the spectral density distributions of u^2, v^2 and w^2, as given in Jiménez (2004). As an example, figure 3.7 shows the energy distribution at a height of roughly 10 wall units above the virtual origin, $y^+ + \ell^+ \approx 10$. For $\ell^+ = 2$, case FP222, the agreement with the smooth channel is excellent, confirming that turbulence remains essentially smooth-wall-like and that the effect of the boundary conditions (3.4) is to ascribe the position of a smooth wall to $y^+ = -\ell^+$. For cases FP333 and FP444, however, there are some differences. Panels (*d-i*) reveal that the variations in intensity in the one-point statistics are caused by contributions from lengthscales that do

not appear over smooth walls. The wall-normal velocity exhibits the most dramatic change. Panels (e) and (h) show the appearance of a new energetic region, short in x and wide in z. The source of the energy can be attributed to the large values of the impedance coefficient $\mathcal{C}^+_{S,vp}$ assigned to small lengthscales, as observed in figure 3.5(a), which excites certain modes. This will be further analysed in the following subsections. Notice that for cases FP333 and FP444, it is not possible to obtain a virtual origin of turbulence *per se*, as by definition the concept of a virtual origin assumes that the near-wall cycle and the turbulence dynamics remain smooth-wall-like, which is no longer the case. This is why table 3.3 does not provide a value for ℓ^+_T for cases FP333 and FP444.

3.3.2 Uncoupled boundary conditions from Stokes model

The implementation of the boundary conditions from equation (3.4) involves the full coupling between the three velocities and the pressure, which makes setting different virtual origins for each component difficult. In what follows, we neglect certain terms from equation (3.4), while still maintaining a common virtual origin at $y^+ = -\ell^+$. The aim is to decouple the boundary conditions on the three velocity components to later impose different origins. We do so by retaining only the dominant terms for each component, that is, the slip coefficients $\mathcal{C}_{S,uu}$ and $\mathcal{C}_{S,ww}$ for u and w, respectively, and the transpiration coefficient $\mathcal{C}_{S,vp}$ for v. Thus, the boundary condition for u is expressed in terms of u alone, the boundary condition for w in terms of w alone and that for v in terms of p. The idea is to later define these three conditions separately, as if due to different virtual origins. For this model, only virtual origins with $\ell^+ = 2$ and 3 were tested, labelled as DIP222 and DIP333, where D($iagonal$) means that only the three coefficients in the diagonal of equation (3.4) are retained, I($nhomogeneous$) means that the coefficients for u and w are wavelength-dependent, and P means that the boundary condition for v is imposed in terms of p. As before, the numbers correspond to the virtual origins for u, w and v that we intend to impose.

For $\ell^+ = 2$, case DIP222, the model reproduces reasonably well the effect of a virtual wall at $y^+ = -2$, as shown by the good collapse of the profiles with smooth-wall data illustrated in figures 3.8(a.1-a.4). On a closer inspection, however, the turbulent fluctuations show a small, but noticeable, deviation from the smooth-wall data. In particular, the depth of the virtual origin of w and v is slightly less than 2 wall-units and, as a result, the shift of the streamwise vorticity and the Reynolds stress, which relate to the origin of quasi-streamwise vortices, is also slightly less than 2 wall units, $\ell^+_T \approx 1.5$ (see table 3.3). The origin of the mean flow, on the other hand, is at $y^+ = -2$. The difference between the virtual origin perceived by the mean flow and that perceived by the quasi-streamwise vortices results in a small upward shift of the log law, as can be appreciated in panel (a.1).

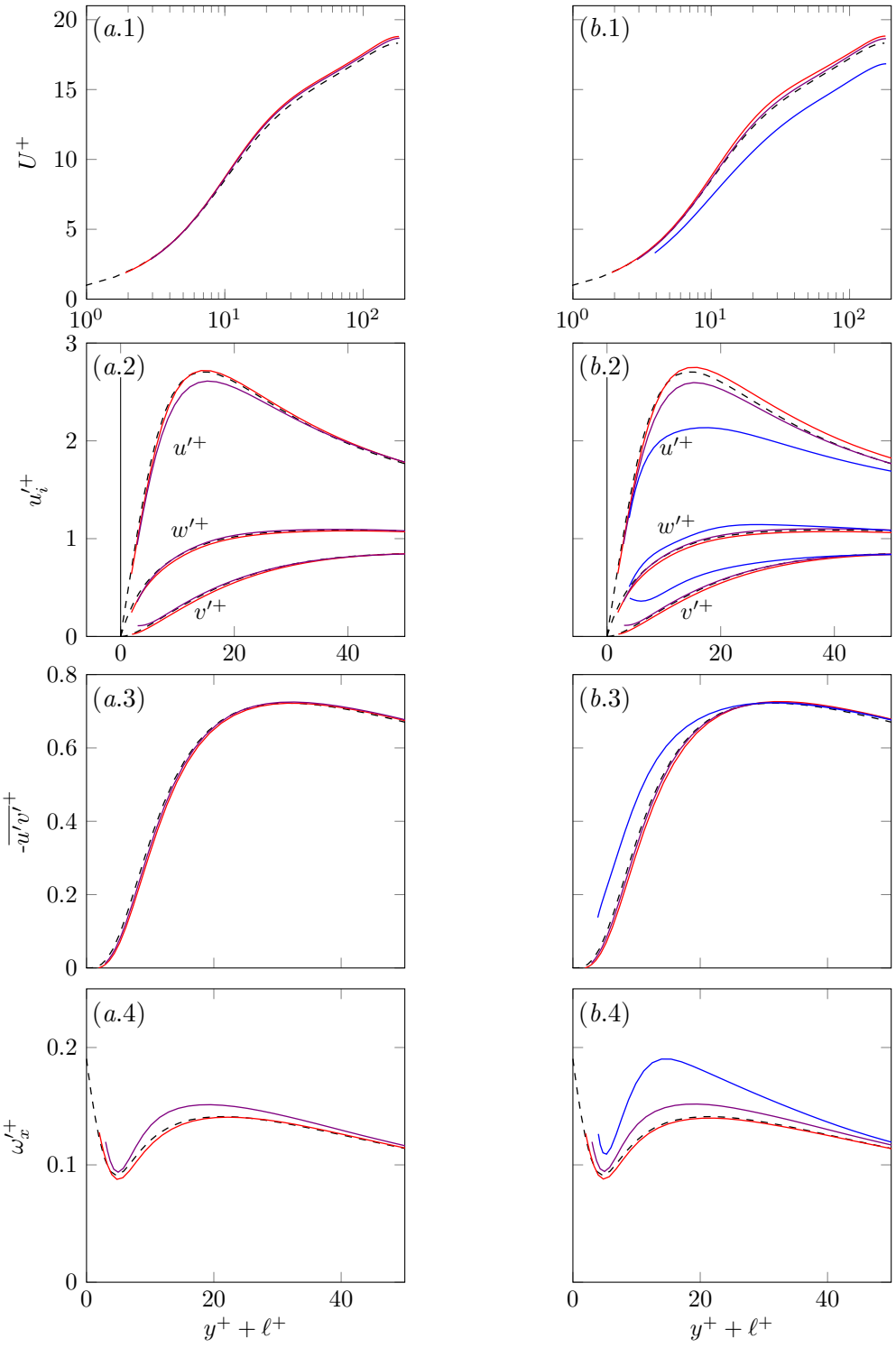

FIGURE 3.8 (a.1-a.4) ——, DIP222; ——, DIP333; – – –, smooth channel. (b.1-b.4) ——, DHP222; ——, DHP333; ——, DHP444; – – –, smooth channel. (a.1-b.1) Mean velocity profiles; (a.2-b.2) rms velocity fluctuations; (a.3-b.3) Reynolds shear stresses; (a.4-b.4) streamwise vorticity fluctuations. All the profiles are scaled with u_τ measured at the virtual wall, $y^+ = -\ell^+$, and shifted by ℓ^+.

For $\ell^+ = 3$, on the other hand, results are, as expected, no better than those observed with full off-wall conditions, case FP333. The current model also fails to mimic a virtual origin at $y^+ = -3$.

3.3.3 Uncoupled boundary conditions from Stokes model with homogeneous slip lengths

To further simplify the boundary conditions, we now impose homogeneous tangential slip lengths (ℓ_x^+ and ℓ_z^+) to model the virtual origins of u and w, removing any dependencies of the slip coefficients on the lengthscales. For v, on the other hand, we keep a wavelength-dependent transpiration, $\mathcal{C}_{S,vp}^+$, as before. This follows from previous studies on slip-only simulations (Min & Kim, 2004; Busse & Sandham, 2012), and is also supported by the observations in figure 3.5(b). This figure shows how $\mathcal{C}_{S,ww}^+$ is essentially homogeneous across the energetically relevant lengthscales in the flow and assuming it to be homogeneous is therefore a sensible approximation. The same can also be argued for $\mathcal{C}_{S,uu}^+$, but not $\mathcal{C}_{S,vp}^+$. For the latter, its wavelength-dependent nature needs to be accounted for. We refer to these simulations as DHP222, DHP333 and DHP444, where compared to the previous cases, the second letter has been switched to H(*omogeneous*) to refer that the boundary conditions for u and w are now homogeneous, that is, the same for all wavelengths.

The results obtained with this model are similar to those from the previous subsection, as shown in figures 3.8(b.1-b.4). For $\ell^+ = 2$, case DHP222 mimics reasonably well a wall at $y^+ = -2$, although, as for DIP222, the origin perceived by quasi-streamwise vortices is slightly shallower than 2 wall units. For larger ℓ^+, cases DHP333 and DHP444 also failed to model a virtual wall at $y^+ = -3$ and $y^+ = -4$, respectively. Additionally, with uncoupled boundary conditions, the profiles of v'^+ near the wall diverge even more than when full Stokes conditions were imposed, i.e. in cases FP333 and FP444 from before. Although not shown here, with uncoupled boundary conditions, the new energetic region observed previously in the v-spectrum of FP333 and FP444 intensifies, supporting the idea that the disparity between these cases and the corresponding smooth channel is indeed due to the large permeability values at small lengthscales. In order to eliminate the appearance of the new lengthscales observed for DHP333 and DHP444, a low-pass filtering on $\mathcal{C}_{S,vp}$ was also tested in a separate simulation. In this case, the boundary condition $v^+ = \mathcal{C}_{S,vp}^+ p^+$ was applied only to large eddies, while eddies smaller than $\lambda_x^+ < 50$ and $\lambda_z^+ < 10$ were free to permeate through a boundary condition of the form $dv^+/dy = 0$, avoiding possible feedback amplification between v and p. However, this was not sufficient to impede the amplification of all the small lengthscales.

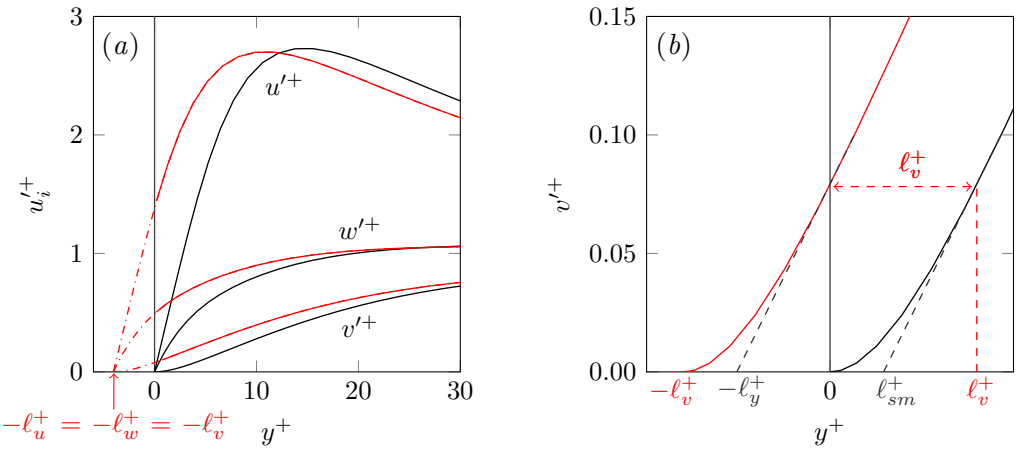

FIGURE 3.9 Schematics showing (a) the definition of the virtual origins ℓ_u^+, ℓ_w^+ and ℓ_v^+ as the shift of the rms velocity fluctuations with respect to a smooth channel; (b) the difference between ℓ_v^+ and ℓ_y^+. ——, smooth channel; ——, curves with equal origins for the three velocity components.

3.3.4 Robin conditions for the three velocities

Given that the model constructed from the Stokes equation breaks down for a virtual origin deeper than two wall units, a different strategy has been pursued. By analogy with the slip-length model for the tangential velocities, we propose Robin conditions for the three velocity components,

$$u|_{y=0} = \ell_x \left.\frac{\partial u}{\partial y}\right|_{y=0}, \quad w|_{y=0} = \ell_z \left.\frac{\partial w}{\partial y}\right|_{y=0} \quad \text{and} \quad v|_{y=0} = \ell_y \left.\frac{\partial v}{\partial y}\right|_{y=0}, \tag{3.5}$$

so that u, w and v are related to their respective wall-normal gradients by three slip lengths, ℓ_x, ℓ_z and ℓ_y. Note that for v, ℓ_y does not convey a slip effect, but, by extension, in the present work, we also refer to ℓ_y as the 'slip length' in the wall-normal direction. In what follows, we will set a homogeneous ℓ_y^+, that is, equal for all wavelengths, except for the mean (i.e. $\lambda_x \to \infty$ and $\lambda_z \to \infty$), since from continuity is set to zero.

While the concepts of slip lengths and virtual origins have been used interchangeably in the literature, there is a subtle, but important, difference. We will denote by ℓ_x^+, ℓ_z^+ and ℓ_y^+ the slip lengths in the streamwise, spanwise and wall-normal directions, respectively, defined as the proportionality coefficients in Robin boundary conditions (3.5). From a physical point of view, the slip lengths simply correspond to the y-locations where the velocity components become zero when linearly extrapolated from the reference plane. In contrast, we define the virtual origins of u, w and v as the locations below the reference plane where each velocity component perceives a virtual, smooth wall. These are at $y^+ = -\ell_u^+$, $y^+ = -\ell_w^+$ and $y^+ = -\ell_v^+$, respectively. These correspond to the heights where the rms profiles of the velocity fluctuations u'^+, w'^+ and v'^+ would go to zero assuming that the shape of the profiles remained smooth-wall-like independently from each other, as illustrated in figure 3.9(a). The

slip lengths for the Robin boundary conditions are therefore chosen according to the virtual origins that we intend to impose, ℓ_u^+, ℓ_w^+ and ℓ_v^+, which in the framework of a smooth wall, would be $\ell_u^+ = \ell_w^+ = \ell_v^+ = \ell^+$. For a virtual origin of a few wall units, we expect the slip lengths ℓ_x^+ and ℓ_z^+ to be approximately equal to the origins ℓ_u^+, ℓ_w^+, as the tangential velocities u^+ and w^+ are essentially linear in the immediate vicinity of the wall. We therefore assume that $\ell_x^+ \approx \ell_u^+$ and $\ell_z^+ \approx \ell_w^+$, and set ℓ_x^+ and ℓ_z^+ equal to 2, 3 and 4. The case of v, however, is slightly more delicate. Due to v' being quadratic with y, the height of the virtual origin of v, ℓ_v^+, differs from the slip length ℓ_y^+, even for small values. We set ℓ_y^+ by matching the ratio between v and $\partial v/\partial y$ at a height ℓ_v^+ above the smooth wall. From figure 3.9(b), we can observe that ℓ_y^+ and ℓ_v^+ relate to each other by $\ell_y^+ = \ell_v^+ - \ell_{sm}^+$, where ℓ_{sm}^+ is obtained from extrapolating the slope of the smooth-wall v'^+-profile at $y^+ = \ell_v^+$. This is the depth where, from the point of view of the plane $y^+ = \ell_v^+$, the v'-profile would extrapolate to zero. Note that the value of ℓ_{sm}^+ is a function of ℓ_v^+, as it depends on the local slope at which the extrapolation of the profile is calculated. The values of the slip lengths and virtual origins for the simulations here analysed are compiled in table 3.3. These cases are labelled DHV222, DHV333 and DHV444, where the third letter has been switched to V to indicate that the boundary condition for v is now set by Robin boundary condition in terms of v alone.

Comparing to the previous models, this technique produces a significant improvement on the results, as shown by the good collapse of the turbulent profiles in figure 3.10 and the spectral energy distribution in figure 3.12. This model reproduces with reasonable accuracy not only a virtual origin at $y^+ = -2$, but also at $y^+ = -3$ and $y^+ = -4$. However, on a closer inspection, the resulting origins for the transverse velocities, and consequently the origin of turbulence, ℓ_T^+, are slightly smaller than expected (see table 3.3). This is due to the curvature of w'^+. Beyond $y^+ \gtrsim 1$, w'^+ is not exactly linear, and hence the actual origin of the spanwise velocity that we have imposed is shallower than originally intended, i.e. $\ell_w^+ < \ell_z^+$, as can be appreciated in figure 3.11. This suggests that we should have accounted for the curvature of w' and define ℓ_z^+ in a similar fashion to ℓ_y^+. In retrospect, contemplating the effect of the curvature, the depth of the origin of the spanwise velocity is $\ell_w^+ = 1.7$, 2.3 and 2.9 for cases DHV222, DHV333 and DHV444, respectively, as indicated by the values between parentheses in table 3.3. This effect of the curvature is also present for u', although is weaker, and for the origins here considered, $\ell^+ \lesssim 4$, this effect is negligible. Considering $\ell_x^+ = \ell_u^+$ is therefore an accurate approximation.

In these simulations, the displacement of quasi-streamwise vortices towards the reference plane would be limited by the spanwise velocity, since ℓ_w is the most restrictive origin between those of v and w, i.e. $\ell_w^+ < \ell_v^+$. This is evidenced from the displacement of the streamwise vorticity and Reynolds stress curves, where the origin of turbulence is approximately coincident with that of w, $\ell_T^+ \approx \ell_w^+$.

Moreover, when displaced by ℓ_T^+, the one-point statistics in figure 3.10 and the spectral density distributions of u^2, v^2 and w^2 in figure 3.12 show a better collapse with the smooth-

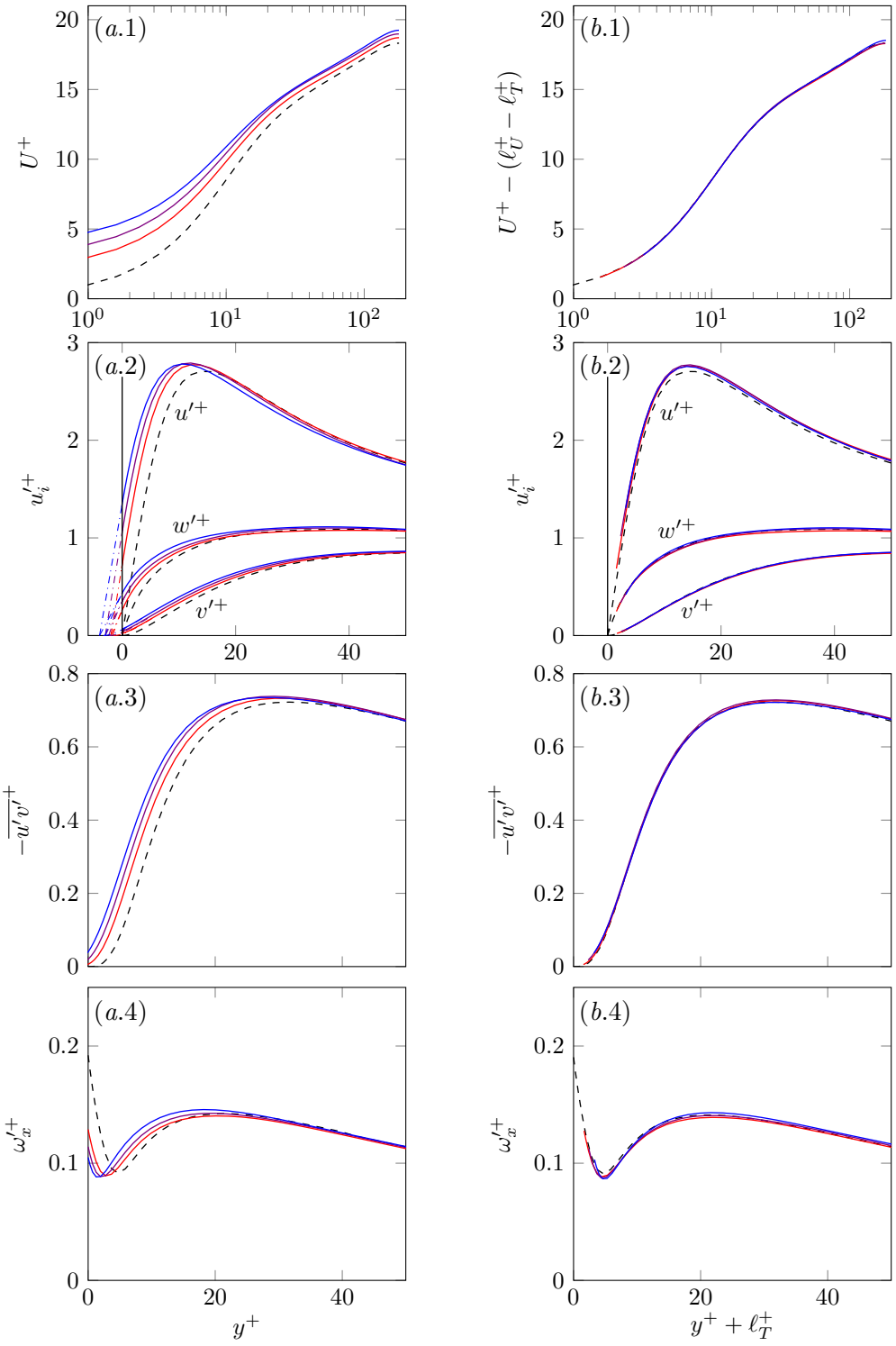

FIGURE 3.10 First column (*a*.1-*a*.4), profiles scaled with u_τ measured at the reference plane where the boundary conditions are imposed, $y^+ = 0$. Second column (*b*.1-*b*.4), profiles scaled with u_τ measured at the origin of turbulence, $y^+ = -\ell_T^+$, and shifted by ℓ_T^+. – – –, smooth channel; ——, DHV222; ——, DHV333; ——, DHV444. (*a*.1,*b*.1) Mean velocity profiles; (*a*.2,*b*.2) rms velocity fluctuations; (*a*.3,*b*.3) Reynolds shear stresses; (*a*.4,*b*.4) streamwise vorticity fluctuations.

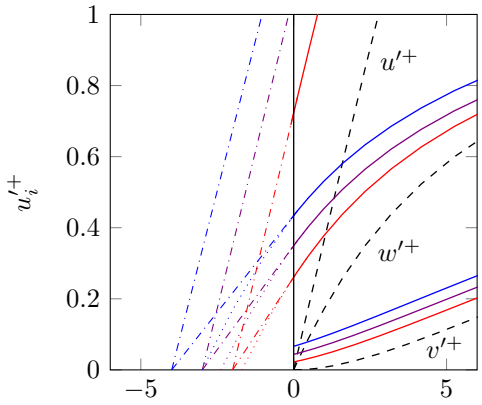

FIGURE 3.11 Rms velocity fluctuations near the reference plane. Zoom of the near-wall region from figure 3.10(*a*.2). - - - -, smooth channel; ——, DHV222; ——, DHV333; ——, DHV444. The dashed-dotted lines show the linear extrapolation of the profiles, which for the spanwise velocity vanish at $y^+ = -\ell_z^+$, giving the spanwise slip length; and the dotted lines show the extrapolation retaining the curvature of smooth-wall profiles, which vanish at the virtual origin $y^+ = -\ell_w^+$.

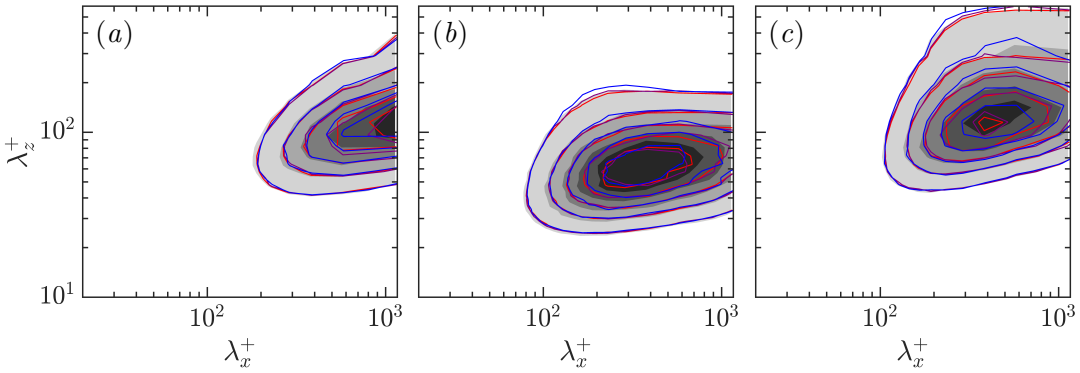

FIGURE 3.12 Premultiplied two-dimensional spectral densities of u^2, v^2 and w^2. Shaded contours correspond to the smooth channel at $y^+ \approx 10$ and the solid lines to the present DNSs shifted by their corresponding virtual origin of turbulence, i.e. at $y^+ \approx 10 - \ell_T^+$, and scaled with u_τ measured at $y^+ = -\ell_T^+$. ——, DHV222; ——, DHV333; ——, DHV444. (*a*) $k_x k_z E_{uu}$, (*b*) $k_x k_z E_{vv}$; (*c*) $k_x k_z E_{ww}$. The contour increments in wall units are 0.3241, 0.0092 and 0.0404, respectively.

wall data than when displaced by their corresponding virtual origins. This suggests that the near-wall cycle, located between $y^+ + \ell_T^+ \approx 10 - 25$, is displaced in block by the origin perceived by turbulence, ℓ_T^+; even though at the reference plane the velocity components decay to their respective virtual origins, enforced by the boundary conditions. Thus, in figures 3.10 and 3.12 we use ℓ_T^+ as the origin for the wall-normal height, with u_τ measured at that height. The differences between the virtual origins of the three velocity components and turbulence, however, are too narrow in these cases for the evidence to be conclusive. The hypothesis that turbulence is displaced in block by ℓ_T^+ needs to be tested by imposing significantly different virtual origins for the different velocity components. This is investigated in the next section.

While for the turbulent fluctuations the origin is at $y^+ = -\ell_T^+$, for the mean flow its origin agrees with the streamwise slip length, i.e. $\ell_U^+ = \ell_x^+$, as the mean velocity profile is much closer to linear in the viscous sublayer than w'^+ or v'^+. The slight upward shift of the logarithmic region observed for the three cases in figure 3.10(a.1) can be attributed to the difference in the origin perceived by the mean flow and turbulence. Therefore, when taking the origin of turbulence as the reference for the wall-normal height, the only difference in U^+ compared to a smooth wall is the offset $\Delta U^+ = \ell_U^+ - \ell_T^+$, and subtracting this offset gives a collapse of the velocity profiles, as shown in figure 3.10(b.1). This confirms the original idea from Luchini (1996): "the law of the wall describing the mean-flow profile of the turbulent stream is modified by the presence of riblets only through a displacement of the origin of an amount equal to the protrusion-height difference. This is what one could expect if the structure of turbulent eddies were unaltered in the reference frame that has the transverse equivalent wall as origin, whereas the mean flow profile obviously starts at the longitudinal equivalent wall."

3.4 Different virtual origins for the tangential and wall-normal velocities with Robin boundary conditions

Now that we have found a technique to impose virtual origins for the three velocities, we can set different origins for each component and see how it affects the overlying flow. In this section, we consider cases with $\ell_x^+ = \ell_z^+ = 2$, 3 and 4 as before, but with $v = 0$. These cases are referred to as DHV220, DHV330 and DHV440, respectively, where, as before, the three numbers correspond to the depths of the virtual origins imposed for u, w and v; although due to the curvature effect of w, its origin is shallower than $y^+ = -2$, 3 and 4, respectively, as indicated in table 3.3. Note that these simulations are analogous to the slip-only simulations studied by Busse & Sandham (2012).

As mentioned before, the displacement of the quasi-streamwise vortices towards the reference plane is determined by the origins of the spanwise and wall-normal velocities, which are set at $y^+ = -\ell_w^+$ and $y^+ = -\ell_v^+ = 0$, respectively. The vortices approach the wall, as they are allowed to slip in the spanwise direction, but their downward displacement is now restricted by v being zero at the simulation boundary. The origin that the vortices perceive, $y^+ = -\ell_T^+$, is therefore at an intermediate height between $y^+ = -\ell_w^+$ and $y^+ = -\ell_v^+$. From the displacement of the profiles of $\omega_x'^+$ and $\overline{u'v'}^+$ in figure 3.13, this origin is at a depth below the reference plane of $\ell_T^+ \approx 1.3$ for case DHV220, $\ell_T^+ \approx 1.7$ for case DHV330 and $\ell_T^+ \approx 1.9$ for DHV440. This is the saturation effect of the spanwise slip discussed in section 3.2. Notice that the v'^+-profiles in panel (a.2) are also shifted in y relative to the smooth-wall profile. This is because, although $v = 0$ at the reference plane, u and w are not, and from continuity, the slope dv/dy is no longer zero. This results in the shift in y of the v'^+-profiles, which

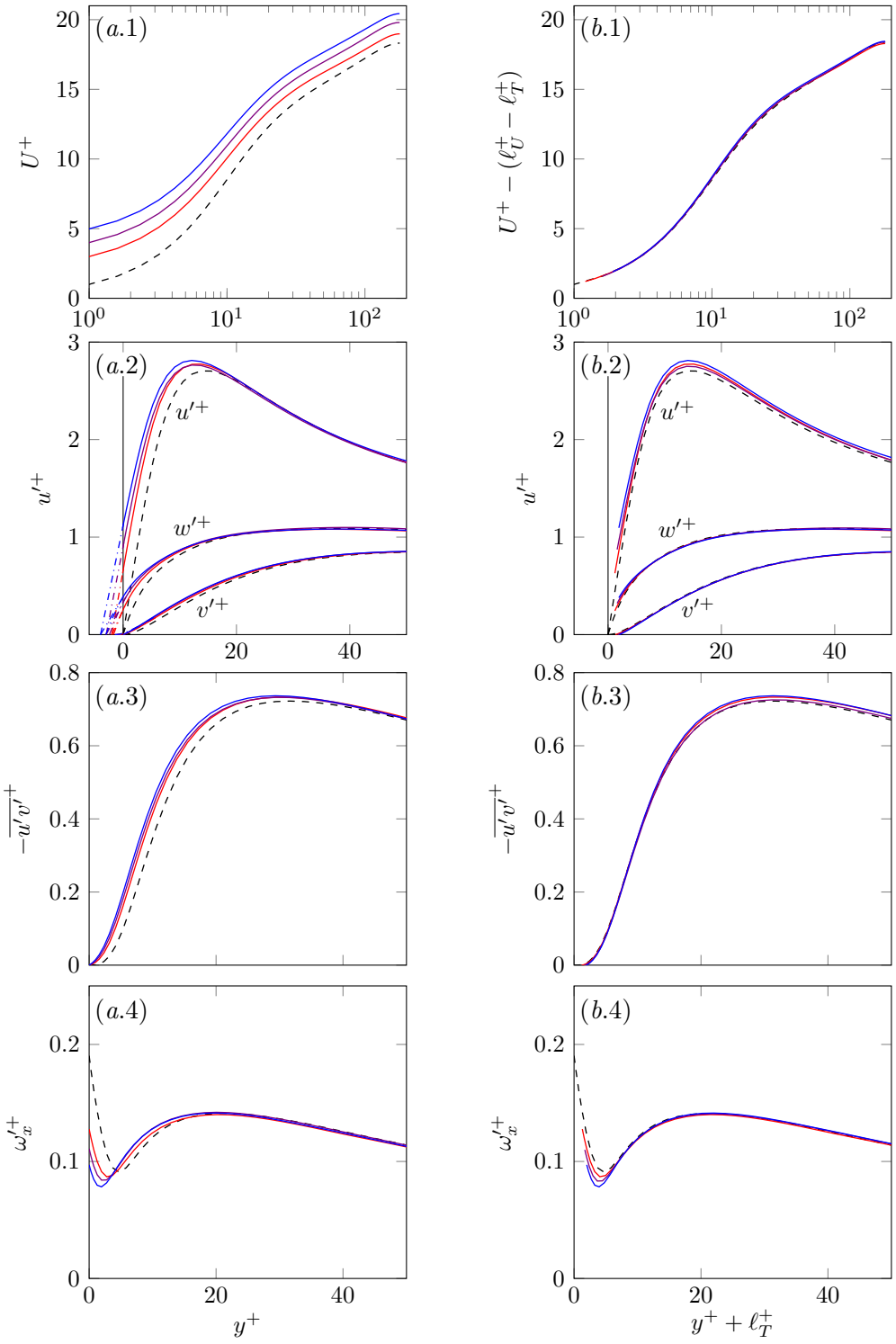

FIGURE 3.13 First column (*a*.1-*a*.4), profiles scaled with u_τ measured at the reference plane where the boundary conditions are imposed, $y^+ = 0$. Second column (*b*.1-*b*.4), profiles scaled with u_τ measured at the origin of turbulence, $y^+ = -\ell_T^+$, and shifted by ℓ_T^+. – – –, smooth channel; ——, DHV220; ——, DHV330; ——, DHV440. (*a*.1,*b*.1) Mean velocity profiles; (*a*.2,*b*.2) rms velocity fluctuations; (*a*.3,*b*.3) Reynolds shear stresses; (*a*.4,*b*.4) streamwise vorticity fluctuations.

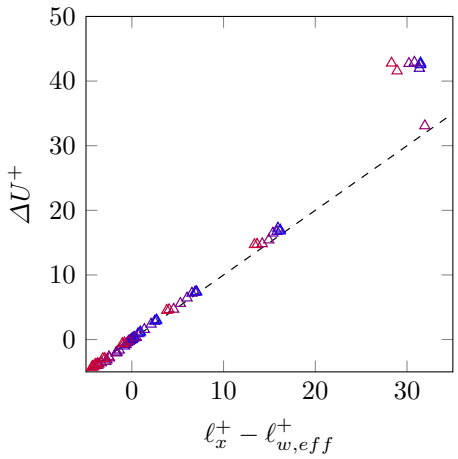

FIGURE 3.14 ΔU^+ as a function of $\ell_x^+ - \ell_{w,eff}^+$, where $\ell_{w,eff}^+$ is given by equation (3.6). Simulations at $\delta_0^+ = 180$. From blue to red the spanwise slip length, and hence ℓ_w^+, increases. The dashed line represents $\Delta U^+ = \ell_x^+ - \ell_{w,eff}^+$. Data obtained from Busse & Sandham (2012).

coincides with ℓ_T^+. This means that the resulting virtual origin perceived by v is not $y^+ = 0$, but $y^+ = -\ell_T^+$.

It was mentioned in section 3.1 that the saturation effect in slip-only simulations could be accounted for by the empirical, effective spanwise slip length given by equation (3.1). There is good agreement between the values of $\ell_{z,eff}^+$ calculated and those of ℓ_T^+ obtained *a posteriori*. However, given that the curvature of w' needs to be accounted for, it would be more appropriate to express the prediction of ℓ_T^+ in terms of ℓ_w^+ instead of ℓ_z^+. This yields a similar expression to equation (3.1),

$$\ell_{w,eff}^+ = \frac{\ell_w^+}{1 + \ell_w^+/5}. \tag{3.6}$$

The good agreement between the values of ℓ_T^+ measured and those provided by $\ell_{w,eff}^+$ for the present simulations can be observed in table 3.3, where the latter are listed in the column, $\ell_{T,pred}^+$. Additionally, using the data from Busse & Sandham (2012), figure 3.14 shows how ΔU^+ agrees with the linear expression $\ell_x^+ - \ell_{w,eff}^+$. Equation (3.6) provides therefore an expression to predict ℓ_T^+ when $\ell_v^+ = 0$.

The present results agree with the observations from the previous section 3.3.4 and support the idea that the near-wall cycle is shifted in block by ℓ_T^+, but remains otherwise smooth-wall-like. This is evidenced by the excellent collapse with the smooth-wall data observed in the one-point statistics and the spectral density distributions in figures 3.13(*b*.1-*b*.4) and 3.15, where they have all been shifted by ℓ_T^+, with u_τ measured at that origin. This implies that the effect of virtual origins on the overlying turbulence is represented well by a single parameter, the origin of turbulence, ℓ_T^+; although there are small differences immediately above the reference plane, caused by the need to meet the specific boundary conditions imposed. The

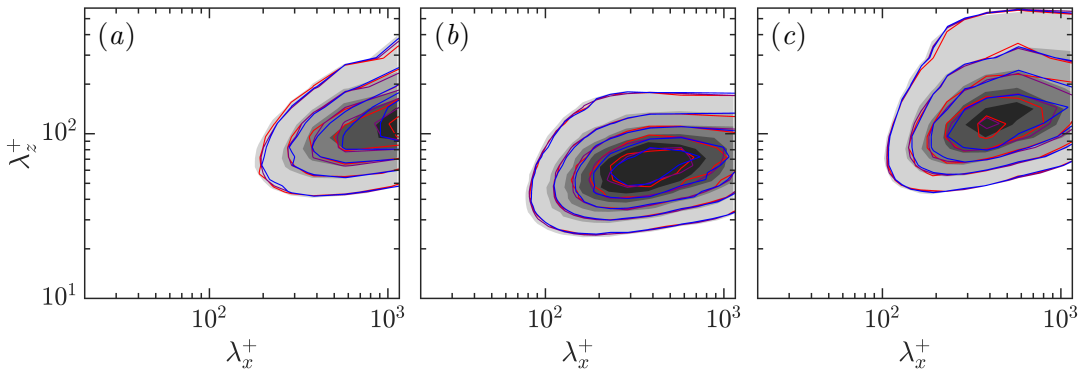

FIGURE 3.15 Premultiplied two-dimensional spectral densities of u^2, v^2 and w^2. Shaded contours correspond to the smooth channel at $y^+ \approx 10$ and the solid lines to the present DNSs shifted by their corresponding virtual origin of turbulence, i.e. at $y^+ \approx 10 - \ell_T^+$, and scaled with u_τ measured at $y^+ = -\ell_T^+$. ——, DHV220; ——, DHV330; ——, DHV440. (a) $k_x k_z E_{uu}$, (b) $k_x k_z E_{vv}$; (c) $k_x k_z E_{ww}$. The contour increments in wall units are 0.3241, 0.0092 and 0.0404, respectively.

u'^+-profiles in figure 3.13(b.2), for instance, decay linearly towards its origin, $y^+ = -\ell_x^+$, which is deeper than $y^+ = -\ell_T^+$. The viscous sublayer, where viscosity acts, is therefore increased, modifying the gradient at $y^+ = 0$ and resulting also in an slight increase of the magnitude of the peak. This, however, does not appear to alter the near-wall dynamics.

The imposed virtual origins ℓ_u^+, ℓ_v^+ and ℓ_w^+ (or alternatively the slip lengths ℓ_x^+, ℓ_y^+ and ℓ_z^+) appear to have separate effects on the overlying flow. The latter two set the origin of turbulence, ℓ_T^+, and hence determine the displacement of the near-wall cycle, while ℓ_u^+ is essentially inactive on modifying the turbulence cycle, and acts on determining the shift of the mean flow instead. This is apparent on the mean velocity profiles shown in panel (a.1), where the origin of the mean flow is at a depth of 2, 3 and 4 wall units below the reference plane for the cases DHV220, DHV330 and DHV440, respectively, and hence $\ell_U^+ = \ell_u^+$ (where $\ell_u^+ = \ell_x^+$). Taking the virtual origin of turbulence, $y^+ = -\ell_T^+$, as the height origin, panel (b.1) shows that the difference between the mean velocity profiles reduces to an offset $\ell_U^+ - \ell_T^+$, constant along the entire height, and which corresponds to the value of U at the origin of turbulence. Drag reduction can then be obtained despite the slip lengths in the streamwise and spanwise directions being equal, as reported in the literature (Min & Kim, 2004; Busse & Sandham, 2012) and in contradiction with Luchini's theory (1.5), due to the wall-normal velocity having a shallower virtual origin.

3.5 Generalisation of the virtual-origin model

Combining the information obtained from the present results, in this section we review the linear theory of slip lengths originally proposed by Luchini (1996).

The excellent collapse observed when the height $y^+ = -\ell_T^+$ is set as the height origin supports Luchini's original idea that the near-wall turbulence and the turbulence dynamics remain smooth-wall-like. We have shown that the effect of virtual origins on turbulence can be reduced to a shift by ℓ_T^+ alone. By this, we implicitly refer not only to a shift by ℓ_T^+, but also to a rescaling of the results by the friction velocity defined at $y^+ = -\ell_T^+$. Recently, García-Mayoral *et al.* (2019) highlighted the effect of choosing different heights as origin. In that work, we reported that setting an origin different to that perceived by turbulence, $y^+ = -\ell_T^+$, may result in an apparent change in magnitude of turbulence intensities, as well as an apparent change in the slope of the mean profile in the logarithmic region, which translates into a modification of Kármán's constant, κ. When using a logarithmic scaling to represent the wall-normal height y^+, the mean velocity profile in the logarithmic region is an oblique line. Due to the logarithmic scaling, setting different height origins produces a stretching of the oblique line, changing the slope of U^+ in the logarithmic layer, which manifests as an apparent change in κ. García-Mayoral *et al.* (2019) illustrated this effect through a Taylor expansion of the logarithmic function. Choosing $y^+ = -\ell_0^+$ as the origin, the expansion of $\log(y^+ + \ell_0^+)$ for $y^+ > \ell_0^+$ is $\log(y^+) + \ell_0^+/y^+$. As y^+ increases, the second term, ℓ_0^+/y^+, eventually vanishes, but it can be appreciable for a large part of the logarithmic layer. The term ℓ_0^+/y^+ induces therefore an apparent change in κ if the friction Reynolds number is not sufficiently large. The results obtained in this chapter suggest that the appropriate origin is given by the origin of turbulence, i.e. $\ell_0^+ = \ell_T^+$, as it recovers the smooth-wall slope in the logarithmic region. This is also proposed by Fairhall *et al.* (2019) for superhydrophobic surfaces and by García-Mayoral *et al.* (2019) in the review on the effect of surface textures. The height origin for a complex surface should therefore be set at the plane $y^+ = -\ell_T^+$, with u_τ defined at that height, and this should also be the position of a reference smooth wall for comparison. We will use this reference plane when obtaining ΔU^+ for permeable substrates in chapter 7 and those for different complex surfaces in chapter 4.

With the proposed scaling, the mean velocity profile is smooth-wall-like, as shown in figures 3.10(b.1) and 3.13(b.1), save for the offset by its value at $y^+ = -\ell_T^+$, which is $\ell_U^+ - \ell_T^+$, and this offset propagates to any height y^+ above that plane. Luchini's linear law, given by equation (1.5), can then be generalised to

$$\Delta U^+ = \ell_U^+ - \ell_T^+. \tag{3.7}$$

This supports the existing understanding that the change in drag is caused by the difference between the virtual origins perceived by the mean flow and that perceived by the overlying turbulence. In general, we can expect $\ell_U^+ \approx \ell_x^+$, because in the viscous sublayer the mean velocity profile is essentially linear, which means that ℓ_U^+ can be predicted by ℓ_x^+. However, the origin of turbulence, determined by the proximity of quasi-streamwise vortices to the reference plane, is not fully defined by ℓ_z^+ alone, as originally postulated by Jiménez (1994)

and Luchini (1996), but by a combination of the origins perceived by the spanwise and wall-normal velocities, ℓ_w^+ and ℓ_v^+.

Our preliminary results suggest that we could predict ℓ_T^+ from these two virtual origins imposed *a priori*, ℓ_w^+ and ℓ_v^+, or, alternatively from the slip lengths ℓ_z^+ and ℓ_y^+, as there is a one-to-one relationship between slip lengths and virtual origins. That is, knowing the slip lengths (ℓ_x^+, ℓ_z^+ and ℓ_y^+) the depths of the virtual origins (ℓ_u^+, ℓ_w^+ and ℓ_v^+) can be obtained and vice-versa.

When the spanwise velocity has a non-zero virtual origin, but that of the wall-normal velocity is set to zero, i.e. $\ell_w^+ > \ell_v^+ = 0$, ℓ_T^+ can be approximated by equation (3.6), as discussed in section 3.4, where $\ell_{w,eff}^+ = \ell_w^+/(1+\ell_w^+/5)$. Let us take this a step further and expand this expression for $\ell_w^+ > \ell_v^+$ in general, when $\ell_v^+ \neq 0$. In this case, we would recover the previous configuration with $\ell_v^+ = 0$ by simply changing the frame of reference to $y^+ = -\ell_v^+$. Therefore, applying this change of reference to the expression (3.6) gives

$$\ell_T^+ \approx \ell_v^+ + \frac{(\ell_w^+ - \ell_v^+)}{1+\frac{1}{5}(\ell_w^+ - \ell_v^+)}. \tag{3.8}$$

The origin of turbulence ℓ_T^+ would then be at an intermediate plane between ℓ_v^+ and ℓ_w^+, as illustrated in figure 3.16(a). The use of ℓ_w^+ instead of ℓ_z^+ for the prediction of ℓ_T^+ can be justified from this change of reference. For example, a configuration with $\ell_u^+ = 4$, $\ell_w^+ = 4$ and $\ell_v^+ = 2$ should be identical to $\ell_u^+ = 2$, $\ell_w^+ = 2$ and $\ell_v^+ = 0$, and the origin of turbulence should be at the same intermediate plane relative to $y^+ = -\ell_v^+$. Notice however that, due to the convex nature of the w'^+-profile, the relative value of ℓ_z^+ is greater for the former than for the latter, and hence using ℓ_z^+ in equation (3.8) instead of ℓ_w^+ would result in different locations for ℓ_T^+, as sketched in figure 3.17. This was not an issue when $\ell_v^+ = 0$.

When the origin of v is coincident with that of w, i.e. $\ell_v^+ = \ell_w^+$, no saturation effect is observed and $\ell_T^+ = \ell_v^+ = \ell_w^+$, as illustrated in figure 3.16(b).

In contrast, if the origin of v is deeper than that imposed for w, i.e. $\ell_v^+ > \ell_w^+$, we would expect the displacement of quasi-streamwise vortices to be essentially governed by the ability of the induced spanwise flow to approach the reference plane. That is, the vortices would approach the reference plane by no more than ℓ_w^+, as below that height the wall-normal velocity is not accompanied by a spanwise flow. We would therefore expect ℓ_T^+ to depend essentially on ℓ_w^+, i.e. $\ell_T^+ \approx \ell_w^+$, as observed for cases DHV222, DHV333 and DHV444. The *w-control* case from Choi *et al.* (1994) also provides some insight into this scenario, where $\ell_w^+ < \ell_v^+$. The drag reduction obtained with *w-control*, where $\ell_w^+ \approx 0$, but ℓ_v^+ is finite, was practically equal to that obtained with *v-w-control*, where both $\ell_v^+ \approx \ell_w^+ \approx 0$. This suggests that with *w-control*, the origin of the vortices is essentially the same as with *v-w-control*, that is, that in both cases $\ell_T^+ \approx 0$. This further supports that, when $\ell_w^+ < \ell_v^+$, the origin of turbulence is set by the origin of the spanwise velocity, i.e. $\ell_T^+ \approx \ell_w^+$, as illustrated in figure 3.16(c).

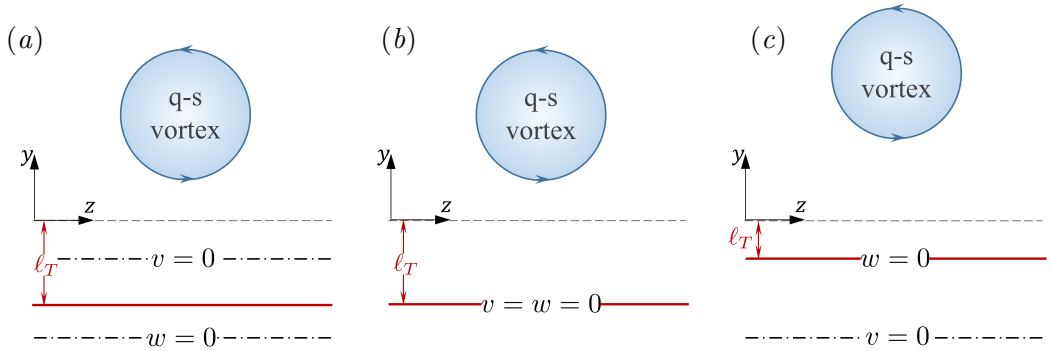

FIGURE 3.16 Schematics of the location of the origin for turbulence, $y = -\ell_T$, when imposing different origins for the spanwise and wall-normal velocities. The planes where $v = 0$ and $w = 0$ correspond to the imposed virtual origins, $y^+ = -\ell_v^+$ and $y^+ = -\ell_w^+$, respectively. The origin of turbulence, $y^+ = -\ell_T^+$, is represented by the red line. (a) $\ell_v^+ < \ell_w^+$, (b) $\ell_v^+ = \ell_w^+$, (c) $\ell_v^+ > \ell_w^+$.

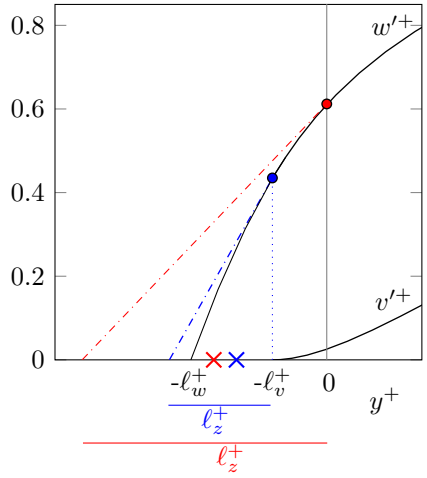

FIGURE 3.17 Sketch of the slip length ℓ_z^+ required for a configuration with $\ell_w^+ > \ell_v^+ \neq 0$ in red, and the equivalent configuration when the frame of reference is shifted to $y^+ = -\ell_v^+$ in blue, so that $\ell_w^+ > \ell_v^+ = 0$. The red and blue crosses correspond to the origin of turbulence, ℓ_T^+, predicted for each configuration if the slip lengths, ℓ_z^+, is used in equation (3.8).

Combining this information, a predictive expression for ℓ_T^+ is

$$\ell_T^+ \approx \begin{cases} \ell_v^+ + \dfrac{(\ell_w^+ - \ell_v^+)}{1 + \dfrac{1}{5}(\ell_w^+ - \ell_v^+)} & \text{if} \quad \ell_w^+ > \ell_v^+, \\ \ell_w^+ & \text{if} \quad \ell_w^+ \lesssim \ell_v^+. \end{cases} \tag{3.9}$$

For the cases here considered, the predicted values of ℓ_T^+ using this equation are displayed in table 3.3 (under the column $\ell_{T,pred}^+$), showing good agreement with the values of ℓ_T^+ obtained from the DNSs. This expression, however, is only preliminary and more simulations are required to validate it. This has already been done by Mr. Joseph Ibrahim from CUED, who carried on with the work on virtual origins and run additional simulations to validate these

hypotheses. The measured values of ℓ_T^+ from the new simulations that were conducted agree reasonably well with those predicted by equation (3.9) (Ibrahim & García-Mayoral, 2019).

In conclusion, in this chapter we have generalised Luchini's virtual-origin theory and developed a technique to model these virtual origins based on Robin boundary conditions. There are, however, two main limitations to the model of Robin boundary conditions. Firstly, the virtual-origin model implicitly assumes that the near-wall cycle remains canonical, that is, it remains as that over a smooth wall, and hence the imposed virtual origins can only be of a few wall units, i.e. $\ell^+ < 10$, so that the near-wall cycle is not completely ingested into the substrate. Secondly, the use of Robin boundary conditions relies on the velocity profiles being smooth-wall-like independently from each other, since the slip lengths are obtained based on the wall-normal gradients of the smooth profiles. This implies that the present model and the expression for ℓ_T^+ defined in equation (3.9) are valid as long as the virtual origins set for the three velocity components differ only by a few wall units from each other. If the origins perceived by the components differ substantially, the resulting wall-normal gradients at the reference plane may be modified from those of a smooth wall, due to the coupling between the velocities just above the reference plane. The actual origins would then be different to those expected. Additionally, assuming that these Robin boundary conditions are applicable to model the effect of real complex surfaces, there is the additional effect of the texture granularity that the model is not able to capture. Further investigation is therefore needed to find if the virtual-origin model developed here can adequately explain the change in drag produced by different complex surfaces. For that purpose, in the next chapter we explore a variety of complex surfaces and study the applicability of the virtual-origin theory.

Chapter 4

Virtual Origins Part II: applicability of the virtual-origin model for complex surfaces*

Chapter 3 showed that the effect that virtual origins have on the flow can be reduced to an offset between the virtual origin perceived by the mean flow and that perceived by the overlying turbulence, $\Delta U^+ = \ell_U^+ - \ell_T^+$. Taking the origin of turbulence as the reference height, turbulence is essentially unchanged with respect to a smooth wall. This chapter reviews several complex surfaces and investigates the applicability of the virtual-origin model for each of them. The aim is to express the effect of a variety of complex surfaces in the unified framework of virtual origins. This unified theory would aid in the formulation of simplified models that capture the effect of surfaces in general on the overlying turbulent flow and on drag, without requiring fully-resolved simulations or experiments.

For small texture sizes, we show that the change in drag for both drag-increasing and -decreasing surfaces can be effectively expressed as a linear function of the offset between the two origins, as anticipated by the virtual-origin theory in chapter 3. For texture sizes lying in this linear regime, the surfaces can be modelled using homogeneous Robin boundary conditions. As the texture sizes become larger, drag-degrading effects emerge that go beyond a mere virtual-origin effect and that are particular to each surface, such as the Kelvin-Helmholtz instability observed for permeable substrates. We present some preliminary work to model the effect of these Kelvin-Helmholtz instabilities using an impedance boundary condition between the wall-normal velocity and the pressure. The results compiled in this chapter allow a direct comparison between the drag reduction produced by permeable substrates and that produced by other drag-reducing surfaces, such as riblets or superhydrophobic surfaces.

*Parts of the content of this chapter have been published in *Proceedings of Summer Program*, 277 – 286, with Akshath Sharma and Ricardo García-Mayoral as co-authors.

4.1 Virtual-origin theory and complex surfaces studied

In chapter 3 we discussed how in flows over smooth surfaces an origin on the wall-normal coordinate can be defined at the surface itself, where all three velocity components vanish. In flows over complex surfaces with small texture sizes, however, the velocity components may appear to vanish at different heights. Different virtual origins can then be defined for the different components. Taking, as reference, the plane of the outermost tips of the texture, where we set $y^+ = 0$, these origins will be at $y^+ = -\ell_u^+$, $y^+ = -\ell_v^+$, and $y^+ = -\ell_w^+$ for the streamwise, wall-normal and spanwise velocities, respectively. We have also discussed that the effect of virtual origins on the flow can be modelled through the use of Robin boundary conditions on the three velocities,

$$u|^+_{y^+=0} = \ell_x^+ \left.\frac{\partial u}{\partial y}\right|^+_{y^+=0} \qquad w|^+_{y^+=0} = \ell_z^+ \left.\frac{\partial w}{\partial y}\right|^+_{y^+=0} \qquad \text{and} \qquad v|^+_{y^+=0} = \ell_y^+ \left.\frac{\partial v}{\partial y}\right|^+_{y^+=0}, \tag{4.1}$$

where the proportionality coefficients ℓ_x^+, ℓ_z^+, ℓ_y^+ are the slip lengths.

We observed that the effect of the virtual origins on the overlying flow can be fully described by two virtual origins, the virtual origin perceived by the mean flow, ℓ_U^+, and that perceived by turbulence, ℓ_T^+, where the former is given by $\ell_U^+ \approx \ell_x^+$ and the latter can be estimated using equation (3.9). Based on this, we proposed that, over a complex surface, the shift of the mean velocity profile in the logarithmic region, and hence the change in drag, can be solely ascribed to the offset $\ell_U^+ - \ell_T^+$, as given by equation (3.7).

This equation, however, is valid only if the virtual origins are displaced by no more than a few wall units, so the near-wall cycle is perturbed but not destroyed. Thus, we would expect the virtual-origin theory for complex surfaces to hold only when the texture size is vanishingly small compared to the characteristic lengthscales of near-wall turbulence. As the size of the texture is increased, the linear behaviour can be expected to eventually break down, either due to the texture modifying the overlying turbulence (Fairhall *et al.*, 2019) or due to additional deleterious effects. These effects depend on the type of complex surface considered. For example, in riblets and anisotropic permeable substrates, the departure from the linear regime can be attributed to the appearance of Kelvin-Helmholtz-like instabilities, as observed by García-Mayoral & Jiménez (2011) for riblets and in chapter 7 for permeable substrates. These instabilities are also known to occur over canopies and would presumably cause the disruption of the linear regime (Sharma & García-Mayoral, 2019). Over superhydrophobic surfaces, in contrast, the deformation of gas pockets (Seo *et al.*, 2015) or the formation of capillary waves (Seo *et al.*, 2018) have been proposed as mechanisms for the breakdown of the linear regime.

In this chapter, we study the applicability of the virtual-origin theory in predicting the flow over different complex surfaces typically used in flow control, in particular, riblets, which are small protrusions aligned with the flow; streamwise-preferential anisotropic permeable

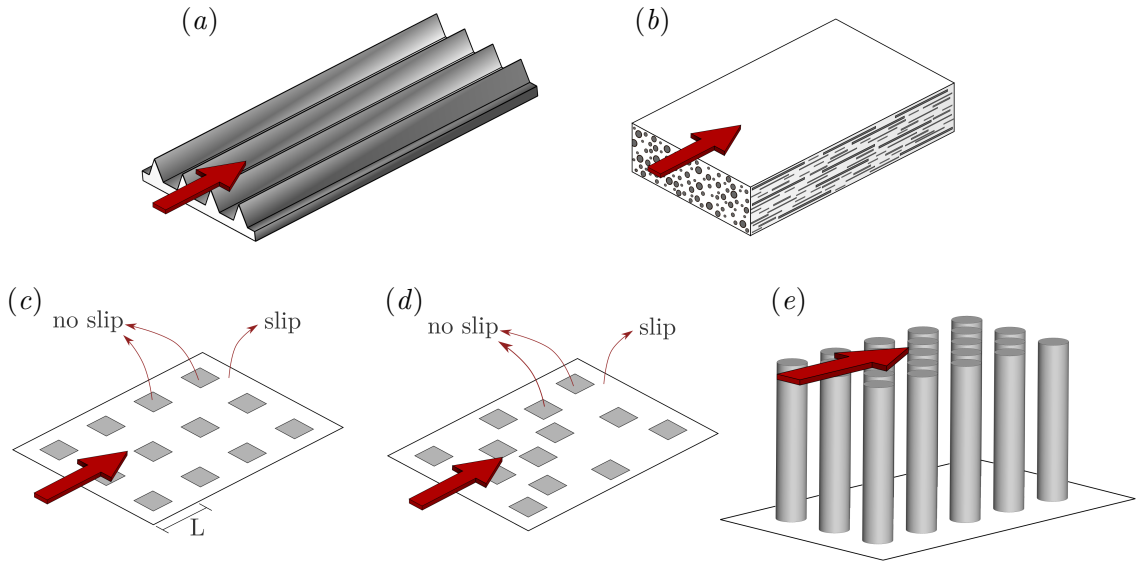

FIGURE 4.1 Sketches of the complex surfaces studied in this chapter: (a) riblets from García-Mayoral (2011), (b) streamwise-preferential anisotropic substrate, (c) regularly distributed superhydrophobic surface, (d) irregularly distributed superhydrophobic surface and (e) canopies.

substrates, as those studied in chapter 7; superhydrophobic surfaces, which are nano-scale surface roughness that can entrap air pockets in-between the roughness protrusions, allowing the overlying flow to slip; and canopies, which are essentially tall roughness elements. Examples of these surfaces are sketched in figure 4.1. The simulations of superhydrophobic surfaces considered here model the surface as alternating free- and no-slip regions, as shown in figure 4.1(c). Two configurations are considered: a regular distribution, where square no-slip elements are arranged in a collocated array, as that in figure 4.1(c); and an irregular distribution, where the square no-slip elements are quasi-randomly distributed. The simulations of streamwise-preferential permeable substrates considered here are modelled using Brinkman's homogenised equation and they will be studied in more detailed in chapter 7. Three configurations are studied, each with a different anisotropy ratio. The DNS data sets studied are taken from García-Mayoral & Jiménez (2011) for riblets; Fairhall *et al.* (2019) and Seo & Mani (2018) for regularly and irregularly distributed superhydrophobic surfaces, respectively; Sharma & García-Mayoral (2019) for canopies; and permeable substrates from chapter 7. The parameters of the simulations studied, except those for permeable substrates, are summarised in table 4.1. The corresponding parameters for the permeable substrates are compiled in table 7.1.

In section 4.2, we obtain the effective slip lengths for the surfaces and explore the extent to which the flow over these surfaces perceives them as imposing Robin boundary conditions (4.1). In section 4.3, we define the virtual origins perceived by the mean flow, ℓ_U^+, and by turbulence, ℓ_T^+, from the slip lengths obtained in the previous section. From these virtual origins, we compare ΔU^+ obtained from the linear theory of equation (3.7), with the

	Case	ϕ_s	L^+		δ^+	ℓ_U^+	ℓ_T^+	ΔU^+
Regular SHS	rSHS1	1/9	6.0		180.0	2.7	1.46	1.24
	rSHS2	1/9	12.0		180.0	4.4	1.84	2.56
	rSHS3	1/9	18.0		180.0	5.8	2.00	3.60
	rSHS4	1/9	24.0		180.0	6.9	2.07	4.00
	rSHS5	1/9	35.0		180.0	8.5	2.22	4.80
	rSHS6	1/9	47.0		180.0	10.0	2.45	5.60
Irregular SHS	iSHS1	1/9	12.9		197.5	4.5	2.01	2.49
	iSHS2	1/9	25.8		197.5	6.3	2.41	4.04
	Case	s^+	ℓ_g^+		δ^+	ℓ_U^+	ℓ_T^+	ΔU^+
Riblets	Rib1	8.09	4.95		185.4	0.73	0.36	0.46
	Rib2	12.05	7.38		184.1	1.08	0.54	0.60
	Rib3	16.01	9.80		183.5	1.41	0.71	0.72
	Rib4	21.29	13.04		183.0	1.86	0.93	0.82
	Rib5	24.07	14.74		183.9	2.08	1.04	0.78
	Rib6	28.41	17.40		186.0	2.42	1.21	0.49
	Rib7	33.41	20.46		191.4	2.75	1.37	0.13
	Case	ϕ_s	L^+	h^+	δ^+	ℓ_U^+	ℓ_T^+	ΔU^+
Canopies	Can1	1/20.25	2.6	10.1	175.9	0.52	0.60	−0.07
	Can2	1/20.25	5.6	22.2	190.7	0.88	1.50	−2.25
	Can3	1/20.25	11.0	43.4	188.2	1.23	3.50	−6.36

TABLE 4.1 DNS cases studied in this chapter. Regularly distributed superhydrophobic surfaces (rSHS) from Fairhall *et al.* (2019), where ϕ_s is the solid area fraction (i.e. ϕ_s = post area/total surface area) and L^+ is the spacing of a texture unit, as defined in figure 4.1(c); irregularly distributed superhydrophobic surfaces (iSHS) from Seo & Mani (2018); riblets (Rib) from García-Mayoral & Jiménez (2011), where s^+ is the riblet spacing and ℓ_g^+ is the square root of the cross-section of the riblet groove; and canopies (Can) from Sharma & García-Mayoral (2019), where ϕ_s and L^+ are the solid fraction and the spacing of the texture unit, and h^+ is the canopy height. For all cases, ℓ_U^+ is the depth of the virtual origin perceived by the mean flow, ℓ_T^+ is that perceived by turbulence, and ΔU^+ is the shift of the velocity profile in the logarithmic region.

actual ΔU^+ measured in the DNSs. Section 4.4 discusses the breakdown of the linear regime for different complex surfaces and we introduce preliminary work to model this breakdown for the specific case of permeable substrates.

4.2 Slip lengths in complex surfaces

In this section, we obtain the slip lengths ℓ_x^+, ℓ_y^+, and ℓ_z^+ from the DNS data sets of the different complex surfaces. If the overlying flow effectively perceives slip-like boundary

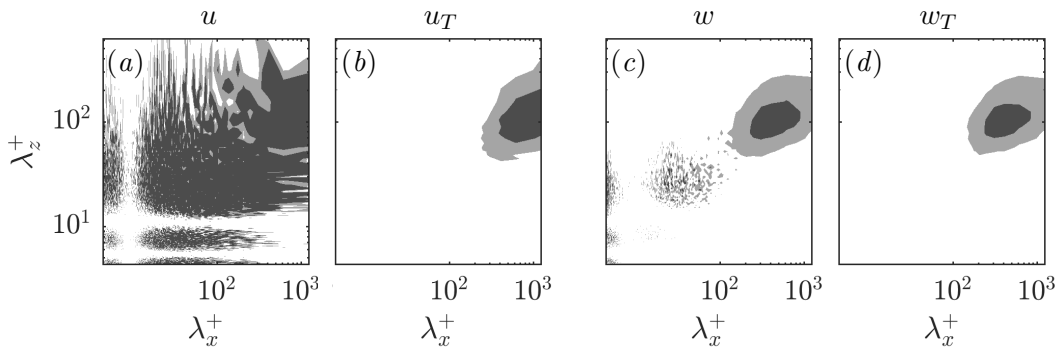

FIGURE 4.2 Premultiplied energy spectra (a,b) $k_x k_z E_{uu}$ and (c,d) $k_x k_z E_{ww}$ for an irregularly distributed superhydrophobic surface, case iSHS2, from Seo & Mani (2018) at a height $y^+ = 0.056$. (a,c) The full velocity components. (b,d) The background turbulent components. Figure courtesy of Mr. Akshath Sharma.

conditions, the velocities and shear at the top of the surface should be correlated at all instants in time, and these correlations would give the slip lengths (Seo & Mani, 2016). However, the surface texture induces a texture-coherent flow in its immediate vicinity that may contaminate the slip lengths obtained from the correlations, as discussed in Fairhall *et al.* (2019) for superhydrophobic surfaces. Therefore, in order to obtain the slip lengths perceived by the overlying turbulence alone, we must first filter out the texture-coherent flow from the flow fields.

4.2.1 Decomposition of the flow for textured surfaces

The filtering of the flow discussed in the present subsection has been done by Mr. Akshath Sharma of CUED. Close to the wall, turbulent flows over textures exhibit a background turbulent component, caused by the overlying turbulence and not coherent with the texture, and a texture-induced, coherent component, through which the footprint of the texture manifests in the flow. In the literature, the triple decomposition from Reynolds & Hussain (1972) is typically used to quantify the intensity of the two contributions, where the texture-coherent contribution is obtained by averaging over time and over the ensemble of texture units. However, subtracting the above ensemble average from the full signal does not completely remove the footprint of the texture. Abderrahaman-Elena *et al.* (2019) and Fairhall *et al.* (2019) noted that the texture-induced flow is modulated in amplitude by the background turbulence and proposed a modified expression for the decomposition of the flow. Following their work, the streamwise velocity, for instance, can be decomposed as

$$u \approx \frac{U+u_T}{U}(U+\widetilde{u}) = U + \widetilde{u}\left(\frac{U+u_T}{U}\right) + u_T, \tag{4.2}$$

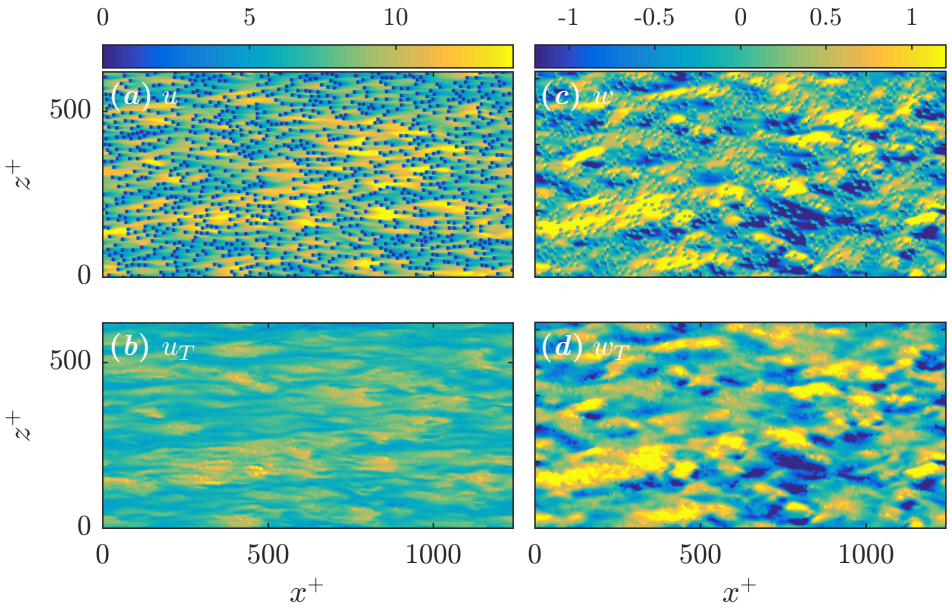

FIGURE 4.3 Instantaneous realisation of the (a,b) streamwise and (c,d) spanwise velocity components over an irregularly superhydrophobic surfaces, case iSHS2, from Seo & Mani (2018) at a height $y^+ = 0.056$. (a) Full streamwise velocity component; (b) background turbulent component for the streamwise velocity, removing the contribution from the texture-coherent flow; (c) full spanwise velocity component; (d) background turbulent component for the spanwise velocity. Figure courtesy of Mr. Akshath Sharma.

where U is the mean velocity profile obtained by averaging in the wall-parallel directions and time, u_T is the background turbulent component, and the tilde indicates ensemble averaging over time and the texture units. In equation (4.2), $U + \widetilde{u}$ is then the total coherent flow, which is modulated in amplitude by the overlying turbulent flow, $U + u_T$. The decomposition for the spanwise velocity and other details about the decomposition can be found in the above references. Using this decomposition, the resulting background turbulent signal, u_T, is essentially devoid of a texture footprint.

We apply the decomposition using two different methods. For surfaces that exhibit a clear separation of scales between the texture-induced, coherent flow and the overlying turbulence, such as for riblets, regular superhydrophobic surfaces and canopies, a Fourier filter can be used to isolate the turbulent component. This is used to filter out the footprint of the texture for riblets and canopies, as the texture sizes are small enough. For the irregular superhydrophobic surfaces from Seo & Mani (2018), on the other hand, there is no single texture wavelength as in the previous cases, and the many texture wavelengths present have scales ranging up to the turbulent scales. This can be observed in the spectral densities in figures 4.2(a,c). These energy spectra show energy at lengthscales of the smooth-wall-like turbulence and at lengthscales of the texture size. Additionally, the modulation of the texture-induced flow with the background turbulent flow results in the texture-induced flow

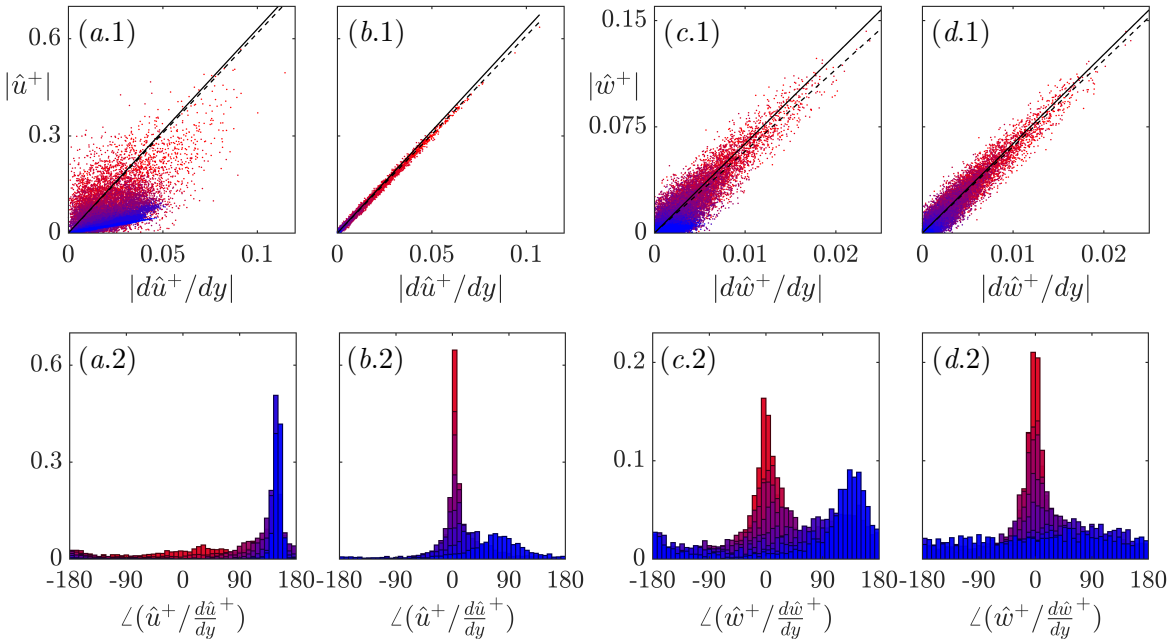

FIGURE 4.4 Instantaneous correlations between (a,b) the streamwise velocity and the wall-normal shear du/dy, and (c,d) the spanwise velocity and the wall-normal shear dw/dy at the interface plane, $y^+ = 0$, for an irregularly distributed superhydrophobic surface from Seo & Mani (2018), case iSHS2. Values are in Fourier space, denoted by the hat superscript, with the spanwise wavelength $\lambda_z^+ \approx 34 - 619$ and the streamwise wavelength increasing from blue to red, $\lambda_x^+ \approx 36 - 1237$. Top row ($a$.1,$b$.1,$c$.1,$d$.1), magnitudes. The dashed line represents the time-averaged slip length, defined by the linear fit of the instantaneous velocities and shear. The solid line represents the slip length perceived by the mean. Bottom row (a.2,b.2,c.2,d.2), phases (where $\angle(A, B)$ represents the phase between A and B). (a,c) The full velocity fields. (b,d) The turbulent components of the velocities.

contaminating the lengthscales of the overlying flow. In this case, instead of Fourier filtering, we apply the decomposition (4.2) algebraically, as in Abderrahaman-Elena *et al.* (2019). The resulting spectral densities of the background turbulent components obtained from the decomposition are shown in figures 4.2(b,d), where the energy induced by the presence of the texture has been effectively removed. These spectra show energy at flow lengthscales that are consistent with smooth-wall-like turbulence. In addition, instantaneous realisations of the full streamwise and spanwise velocity signals for the same irregular superhydrophobic surface at a plane parallel to the surface, and their corresponding background turbulent components once the texture-induced flow has been removed are portrayed in figure 4.3. This figure shows that the decomposition leaves only a residual footprint of the texture on the turbulent component. Once the decomposition has been applied, we analyse the correlation between velocities and their wall-normal gradients on the background turbulent signal alone, u_T. Note that the DNSs for anisotropic permeable substrates do not require filtering, as the boundary conditions implemented to model the substrate are already derived from homogenised models and have no texture granularity effects.

4.2.2 Slip lengths from velocity/shear correlations

Fairhall *et al.* (2019) showed that once the turbulent component of the flow has been extracted, velocity-shear correlations can be used to obtain the tangential slip lengths, as experienced by the overlying turbulence. Following Fairhall *et al.* (2019), we calculate the correlations in Fourier space, so that we can discriminate between different lengthscales in the flow. We calculate the correlations between the three velocity components, $\hat{u}^+$, $\hat{w}^+$ and $\hat{v}^+$, and their wall-normal gradients, $d\hat{u}^+/dy$, $d\hat{w}^+/dy$ and $d\hat{v}^+/dy$, at the top plane of the surfaces, which yields the slip lengths, ℓ_x^+, ℓ_z^+ and ℓ_y^+, respectively. Note that in Fourier space, these slip lengths are characterised by a magnitude and a phase. For a homogeneous slip length to be defined, the velocities and their wall-normal gradients should be correlated in time and across all wavelengths, with phase 0°.

As an example, in figure 4.4 we portray, for an irregularly distributed superhydrophobic texture from Seo & Mani (2018), instantaneous magnitudes of the interfacial tangential velocities versus their respective shear, as well as the phase between them. As observed by Fairhall *et al.* (2019) for regular superhydrophobic surfaces, the background-turbulent velocities and shears are much better correlated than their full-signal counterparts. Panels (*b*,*d*) show that the turbulent components of the tangential velocities and their wall-normal gradients are correlated in time and across all wavelengths, with no phase lag between them, so that we can define wavelength-independent slip lengths, ℓ_x^+ and ℓ_z^+, from the slope of the linear fit of the correlations. The scatter observed in figure 4.4(*d*.1), which even if small did not occur for the regular textures studied by Fairhall *et al.* (2019), is likely due to the decomposition in equation (4.2) not being able to completely remove the footprint of the texture for irregularly distributed textures, as can be observed in figure 4.3(*d*). Note that in these simulations, the wall-normal velocity is set to zero at the texture surface, so $\ell_y^+ = 0$. The overlying turbulence therefore experiences the surface as homogeneous slip conditions, and homogeneous Robin boundary conditions defined in equation (4.1) can be used to model the surface.

For anisotropic substrates, the slip lengths are obtained analytically by solving the homogenised Brinkman equation that models the flow within the substrate, as discussed in chapter 6, where $\ell_x^+ \approx \sqrt{K_x^+}$ and $\ell_z^+ \approx \sqrt{K_z^+}$. These slips lengths agree reasonably well with those obtained *a posteriori* from the velocity-shear correlations.

In this chapter, the slip lengths are obtained *a posteriori* from texture-resolved DNSs, except those for anisotropic permeable substrates. Note, however, that predictive expressions for the slip lengths exist for some of the textures. This is the case for superhydrophobic surfaces (Seo *et al.*, 2015) or for anisotropic permeable substrates, as discussed in chapter 6. Additionally, it is also possible to estimate the slip lengths for small surface textures using computationally inexpensive Stokes or laminar simulations (García-Mayoral & Jiménez, 2011; Seo & Mani, 2016; Fairhall *et al.*, 2019).

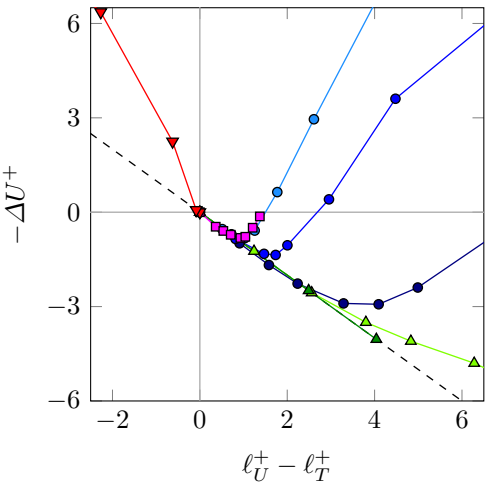

FIGURE 4.5 ΔU^+ for various surfaces as a function of the difference between the virtual origins, $\ell_U^+ - \ell_T^+$. Anisotropic permeable substrates from chapter 7, —●—, substrates C1-C7 with anisotropy ratio $\sqrt{K_x/K_y} = 11.4$, —●—, substrates B1-B7 with $\sqrt{K_x/K_y} = 5.5$ and —●—, substrates A1-A8 with $\sqrt{K_x/K_y} = 3.6$; —▲—, regularly distributed superhydrophobic surfaces (rSHS) from Fairhall *et al.* (2019); —▲—, irregularly distributed superhydrophobic surfaces (iSHS) from Seo & Mani (2018); —■—, riblets from García-Mayoral & Jiménez (2011); —▼—, canopies from Sharma & García-Mayoral (2019).

4.3 The linear regime: comparison of DNSs and theory

From the slip lengths obtained, the depths of the virtual origins for the mean flow, ℓ_U^+, and turbulence, ℓ_T^+, can now be estimated. Obtaining ℓ_U^+ is straightforward. For the small values of streamwise slips observed ($U_{slip} \lesssim 6$ for most of the surface textures), the mean flow profile is essentially linear immediately above the reference plane and it follows from chapter 3 that $\ell_U^+ \approx \ell_x^+$. To obtain ℓ_T^+, in turn, we first need to determine the spanwise and wall-normal origins, ℓ_w^+ and ℓ_v^+, that correspond to the slip lengths ℓ_z^+ and ℓ_y^+ obtained from the correlations. As mentioned in chapter 3, there is a one-to-one relationship between slip lengths and virtual origins. Once ℓ_w^+ and ℓ_v^+ are determined we can then use equation (3.9) to estimate ℓ_T^+. The virtual-origin theory, however, implicitly assumes that the near-wall turbulence remains smooth-wall-like, and hence ℓ_T^+ is defined only in the linear regime for vanishingly small texture sizes discussed in chapter 1 and sketched in figure 1.2, where this assumption holds. Beyond the breakdown of the linear regime, turbulence is no longer smooth-wall-like and ℓ_T^+ loses physical significance. For this reason, for the cases lying in the degraded regime, i.e. beyond the breakdown of the linear regime, we define an origin ℓ_T^+ by linearly extrapolating from the values obtained in the linear regime. The values of ℓ_U^+ and ℓ_T^+ for different cases are compiled in table 4.1. For the permeable substrates, we use $\ell_U^+ = \sqrt{K_x^+}$ and $\ell_T^+ = \sqrt{K_z^+}$, as it will be discussed in chapter 7, with the values given in table 7.1.

The drag curves for all the surfaces studied are compared in figure 4.5, where we show the actual ΔU^+ measured from the DNSs as a function of $\ell_U^+ - \ell_T^+$. For small texture sizes, the

curves exhibit a linear regime. In this linear regime, the actual ΔU^+ measured in the DNSs is described well by the offset between the two virtual origins, independently of the complex surface. Equation (3.7), however, eventually stops holding. This breakdown is discussed in the next section. Notably, for the canopy geometries studied here, only the canopy with the smallest spacing (case Can1 in table 4.1), appears to lie in the linear regime. Note also that figure 4.5 shows a substantial performance improvement of permeable substrates compared to riblets.

As discussed in chapter 3, the basis behind the virtual-origin theory is that, over small texture sizes, turbulence remains smooth-wall-like, save for the shift by ℓ_T^+ in the wall-normal direction. This is supported by the mean velocity profiles and the turbulence fluctuations shown in figures 4.6(*a*.1-*a*.4). Given that the origin perceived by turbulence is at $y^+ = -\ell_T^+$, results are scaled with u_τ measured at this height. The profiles have also been shifted by ℓ_T^+ in y, so that they all have a common reference plane. When defined this way, the profiles for the cases lying in the linear regime show a good collapse with smooth-wall data, confirming that the surface texture only acts to offset the origins perceived by the mean flow and the overlying turbulence, and turbulence is otherwise essentially unmodified. There is a small deviation in the profiles of u'^+ in the region close to the surface for most of the complex surfaces, as u'^+ perceives essentially the same origin as the mean U, as shown in figure 4.4(*b*.1). The fluctuating u' therefore goes to zero at $y^+ = -\ell_x^+$ instead of $y^+ = -\ell_T^+$, as we have already observed for the simulations with $\ell_v^+ = 0$ studied in chapter 3. For superhydrophobic surfaces, the rms fluctuations include the texture-coherent flow, and therefore deviate in a small region immediately above the reference plane. This, however, does not affect the change in drag or modify the near-wall cycle and its dynamics, as reported by Fairhall *et al.* (2019). There are also minor deviations in the Reynolds stresses for irregularly distributed superhydrophobic surfaces, which extend beyond the immediate vicinity of the surface, $y^+ \gtrsim 20$. These can be attributed to the differences in the friction Reynolds number used in these simulations, $\delta^+ \approx 197.5$, compared to $\delta^+ \approx 180$ for the other simulations. For the mean velocity profiles in figure 4.6(*a*.2,*b*.2) we have subtracted its value at the origin of turbulence $U_{slip}^+ - \ell_T^+$. For surfaces lying in the linear regime, as those portrayed in panel (*a*.2), $U_{slip}^+ \approx \ell_U^+$, recovering the offset between the two virtual origins, $\ell_U^+ - \ell_T^+$. However, for surfaces lying in the degraded regime, as those in panel (*b*.2), the slip velocity at the top plane of the surface can no longer be approximated by the virtual origin, since the Reynolds stresses at that height are not negligible and, as a result, dU^+/dy is no longer unity. This will be clarified in chapter 7.

In essence, figures 4.5 and 4.6 show that, in the linear regime, the effect of the surface textures on the overlying turbulence is captured by ℓ_U^+ and ℓ_T^+. The virtual-origin theory provides therefore a unified framework to quantify the effect that these complex surfaces have on the overlying flow, and modelling them using the Robin boundary conditions of equation (4.1) is justified. For superhydrophobic surfaces, the validity of this model has been shown by Fairhall *et al.* (2019) up to a texture size $L^+ \sim 20$, at least for textures where

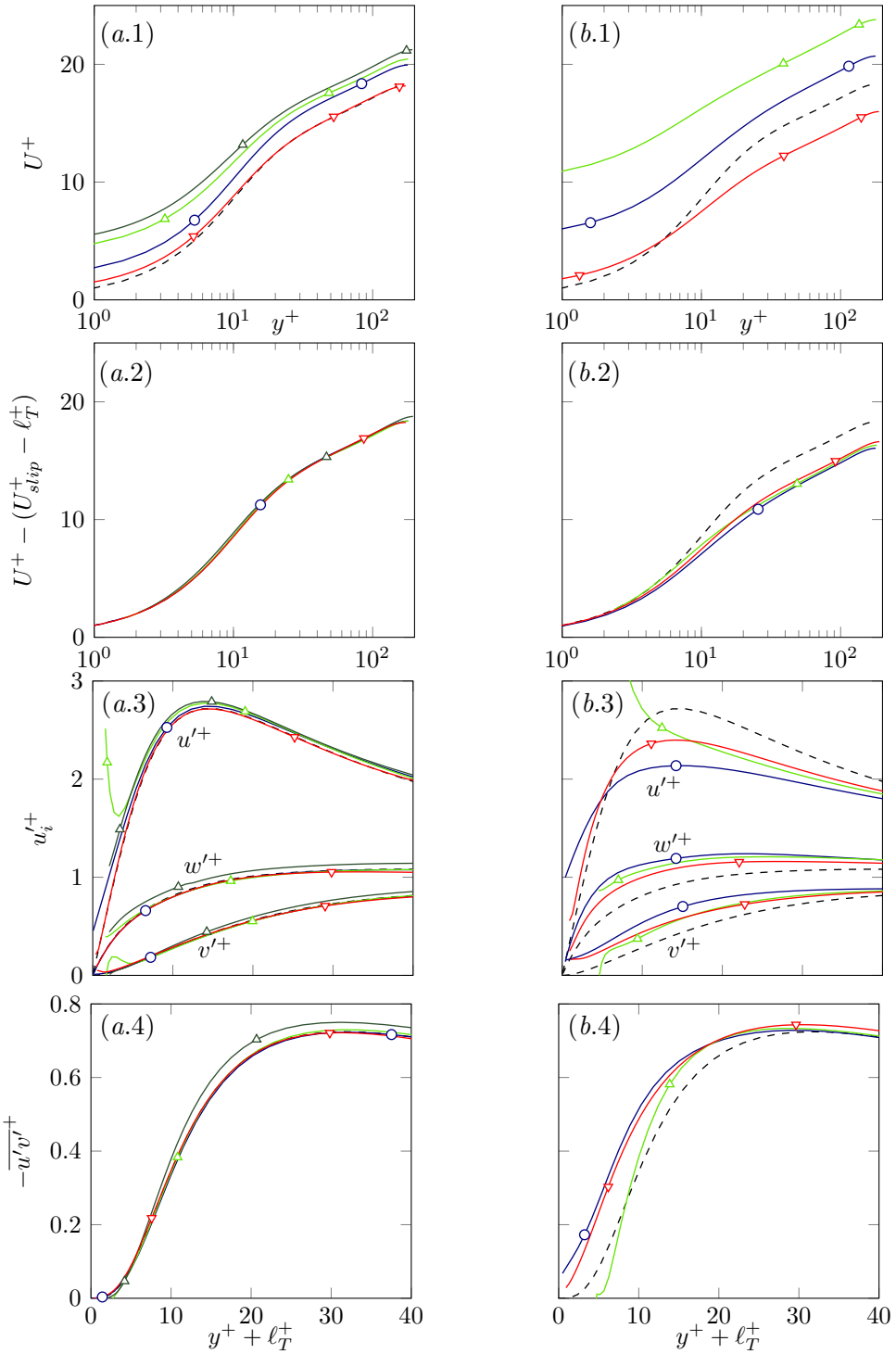

FIGURE 4.6 One-point turbulent statistics for various surfaces. (*a*.1-*a*.4) Surfaces lying in the linear regime, cases iSHS1, rSHS2, Can1 from table 4.1 and C2 from table 7.1. (*b*.1-*b*.4) Surfaces lying in the degraded regime, cases rSHS6, Can2 and C6, with symbols and colours corresponding to the complex surfaces presented in figure 4.5. – – –, smooth-channel data. (*a*.1,*b*.1) Mean velocity profiles portrayed with the origin at the reference plane, $y = 0$, and scaled with u_τ measured at that plane. (*a*.2,*b*.2) Mean velocity profiles shifted by ℓ_T^+ and scaled with the corresponding u_τ at $y = -\ell_T$, where the value at the origin has been subtracted. (*a*.3,*b*.3) Rms velocity fluctuations and (*a*.4,*b*.4) Reynolds stresses scaled with the corresponding u_τ at $y = -\ell_T$.

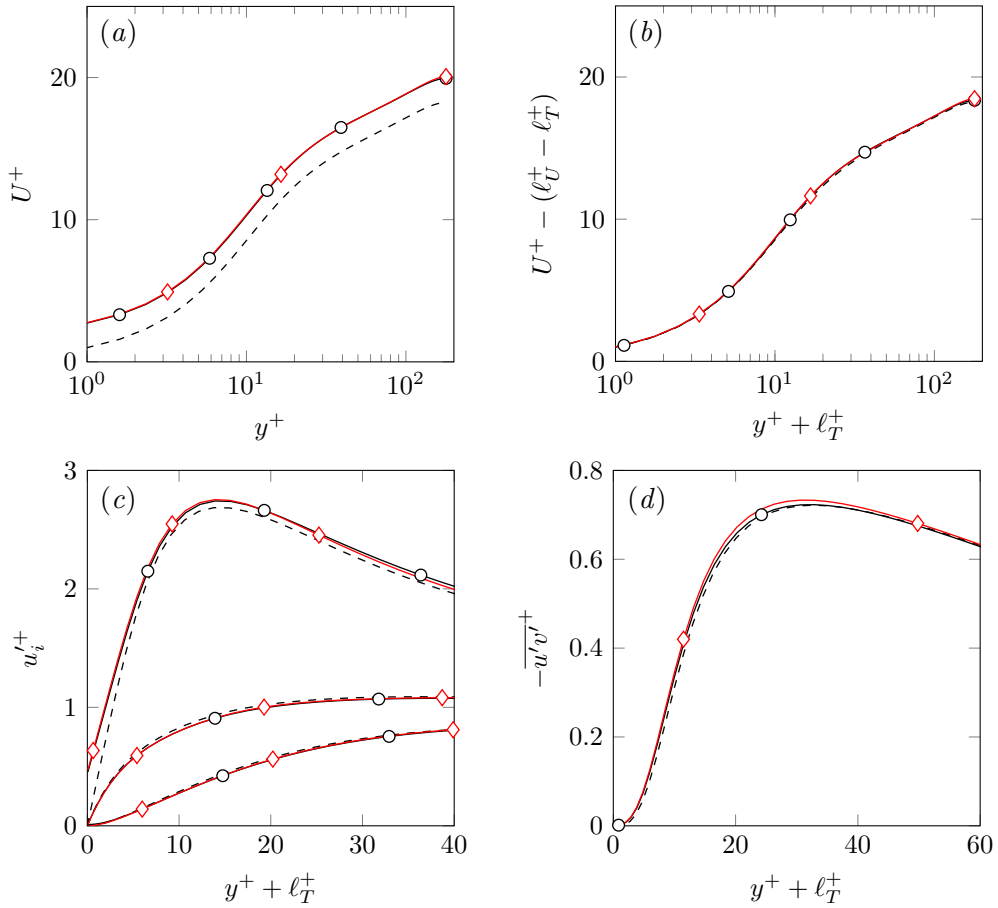

FIGURE 4.7 One-point turbulent statistics for a permeable substrate with $\sqrt{K_x^+} = 1.73$ and $\sqrt{K_z^+} = \sqrt{K_y^+} = 0.15$, case C2 in table 7.1. -○-, actual permeable case; -◇-, model with $\ell_x^+ = \sqrt{K_x^+}$ $\ell_x^+ = \sqrt{K_z^+}$ and $\ell_y^+ = 0$; – – –, smooth-wall data. (*a*) Mean velocity profiles scaled with u_τ measured at $y = 0$. (*b*) Mean velocity profiles shifted by ℓ_T^+ and scaled with the corresponding u_τ at $y = -\ell_T^+$, where the value at the origin has been subtracted. (*c*) Rms velocity fluctuations. (*d*) Reynolds stress for a permeable substrate.

interface deformation effects are negligible. Good agreement was also observed for anisotropic permeable substrates, as shown in figure 4.7. In this case, we have assumed $\ell_y^+ \approx 0$, since the values of wall-normal transpiration observed at the reference plane were negligible.

4.4 The departure from the linear regime

As the texture sizes increase, the linear regime eventually breaks down, as observed in figure 4.5, and the effect of the texture on the overlying turbulence can no longer be reduced to a mere shift of virtual origins, as observed in figures 4.6(*b*.1-*b*.4). This breakdown occurs when the overlying turbulence, and consequently the Reynolds stress, are no longer smooth-wall-like (García-Mayoral & Jiménez, 2011; Fairhall *et al.*, 2019). The source of the excess

Reynolds stresses depends on the type of complex surface. For superhydrophobic surfaces with non-deformable interfaces, for example, it is due to the overlying turbulent flow perceiving the granularity of the texture (Fairhall *et al.*, 2019). For riblets and permeable substrates, the breakdown is a result of the appearance of Kelvin-Helmholtz-like instabilities, as observed by García-Mayoral & Jiménez (2011) for riblets and in chapter 7 for permeable substrates. In this section, we focus on producing effective boundary conditions that reproduce the onset of Kelvin-Helmholtz-like instabilities for anisotropic permeable substrates.

4.4.1 Boundary conditions that reproduce Kelvin-Helmholtz-like instabilities

We have shown in chapter 3 that the relaxation of the impermeability condition at the wall is capable of eliciting the formation of Kelvin-Helmholtz-like instabilities. These have been observed in the literature for a variety of complex surfaces (Jiménez *et al.*, 2001; Breugem *et al.*, 2006; García-Mayoral & Jiménez, 2011). The instability has been reported to occur through a coupling of v and p at the interface plane. Following these observations, we explore impedance boundary conditions of the form $\hat{v} = \mathcal{B}\hat{p}$ as in Jiménez *et al.* (2001) to model the instability. We consider wavelength-dependent β, and the hat denotes variables in Fourier space. For the streamwise and spanwise velocities, we use Robin boundary conditions from equation (4.1) with homogeneous slip lengths given by $\ell_x^+ = \sqrt{K_x^+}$ and $\ell_z^+ = \sqrt{K_z^+}$.

We use two approaches to obtain the impedance coefficient between $\hat{v}$ and $\hat{p}$. In the first approach, we calculate the correlations between the wall-normal velocity and the pressure at the top of the permeable substrate obtained from the DNS *a-posteriori*, as we have done for the velocity and shears in section 4.2.2. The magnitude and phase of the correlations using instantaneous realisations for two substrates, cases C4 and C6 from table 7.1, are shown in figure 4.8. The impedance coefficient, β, thus obtained is wavelength-dependent and maps of the magnitude and phase of β across different wavelengths for cases C4 and C6 are shown in figures 4.9(a.2-a.3) and (b.2-b.3), respectively. In the black regions of this figure, v and p are essentially decorrelated, and β is thus set to zero. These figures illustrate the wavelength-dependent nature of the β coefficient. The values we are most interested in are those in the region marked by the red box, as they correspond to the lengthscales of the spanwise-coherent structures that are associated to the Kelvin-Helmholtz-like instability. In the second approach, we use a reduced form of the boundary condition obtained *a priori* to represent the permeable substrate in the DNSs. In chapter 2, we obtained the homogenised boundary conditions (2.3) for permeable substrates of equation (2.1). For the wall-normal velocity, we had

$$\hat{v} = \mathcal{C}_{vp}\hat{p} + \mathcal{C}_{vu}\frac{d\hat{u}}{dy} + \mathcal{C}_{vw}\frac{d\hat{w}}{dy}. \tag{4.3}$$

Here we assume that, once the instability sets in, the coupling between $\hat{v}$ and $\hat{p}$ dominates, so the modelled boundary condition for $\hat{v}$ reduces to $\hat{v} \approx \mathcal{C}_{vp}\hat{p}$, where $\mathcal{C}_{vp}$ is wavelength-

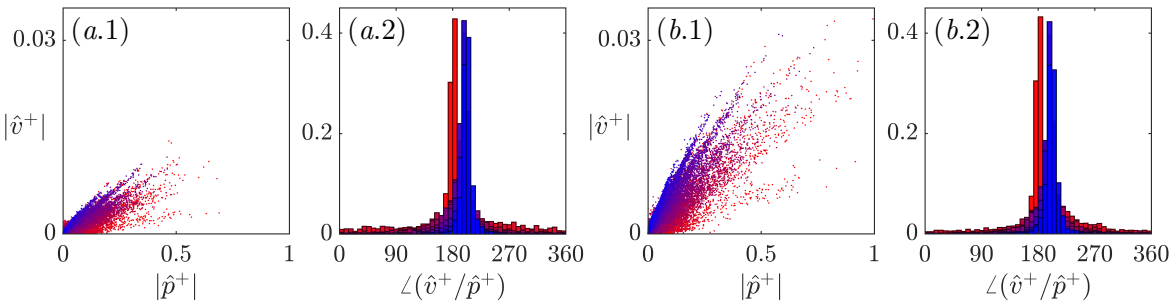

FIGURE 4.8 Instantaneous correlations between the wall-normal velocity and pressure at the interface plane, $y^+ = 0$, for (a.1,a.2) an anisotropic permeable substrate near the breakdown, case C4 in table 7.1; and (b.1,b.2) a substrate lying in the degraded regime, case C6. Variables are in Fourier space, with the spanwise wavelength $\lambda_z^+ \approx 31 - 565$ and the streamwise wavelength increasing from blue to red, $\lambda_x^+ \approx 34 - 1130$. ($a$.1,$b$.1) Instantaneous correlation of the magnitudes. (a.2,b.2) Phase difference.

dependent. Note that here the impedance coefficient coupling $\hat{v}$ and $\hat{p}$ is termed $\mathcal{C}_{vp}$ instead of β, to emphasize that in the first model β is measured *a posteriori* and in the second $\mathcal{C}_{vp}$ is calculated *a priori*. The phase of $\mathcal{C}_{vp}$ is always 180° and the magnitude across different wavelengths is shown in figures 4.9(a.1,b.1).

The mean velocity and turbulent fluctuations obtained from the modelled boundary conditions are compared with those from the original simulations in figure 4.10. Results for two different permeable substrates are shown, which correspond to a substrate just beginning to depart from the linear regime, case C4 from table 7.1; and a substrate for which Kelvin-Helmholtz mechanism is fully set in, case C6. For the latter, the $\mathcal{C}_{vp}$ model provides a better approximation for the flow than the β model, as shown in figures 4.10(b.1-b.4). Figure 4.9 shows that, although the coefficients $\mathcal{C}_{vp}$ and β are qualitatively similar, their magnitudes and phases are different. The underlying reason for the discrepancy, however, is unknown at present and it needs to be further investigated. In essence, the incomplete, truncated $v = \mathcal{C}_{vp}p$ condition seems to work better than imposing the actual, observed correlation, $v = \beta p$. For the substrate just beginning to depart from the linear regime, however, none of the models captures effectively the change in drag or the effect that this substrate has on the overlying turbulence, as shown in figures 4.10(a.1-a.4). Even if the $\mathcal{C}_{vp}$ model shows a better approximation than the β model, with these two approaches the overlying flow appears to be too smooth-wall-like. These models are no better than imposing only tangential slip lengths with $v = 0$. They are not able to capture the deviation from the smooth-wall data observed with full boundary conditions. This is because for a substrate just beginning to depart from the linear regime the coupling between $\hat{v}$ and $\hat{p}$ in equation (4.3) does not dominate over the other two terms, since the instability is still weak. Thus, the transpiration due to $\hat{p}$ is as important as that due to $\hat{u}$ and $\hat{w}$. Given that the streamwise permeability is greater than those in the spanwise and wall-normal directions, we would expect the contribution of the

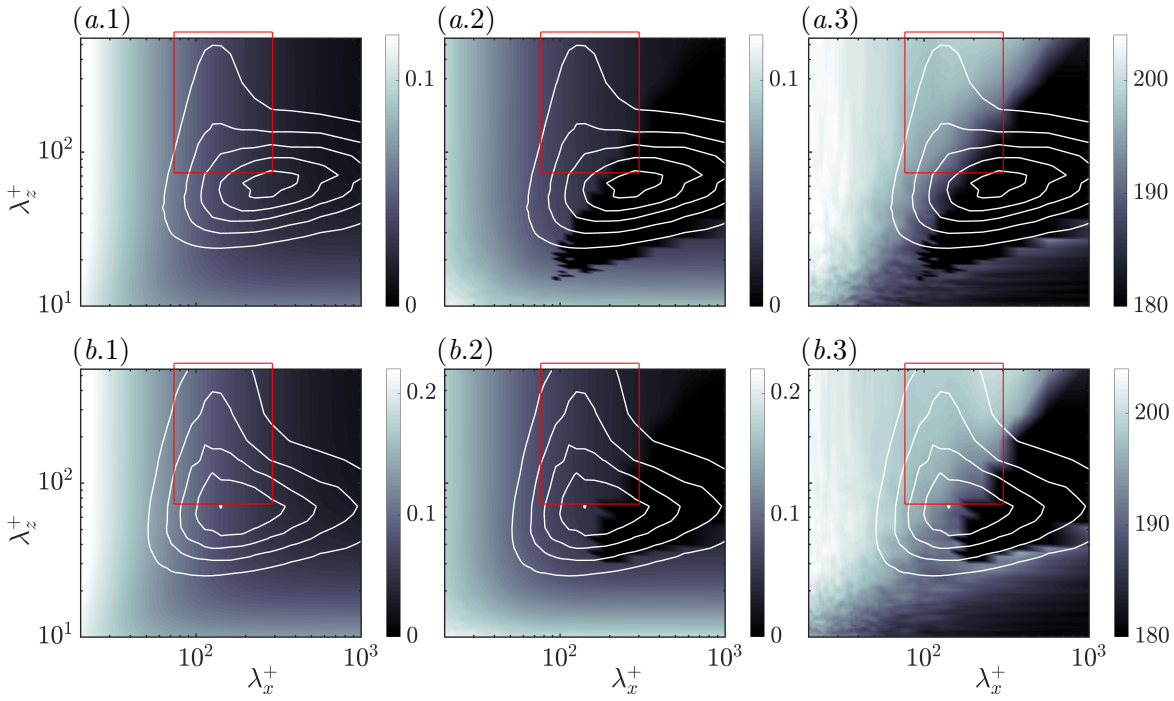

FIGURE 4.9 Magnitudes and phases of the impedance coefficients between wall-normal velocity and pressure (*a*.1-*a*.3) an anisotropic permeable substrate near the breakdown, case C4 in table 7.1; and (*b*.1-*b*.3) a substrate lying in the degraded regime, case C6. (*a*.1,*b*.1) Magnitude of the analytically obtained coefficient $\mathcal{C}_{vp}^+$ (the phase is always 180°). (*a*.2,*b*.2) Magnitude of β^+. (*a*.3,*b*.3) Phase of β^+. The darkest regions in (*a*.2,*b*.2,*a*.3,*b*.3) correspond to wavelengths that are not correlated. The line contours correspond to the spectral energy density of the wall-normal velocity at $y^+ \approx 15$ with contour levels (0, 0.02133, 0.04266, 0.06399, 0.08532, 0.10670)u_τ^2. The red box indicates the relevant region of the spectrum for the spanwise-coherent structures.

coefficient $\mathcal{C}_{vu}$, that is, the coupling between $\hat{v}$ and $d\hat{u}/dy$, to be significant, and perhaps even to dominate. The coupling between $\hat{v}$ and $\hat{p}$ only becomes dominant in the degraded regime, once the spanwise-coherent structures that arise from the Kelvin-Helmholtz-like instability become prevalent in the flow. This is why for case C6, the $\mathcal{C}_{vp}$ model provides a reasonable approximation.

In essence, for small texture sizes the virtual-origin theory provides a unified framework to explain the change in drag experienced by textured surfaces. For the specific case of permeable substrates, the addition of an impedance condition between v and p is useful to model flows where Kelvin-Helmholtz instability is fully developed, but not flows where its effect is incipient. New models should be investigated to capture the departure from the linear regime, for example through boundary conditions that relate the wall-normal velocity with the streamwise shear, as discussed above.

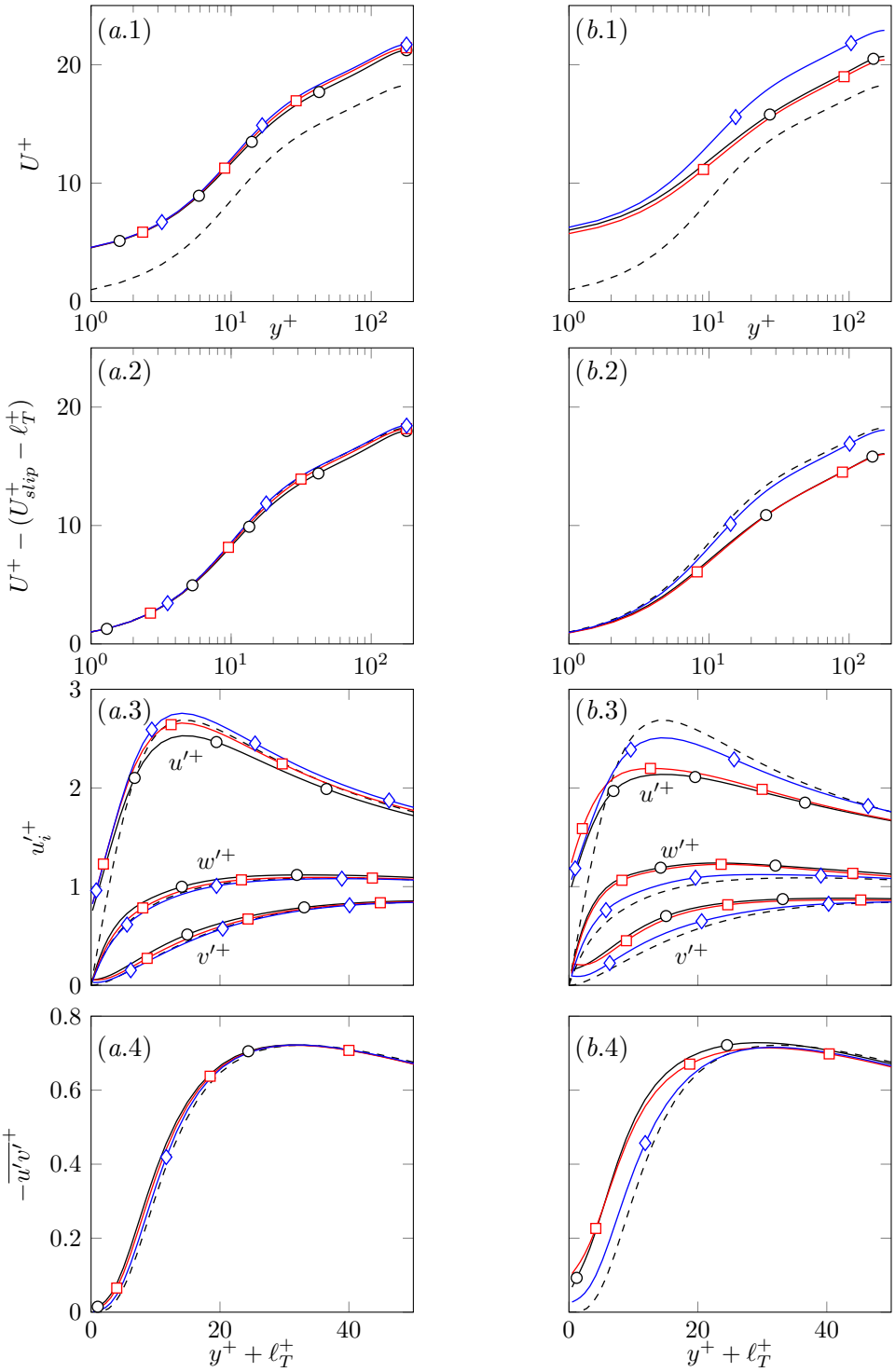

FIGURE 4.10 One-point turbulent statistics for permeable substrates. (*a*.1-*a*.4) Case C4, near the breakdown; (*b*.1-*b*.4) Case C6, in the degraded regime. -○-, actual permeable case; -□-, model with $\hat{v} = \mathcal{C}_{vp}\hat{p}$; -◇-, model with $\hat{v} = \beta\hat{p}$; – – –, smooth-channel data. (*a*.1,*a*.2) Mean velocity profiles portrayed with the origin at the reference plane, $y = 0$, and scaled with u_τ measured at that plane. (*b*.1,*b*.2) Mean velocity profiles shifted by ℓ_T^+ and scaled with the corresponding u_τ at $y = -\ell_T$, where the value at the origin has been subtracted. (*c*.1,*c*.2) Rms velocity fluctuations and (*d*.1,*d*.2) Reynolds stresses scaled with the corresponding u_τ at $y = -\ell_T$.

Chapter 5

Analysis of Kelvin-Helmholtz-like instabilities over anisotropic permeable substrates*

In chapter 1 we mentioned that spanwise-coherent rollers, which are associated with a Kelvin-Helmholtz-like instability, are ubiquitous over permeable substrates. The formation of these structures increase the Reynolds stress, resulting in a significant increase of drag, which might cause the breakdown of the drag-reducing behaviour for anisotropic permeable substrates. In this chapter we propose a linear stability analysis to capture the onset of Kelvin-Helmholtz-like instabilities. The sensitivity of the substrate parameters on the formation of the instabilities is investigated, with the aim of building a simple predictive model to capture their onset. We conduct inviscid and viscous stability analyses about a turbulent mean flow, where the permeable substrates are represented by boundary conditions derived from the analytic solution of Brinkman's equation, discussed in chapter 2. The results obtained are also compared to poorly-connected permeable substrates, previously studied by Abderrahaman-Elena & García-Mayoral (2017) using Darcy's equation, and differences between the two types of substrates are highlighted. We show that when using Brinkman's model, the formation of the instabilities is governed by different parameters depending on the ratio of streamwise (K_x) to wall-normal (K_y) permeability.

This chapter is organised as follows. Section 5.1 outlines the equations for the stability analysis and validates Brinkman's model with the VANS model of Tilton & Cortelezzi (2008). Sections 5.2 and 5.3 present and discuss the results for the inviscid and viscous stability analyses, respectively, and section 5.3 also provides a comparison between the two.

*Parts of the content of this chapter have been published in *Flow, Turbulence and Combustion*, 100 (4), 995 – 1014, with Akshath Sharma and Ricardo García-Mayoral as co-authors. The work presented in section 5.2 was done in collaboration with Mr. Akshath Sharma.

5.1 Governing equations for linear stability analysis

The analysis is conducted on the same domain as that sketched in figure 1.9, where the half-channel height is taken as $\delta = 1$. As described in chapter 2, the Brinkman equation within the permeable substrates is solved analytically to provide the boundary conditions at the substrate-channel interface. Thus, the initial problem of solving the stability of the complete geometry – a channel bounded by two identical permeable substrates – is simplified to solving the stability of a channel with boundary conditions that account for the presence of the substrates. When the boundary conditions are obtained from Darcy's equation within the substrate, Abderrahaman-Elena & García-Mayoral (2017) showed, using Squire's transformation, that oblique modes are more stable than the corresponding two-dimensional modes. The same cannot be formally derived when including a Brinkman term, due to the complexity of the boundary conditions. However, based on previous evidence that the Kelvin-Helmholtz rollers are predominantly spanwise-coherent, we restrict ourselves to spanwise-homogeneous modes and perform a two-dimensional analysis. We consider both the inviscid and viscous cases.

5.1.1 Equations for linear stability analysis within the channel

The mean turbulent profile within the channel, $U(y)$, is approximated using the analytic expression derived by Cess (1958), where the Reynolds shear stress is modelled using a y-dependent eddy viscosity. The mean profile is therefore expressed as a function of a molecular plus an eddy viscosity, referred to as $\nu_T(y)$, to match closely the mean profile of a conventional turbulent smooth channel (see appendix C for details). Note that using a smooth-channel mean profile implicitly assumes that pore size of the substrate is small, so that the overlying turbulence does not penetrate within the substrate. Note that this profile implicitly assumes that turbulence in a channel bounded by permeable substrates is the same as for a smooth channel. This $\nu_T(y)$ and $U(y)$ profile have been extensively used in the literature for stability analyses (Reynolds & Hussain, 1972; del Álamo & Jiménez, 2006; Cossu *et al.*, 2009; García-Mayoral & Jiménez, 2011; Abderrahaman-Elena & García-Mayoral, 2017).

Let us now lay out the equations for a viscous stability analysis with viscosity $\nu_T(y)$. The flow field within the channel is decomposed into the sum of the mean flow, $U(y)$, and small-amplitude disturbances, $\boldsymbol{u}(x, y, t) = (u, v)$ and $p(x, y, t)$, where $\boldsymbol{u} \ll U$. The linearised

equations in the channel region are

$$\frac{\partial u}{\partial x} + \frac{\partial v}{\partial y} = 0, \tag{5.1a}$$

$$\frac{\partial u}{\partial t} + U\frac{\partial u}{\partial x} + v\frac{dU}{dy} = -\frac{\partial p}{\partial x} + \frac{\partial}{\partial x}\left(2\nu_T\frac{\partial u}{\partial x}\right) + \frac{\partial}{\partial y}\left(\nu_T\left(\frac{\partial u}{\partial y} + \frac{\partial v}{\partial x}\right)\right), \tag{5.1b}$$

$$\frac{\partial v}{\partial t} + U\frac{\partial v}{\partial x} = -\frac{\partial p}{\partial y} + \frac{\partial}{\partial x}\left(\nu_T\left(\frac{\partial v}{\partial x} + \frac{\partial u}{\partial y}\right)\right) + \frac{\partial}{\partial y}\left(2\nu_T\frac{\partial v}{\partial y}\right). \tag{5.1c}$$

These equations differ from the linearised Navier-Stokes equations in that a variable viscosity $\nu_T(y)$ is used instead of a molecular viscosity, ν, to model the effect of turbulent stresses. We seek normal-mode solutions of the form $(u, v, p) = (\hat{u}(y), \hat{v}(y), \hat{p}(y))e^{i(\alpha x - \omega t)}$, and consider a temporal stability problem, where the streamwise wavenumber α, or alternatively the wavelength $\lambda = 2\pi/\alpha$, is real, and the ω is complex, $\omega = \omega_r + i\omega_i$. The real and imaginary parts of ω, ω_r and ω_i, represent the angular frequency and growth rate of the wave, respectively. A perturbation is therefore unstable when the imaginary part, ω_i, is positive. Following a similar derivation to that shown in Schmid & Henningson (2000), but with variable $\nu_T(y)$, the Orr-Sommerfeld equation is

$$\Big[(\alpha U - \omega)\left(D^2 - \alpha^2\right) - \alpha\frac{d^2U}{dy^2} + i\nu_T(D^2 - \alpha^2)^2 + 2i\frac{d\nu_T}{dy}\left(D^3 - \alpha^2 D\right) + i\frac{d^2\nu_T}{dy^2}\left(D^2 + \alpha^2\right)\Big]\hat{v} = 0, \tag{5.2}$$

where D denotes the operator d/dy. Equation (5.2) is an eigenvalue problem, where ω is the eigenvalue and $\hat{v}$ the corresponding eigenfunction. This same equation was also used in the works by Reynolds & Hussain (1972), del Álamo & Jiménez (2006) or Pujals *et al.* (2009). In this study, we also perform a viscous analysis with molecular viscosity alone, as well as an inviscid analysis, and the corresponding equations can be obtained directly from equation (5.2) for $\nu_T = \nu$ and $\nu_T = 0$, respectively.

As we mentioned is section 1.6, the term $\alpha d^2U/dy^2\hat{v}$ in equation (5.2) is responsible for triggering the Kelvin-Helmholtz instabilities (Jiménez *et al.*, 2001; García-Mayoral & Jiménez, 2011; Jiménez, 2013*a*). This is because the second wall-normal derivative of U, d^2U/dy^2, which in a turbulent channel is larger near the wall, can act as a source of energy for the perturbations through the interaction with $\hat{v}$. For an impermeable wall, the instability is inhibited by the impermeability condition at the wall, $\hat{v} = 0$, which is why a turbulent channel flow with impermeable walls is linearly stable (Reynolds & Tiederman, 1967; Reynolds & Hussain, 1972). If the impermeability condition is relaxed, however, the term $\alpha d^2U/dy^2\hat{v}$ feeds energy into the system and a Kelvin-Helmholtz instability may develop. This is the case for permeable substrates (Jiménez *et al.*, 2001) and other complex surfaces, such as riblets (García-Mayoral & Jiménez, 2011).

5.1.2 Boundary conditions

To obtain the boundary conditions for the Orr-Sommerfeld equation (5.2), we apply continuity of the velocity at the substrate-channel interfaces. These velocities are obtained from the analytic solution of the Brinkman equation (2.1) within the substrate, but for the linear stability analysis, we restrict ourselves to a two-dimensional problem. The procedure to solve the two-dimensional Brinkman equation for (u,v) corresponds to the solution of the modes ($\alpha_x \neq 0$, $\alpha_z = 0$) detailed in appendix A.1. After some manipulation, the two-dimensional Brinkman equation is reduced to a fourth order equation in $\hat{p}$, as given by equation (A.16) and rewritten below for convenience,

$$\left\{ D^4 + \left[-2\alpha^2 - \frac{1}{K_x} \right] D^2 + \alpha^2 \left[\alpha^2 + \frac{1}{K_y} \right] \right\} \hat{p} = 0. \tag{5.3}$$

The corresponding characteristic equation is biquadratic, $m^4 + m^2(-2\alpha^2 - 1/K_x) + (\alpha^4 + \alpha^2/K_y) = 0$, with roots

$$\pm m_1 = \pm \sqrt{\frac{1 + 2\alpha^2 K_x + \sqrt{4\alpha^2 K_x \left(1 - \frac{K_x}{K_y}\right) + 1}}{2K_x}}, \tag{5.4a}$$

$$\pm m_2 = \pm \sqrt{\frac{1 + 2\alpha^2 K_x - \sqrt{4\alpha^2 K_x \left(1 - \frac{K_x}{K_y}\right) + 1}}{2K_x}}. \tag{5.4b}$$

The general solutions for $\hat{p}$, $\hat{u}$ and $\hat{v}$ are sums of exponentials, as given by equations (A.18), (A.19) and (A.20), respectively, with terms of the form of $e^{m_1 y}$, $e^{-m_1 y}$, $e^{m_2 y}$ and $e^{-m_2 y}$. The nature of the flow within the substrate is therefore governed by the exponents, that is, the roots (5.4). Note that depending on the sign of the discriminant, the roots are real or complex, and the solution of the flow changes qualitatively. We would therefore expect the flow to behave differently depending on whether the anisotropy ratio, K_x/K_y, is greater or lower than $1 + 1/(4\alpha^2 K_x)$.

Let us take the substrate bounding the channel at $y = 0$. The unique solution of the flow within the substrate is obtained by imposing the boundary conditions, continuity of tangential and normal stresses at the substrate-channel interface, $y = 0$; and impermeability and no-slip condition at the substrate bottom, $y = -h$, as detailed in chapter 2. Particularising the solution at the substrate-channel interface, $y = 0$, the streamwise and wall-normal velocities are reduced to

$$\hat{u}|_{y=0^-} \equiv \mathcal{C}_{up}\hat{p}|_{y=0^+} + \mathcal{C}_{uu}\left.\frac{d\hat{u}}{dy}\right|_{y=0^+}, \tag{5.5a}$$

$$\hat{v}|_{y=0^-} \equiv \mathcal{C}_{vp}\hat{p}|_{y=0^+} + \mathcal{C}_{vu}\left.\frac{d\hat{u}}{dy}\right|_{y=0^+}, \tag{5.5b}$$

which is a simplification of the more general expression presented in chapter 2. As before, the coefficients $\mathcal{C}_{vp}$, $\mathcal{C}_{vu}$, $\mathcal{C}_{up}$ and $\mathcal{C}_{uu}$ depend on the geometry of the permeable substrate through K_x, K_y and h, but also on the wavenumber α. By symmetry, the interface conditions for the upper substrate, at $y = 2\delta$, are

$$\hat{u}|_{y=(2\delta)^+} \equiv \mathcal{C}_{up}\hat{p}|_{y=(2\delta)^-} - \mathcal{C}_{uu}\left.\frac{d\hat{u}}{dy}\right|_{y=(2\delta)^-}, \tag{5.6a}$$

$$\hat{v}|_{y=(2\delta)^+} \equiv -\mathcal{C}_{vp}\hat{p}|_{y=(2\delta)^-} + \mathcal{C}_{vu}\left.\frac{d\hat{u}}{dy}\right|_{y=(2\delta)^-}, \tag{5.6b}$$

and together with equation (5.5), they provide the boundary conditions for the channel flow.

The Orr-Sommerfeld equation (5.2), however, is only a function of $\hat{v}$, so the boundary conditions (5.5) and (5.6) must be also expressed in terms of $\hat{v}$ alone. The streamwise velocity $\hat{u}$ can be eliminated by simply using continuity, but to eliminate $\hat{p}$, we need an additional equation. For that, we take the x-derivative of equation (5.1b) and use continuity to express $\hat{u}$ in terms of $\hat{v}$, which yields

$$\alpha^2\hat{p} = \left[i\alpha\frac{dU}{dy} + i\left(\omega - \alpha U\right)D + \nu_T\left(D^3 - \alpha^2 D\right) + \frac{d\nu_T}{dy}\left(D^2 + \alpha^2\right)\right]\hat{v}. \tag{5.7}$$

The first boundary condition is obtained by substituting equation (5.5b) (or alternatively (5.6b) for the top interface) into equation (5.7). The second boundary condition is obtained by combining equations (5.5b) and (5.5a) (or equations (5.6b) and (5.6a) for the top interface) to eliminate $\hat{p}$. The boundary conditions for the Orr-Sommerfeld equation (5.2) in terms of $\hat{v}$ are then

$$\left[\mp i\frac{\alpha^2}{\mathcal{C}_{vp}} \mp \alpha\frac{\mathcal{C}_{vu}}{\mathcal{C}_{vp}}D^2 - \alpha\frac{dU}{dy} + \alpha U_{slip}D + i\nu_T\left(D^3 - \alpha^2 D\right) + i\frac{d\nu_T}{dy}\left(D^2 + \alpha^2\right)\right]\hat{v} = \omega D\hat{v}, \tag{5.8a}$$

$$\left[\pm\frac{1}{\mathcal{C}_{vp}} - i\frac{1}{\alpha\mathcal{C}_{up}}D \pm \frac{i}{\alpha}\left(\frac{\mathcal{C}_{uu}}{\mathcal{C}_{up}} - \frac{\mathcal{C}_{vu}}{\mathcal{C}_{vp}}\right)D^2\right]\hat{v} = 0, \tag{5.8b}$$

where the top and bottom signs present apply to the bottom and top interfaces, respectively, and U_{slip} denotes the mean velocity at the substrate-channel interfaces. This slip velocity at the interface is defined from the mean velocity within the permeable substrate and is identical for both the top and bottom interfaces. For the bottom substrate, solving Brinkman's equation (2.1) for a mean flow, $U(y)$, and imposing as boundary conditions $U|_{y=-h} = 0$ and $dU/dy|_{y=0^-} = dU/dy|_{y=0^+}$, the mean slip velocity is

$$U_{slip} = \sqrt{K_x}\tanh\left(\frac{h}{\sqrt{K_x}}\right)\left.\frac{dU}{dy}\right|_{y=0^+} - \frac{K_x}{\nu}\frac{dP}{dx}\left(1 - \frac{1}{\sinh\left(h/\sqrt{K_x}\right)}\right), \tag{5.9}$$

where the first term is the mean flow due to an overlying shear, also referred to as Brinkman's velocity, and the second term is that due to a pressure gradient, also referred to as Darcy's velocity. However, the slip velocity, U_{slip}, does not affect the amplification of the instability and can therefore be omitted from the analysis. From the two boundary conditions, U_{slip} appears only in equation (5.8a), which can be rearranged as

$$\left[(\alpha U_{slip} - \omega_r) - i\left(\omega_i + \nu_T\alpha^2\right)\right] D\hat{v} + \left(\mp i\frac{\alpha^2}{\mathcal{C}_{vp}} - \alpha\frac{dU}{dy} + i\frac{d\nu_T}{dy}\alpha^2\right)\hat{v} + \left(\mp\alpha\frac{\mathcal{C}_{vu}}{\mathcal{C}_{vp}} + i\frac{d\nu_T}{dy}\right) D^2\hat{v} + i\nu_T D^3\hat{v} = 0. \tag{5.10}$$

In this equation, U_{slip} appears only in the real part of the multiplication factor of the first order terms, i.e. $(\alpha U_{slip} - \omega_r)$. Therefore, U_{slip} affects only ω_r, the angular frequency, modifying it by a Galilean translation, and has no effect on the amplification of the instability, ω_i. The slip velocity can then be dropped for simplicity, as was done by García-Mayoral & Jiménez (2011) for the inviscid stability analysis over riblets. The angular frequency obtained when neglecting U_{slip}, however, is lower than the original, but it can be recovered by simply adding αU_{slip} to it.

In summary, the initial problem of solving the stability of a channel delimited by two permeable substrates is now reduced to solving the Orr-Sommerfeld equation with two boundary conditions at each wall that account for the presence of the substrates. To solve the Orr-Sommerfeld equation, the wall-normal direction is discretised using Chebyshev polynomials. The analysis has been conducted at three different friction Reynolds numbers, $\delta^+ = u_\tau\delta/\nu = 180$, 550 and 1000. Results are, however, independent of the Reynolds number when scaled in viscous units, in agreement with Abderrahaman-Elena & García-Mayoral (2017) and García-Mayoral & Jiménez (2011). In this chapter, only results for $\delta^+ = 180$ are shown, for which $N_{ch} = 256$ Chebyshev points are used. Hereafter, results are either nondimensionalised in viscous units, i.e. with the kinematic viscosity ν and the friction velocity u_τ, or in outer units, i.e. using the channel half-height δ and the bulk velocity of the mean flow U_b.

5.1.3 Validation

The methodology described above is validated with the work by Tilton & Cortelezzi (2008). Those authors performed a viscous, linear stability analysis of a laminar Poiseuille flow with isotropic permeable substrates on both walls. They used the VANS equations to model the flow within the permeable substrates, with the interface conditions derived by Ochoa-Tapia & Whitaker (1995*b*), which consist of continuity of velocities and pressure, and a jump in the shear stresses controlled by a momentum transfer coefficient τ. In particular, we focus on the cases where they explore the effect of the permeability. The dimensionless permeabilities considered by Tilton & Cortelezzi (2008) vary between $\sqrt{K}/\delta = 0.0002 - 0.02$, while the porosity is fixed to $\epsilon = 0.6$ and the thickness of the substrate is $h = \delta$ for all cases. For such small permeabilities, the advective terms in the VANS equations are negligible with respect to the viscous terms, and the equations reduce approximately to the Brinkman equation with an additional unsteady term. The porosity parameter, ϵ, in the VANS equations would then play the same role that the ratio between the viscosities, $\nu/\tilde{\nu}$, plays in Brinkman's equation. For the results shown here, the same values of permeabilities and substrate thickness are considered, although in our case we consider $\tilde{\nu} = \nu$, as opposed to $\epsilon = 0.6$ considered by Tilton & Cortelezzi (2008). However, comparing the effects of ϵ and K on the overlying flow, Rosti *et al.* (2015) observed that the permeability is the most relevant parameter to capture the effect of a permeable substrate on the overlying flow, and for large porosity values, where $\epsilon \gtrsim 0.6$, variations of ϵ have little effect on the flow. Hence, the discrepancy between the values of ϵ and the ratio between viscosities should, in principle, have no major effect. At the interface, apart from continuity of velocities and pressure, we apply continuity in shear stresses, which is equivalent to setting $\tau = 0$ in VANS equations, as in the results from Tilton & Cortelezzi (2008) considered here.

Considering the same Reynolds number as in Tilton & Cortelezzi (2008), $Re = 3000$, the trajectory of the Orr-Sommerfeld eigenvalues, ω, for increasing permeabilities is shown in figure 5.1(a). A comparison with the eigenvalue spectra from Tilton & Cortelezzi (2008) portrayed in figure 5.1(b) shows that the current methodology captures the main features of their results, although there are some differences. Most notably, the modes associated with the flow within the permeable substrate are absent, as we have omitted any temporal terms in the Brinkman equation. These modes, however, remain stable even for large permeabilities and can then be neglected, since they do not affect the instability of the flow. Other discrepancies in the trajectories of some modes may result from the difference in value between $\epsilon = 0.6$ used in Tilton & Cortelezzi (2008) and $\tilde{\nu} = \nu$ used in the current analysis. Note also that in figure 5.1 we are not representing the original angular frequency, ω_r, but $\omega_r - \alpha U_{slip}$.

The amplification of the most unstable mode as the permeability increases is in good agreement with Tilton & Cortelezzi (2008). This is the dominant mode of the problem, labelled as ① in figure 5.1. The critical value of the permeability, $\sqrt{K_{crit}}/\delta$, defined as

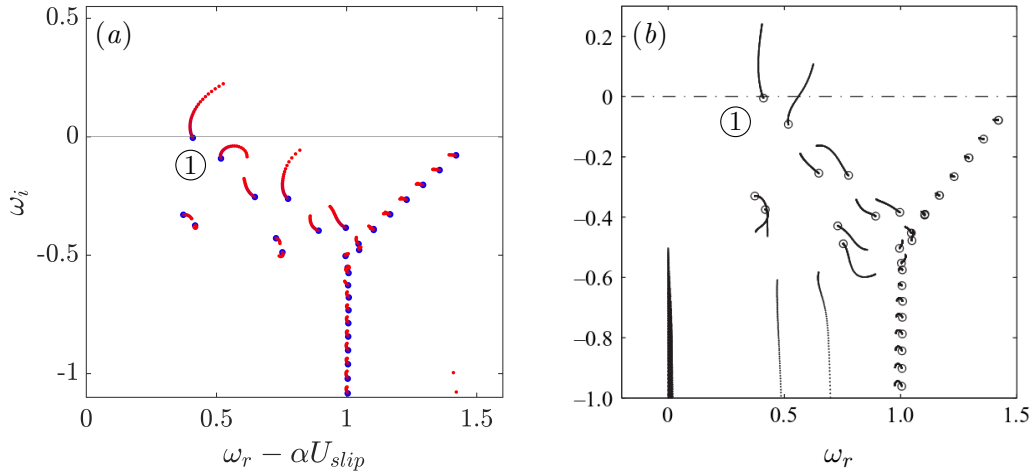

FIGURE 5.1 Comparison of the trajectory of the eigenvalues – growth rate and angular frequency – for a laminar channel flow with isotropic permeable substrates, with $\alpha = 1$ ($\lambda/\delta = 6.28$), $Re = 3000$ and $h = \delta$, when varying the permeability from $\sqrt{K}/\delta = 0.0002$ (large circles) to $\sqrt{K}/\delta = 0.02$, between (a) using our Brinkman's model and (b) using the VANS equations, with $\epsilon = 0.6$ and $\tau = 0$ (figure extracted from Tilton & Cortelezzi (2008)). In (a) and (b) values are normalised in outer units, i.e. using the channel half-height δ and the bulk velocity of the mean flow U_b, and ① represents the most unstable eigenvalue.

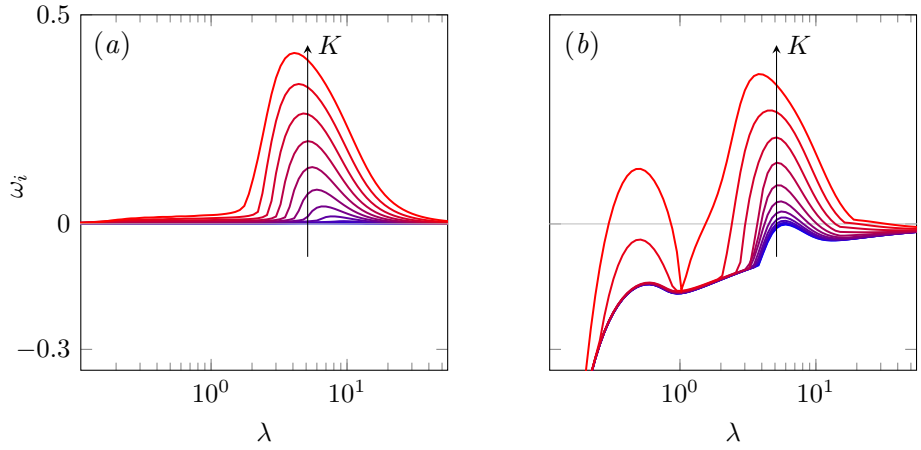

FIGURE 5.2 Growth rate, ω_i, as a function of the wavelength, λ, for an isotropic permeable substrate with $Re = 3000$ and $h/\delta = 1$ when varying the permeability. From blue to red the permeability increases between $\sqrt{K}/\delta = 0.0002 - 0.025$. (a) Inviscid stability analysis. (b) Viscous stability analysis. Magnitudes are scaled in outer units.

the value above which mode ① becomes unstable, agrees with that observed by Tilton & Cortelezzi (2008). They obtained $\sqrt{K_{crit}}/\delta = 0.00222$ compared to $\sqrt{K_{crit}}/\delta = 0.00250$ obtained with our model.

In order to analyse whether a viscous or inviscid mechanism leads to the amplification of mode ①, we have also conducted an inviscid analysis. The growth rate of the most amplified mode obtained from both the inviscid and viscous analyses is compared in figure 5.2. In

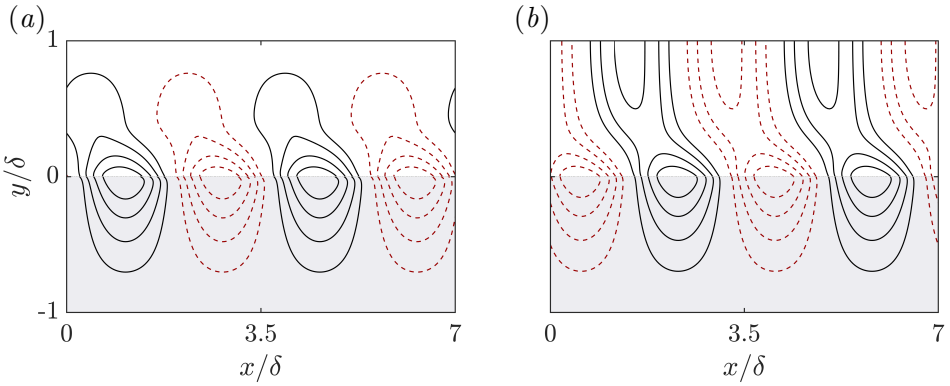

FIGURE 5.3 Equispaced isocontours of the streamfunction, $\Phi = (i/\alpha)\hat{v}e^{i(\alpha x-\omega t)}$, for the most unstable mode at $\lambda/\delta = 3.5$ obtained from a viscous stability analysis of a Poiseuille flow bounded by isotropic permeable substrates with $\sqrt{K}/\delta = 0.025$ and $h/\delta = 1$. Solid lines correspond to clockwise rotation, while dashed lines correspond to counterclockwise rotation. (a) Varicose mode. (b) Sinuous mode. Shading represents the permeable substrate.

the viscous case, there are two different peaks. The second peak, formed at $\lambda/\delta = [3-6]$, is the most unstable. This peak is also present in the inviscid analysis, as shown in panel (a). This suggests that the leading instability of a laminar channel flow with permeable substrates is inviscid. To visualise the instability, figure 5.3(a) portrays the isocontours of the streamfunction for the most amplified wavelength, $\lambda/\delta \approx 3.5$, which resembles the rotating rollers characteristic of the Kelvin-Helmholtz instability.

The most unstable mode, mode ① as specified in figure 5.1, consists of two eigenvalues merged together, as in Jiménez *et al.* (2001). The first is a varicose mode, symmetric with respect to the centreline of the channel. The second is a sinuous mode, antisymmetric with respect to the centreline. For small wavelengths, the corresponding eigenfunctions are localised near the surface. The top and bottom surfaces do not interact and the sinuous and varicose modes coincide. As the wavelength increases, however, the two modes diverge. For the sinuous mode, the rollers from the top and bottom surfaces merge together, owing to their large size, as shown in figure 5.3(b). This merged instability has a larger amplification than the varicose mode, which does not merge, as illustrated in figure 5.3(a). This discrepancy between the two modes for large wavelengths is a result of conducting the analysis in a channel. However, if the aim is to study boundary layers using channel flow simulations for simplicity, only the behaviour of the varicose mode would be relevant (Jiménez *et al.*, 2001).

5.2 Inviscid analysis

In this section, we present the results for the inviscid analysis, as in Jiménez *et al.* (2001), García-Mayoral & Jiménez (2011) and Abderrahaman-Elena & García-Mayoral (2017), to capture the formation of Kelvin-Helmholtz-like instabilities over anisotropic permeable substrates,

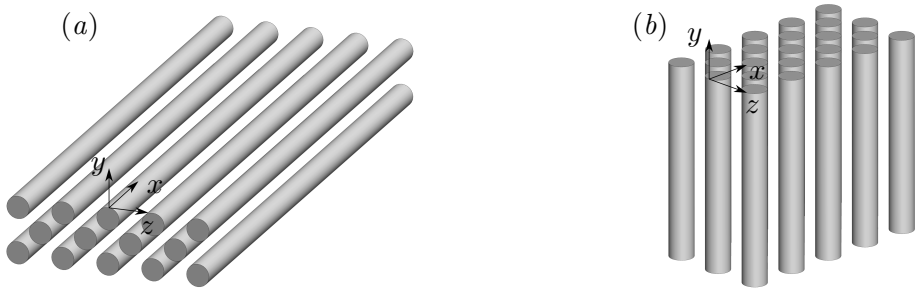

FIGURE 5.4 Conceptual sketches of two highly-connected anisotropic permeable substrates with different preferential directions. (a) Streamwise-preferential substrate, with $K_x > K_y$. (b) Wall-normal-preferential substrate, with $K_x < K_y$.

since this instability is an inviscid phenomenon. For $\nu_T = 0$, the stability equation (5.2) is reduced to Rayleigh's equation. At the interface, the perturbations cannot exert any shear on the flow within the substrate and only the continuity of the wall-normal velocity can be imposed. The boundary condition (5.5a) is no longer needed, and (5.5b) simplifies to $\hat{v}|_{y=0^+} = \mathcal{C}_{vp}\hat{p}|_{y=0^+}$. Expressing this condition in terms of $\hat{v}$ alone, the corresponding boundary condition (5.8a) reduces to

$$\Big[\mp i\frac{\alpha^2}{\mathcal{C}_{vp}} - \alpha\frac{dU}{dy} + i\nu_T\left(D^3 - \alpha^2 D\right) + i\frac{d\nu_T}{dy}\left(D^2 + \alpha^2\right) \Big]\hat{v} = \omega D\hat{v}. \tag{5.11}$$

We noted in the previous section that the solution within the permeable substrate changes qualitatively depending on whether the anisotropy ratio is $K_x/K_y \lessgtr 1 + 1/(4\alpha^2 K_x)$, defining two separate regimes. For the most unstable wavenumber α, we will show that the distinction between the two regimes can be approximated to $K_x/K_y \lessgtr 1$. We would therefore expect the instability to be characterised differently depending on whether the substrate is preferential in x or in y, that is, depending on whether the permeability of the substrate is higher in the streamwise or in the wall-normal direction. Examples of permeable substrates corresponding to each regime are sketched in figure 5.4. For drag reduction purposes, we are interested in the case with streamwise-preferential substrates, where $K_x \gg K_y$, as it will be shown in the next chapter, but here results for the two regimes are discussed.

5.2.1 Influence of the permeabilities and substrate thickness

Permeable substrates destabilise the flow, as observed in figure 5.5. The panels illustrate the growth rate of the most unstable eigenmode at each wavelength λ^+ for both streamwise-preferential and wall-normal-preferential substrates. The amplification increases as the permeabilities increase, eventually reaching an asymptote, and peaking at $\lambda^+ \approx 60$, in

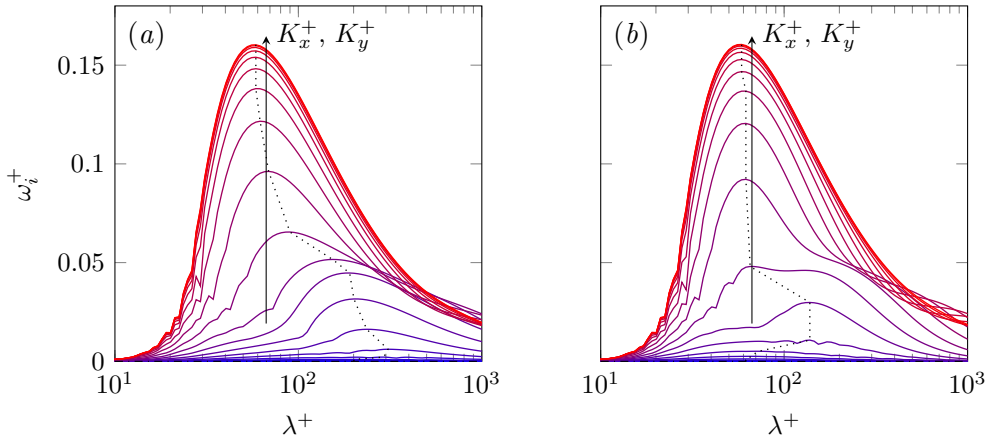

FIGURE 5.5 Growth rate, ω_i^+, as a function of the wavelength, λ^+, for substrates with $h^+ = 100$ and a fixed anisotropy ratio, K_x/K_y, when varying the permeabilities. (a) $K_x/K_y = 100$, from blue to red permeabilities increase between $K_x^+ = [10^{-1} - 10^5]$. (b) $K_x/K_y = 0.01$, from blue to red permeabilities increase between $K_y^+ = [10^{-1} - 10^5]$. The dotted line connects the maxima of the amplification curves.

agreement with previous studies by García-Mayoral & Jiménez (2011) and Abderrahaman-Elena & García-Mayoral (2017).

Jiménez *et al.* (2001) and Abderrahaman-Elena & García-Mayoral (2017) performed an inviscid analysis of a piecewise-linear velocity profile limited by a permeable wall. They showed that in the limit of very large permeabilities, $K \to \infty$, the interface acts as a mirror boundary condition, that is, the analysis is then equivalent to anti-symmetrically extending the mean velocity profile to $y < 0$, giving a free-shear layer, whose solution is the well-known Kelvin-Helmholtz instability. By analogy, the peak of the asymptote in figure 5.5 would correspond to the fully-amplified Kelvin-Helmholtz limit. We are therefore interested in the most amplified mode for each substrate, approximately $\lambda^+ \approx 60$, as it would be the most prevalent. This instability can be visualised with the perturbation streamlines of the most unstable mode, as shown in figure 5.6. This mode forms alternating clockwise and anticlockwise rollers separated by $\lambda^+ = 60$, which resemble the Kelvin-Helmholtz rollers observed in shear-layer flows.

The most amplified wavelength, $\lambda^+ \approx 60$, as well as the amplification curves observed in figure 5.5, are independent of the friction Reynolds number when scaled in viscous units. This is illustrated in figure 5.7. Note that this viscous scaling is obtained despite the analysis being inviscid. This is because the lengthscale of the instability is determined by the turbulent mean profile used. For a free-shear flow, the Kelvin-Helmholtz instability scales with the shear-layer length or mixing-layer thickness, defined as the height between the singularities in d^2U/dy^2 (Abderrahaman-Elena & García-Mayoral, 2017). In the present analysis, we only consider half the mean profile. We then define the shear-layer length as the distance between the interface, at $y = 0$, and the height where the mean vorticity gradient, d^2U/dy^2,

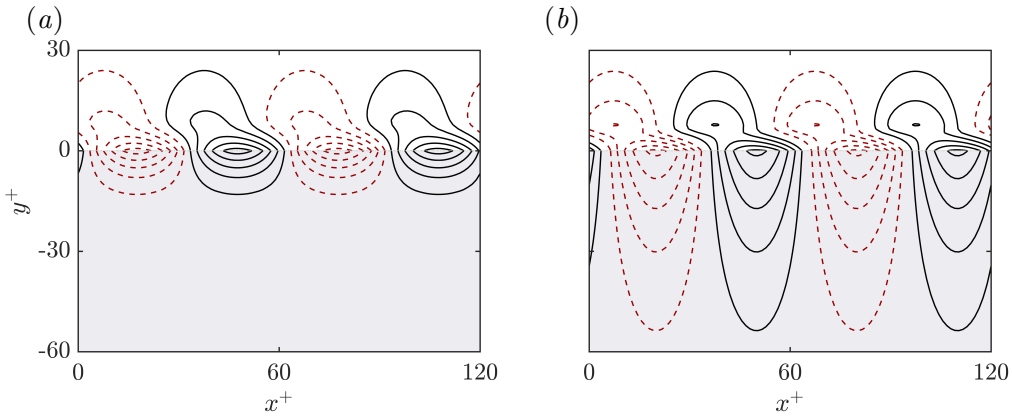

FIGURE 5.6 Isocontours of the streamfunction for the most unstable eigenvalue at $\lambda^+ = 60$ and for two specific substrates with $K_y^+ = 10$ and $h^+ = 100$. (a) $K_x/K_y = 10^1$. (b) $K_x/K_y = 10^{-1}$. Solid lines correspond to clockwise rotation, while dashed lines correspond to counterclockwise rotation.

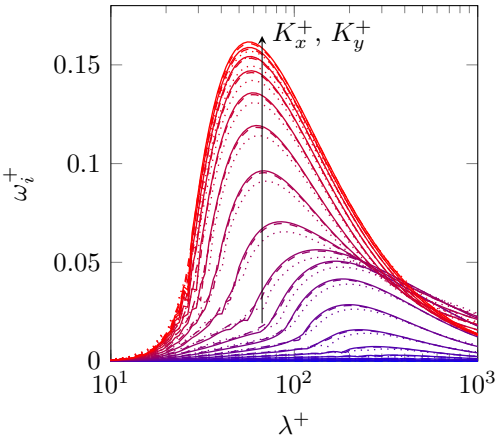

FIGURE 5.7 Growth rate, ω_i^+, versus the wavelength, λ^+, for substrates with $h^+ = 100$ and $K_x/K_y = 100$ when varying the permeabilities and for three different friction Reynolds numbers. From blue to red permeabilities increase between $K_x^+ = [10^{-1} - 10^5]$. $\cdots\cdots$, $\delta^+ = 180$; $- - -$, $\delta^+ = 550$; ——, $\delta^+ = 1000$.

concentrates (García-Mayoral & Jiménez, 2011; Abderrahaman-Elena & García-Mayoral, 2017). For turbulent profiles for which the Cess profile provides a valid representation, this height is $y_c^+ \approx 9$ independently of the Reynolds number δ^+, which leads to the scaling of the instability in viscous units. Note that the wavenumber that corresponds to y_c^+ is $1/y_c^+$ and its associated wavelength is then $2\pi y_c^+ \approx 60$, which is consistent with the wavelength observed for the most unstable mode in figures 5.5(a) and (b) for the two regimes.

The amplification increases with the substrate thickness, h^+. This is shown in figure 5.8 by comparing substrates with fixed values of K_x^+ and K_y^+ and different thickness. The effect of h^+, however, is only appreciable for shallow substrates, where $h^+ \lesssim \sqrt{K_x^+}$ and $h^+ \lesssim \sqrt{K_y^+}$. Otherwise, the channel flow does not perceive the impermeable wall that

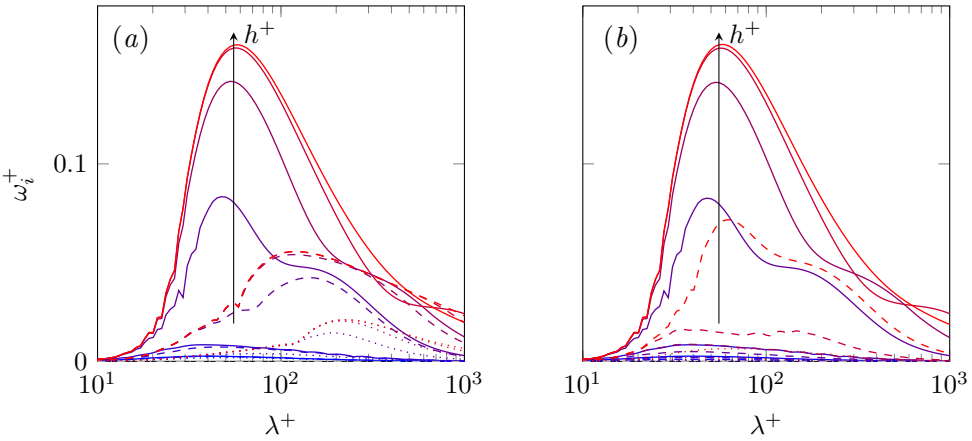

FIGURE 5.8 Amplification of the instability versus λ^+ for substrates with fixed permeabilities when varying the thickness. From blue to red h^+ increases as $[2, 3, 6, 10, 20, 100]$. Each linestyle represents substrates with same K_x^+ and K_y^+. (a) Substrates with $K_x^+/K_y^+ = 10^2$: $\cdots\cdots$, $K_x^+ = 10$; $- - -$, $K_x^+ = 100$; ——, $K_x^+ = 10^5$. (b) Substrates with $K_x^+/K_y^+ = 10^{-2}$: $\cdots\cdots$, $K_y^+ = 10$; $- - -$, $K_y^+ = 100$; ——, $K_y^+ = 10^5$.

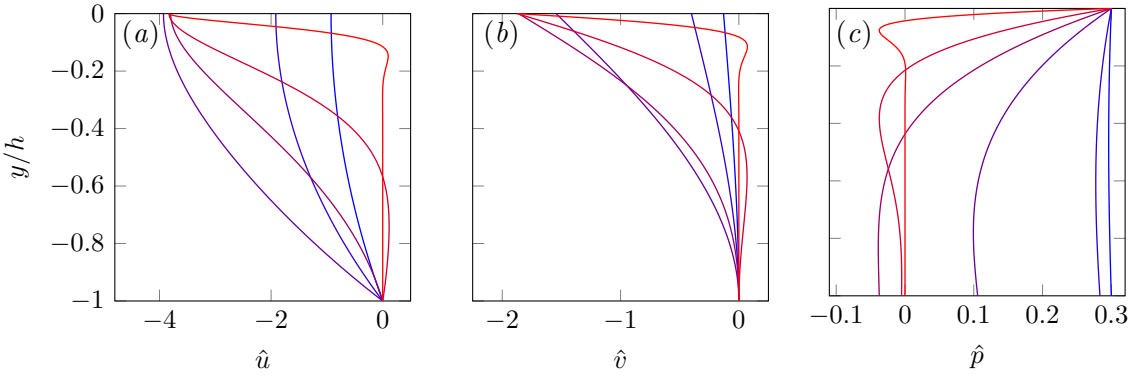

FIGURE 5.9 Flow within the permeable substrate. (a) Streamwise velocity, (b) wall-normal velocity, and (c) pressure profiles for a substrate with $K_x/K_y = 100$, $K_x^+ = 100$ and $\lambda^+ = 60$, when varying the thickness h^+. From blue to red h^+ increases as $[2, 3, 6, 10, 20, 100]$. These curves correspond to the case represented by $- - -$ in figure 5.8(a).

bounds the substrate and h^+ has no effect on the overlying flow. For shallow substrates, the transpiration at the substrate-channel interface increases with h^+, as shown by the value of the wall-normal velocity at $y = 0$ in figure 5.9(b), and the flow becomes more unstable. The amplification of the instability asymptotes when h^+ is sufficiently large for the pressure and wall-normal velocity fluctuations within the substrate to decay to zero before reaching the bottom impermeable wall.

There are two qualitatively different asymptotes that can be reached for increasing h^+ at fixed K_x^+ and K_y^+ depending on the permeability values. This is illustrated in figures 5.8$(a$-$b)$. One asymptote is the aforementioned Kelvin-Helmholtz limit. For large K_x^+ and K_y^+, h^+ is the only limiting parameter, so the amplification of the instability is governed by the value of

substrate thickness. As h^+ increases, the Kelvin-Helmholtz limit is approached, and beyond a certain value a further increase of any of the parameters (K_x^+, K_y^+ or h^+) has no effect on the instability. This is illustrated in figures 5.8(a) and 5.8(b) for the sets of curves with the greatest permeabilities, $K_x^+ = 10^5$ and $K_y^+ = 10^5$, respectively. The amplification curves for these cases are essentially identical despite the permeability values being different, and reach the same asymptote as h^+ increases. For the Kelvin-Helmholtz limit to be reached, all the three parameters (K_x^+, K_y^+ or h^+) need to be large enough. Note, however, that for realistic substrates with such large values of permeabilities, our assumptions for using Brinkman's homogenised model would no longer hold, as the flow within the substrate would stop being dominantly viscous. Nonetheless, these large values of permeabilities have been included to indicate the asymptotic trend.

For smaller permeabilities, on the other hand, the asymptote does not correspond to the Kelvin-Helmholtz limit and is set by the values of the permeabilities instead. This is also observed in figures 5.8(a-b) for the two sets with lower values of permeabilities, $K_x^+ = 10$ and $K_x^+ = 100$ in panel (a); and $K_y^+ = 10$ and $K_y^+ = 100$ in panel (b). As h^+ increases for fixed values of K_x^+ and K_y^+, the permeability lengths $\sqrt{K_x^+}$ and $\sqrt{K_y^+}$ become comparable to h^+. Eventually, h^+ has no effect on the instability, and $\sqrt{K_x^+}$ and $\sqrt{K_y^+}$ become the only relevant parameters. The asymptote in this case is set by the values of $\sqrt{K_x^+}$ and $\sqrt{K_y^+}$, and the amplification and the wavelength of the instability is different for each substrate.

Note that the amplification is driven by the wall-normal velocity at the substrate-channel interface, and hence depends on the flow within the permeable substrate. Within the substrate, there is a layer that develops immediately below the interface, where the overlying flow penetrates, which we call 'Brinkman layer'. The thickness of this layer is what we refer to as penetration length, L_p. This sets a lengthscale for the flow within the substrate and hence has an influence on the amplification of the instability observed in figure 5.5.

In anisotropic substrates, the penetration depth is a function of the substrate lengthscales available – the permeability lengths $\sqrt{K_x}$ and $\sqrt{K_y}$ and the thickness h –, along with the wavelength λ considered (or alternatively the wavenumber α). The expression for the penetration depth, L_p, can be derived from the solution of the flow within the substrate. Let us consider sufficiently deep substrates, $h > \sqrt{K_x}$ and $h > \sqrt{K_y}$, so that the Brinkman layer does not perceive the effect of the impermeable wall, removing the effect of the thickness h and simplifying the analysis to determine L_p.

As mentioned in section 5.1, the general solution of Brinkman's equation is a sum of four exponential terms (see details in appendix A.1). For the permeable substrate at the lower-channel wall, $y < 0$, only the terms with a positive exponent, m_1 and m_2, are relevant, as the coefficients multiplying the other two exponentials need to be close to zero in order to obtain a bounded solution. The penetration depth would then be set by the dominant exponent, either the inverse of the root m_1 or m_2 from equation (5.4).

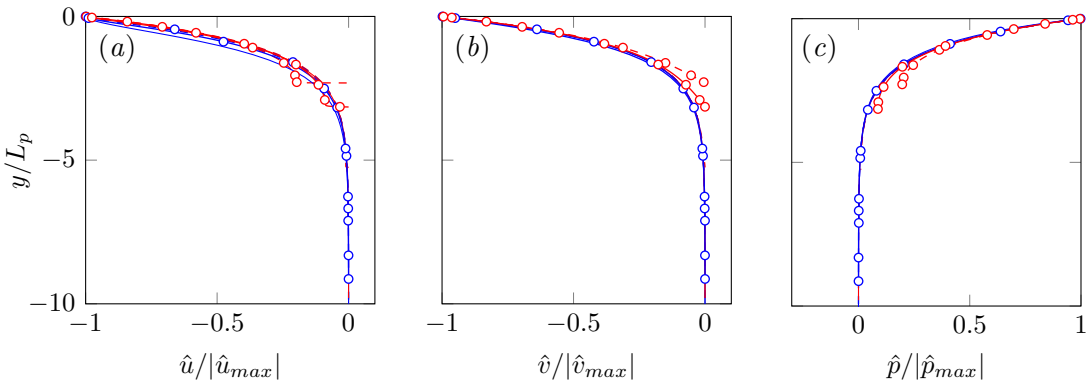

FIGURE 5.10 Pressure and velocity profiles within the permeable substrate scaled with the penetration depth, L_p, for different substrate configurations when $K_x/K_y \ll 1$. Blue, $K_x/K_y = 10^{-1}$; red, $K_x/K_y = 10^{-2}$; with – – –, $K_y^+ = 10$; ——, $K_y^+ = 100$, and two different wavenumbers: no markers, $\alpha^+ = 0.21$ ($\lambda^+ = 30$); circles, $\alpha^+ = 0.1$ ($\lambda^+ = 60$). (a) Streamwise velocity, (b) wall-normal velocity, and(c) pressure.

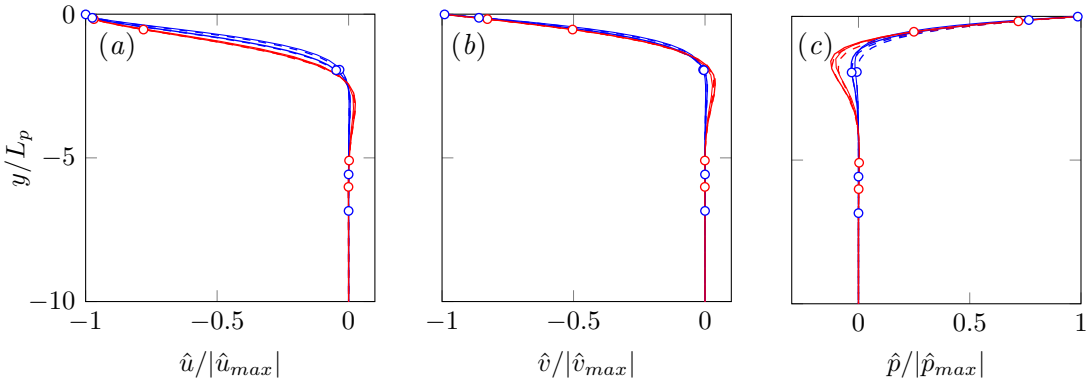

FIGURE 5.11 Pressure and velocity profiles within the permeable substrate scaled with the penetration depth, L_p, for different substrate configurations when $K_x/K_y \gg 1$. Blue, $K_x/K_y = 10^{1}$; red, $K_x/K_y = 10^{2}$; with – – –, $K_x^+ = 10$; ——, $K_x^+ = 100$, and two different wavenumbers: no markers, $\alpha^+ = 0.21$ ($\lambda^+ = 30$); circles, $\alpha^+ = 0.1$ ($\lambda^+ = 60$). (a) Streamwise velocity, (b) wall-normal velocity, and(c) pressure.

For $K_x/K_y < 1 + 1/(4K_x\alpha^2)$, the roots m_1 and m_2 in equation (5.4) are always real. In this case, the lengthscale of the solution is determined by m_2, the smallest exponent between the two, as the corresponding exponential decays slower to meet the impermeability condition at $y = -h$. The penetration depth, L_p, is then

$$L_p = \frac{1}{m_2}. \tag{5.12}$$

Figure 5.10 shows that the velocities and pressure profiles for different substrates essentially collapse to a single curve when scaled with this penetration depth. In the limit when $K_x \ll K_y$

and assuming that $(K_x\alpha^2) < 1$, L_p reduces to

$$L_p|_{\frac{K_x}{K_y}\ll 1} \approx \frac{1}{\alpha\sqrt{K_x/K_y + \alpha^2 K_x}}. \tag{5.13}$$

This shows that in this regime, both permeabilities K_x and K_y are relevant.

In the opposite limit, $K_x/K_y > 1 + 1/(4K_x\alpha^2)$, m_1 and m_2 are complex conjugates. In this case, the lengthscale is set by the imaginary part,

$$L_p|_{\frac{K_x}{K_y}>1} = \frac{\sqrt{2}}{\alpha}\frac{1}{\sqrt{-1 - \dfrac{1}{2\alpha^2 K_x} + \sqrt{1 + \dfrac{1}{\alpha^2 K_y}}}}, \tag{5.14}$$

as evidenced by the good collapse of the velocity and pressure profiles observed in figure 5.11. In the limit when $K_x \gg K_y$, we may also assume that $(K_x\alpha^2) \gtrsim 1$ and $(\sqrt{K_y}\alpha) \ll 1$ for the wavenumbers in the range of interest, i.e. $\lambda^+ \approx 60$. Within these constraints, equation (5.14) simplifies further into

$$L_p|_{\frac{K_x}{K_y}\gg 1} = \sqrt[4]{\frac{4K_y}{\alpha^2}}. \tag{5.15}$$

In sum, the flow within the substrate is qualitatively different depending on the directionality of the substrate. For substrates preferential in the wall-normal direction, $K_x \ll K_y$, the penetration depth depends on the wavelength considered and the streamwise and wall-normal permeabilities. In turn, for substrates preferential in the streamwise direction, $K_x \gg K_y$, the penetration depth depends only on the wavelength and the wall-normal permeability.

5.2.2 Characterisation of the instability

Let us now focus on the maximum amplification of the most unstable mode for each substrate, as this can be expected to be the most prevalent. In figure 5.5, this corresponds to the maxima of the curves, linked by the black line. As in Abderrahaman-Elena & García-Mayoral (2017), we propose a single, empirically-fitted parameter to capture the effect of the parameters that characterise the substrates, namely the directional permeabilities and the thickness, on the amplification of the instability. This parameter, referred to as $K^+_{Br,\nu=0}$, is given by

$$K^+_{Br,\nu=0} = \begin{cases} K_y^+ \tanh\left(\sqrt{2}\dfrac{\sqrt{K_x^+}}{y_c^+}\right)\tanh^2\left(\dfrac{h^+}{2.5\sqrt{K_y^+}}\right) & \text{if } K_x^+ \gtrsim K_y^+, \text{(5.16a)} \\ \sqrt{K_x^+ K_y^+}\tanh\left(\dfrac{h^+}{\sqrt{2}y_c^+}\sqrt{\dfrac{K_x^+}{K_y^+}}\right)\tanh^2\left(\dfrac{h^+}{1.2\sqrt{K_x^+}}\right) & \text{if } K_x^+ \lesssim K_y^+. \text{(5.16b)} \end{cases}$$

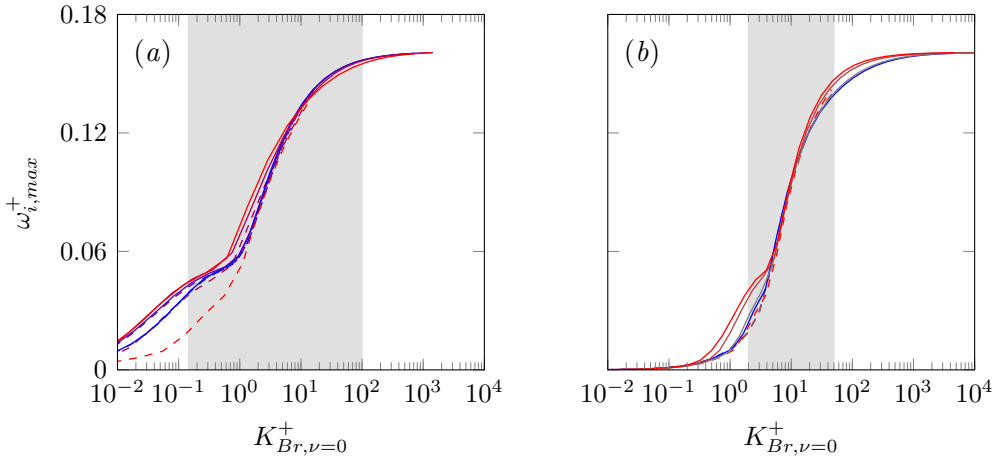

FIGURE 5.12 Maximum growth rate, $\omega^+_{i,max}$, versus $K^+_{Br,\nu=0}$ for different substrates. – – –, $h^+ = 10$; ——, $h^+ = 100$. (a) Anisotropy ratios $K_x/K_y \geq 1$. From blue to red $K_x/K_y = 10^3$, 10^2, 10 and 1. (b) Anisotropy ratios $K_x/K_y \leq 1$. From blue to red $K_x/K_y = 10^{-3}$, 10^{-2}, 10^{-1} and 1. The shaded region corresponds to the estimated range for the onset of Kelvin-Helmholtz instabilities.

The exact limit between the two regimes is actually $K_x/K_y = 1 + 1/(4K_x\alpha^2)$, as discussed above, but for wavelengths in the range of interest and for values of K_x for which the amplification of the instability is significantly above zero, we have $(4K_x\alpha^2) \gtrsim 1$, and the limit between the two regimes can be approximated to $K_x/K_y \approx 1$. For highly-connected permeable substrates, therefore, the parameter $K^+_{Br,\nu=0}$ in equation (5.16a) captures the dependence of the amplification of the instability on the substrate topology, as shown in figure 5.12. Different substrates with different geometrical parameters, but the same value of $K^+_{Br,\nu=0}$, would exhibit essentially the same stability properties. There is however some deviation for low values of the permeabilities. The reason behind this is the secondary instability that occurs at higher wavelengths, which becomes dominant at low permeability values. This secondary instability arises from the same eigenvalue and it can be observed in the second bump that appears in figure 5.5 at higher wavelengths.

As expected, the parameter $K^+_{Br,\nu=0}$ differs depending on the directionality of the substrate, and hence the amplification of the instability behaves differently in each regime. The reason for this dichotomy in the governing parameter is discussed in sections 5.1 and 5.2.1, where we showed the qualitatively different nature of the flow within the substrate depending on the anisotropy ratio. In any event, three different regions can be distinguished in figures 5.12(a-b): a low $K^+_{Br,\nu=0}$ region, $K^+_{Br,\nu=0} \lesssim 0.15$ for $K_x > K_y$ and $K^+_{Br,\nu=0} \lesssim 2$ for $K_x < K_y$, where the Kelvin-Helmholtz-like instability is weak and would not be expected to appear in the flow; a large $K^+_{Br,\nu=0}$ region, $K^+_{Br,\nu=0} \gtrsim 100$ for $K_x > K_y$ and $K^+_{Br,\nu=0} \gtrsim 50$ for $K_x < K_y$, where the amplification is fully amplified; and an intermediate, transitional region, where the instability begins to develop. These regions are indicated in figure 5.12. As before, in figures 5.5 and 5.12 we have included large values of permeabilities for completeness, so

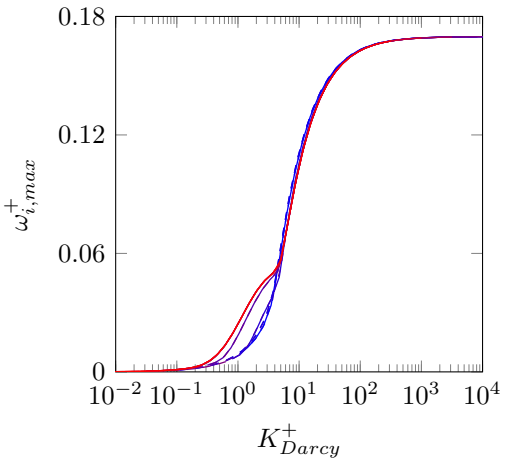

FIGURE 5.13 Maximum growth rate, $\omega^+_{i,max}$, versus K^+_{Darcy} for different substrates. – – –, $h^+ = 10$; ——, $h^+ = 100$. From blue to red $K_x/K_y = 10^{-3}$, 10^{-2}, 10^{-1}, 1, 10^1, 10^2 and 10^3.

that the asymptotic trend could be illustrated. For such large permeabilities, however, the assumptions stated in section 1.5 are no longer satisfied and the results may not quantify adequately the amplification of the instability. Nonetheless, the relevant range of values for this study lies on the intermediate region, where the instability starts to develop, and its onset is characterised by $K^+_{Br,\nu=0}$. The present model can be used to obtain estimates of the permeability values for which the Kelvin-Helmholtz rollers would develop, as we will see in the next chapter.

The expressions for $K^+_{Br,\nu=0}$ can be further simplified for deep substrates, $h^+ \gg \sqrt{K^+_x}$ and $h^+ \gg \sqrt{K^+_y}$, and, in the case of streamwise-preferential substrates, for large values of K^+_x. The hyperbolic tangents in equation (5.16a) tend then to unity and the instability is essentially driven by

$$K^+_{Br,\nu=0} \approx \begin{cases} K^+_y & \text{if } K^+_x \gtrsim K^+_y, \quad (5.17a) \\ \sqrt{K^+_x K^+_y} & \text{if } K^+_x \lesssim K^+_y. \quad (5.17b) \end{cases}$$

Thus, for $K_x/K_y > 1$, K^+_x has little effect and the onset of the instability, which is essentially governed by the wall-normal permeability, K^+_y, alone, while for $K_x/K_y < 1$, both K^+_x and K^+_y are equally relevant, as was also the case for L_p in section 5.2.1.

The above analysis applies to highly-connected permeable substrates, for which the flow within the substrate can be modelled using Brinkman's equation. Results valid for poorly-connected substrates were reported by Abderrahaman-Elena & García-Mayoral (2017), who used Darcy's equation instead to model the flow. The authors performed an inviscid stability analysis of a channel flow, where the conditions at the interface were obtained from the solution of Darcy's equation and were of the form $\hat{v}|_{y=0^+} = \mathcal{C}_{Darcy}\hat{p}|_{y=0^+}$. The analytic

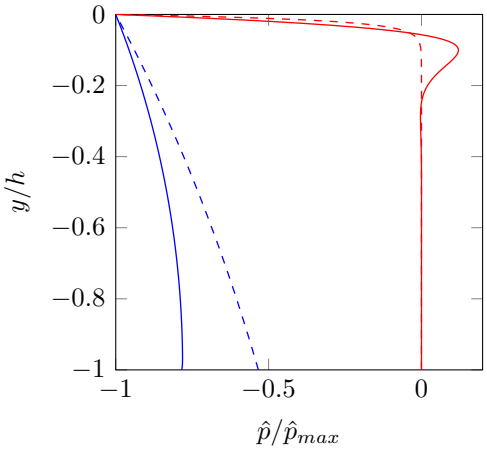

FIGURE 5.14 Variation of pressure within the permeable substrate for substrates with $\lambda^+ = 100$ and $h^+ = 100$. – – –, Darcy's model; ——, Brinkman's models. Red, streamwise-preferential substrate, $K_x/K_y = 10^2$; blue, wall-normal-preferential substrate, $K_x/K_y = 10^{-2}$.

solution of Darcy's equation can be found in appendix D, where the specific expression for $\mathcal{C}_{Darcy}$ is detailed. The impedance coefficient, $\mathcal{C}_{Darcy}$, is qualitatively different from the coefficient $\mathcal{C}_{vp}$ obtained from Brinkman's solution. Abderrahaman-Elena & García-Mayoral (2017) observed that the parameter that drives the instability in this case is essentially

$$K^+_{Darcy} = \sqrt{K^+_x K^+_y}\tanh\left(\frac{h^+}{y^+_c}\sqrt{\frac{K^+_x}{K^+_y}}\right), \tag{5.18}$$

regardless of the directionality of the substrate, as shown in figure 5.13. Assuming sufficiently deep substrates, K^+_{Darcy} becomes approximately

$$K^+_{Darcy} \approx \sqrt{K^+_x K^+_y}, \tag{5.19}$$

which agrees with expression (5.17b) obtained for highly-connected substrates when $K_x/K_y < 1$.

This agreement between poorly-connected substrates and wall-normal-preferential, highly-connected substrates is connected to the variation of the streamwise pressure gradient, $\partial p/\partial x$, within the substrates. The variation of $\hat{p}$ for the two models, which relates directly to the variation of $\partial p/\partial x$, as the latter is $i\alpha\hat{p}$ in Fourier space, is shown in figure 5.14. For highly-connected substrates with $K_x/K_y < 1$, the flow is less impeded in the wall-normal direction. It can penetrate easily into the substrate, which results in a mild change of the streamwise pressure gradient with depth. This, in turn, implies that the flow within is driven by a streamwise pressure gradient relatively homogeneous in y, and there would be little macroscale shear between layers at different heights. The diffusive terms in Brinkman's equation are therefore small and can be neglected, recovering Darcy's equation. Hence, in this limit, Darcy's equation is sufficient to model the flow, even if the substrate is highly-connected.

In contrast, for highly-connected substrates with $K_x/K_y > 1$, the flow is more obstructed in the wall-normal direction than in the streamwise one. There is therefore a comparatively large variation of the streamwise pressure gradient with height, as the pressure at the interface decreases rapidly as it penetrates into the substrate. Hence, the pressure gradient drives less streamwise velocity deep within the substrate than near the interface, resulting in velocity profiles that decay rapidly with depth. For highly-connected substrates, the macroscale diffusive terms within are no longer small and the results are qualitatively different when they are taken into account. Darcy's equation is therefore not sufficient to model the flow and Brinkman's term must be included. For substrates with low connectivity, in turn, the high shear within the substrate cannot be transmitted between different heights, independently of the ratio between the permeabilities, and Darcy's model is suitable.

The discrepancy in the relevance of the Brinkman term depending on the anisotropy ratio is also shown by the order of magnitude analysis presented in appendix E. This analysis also illustrates that while macroscale diffusive terms within a highly-connected substrate must be retained, especially when $K_x > K_y$, for high Reynolds numbers these can be neglected in the channel region with respect to the advective terms, which justifies the inviscid stability analysis conducted here. Nevertheless, results from the viscous stability analysis presented in the next section corroborate this assumption.

5.3 Viscous analysis

In this section, we extend the previous analysis and perform a two-dimensional, viscous stability analysis to evaluate the role of viscosity on the formation of the Kelvin-Helmholtz-like instabilities. Given that viscosity is a damping factor, we would now expect the triggered instabilities to have lower amplifications. The viscosity acts more efficiently at small lengthscales, so small wavelengths would be more affected.

The governing equation is the Orr-Sommerfeld equation (5.2) with viscosity $\nu_T(y)$, which includes an eddy viscosity, and where the boundary conditions are given by equation (5.8). The addition of viscous terms within the channel modifies the problem qualitatively. The overlying flow can no longer slip freely in the streamwise direction, and continuity of the wall-normal velocity at the interface, imposed in the inviscid analysis, is complemented by the continuity of the streamwise velocity. Although not shown here, we have also performed viscous analysis using the molecular viscosity alone and similar results were obtained, with the only difference being the slightly higher amplification values reached with ν alone. The viscosity $\nu_T(y)$ has been shown to be important to capture the phenomena in the logarithmic layer or far away from the wall (del Álamo & Jiménez, 2006; Pujals *et al.*, 2009; Illingworth *et al.*, 2018). In the present study, however, we are interested in near-wall layer, at $y^+ \sim 20$, where the effect of the eddy viscosity is not that significant, which explains the similar results obtained with ν and $\nu_T(y)$.

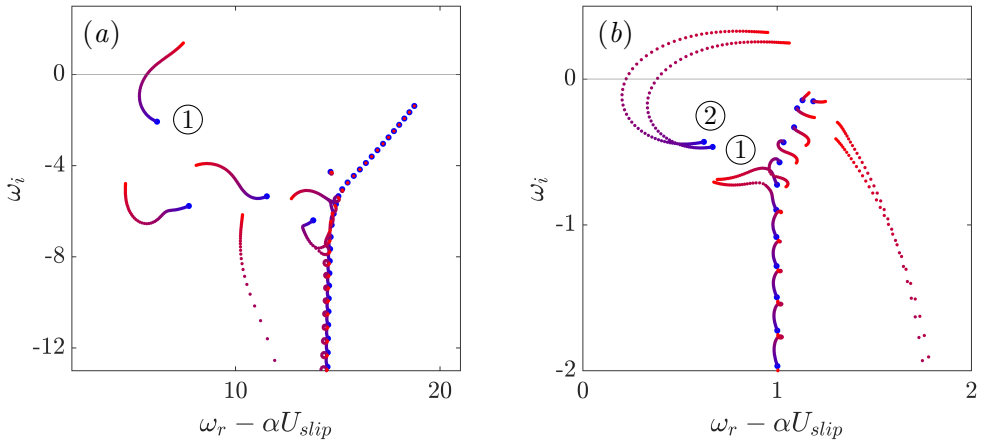

FIGURE 5.15 Trajectory of the eigenvalues for a turbulent channel with permeable substrates with $h^+ = 100$ and $K_x/K_y = 100$ when varying the permeabilities. From blue to red K_x^+ increases between $K_x^+ = [10^{-2} - 10^4]$. (a) $\lambda^+ = 68$. Impermeable spectrum in black. (b) $\lambda^+ \approx 1000$. Values are normalised in outer units, i.e. using the channel half-height δ and the bulk velocity of the mean flow, and U_{slip} refers to the mean slip velocity at the substrate-channel interface. ① and ② represent unstable eigenvalues.

In the viscous analysis, there are four spurious eigenvalues that arise from the boundary conditions, which must be eliminated to avoid any interference in the subsequent analysis. Two of these spurious eigenvalues can be set to a fixed value with a large negative imaginary part. The other two can be easily identified and filtered out by tracking their rapid fluctuation as the number of Chebyshev points varies (Dawkins *et al.*, 1998; Jiménez *et al.*, 2001).

5.3.1 Influence of the permeabilities and substrate thickness

The main observations from the inviscid analysis apply also to the viscous one. The presence of permeable substrates destabilises the channel flow. This can be observed in figure 5.15(a) for $\lambda^+ = 68$, which corresponds to the most amplified wavelength in the viscous case. This figure shows the trajectory of the eigenvalues as the permeabilities in viscous units, K_x^+ and K_y^+, increase for a substrate with a fixed permeability ratio, K_x/K_y. Only an instance for streamwise-preferential configurations, $K_x/K_y > 1$, is shown, and although not shown, wall-normal-preferential substrates, $K_x/K_y < 1$, exhibit a similar trend. When permeabilities tend to zero, the solution for the corresponding impermeable channel is recovered, confirming the results by Reynolds & Tiederman (1967) that a turbulent channel flow with impermeable walls at this Reynolds number is stable. Low permeability values are now stable and instabilities only arise when one of the modes crosses the $\omega_i = 0$ line. In this case, there is one wall mode that becomes unstable, here denoted as mode ①.

On a close examination, we observe that this unstable mode is not one, but two modes merged together, following what we previously observed for the laminar case in section 5.1.3.

To illustrate this, panel (b) portrays the same spectrum from panel (a) but for a much larger wavelength, $\lambda^+ \approx 1000$, where there are two separate modes, labelled ① and ②, that become unstable when permeabilities increase. Although mode ① is the first mode to become unstable, mode ② reaches higher amplification values and becomes the most unstable mode for large permeabilities. As mentioned previously, this is because in channels, modes can be classified into symmetric (or varicose) and antisymmetric (or sinuous) modes. Here mode ① corresponds to a symmetric mode, which forms rollers rotating symmetrically with respect to the centreline of the channel, while mode ② corresponds to an antisymmetric mode and the corresponding rollers rotate antisymmetrically. For short wavelengths, both modes have the same appearance, but for large wavelengths, they diverge, as the top and bottom rollers of mode ② merge together and become more intense than those of mode ①, which do not merge. In a channel both modes develop, but, as mentioned in section 5.1.3, only the symmetric mode would be observed in boundary layers (Jiménez *et al.*, 2001). Hence, hereafter we focus on the symmetric mode. Nevertheless, the amplification of mode ② at large wavelengths is still much smaller than that at $\lambda^+ \approx 68$, as illustrated in figure 5.15, and thus for the most amplified wavelengths, which are the ones we are interested in, both modes are identical.

Focusing on mode ①, figure 5.16 shows the amplification of this mode versus the wavelength for both streamwise-preferential and wall-normal preferential substrates. As in the inviscid case, the amplification increases with K_x^+ and K_y^+, and tends to an asymptotic limit, the fully-amplified Kelvin-Helmholtz limit. The effect of the substrate thickness is also analogous to that discussed in the inviscid case and is therefore not shown. The flow becomes more unstable as h^+ increases, since the wall-normal velocity at the interface increases and as h^+ increases, the amplification eventually reaches an asymptote when the fluctuations within the permeable substrate become zero before reaching the impermeable wall.

The Kelvin-Helmholtz rollers associated with the instability can be recognised in the perturbation streamlines shown in figure 5.17 and have a similar shape to those observed for the inviscid analysis in figure 5.6. The main difference is the continuity in the slope of the isocontours across the interface.

As expected, the maximum growth rate in figure 5.16 is reduced with respect to the inviscid results due to the effect of viscosity. This effect is stronger for short wavelengths, which were neutral in the inviscid case and are now stable. In addition, the growth rate now peaks at $\lambda^+ \approx 70$, which is slightly shifted from $\lambda^+ \approx 60$ observed previously in the inviscid analysis, probably due to the stronger effect of viscosity on smaller wavelengths. The similarity in the wavelength was indeed expected, since the Kelvin-Helmholtz instability is an inviscid phenomenon and its wavelength is set by the shear-layer length, as explained in section 5.2, which is still given by $y_c^+ \approx 9$. The resulting wavelength, however, is roughly half that observed from the DNSs over anisotropic permeable substrates, as we will show in chapter 7. The studies by García-Mayoral & Jiménez (2011) for riblets and Jiménez *et al.* (2001) for permeable walls also predict shorter wavelengths from linear stability analysis than

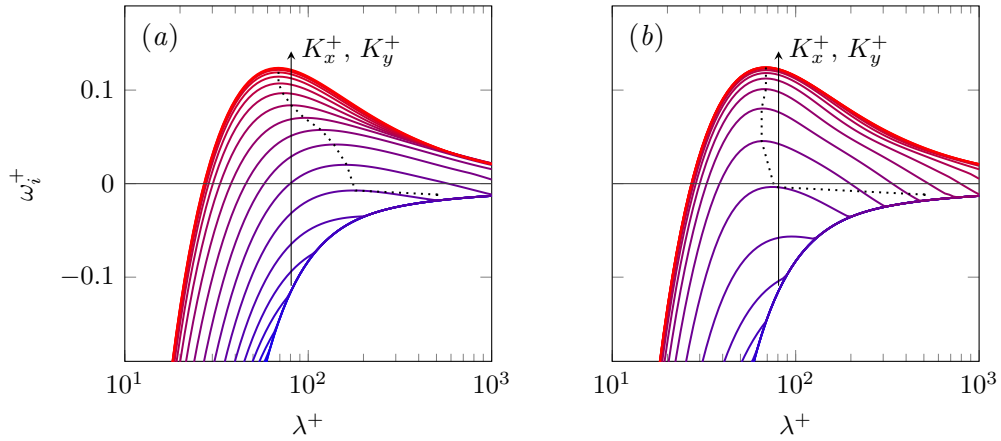

FIGURE 5.16 Growth rate, ω_i^+, as a function of λ^+ for substrates with $h^+ = 100$ and a fixed anisotropy ratio, K_x/K_y, when varying the permeabilities. (a) $K_x/K_y = 100$, from blue to red permeabilities increase between $K_x^+ = [10^{-1} - 10^5]$. (b) $K_x/K_y = 0.01$, from blue to red permeabilities increase between $K_y^+ = [10^{-1} - 10^5]$. The dotted line links the maxima of the amplification curves.

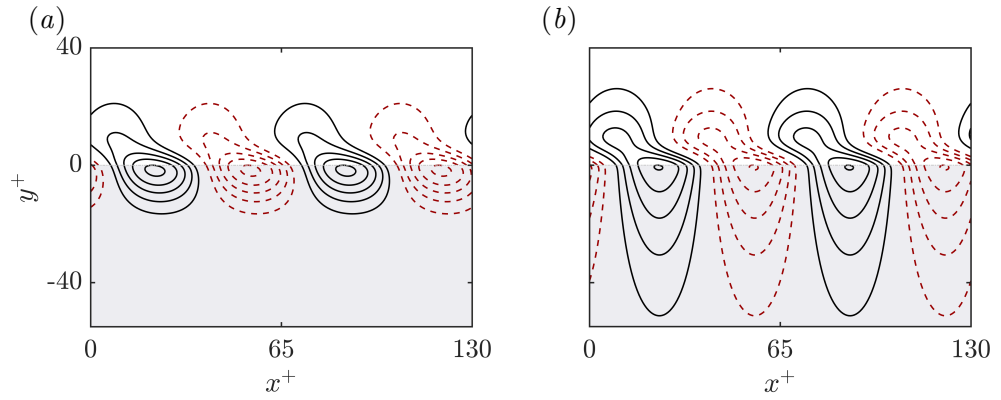

FIGURE 5.17 Isocontours of the streamfunction for the most unstable eigenvalue at $\lambda^+ = 68$ and for two specific substrates with $K_y^+ = 10$ and $h^+ = 100$. (a) $K_x/K_y = 10^1$. (b) $K_x/K_y = 10^{-1}$. Solid lines correspond to clockwise rotation, while dashed lines correspond to counterclockwise rotation.

those observed in DNSs. This discrepancy may result from the assumptions made regarding the mean velocity profile and the approach adopted for the stability analysis. In the present analysis, we have performed the stability of the channel region alone, where the effect of the permeable substrates is included through the boundary conditions. Consequently, the mean profile is applied between the substrate-channel interfaces and only part of the total shear-layer length is taken into account. In reality, the profile extends inside the substrate, making the shear-layer length roughly twice as thick, which may result in the value of the wavelength observed in real flows. In addition, the same mean profile is used regardless of the permeability values. For large permeabilities, we would expect turbulence to penetrate into the substrate, thereby altering the distribution of Reynolds stresses, which is accounted by the eddy viscosity, and the mean velocity profile. Consequently the shear-layer length

and the wavelength of the instability would also be modified. The changes in the mean velocity profile, however, cannot be anticipated without performing a DNS, which exceeds the goal of the present study of building a predictive model to characterise the instability. As it will be shown in chapter 7, the present model, although simple, provides reasonably good predictions.

5.3.2 Characterisation of the instability

As in the inviscid analysis, we propose a single, empirically fitted parameter, K^+_{Br}, to characterise the amplification of the instability for different substrates,

$$K^+_{Br} = \begin{cases} K^+_y \tanh\left(\frac{\sqrt{2K^+_x}}{y^+_c}\right) \tanh^2\left(\frac{h^+}{3.5\sqrt{K^+_y}}\right) & \text{if } K^+_x \gtrsim K^+_y, \quad (5.20a) \\ \sqrt{K^+_x K^+_y} \tanh\left(\frac{h^+}{\sqrt{2}y^+_c}\sqrt{\frac{K^+_x}{K^+_y}}\right) \tanh^2\left(\frac{h^+}{2.5\sqrt{K^+_x}}\right) & \text{if } K^+_x \lesssim K^+_y. \quad (5.20b) \end{cases}$$

This parameter is similar to that defined for the inviscid case, lending further support to the idea that the observed instability is essentially inviscid and can be effectively characterised by inviscid analysis. As in section 5.2.2, there are two qualitatively different behaviours depending on the anisotropy ratio, where the exact limit between the two regimes would be given by $K_x/K_y = 1 + (4\alpha^2 K_x)$, but becomes roughly $K_x/K_y \approx 1$ for the values of α and K_x under consideration. Figure 5.18 shows that K^+_{Br} essentially captures the effect of the substrate on the amplification of the instability. In this case, the deviation between the curves is even less pronounced than in figure 5.12 for the inviscid analysis, which is consistent with the absence of the second bump in figure 5.16.

As in the inviscid analysis, three different regions can be identified based on K^+_{Br}, the stable one, the transitional one and the one where the instability is fully amplified. The limiting values set in figure 5.18 for K^+_{Br} are roughly the same as those reported for the inviscid analysis. For small values of K^+_{Br}, the dominant mode is stable and the instability is not expected to manifest in the flow. For intermediate values, the instability would begin to develop, and for large K^+_{Br}, it would become fully amplified. When compared to the inviscid curves in figure 5.12, the asymptotic value of the amplification is now lower due to the effect of viscosity, but the trend agrees well with that predicted by the inviscid analysis. For $K_x/K_y > 1$, the leading parameter that describes the instability is essentially K^+_y, whereas for $K_x/K_y < 1$ is $\sqrt{K^+_x K^+_y}$, as was the case for the inviscid analysis. As discussed in chapter 1, the onset of Kelvin-Helmholtz-like instabilities here studied represents a possible failure mechanism for drag-reducing permeable substrates. In the next chapter, we will use figure 5.18(a) to bound the values of permeabilities for a realisable drag reduction and select

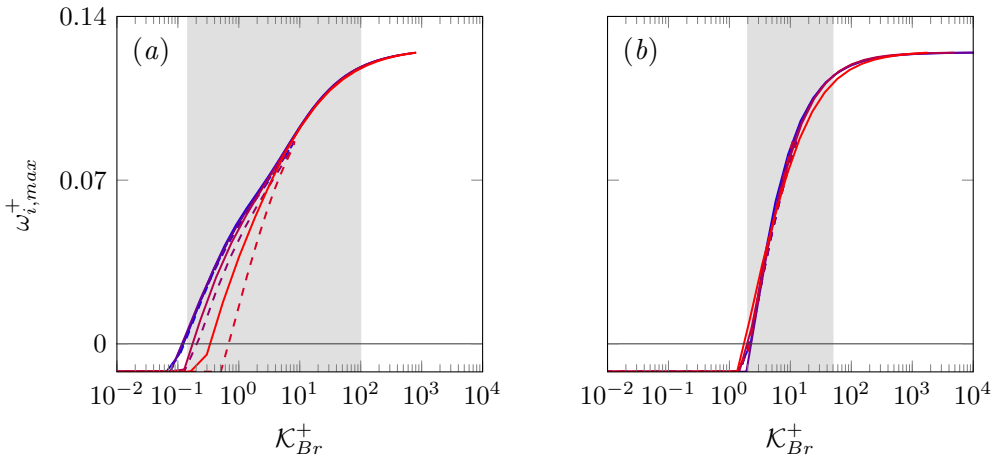

FIGURE 5.18 Maximum growth rate, $\omega^+_{i,max}$, versus K^+_{Br} for different substrates. – – –, $h^+ = 10$; ——, $h^+ = 100$. (*a*) Anisotropy ratios $K_x/K_y \geq 1$. From blue to red $K_x/K_y = 10^3$, 10^2, 10 and 1. (*b*) Anisotropy ratios $K_x/K_y \leq 1$. From blue to red $K_x/K_y = 10^{-3}$, 10^{-2}, 10^{-1} and 1. The shaded region corresponds to the estimated range for the onset of Kelvin-Helmholtz instabilities.

the parameters of the substrates for the DNSs shown in chapter 7.

After performing both inviscid and viscous stability analyses, we can conclude that the triggering of Kelvin-Helmholtz-like instabilities is captured adequately by the former. From the point of view of the instabilities, viscous terms in the channel can therefore be neglected. In contrast, the macroscale diffusive terms within the permeable substrate, represented by the Brinkman term, may or may not be negligible depending on the connectivity of the medium that we aim to represent. For highly-connected permeable substrates, the macroscale diffusion must be retained, especially for streamwise-preferential substrates with $K_x > K_y$. Note that for the viscous analysis there are four coefficients in the boundary condition (5.5), $\mathcal{C}_{vp}$, $\mathcal{C}_{vu}$, $\mathcal{C}_{up}$ and $\mathcal{C}_{uu}$, while for the inviscid analysis only $\mathcal{C}_{vp}$ is present. Given that an inviscid analysis is sufficient to characterise the Kelvin-Helmholtz-like instability, we can argue that $\mathcal{C}_{vp}$ is the dominant coefficient for its onset, and the others have only a secondary effect. Thus, the relaxation of the impermeability condition, expressed through the coupling between the wall-normal velocity and the normal stresses (i.e. the $\hat{v}$-$\hat{p}$ coupling), is the necessary condition to capture the Kelvin-Helmholtz-like instability. For poorly-connected substrates, the diffusive effects within the substrates can be neglected. For a viscous stability analysis, this poses the question of what condition to impose on the tangential velocity across the substrate-channel interface. Even if in the present study we have not performed a viscous analysis for poorly-connected substrates, the observations for highly-connected substrates can also be extended to this case. Our results suggest that an inviscid analysis would suffice to capture the Kelvin-Helmholtz instabilities. This implies that the tangential slip would only have a secondary effect, and the boundary conditions applied at the interface, continuity

or jump of the tangential velocity and stress, would have only a minor effect on the onset of the instability.

Chapter 6

Drag reduction by anisotropic permeable substrates: theoretical models*

In the next two chapters, we explore the ability of anisotropic permeable substrates to reduce turbulent skin-friction. Based on the outcomes from the previous chapters, here we develop theoretical models to estimate the drag reduction that permeable substrates can achieve. On one hand, the virtual-origin theory explored in chapter 3 provides estimates for the expected drag reduction in the linear regime, while on the other hand, the model for the onset of Kelvin-Helmholtz instability developed in chapter 5 bounds the achievable drag reduction. These models allow us to bound the range of permeabilities for drag reduction and select specific substrates for the subsequent DNS study in chapter 7. Additionally, we also discuss the effect of permeable substrates on internal and external flows and how they relate.

6.1 Drag reduction from virtual origins

In chapters 1, 3 and 4 we discussed how the drag reduction from non-smooth surfaces can be expressed as a virtual-origin effect, where the reduction of drag is essentially caused by an offset between the positions of the virtual, equivalent smooth walls perceived by the mean flow and the overlying turbulent flow, i.e. $\Delta U^+ = \ell_U^+ - \ell_T^+$, as given by equation (3.7) and sketched in figure 1.7, but turbulence remains otherwise smooth-wall-like (Luchini *et al.*, 1991; Jiménez, 1994; Luchini, 1996; García-Mayoral *et al.*, 2019). Note that these virtual origins are measured from a reference plane, which for the permeable substrates studied, is taken at the substrate-channel interface plane. This is where we set $y = 0$.

*Parts of the content of this chapter have been published in *Journal of Fluid Mechanics*, 875, 124 – 172, with Ricardo García-Mayoral as co-author.

Given that for small values of permeabilities the mean streamwise profile near the surface is linear, the origin of the mean flow is equal to the streamwise slip length, i.e. $\ell_U^+ \approx \ell_x^+$ (Luchini, 1996). For the DNSs presented in the next chapter, we consider equal wall-normal and spanwise permeabilities, $K_y^+ = K_z^+$. The slip in the spanwise direction is then always accompanied by the corresponding wall-normal transpiration. It follows from equation (3.9) that the virtual origin perceived by turbulence in this case is that experienced by the spanwise velocity, i.e. $y^+ = -\ell_w^+$, with no saturation, and since the cross permeability lengths considered will not exceed the value of $1-2$ wall units ($\sqrt{K_z^+}, \sqrt{K_y^+} \lesssim 1-2$), ℓ_T^+ is roughly equal to the spanwise slip length, $\ell_T^+ \approx \ell_z^+$. Therefore, for the linear regime, we would expect the drag reduction of the anisotropic permeable substrates studied in this thesis to be given by

$$\Delta U^+ = \ell_x^+ - \ell_z^+, \tag{6.1}$$

which agrees with the expression derived by Luchini *et al.* (1991). For a more general case where $K_z^+ \neq K_y^+$, however, the virtual origin of turbulence would deviate from ℓ_z^+, as discussed in chapter 3. This is, for instance, the case for the drag-reducing substrates studied by Rosti *et al.* (2018). They considered substrates with equal tangential permeabilities, $K_x = K_z$, and zero or unrealistically low values of wall-normal permeabilities, so that $v \approx 0$ at the interface, and thus the drag reduction that they observed results from the saturation effect of ℓ_z^+ on ΔU^+, as explained in chapter 3. Such substrates are closer to the idealised impermeable substrates of Hahn *et al.* (2002) or the slip-only simulations of Min & Kim (2004) and Busse & Sandham (2012), and do not exploit the full potential of the anisotropy for drag reduction.

Abderrahaman-Elena & García-Mayoral (2017) derived analytical expressions for the streamwise and spanwise slip lengths caused by a permeable substrate. The authors calculated ℓ_x^+ and ℓ_z^+ by solving the flow within the permeable medium in response to an overlying shear, obtaining a solution of the form of Robin conditions (1.6) for the tangential velocities, a procedure that has also been followed for riblets or superhydrophobic textures (Luchini *et al.*, 1991; Ybert *et al.*, 2007). Abderrahaman-Elena & García-Mayoral (2017) solved Brinkman's equation (2.1) for u and w under homogeneous shear, for which the pressure terms zero out. This is actually the solution for mode zero in appendix A, i.e. $\alpha_x = 0$ and $\alpha_z = 0$. Obtaining the relationships between the velocities and their corresponding shears at the interface, ℓ_x^+ and ℓ_z^+ are

$$\ell_x^+ = \xi\sqrt{K_x^+}\tanh\left(\frac{h^+}{\sqrt{K_x^+}}\right), \tag{6.2a}$$

$$\ell_z^+ = \xi\sqrt{K_z^+}\tanh\left(\frac{h^+}{\sqrt{K_z^+}}\right), \tag{6.2b}$$

where $\xi = \sqrt{\nu/\tilde{\nu}}$ is the ratio between the molecular and effective viscosities of the permeable substrate, and would be $\xi \approx 1$ for highly-connected substrates with $\tilde{\nu} \approx \nu$. Note that ℓ_x^+ and ℓ_z^+ in equation (6.2) are the coefficients $\mathcal{C}_{uu}^+$ and $\mathcal{C}_{ww}^+$ for mode $(\alpha_x = 0, \alpha_z = 0)$ in equation (2.3) with $\xi = 1$.

The expression for ΔU^+ for permeable substrates can be obtained by introducing the slip lengths given by equation (6.2) into equation (6.1). In order to obtain drag reduction, we focus on substrates where $K_x^+ > K_z^+$, so that $\Delta U^+ > 0$. Depending on the relative depth of the substrate with respect to $\sqrt{K_x^+}$ and $\sqrt{K_z^+}$, Abderrahaman-Elena & García-Mayoral (2017) distinguished three different regimes. For small substrate thicknesses, $h^+ < \sqrt{K_x^+}, \sqrt{K_z^+}$, both slip lengths approximate to the same value, $\ell_x^+ \approx \ell_z^+ \approx \xi h^+$, yielding no drag reduction. For intermediate thicknesses, where $\sqrt{K_z^+} < h^+ < \sqrt{K_x^+}$, we would have $\ell_x^+ \approx \xi h^+$ and $\ell_z^+ \approx \xi\sqrt{K_z^+}$, resulting in a positive drag reduction. The highest performance for a given anisotropic substrate, however, would be achieved for sufficiently deep substrates, where $h^+ \gtrsim \sqrt{K_x^+}, \sqrt{K_z^+}$ (Abderrahaman-Elena & García-Mayoral, 2017). In this case, both hyperbolic tangents in equation (6.2) tend to unity and the slip lengths become $\ell_x^+ \approx \xi\sqrt{K_x^+}$ and $\ell_z^+ \approx \xi\sqrt{K_z^+}$. In the following two chapters, we focus primarily on the latter case and consider deep substrates. This implies that the flow near the substrate-channel interface does not perceive the bottom no-slipping wall, which eliminates the substrate thickness, h^+, from the parameter space under consideration. Nevertheless, in the next chapter we will also explore substrates with intermediate thickness, i.e. $\sqrt{K_z^+} < h^+ < \sqrt{K_x^+}$, to investigate whether shallower substrates can mitigate the drag-degrading effects observed.

Introducing the slip lengths for sufficiently deep substrates, $\ell_x^+ \approx \xi\sqrt{K_x^+}$ and $\ell_z^+ \approx \xi\sqrt{K_z^+}$, into equation (6.1), ΔU^+ becomes

$$\Delta U^+ \approx \xi \left(\sqrt{K_x^+} - \sqrt{K_z^+} \right). \tag{6.3}$$

The microstructure of the substrate, represented by ξ, has therefore an important effect on the drag-reducing performance. The optimum configuration, which would yield maximum drag reduction, would be obtained for highly-connected materials with $\xi \approx 1$ (i.e. $\tilde{\nu} \approx \nu$), which supports our previous assumption in chapter 2, yielding

$$\Delta U^+ \approx \sqrt{K_x^+} - \sqrt{K_z^+}. \tag{6.4}$$

To maximise drag reduction, we seek highly anisotropic materials, maximising the streamwise permeability, K_x^+, while minimising the spanwise one, K_z^+.

The linear theory that results in equation (6.4) is valid only if the texture lengthscales are small compared to the characteristic lengthscales of near-wall turbulence, so that the near-wall cycle is not altered. For a given permeable material (i.e. with fixed permeability values K_x, K_z and K_y), the permeabilities K_x^+ and K_z^+ in viscous units would increase as

the friction Reynolds number increases, thereby increasing ΔU^+. As K_x^+ and K_z^+ increase, equation (6.4) would eventually stop holding, as other mechanisms set in, degrading the drag-reducing performance.

6.2 Onset of Kelvin-Helmholtz rollers

Equation (6.4) does not explicitly include the wall-normal permeability, or any transpiration in general. However, most complex surfaces that produce slip produce also a non-zero wall-normal velocity at the reference plane, such as permeable substrates (Breugem & Boersma, 2005), riblets (García-Mayoral & Jiménez, 2011) or superhydrophobic surfaces (Seo *et al.*, 2018), and this effect induces generally a degradation in drag. As discussed in the previous chapters, the Kelvin-Helmholtz instability and the drag-increasing rollers associated with it are excited when the impermeability condition at the interface is relaxed. We could then expect the onset of this instability to disrupt the linear regime of equation (6.4) and it could therefore be used to establish an *a priori* limit for the range of validity of the equation, as proposed by Abderrahaman-Elena & García-Mayoral (2017).

Originally, Abderrahaman-Elena & García-Mayoral (2017) developed a model based on Darcy's equation to characterise the onset of Kelvin-Helmholtz rollers, which is well-suited for poorly-connected permeable substrates. In chapter 5, we extended their analysis for highly-connected substrates, which have a greater potential for drag reduction, and showed that the latter exhibit a different behaviour for the onset of the instability. For streamwise-preferential, highly-connected substrates, which according to the linear theory (6.4) are the most suitable for drag reduction, we proposed a single, empirically-fitted parameter, given by equation (5.20a), to capture the effect of the substrate topology on the amplification of the instability. For reference, we rewrite the expression below,

$$K_{Br}^+ = K_y^+ \tanh\left(\frac{\sqrt{2K_x^+}}{y_c^+}\right)\tanh^2\left(\frac{h^+}{3.5\sqrt{K_y^+}}\right). \tag{6.5}$$

Figure 5.18 showed how the amplification for different substrates is a function of this parameter, and it is shown again in figure 6.1 using the equivalent lengthscale, $\sqrt{K_{Br}^+}$. Hereafter, this representation in terms of permeability lengthscales is used for consistency with virtual origins. From an application point of view, we are interested in sufficiently deep and streamwise-preferential substrates, $h^+ \gtrsim \sqrt{K_x^+} \gg \sqrt{K_y^+}$. If this is the case, the second hyperbolic tangent in equation (6.5), $\tanh(h^+/(3.5\sqrt{K_y^+}))$, is approximately 1. For $\sqrt{K_x^+} \gtrsim 5$, the first hyperbolic tangent, $\tanh(\sqrt{2K_x^+}/y_c^+)$, is also approximately 1, and K_{Br}^+ becomes

$$K_{Br}^+ \approx K_y^+. \tag{6.6}$$

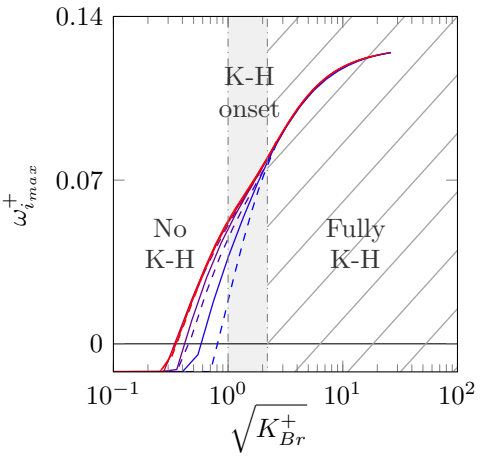

FIGURE 6.1 Maximum amplification, $\omega^+_{i_{max}}$, versus the permeability lengthscale $\sqrt{K^+_{Br}}$ for different permeable substrates. – – –, $h^+ = 10$; ——, $h^+ = 100$; from blue to red, anisotropy ratios $\phi_{xy} = \sqrt{K_x/K_y} \approx 1$, 3, 10, 30. The shaded region corresponds to the estimated range for the onset of Kelvin-Helmholtz rollers (K-H), with the dashed-dotted lines corresponding to $\sqrt{K^+_{Br}} \approx 1$ and 2.2.

Hence, as mentioned in chapter 5, the amplification of the instability is mainly determined by K^+_y, and h^+ and K^+_x have only a secondary effect.

Depending on the value of K^+_{Br}, in chapter 5 we defined three regimes for the instability: a low-permeability regime, where the instability would be weak and not expected to emerge in the flow; a high-permeability regime, where the amplification approaches an asymptote and the instability would be fully developed; and an intermediate regime, where the instability would set in. García-Mayoral & Jiménez (2011) found that, for riblets, the instability sets in for amplifications of approximately half the maximum. Following this, we hypothesise that the intermediate regime would occur for $\sqrt{K^+_y} \approx \sqrt{K^+_{Br}} = 1 - 2.2$, as indicated in figure 6.1, and the linear drag reduction of equation (6.4) could only hold for lower values of $\sqrt{K^+_y}$. This hypothesis will be re-assessed based on the present DNS results in chapter 7.

6.3 Theoretical prediction of drag reduction curves

Combining the information on the linear drag reduction law of equation (6.4) and the range of $\sqrt{K^+_y}$ for the onset of Kelvin-Helmholtz rollers, the trend of the drag reduction curves for anisotropic permeable substrates can be estimated (Abderrahaman-Elena & García-Mayoral, 2017; Gómez-de-Segura *et al.*, 2018*b*). An optimal substrate should seek to maximise the difference $\sqrt{K^+_x} - \sqrt{K^+_z}$ to obtain a large slip effect, while maintaining $\sqrt{K^+_y}$ as low as possible to inhibit the appearance of Kelvin-Helmholtz rollers. Fibrous substrates, as those proposed in figure 1.10(*a*), for instance, would conform such a material.

In this study, a substrate configuration will be represented by three dimensionless parameters; the anisotropy ratios $\phi_{xy} = \sqrt{K_x/K_y}$ and $\phi_{zy} = \sqrt{K_z/K_y}$, and the dimensionless

thickness, $h/\sqrt{K_y}$. Given that both K_y^+ and K_z^+ have an adverse effect on the drag, in what follows we consider materials with preferential permeability in x and equally low permeabilities in y and z, $K_x^+ > K_z^+ = K_y^+$. This implies $\phi_{xy} > 1$ and $\phi_{zy} = 1$. In addition, we consider deep substrates with large $h/\sqrt{K_y}$, so that the substrate thickness does not affect the overlying flow. In chapter 7, we study substrates with $\sqrt{K_x^+} \lesssim 10$, so a thickness $h^+ \gtrsim 50$ would suffice. In practical aeronautic applications, for instance, this would imply permeable layers with sub-millimetre thickness.

For substrates with $\phi_{zy} = 1$, the expression for ΔU^+ in equation (6.4) becomes

$$\Delta U^+ = (\phi_{xy} - 1)\sqrt{K_y^+}. \tag{6.7}$$

The drag reduction for a given substrate configuration (i.e. for a fixed ϕ_{xy}) can then be expressed solely as a function of the wall-normal permeability lengthscale, $\sqrt{K_y^+}$, as sketched in figure 6.2(a), which can be interpreted as a substrate Reynolds number. For instance, in a wind-tunnel experiment $\sqrt{K_y^+}$ could be changed by changing the friction velocity, while ϕ_{xy} remained unaltered for a given substrate.

From the present analysis, the resulting drag reduction curves would be analogous to those for riblets (Bechert *et al.*, 1997; García-Mayoral & Jiménez, 2011). The curves would exhibit a linear increase of ΔU^+ with $\sqrt{K_y^+}$, breaking down no later than in the shaded region in the figure, where the onset of the Kelvin-Helmholtz instability would be expected. According to equation (6.7), the slope in the linear regime is predicted to depend on ϕ_{xy}, and the maximum ΔU^+ for a given ϕ_{xy} would be determined by the intercept of the corresponding curve with the shaded region. The exact value of $\sqrt{K_y^+}$ for the breakdown, as well as the form of the curves in its proximity and for larger values, will be obtained from the DNSs presented in the next chapter.

The ideas illustrated in figure 6.2(a) for a few substrate configurations can be summarised for a wide range of anisotropy ratios. This is done in figure 6.2(b). Following a drag reduction curve as $\sqrt{K_y^+}$ increases in panel (a) would be equivalent to ascending vertically along a constant-ϕ_{xy} line in panel (b). The linear drag-reducing behaviour of equation (6.7) is expected to begin to fail in the shaded region. This shaded region represents the permeability values for which the drag-degrading Kelvin-Helmholtz rollers are expected to appear and is the same as in panel (a). It is determined by introducing the limiting values of $\sqrt{K_y^+}$ specified in section 6.2, $\sqrt{K_y^+}|_{lim} \approx 1 - 2.2$, into equation (6.7). Although additional adverse phenomena cannot be ruled out, figure 6.2(b) allows us to bound the parameter space for realisable drag reduction. This figure was used to select the region in the parametric space subsequently investigated in chapter 7. Most cases considered are in the drag-reducing region, where equation (6.7) is expected to hold, and a few cases have been selected in the shaded region to capture the breakdown. We have considered three substrate configurations, $\phi_{xy} \approx 3.6$, 5.5 and 11.4, represented by the three vertical lines of symbols in figure 6.2(b),

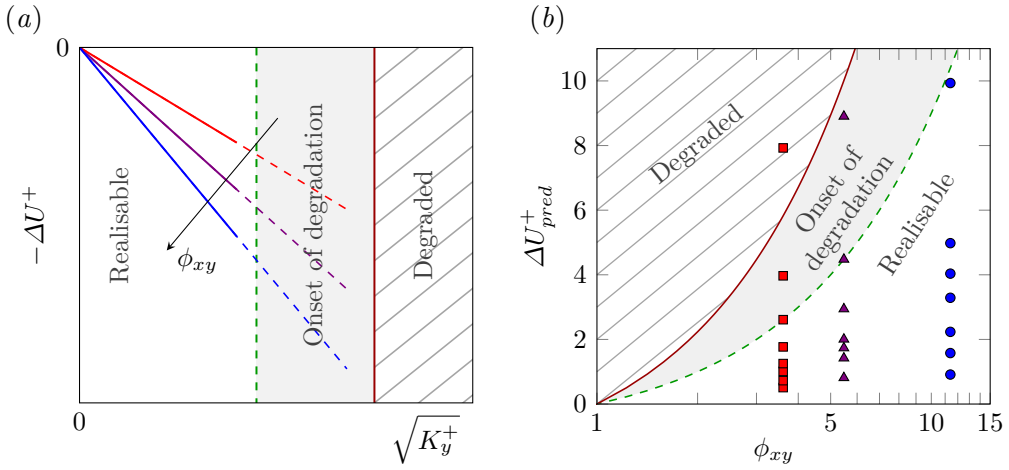

FIGURE 6.2 (*a*) Sketch of the predicted ΔU^+ as a function of $\sqrt{K_y^+}$. Each line corresponds to a substrate with a different anisotropy ratio, $\phi_{xy} = \sqrt{K_x^+/K_y^+}$, and follows the behaviour of the linear expression (6.7). The shaded region corresponds to the permeability values for which the Kelvin-Helmholtz rollers would be expected to develop, as in figure 6.1. (*b*) Predicted values of ΔU^+ using the linear expression (6.7) as a function of the anisotropy ratio ϕ_{xy}. In both panels, the dashed-green and solid-red lines define the limits for the onset of Kelvin-Helmholtz rollers estimated at $\sqrt{K_{Br}^+}|_{lim} \approx \sqrt{K_y^+} \approx 1$ and 2.2, and they separate three regions: the empty-coloured one, where no Kelvin-Helmholtz instability would be expected; the shaded one, where the instability would set in; and the hatched one, where the instability would be fully developed. Symbols represent the DNS cases studied in the next chapter for three substrates with different anisotropies, from red to blue $\phi_{xy} \approx 3.6$, 5.5 and 11.

and simulated them at different substrate Reynolds numbers, $\sqrt{K_y^+}$, so that complete drag reduction curves could be obtained.

6.4 Change in drag in internal vs. external flows

The expressions for ΔU^+ of equations (3.7) and (6.4) are valid only for external flows with mild or zero pressure gradients, where the flow near the wall is essentially driven by the overlying shear and the effect of the mean pressure gradient within the permeable substrate is negligible. We are mainly interested in vehicular applications, where the flow falls into that category, but for completion let us discuss the differences with internal flows. In the latter, the effect of the mean pressure gradient could be significant. This effect is essentially additive, so in the following discussion we will leave out turbulence for simplicity, and consider the laminar case.

Sketches of the mean velocity profiles in a boundary layer and in a channel are depicted in figures 6.3(*a*) and 6.3(*b*), respectively. In a boundary layer over a permeable substrate, there would be a slip velocity at the interface, U_{Br}, due solely to the formation of a Brinkman layer within the substrate. It follows from equation (6.2a) that, provided that the substrate is sufficiently deep, this slip velocity is $U_{Br}^+ \approx \sqrt{K_x^+}$. Compared with a smooth wall, the only

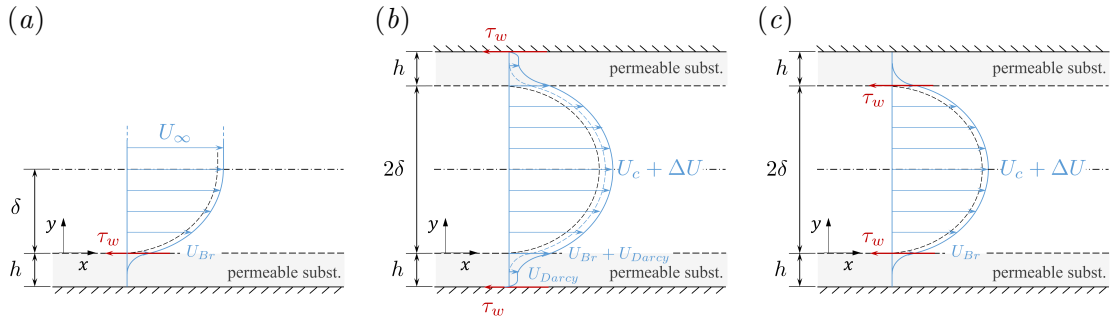

FIGURE 6.3 Mean velocity in internal and external flows. The black-dashed line represents the mean velocity profiles for smooth walls. (a) Boundary layer. (b) Channel flow, where the mean pressure gradient is applied through the whole section of height $2(\delta + h)$, including the permeable substrates. (c) Artificial internal setup to produce only slip that appears in an external flow, by not applying the mean pressure gradient in the substrate regions.

change in the mean velocity profile would be a shift by U_{Br}, that is $\Delta U^+ \approx \sqrt{K_x^+}$, and the drag reduction experienced would arise entirely from this slip effect.

In channel flows, there are two limiting forms of applying the permeable substrates to the reference smooth channel of height 2δ. They can substitute a layer of solid material, increasing the height to $2(\delta + h)$, or they can be placed on top of the reference smooth channel, reducing the free flow area. In the first case, depicted in figure 6.3(b), the mean pressure gradient acts on the region $2(\delta + h)$, which includes the permeable substrates. This produces two opposite effects on the drag: a positive effect due to an increment in the flow rate, not only within the substrate but also in the channel core, and a negative effect due to the pressure gradient being applied across a larger cross-section. In order to evaluate these two effects, we compare the friction coefficient for the permeable and the smooth channel under equal mean pressure gradient P_x. The integral force balance yields

$$\tau_w = -P_x\,(\delta + h)\,, \tag{6.8}$$

where τ_w accounts for the net force applied on the substrates. As we are now solely considering internal flows, we use the conventional bulk velocity, U_b, to define c_f,

$$c_f = 2\frac{\tau_w}{U_b^2} = 2\frac{\tau_w}{(U_{b0} + \Delta U_b)^2} = c_{f0}\frac{1 + h/\delta}{(1 + \Delta U_b/U_{b0})^2} = c_{f0}\frac{(1 + h/\delta)^3}{(1 + \Delta q/q_0)^2}, \tag{6.9}$$

where the subscript '0' refers to the smooth channel. The friction coefficient of the smooth channel, c_{f0}, is defined as $c_{f0} = -2P_x\delta/U_{b0}$, and $q = 2(\delta + h)U_b$ is the mass flow rate. The opposing effects of the increase in cross-section where the pressure gradient acts, $2h$, and the extra flow rate, Δq, are evidenced in equation (6.9). The result can be either a drag reduction or a drag increase depending on the values of Δq and h.

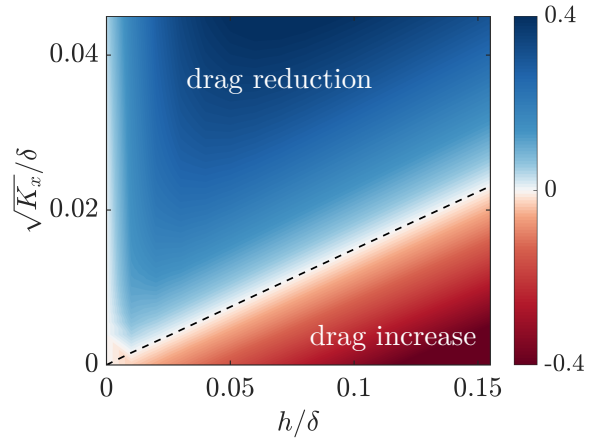

FIGURE 6.4 Map of $DR = -\Delta c_f/c_{f0}$ in an internal channel flow with permeable substrates as a function of the permeability length, $\sqrt{K_x}$, and the thickness of the substrate, h, for a friction Reynolds number $\delta^+ = 180$. The channel with substrates has a total height of $2(h+\delta)$, and is compared to a smooth channel of height 2δ, as in figure 6.3(b). – – –, the first order approximation of zero drag reduction line, with a slope of 0.15 obtained from equation (6.11) (valid for $h/\delta > 0.01$).

The extra flow rate, Δq, can be expressed in terms of K_x. From figure 6.3(b), Δq is

$$\Delta q \approx 2\delta\,(U_{Br} + U_{Darcy}) + 2q_{substrate}, \tag{6.10}$$

where, in addition to the slip velocity caused by the overlying shear, U_{Br}, as in figure 6.3(a), there is an extra slip velocity caused by the mean pressure gradient, U_{Darcy}, and a resulting extra flow rate within the substrate, $q_{substrate}$. The former is obtained from Darcy's law, $U_{Darcy} = -P_x K_x/\nu$, and $q_{substrate}$ is obtained using U_{Darcy} and Brinkman's velocity within the substrate, as defined by expression (A.31a). Substituting expression (6.10) into equation (6.9), the resulting change in c_f depends on $\sqrt{K_x}/\delta$, h/δ and the Reynolds number. This dependency for a friction Reynolds number $\delta^+ = 180$ is illustrated in figure 6.4. The figure shows how the beneficial effect of adding a streamwise permeability is opposite to the deleterious effect of the increased area and, for certain substrate geometries, can even outweigh it, resulting in a net drag reduction. Note that in the turbulent case the effect of the spanwise, Brinkman contribution would also need to be included, as given by equation (6.4).

To better understand the relationship between K_x and h, expression (6.9) can be simplified further for $\delta \gg h \gtrsim \sqrt{K_x}$. The extra flow rate is then dominated by $\Delta q \approx 2\delta U_{Br} \approx 2\delta\sqrt{K_x}\,dU/dy|_{y=0}$, and in a first order approximation, equation (6.9) simplifies to

$$c_f \approx c_{f0}\frac{1+3h/\delta}{1+\dfrac{2\sqrt{K_x}}{U_{b0}}\left.\dfrac{dU}{dy}\right|_{y=0}}. \tag{6.11}$$

It follows from this equation that, in $(h, \sqrt{K_x})$ parameter space, the isocontours of DR are approximately oblique straight lines, as observed in figure 6.4. Specifically the neutral drag curve is $\sqrt{K_x} = 3/2\ U_{b0}/(dU/dy|_{y=0})\ h$, which depends on the friction Reynolds number through U_{b0} and $dU/dy|_{y=0}$. For $\delta^+ = 180$, the zero drag reduction line is given by $\sqrt{K_x} \approx 0.15h$, as indicated in figure 6.4, while for $\delta^+ = 5000$, $\sqrt{K_x} \approx 0.007h$.

The above analysis applies to channel flows where the permeable substrates substitute a layer of solid material and shows that, in this case, the drag can be either reduced or increased. If, on the other hand, the permeable coating was added on top of an existing smooth channel, the pressure gradient would still be applied over the whole height of 2δ, which now includes the permeable coatings, and the resulting friction coefficient would be $c_f = c_{f0}/(1 + \Delta q/q_0)^2$. In this case, the flow rate would always decrease, $\Delta q < 0$, resulting in an increase of drag independently of the values of $\sqrt{K_x}$ and h.

In the next chapter, simulations are performed in channel flows for convenience, but with a view to external flows. To allow a quantitative comparison with external flows, the mean pressure gradient is applied only in the channel region, omitting its effect within the substrate, as sketched in figure 6.3(c).

Chapter 7

Drag reduction by anisotropic permeable substrates: DNS*

In this chapter, we present results from DNSs to investigate in detail the effect that permeable substrates have on the overlying flow and assess the validity of the predictions presented in the previous chapter. We will show that the results confirm the theoretical predictions, and the resulting drag curves are similar to those introduced in figure 1.2. For small permeabilities, the drag reduction is proportional to the difference $\sqrt{K_x^+} - \sqrt{K_z^+}$. This linear regime breaks down for a critical value of the wall-normal permeability, beyond which the performance begins to degrade. We observe that the degradation in performance is, as initially hypothesised, caused by the appearance of spanwise-coherent structures, attributed to a Kelvin-Helmholtz-like instability of the mean flow. For large permeabilities, these structures become prevalent in the flow, outweighing the drag-reducing effect of the slip and eventually leading to an increase of drag.

7.1 Simulations of permeable substrates

The numerical set-up for the DNSs of the domain sketched in figure 6.3(c), was detailed in chapter 2 and, as in the previous chapters, the presence of the substrates is taken into account through the boundary conditions defined by equation (2.3). All simulations are, as mentioned, conducted at a fixed friction Reynolds number $\delta^+ = u_\tau \delta/\nu = 180$ by imposing a constant mean pressure gradient in $y \in [0, 2\delta]$ and we use a smooth-wall channel with the same mean pressure gradient as reference. Although for convenience the present DNSs are conducted in channels, our scope of application is mainly external flows with mild pressure gradients. In a channel, by comparison, there would be an additional flow rate from Darcy's contribution discussed in section 6.4. To allow direct extrapolation to external flows, we

*Parts of the content of this chapter have been published in *Journal of Fluid Mechanics*, 875, 124 – 172, with Ricardo García-Mayoral as co-author.

	Cases	$\sqrt{K_x^+}$	$\sqrt{K_y^+}$	$\sqrt{K_z^+}$	h^+	$U_b/U_{b_{sm}}$	ΔU^+	DR_{180}	DR_{5000}
Smooth		0	0	0	0	1.0	-	-	-
$\phi_{xy} = \sqrt{\frac{K_x}{K_y}} \approx 3.6$	A1	0.71	0.20	0.20	19.5	1.037	0.51	5.64	3.93
	A2	1.00	0.28	0.28	28.1	1.045	0.68	7.26	5.08
	A3	1.42	0.39	0.39	38.8	1.052	0.80	8.44	5.92
	A4	1.74	0.48	0.48	48.1	1.041	0.54	6.10	4.25
	A5	2.45	0.68	0.68	68.1	0.963	-0.68	-7.38	-4.99
	A6	3.61	1.00	1.00	100.2	0.819	-3.02	-42.31	-26.58
	A7	5.50	1.52	1.52	152.7	0.616	-6.59	-143.84	-76.46
	A8	10.97	3.04	3.04	304.2	0.381	-11.03	-546.15	-194.20
$\phi_{xy} = \sqrt{\frac{K_x}{K_y}} \approx 5.5$	B1	1.00	0.18	0.18	18.0	1.053	0.84	8.63	6.06
	B2	1.79	0.32	0.32	32.1	1.085	1.29	12.71	9.01
	B3	2.12	0.39	0.39	39.0	1.086	1.31	12.93	9.17
	B4	2.45	0.45	0.45	45.0	1.070	1.01	10.22	7.20
	B5	3.61	0.66	0.66	65.7	0.979	-0.46	-5.24	-3.56
	B6	5.48	1.00	1.00	100.0	0.792	-3.66	-56.35	-34.47
	B7	10.89	1.99	1.99	198.4	0.517	-8.66	-261.34	-120.00
$\phi_{xy} = \sqrt{\frac{K_x}{K_y}} \approx 11.4$	C1	1.00	0.09	0.09	9.0	1.062	0.98	9.89	6.96
	C2	1.73	0.15	0.15	14.0	1.106	1.67	16.01	11.45
	C3	2.45	0.21	0.21	22.0	1.145	2.24	20.63	14.93
	C4	3.6	0.32	0.32	32.0	1.178	2.84	25.10	18.38
	C5	4.48	0.39	0.39	39.1	1.183	2.87	25.34	18.56
	C6	5.47	0.48	0.48	47.9	1.152	2.34	21.38	15.50
	C7	10.89	0.96	0.96	95.6	0.898	-2.21	-29.35	-18.92
$\frac{h}{\sqrt{K_x}} = 1.5$	C′1	2.45	0.21	0.21	3.67	1.130	2.00	18.74	13.49
	C′2	3.61	0.32	0.32	5.40	1.171	2.70	24.12	17.62
	C′3	5.49	0.48	0.48	8.23	1.156	2.40	21.87	15.88
	C′4	10.84	0.95	0.95	16.26	0.962	-0.90	-10.84	-7.27
$\frac{h}{\sqrt{K_x}} = 1.0$	C″1	3.61	0.32	0.32	3.61	1.154	2.42	22.02	15.99
	C″2	5.48	0.48	0.48	5.51	1.163	2.53	22.86	16.64
	C″3	7.01	0.62	0.62	7.01	1.127	1.90	17.93	12.88
	C″4	9.03	0.79	0.79	9.03	1.066	0.84	8.62	6.05
	C″5	10.85	0.95	0.95	11.03	1.001	-0.12	-1.32	-0.91
$\frac{h}{\sqrt{K_x}} = 0.5$	C‴1	2.45	0.21	0.21	1.22	1.063	0.93	9.46	6.65
	C‴2	3.62	0.32	0.32	1.86	1.091	1.36	13.35	9.48
	C‴3	5.47	0.48	0.48	2.74	1.133	2.04	19.11	13.77
	C‴4	7.01	0.62	0.62	3.50	1.153	2.39	21.81	15.83
	C‴5	9.03	0.79	0.79	4.52	1.129	1.95	18.34	13.19
	C‴6	10.83	0.95	0.95	5.42	1.092	1.30	12.88	9.13

TABLE 7.1 DNS parameters. $\sqrt{K_x^+}$, $\sqrt{K_y^+}$ and $\sqrt{K_z^+}$ are the streamwise, wall-normal and spanwise permeability lengths, h^+ is the thickness of the substrate, ΔU^+ is the shift of the velocity profile in the logarithmic region, and DR_{180} and DR_{5000} are the values of drag reduction for $\delta^+ = 180$ and $\delta^+ = 5000$, respectively, obtained using expression (1.3). The values DR_{5000} have been calculated using the smooth-channel centreline velocity from Lee & Moser (2015). Substrate configurations A, B and C have thickness $h = 100\sqrt{K_y}$ and different anisotropy ratios ϕ_{xy}. Substrate configurations C′, C″ and C‴, have $\phi_{xy} \approx 11.4$, same as substrate C, but different thickness $h/\sqrt{K_x}$.

simply do not include this contribution when implementing the boundary conditions on the mean flow, that is, mode $(0,0)$, which would be the only Fourier mode affected. This numerical artefact would be equivalent to applying the mean pressure gradient in the channel region only, as depicted in figure 6.3(c). The drag reduction in the present simulations results then entirely from the slip velocity due to an overlying shear, as in external flows.

As indicated in figure 6.2(b), we study three substrate configurations, given by three different anisotropy ratios $\phi_{xy} \approx 3.6$, 5.5 and 11.4. For our main set of simulations, the substrates have thickness $h = 100\sqrt{K_y}$, large enough for the problem to become independent of h, and the same permeabilities in y and z, $\phi_{zy} = 1$. An additional subset of simulations has been also conducted to explore the effect of a finite h on the substrate performance. For a given configuration (i.e. a fixed ϕ_{xy} and $h/\sqrt{K_y}$), we vary proportionately the permeabilities in viscous units, K_x^+, K_z^+ and K_y^+, which is equivalent to varying the viscous length. For each configuration, $\sqrt{K_x^+}$ varies between $0.7 - 11$. The simulations under study are summarised in table 7.1, where each case is labelled with a letter and a number. In the main set of simulations, the letter refers to the anisotropy ratio ϕ_{xy} of the substrate and the number to the specific substrate, with fixed permeabilities in viscous units. In the secondary set, additional subscripts $'$, $''$ and $'''$ indicate decreasing substrate depth.

The virtual-origin model presented in sections 1.3 and 3.5 is based on the idea that the near-wall cycle remains smooth-wall-like, other than by being displaced a depth ℓ_T towards the substrate. Given that the origin perceived by turbulence is at $y = -\ell_T \approx -\sqrt{K_z}$, we set that plane as the reference for the wall-normal height and scale the results with the values at that height. The friction velocity is obtained by extrapolating the total stresses to that height, $u_\tau = u_{\tau_{y=0}} \left(1 + \sqrt{K_z}/\delta\right)^{1/2}$, and the effective half-channel height becomes $\delta' = \delta + \sqrt{K_z}$ (García-Mayoral *et al.*, 2019), although the effect is negligible for the small values of $\sqrt{K_z}/\delta$ considered here. Beyond the breakdown of the linear regime, the virtual-origin model begins to fail and the effect of the substrates can no longer be solely ascribed to a shift in origins. Nonetheless, as in chapter 4, for the cases lying in the degraded regime, we still use the virtual origin that would be valid in the linear regime, $y = -\sqrt{K_z}$, to measure u_τ. In this framework, any further effect can be interpreted as additive. The values of ΔU^+ have been obtained using this u_τ and comparing the velocity profiles with smooth-wall profiles with the origin shifted to $y = -\sqrt{K_z}$, although the effect of this shift on ΔU^+ is also negligible.

7.2 Drag reduction curves

The drag reduction curves obtained from the main set of DNSs are shown in figure 7.1. For small permeabilities, a linear drag-reduction regime is observed. In section 6.1, we predicted ΔU^+ in this regime to be equal to the difference between the virtual origin perceived by the mean flow, ℓ_U^+, and that perceived by turbulence, ℓ_T^+. For the substrates under consideration, these would be $\ell_U^+ \approx \sqrt{K_x^+}$ and $\ell_T^+ \approx \sqrt{K_z^+}$, as given by equation (6.4). This prediction

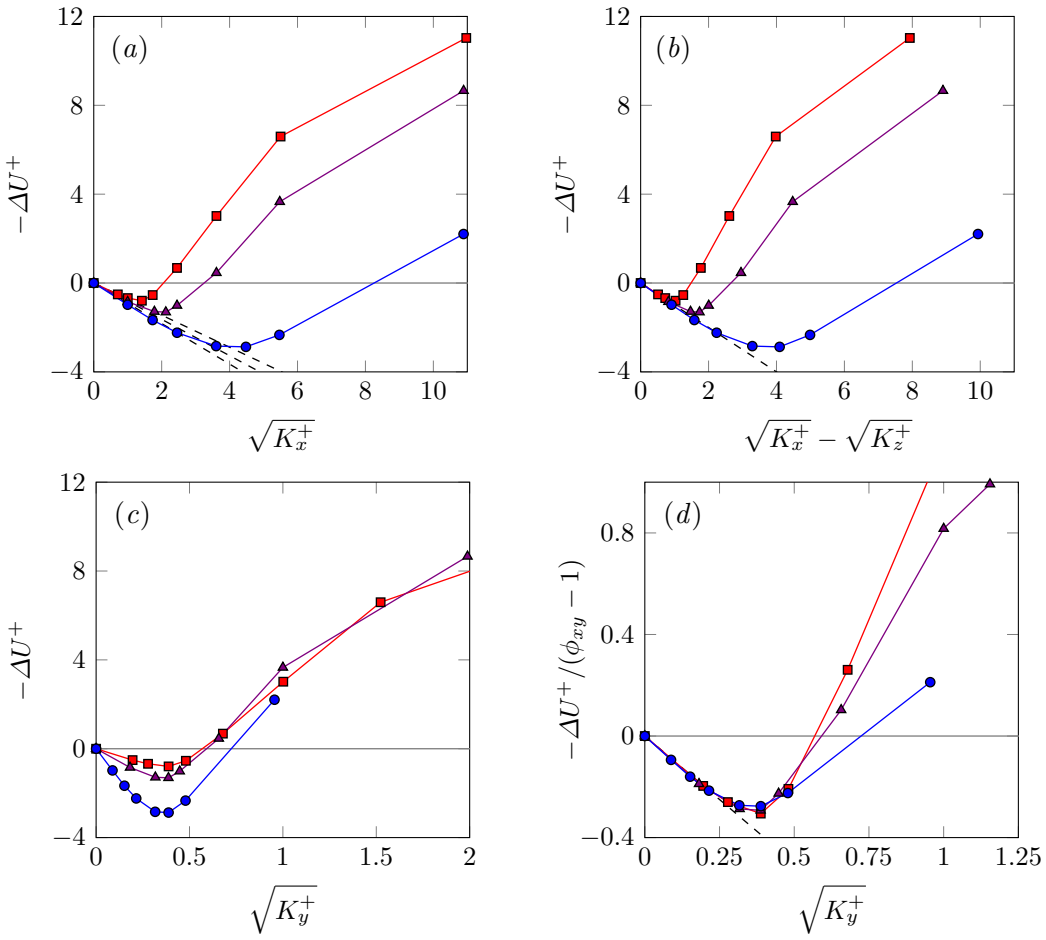

FIGURE 7.1 Drag reduction curves for substrates with different anisotropy ratios. —●—, $\phi_{xy} \approx 11.4$; —▲—, $\phi_{xy} \approx 5.5$; and —■—, $\phi_{xy} \approx 3.6$. The symbols correspond to DNSs listed in table 7.1. ΔU^+ is represented versus (a) the streamwise permeability lengthscale, $\sqrt{K_x^+}$; (b) its predicted value in the linear regime, $\sqrt{K_x^+} - \sqrt{K_z^+}$; ($c$) the wall-normal permeability lengthscale, $\sqrt{K_y^+}$. (d) ΔU^+, reduced with its predicted slope, versus the wall-normal permeability lengthscale, $\sqrt{K_y^+}$. – – –, theoretical prediction $\Delta U^+ = \sqrt{K_x^+} - \sqrt{K_z^+}$.

agrees well with the DNS results, and the three substrate configurations exhibit roughly the same initial unit slope in figure 7.1(b). These curves correspond to those included in figure 4.5. The breakdown of the linear drag reduction, however, occurs for different values of $\sqrt{K_x^+} - \sqrt{K_z^+}$ depending on the substrate.

In contrast, when the lengthscale is represented using $\sqrt{K_y^+}$ – the parameter predicted in section 6.2 to trigger the Kelvin-Helmholtz instability – the location of the breakdown coincides for all the curves, as shown in figure 7.1(c). For all substrate configurations, the drag reduction is maximum for $\sqrt{K_y^+}|_{opt} \approx 0.38$ and the drag becomes greater than for a smooth wall for $\sqrt{K_y^+} \gtrsim 0.6$.

The common linear drag reduction behaviour, observed in figure 7.1(b), and its common breakdown, observed in figure 7.1(c), are condensed in figure 7.1(d). This is done by dividing ΔU^+ from figure 7.1(c) by the slope for each curve expected from equation (6.7), $\phi_{xy} - 1$. Given that in this equation ΔU^+ depends only on ϕ_{xy} and $\sqrt{K_y^+}$, the general collapse suggested by this figure could be used to predict the performance of permeable substrates different to those explored in this work. Considering that the maximum ΔU^+ in figure 7.1(d) occurs for $\sqrt{K_y^+}|_{opt} \approx 0.38$ and is approximately 80% of that estimated by equation (6.7), the maximum ΔU^+ would depend only on the anisotropy ratio,

$$\Delta U^+_{max} \approx 0.8 \times 0.38 \times (\phi_{xy} - 1)\,. \tag{7.1}$$

For substrates with different cross permeabilities, $\phi_{zy} \neq 1$, it follows from equation (6.4) that the maximum ΔU^+ would be $\Delta U^+_{max} \approx 0.8 \times 0.38 \times (\phi_{xy} - \phi_{zy})$, provided that $\sqrt{K_z^+}$ is still a good approximation for the origin of turbulence.

The secondary set of simulations aims to explore the effect of the substrate depth on ΔU^+ and to test if the performance could be improved by reducing the depth enough for it to become a parameter in the problem. For this, the same substrate of cases C1-C7 is studied with depths $h/\sqrt{K_x} = 1.5$, 1.0 and 0.5. From equations (6.2), we can expect shallower substrates to have smaller ℓ_U^+ and ℓ_T^+, as the hyperbolic tangent terms become smaller than unity. This would reduce the slope of the ΔU^+ curve in the linear regime and be an adverse effect. However, a reduced depth would also have the beneficial effect of making the substrate more robust to the onset of Kelvin-Helmholtz-like rollers, as at a given Reynolds number (i.e. $\sqrt{K_x^+}$, $\sqrt{K_y^+}$) equation (6.5) would predict a smaller $\sqrt{K_{Br}^+}$. Note also that $\sqrt{K_{Br}^+}$ is a parameter empirically fitted to the results from the linear stability model, and that the actual results in section 6.2 show that shallower substrates have in fact a delayed onset in terms of $\sqrt{K_{Br}^+}$, as shown in figure 6.1.

The results for ΔU^+ for the shallow substrates of the secondary set of simulations are portrayed in figure 7.2, compared with the corresponding deep substrate from the main set, cases C1-C7. Given that all our substrates have higher permeability in x, the first terms to experience the effect of a finite h in equations (6.2) and (6.5) are those where h appears scaled with $\sqrt{K_x}$. Note that if we had considered values of h small enough for $h/\sqrt{K_z}$ to be also small, we would have $\ell_U^+ \approx \ell_T^+ \approx h^+$, which would yield no drag-reducing effect. For the values of $h/\sqrt{K_x}$ studied, we have $h/\sqrt{K_y} = h/\sqrt{K_z} = 6$, 11 and 17, so the corresponding hyperbolic tangent terms in equations (6.2) and (6.5) are still essentially unity. This can be appreciated for instance in figure 7.2(a), where the predicted slope in the linear regime has been adjusted for the effect of h^+ on the streamwise slip, $\ell_U^+ \approx \sqrt{K_x^+}\tanh(h^+/\sqrt{K_x^+})$, but the spanwise slip remains $\ell_T^+ \approx \sqrt{K_z^+}$. Figure 7.2($b$), however, shows that $\sqrt{K_y^+}$ is no longer adequate to parametrise the onset of the drag degradation. Panel (c), in turn, suggests that a suitable alternative is $\sqrt{K'^+_{Br}} = \sqrt{K_y^+}\tanh(h^+/(9\sqrt{K_y^+}))$,

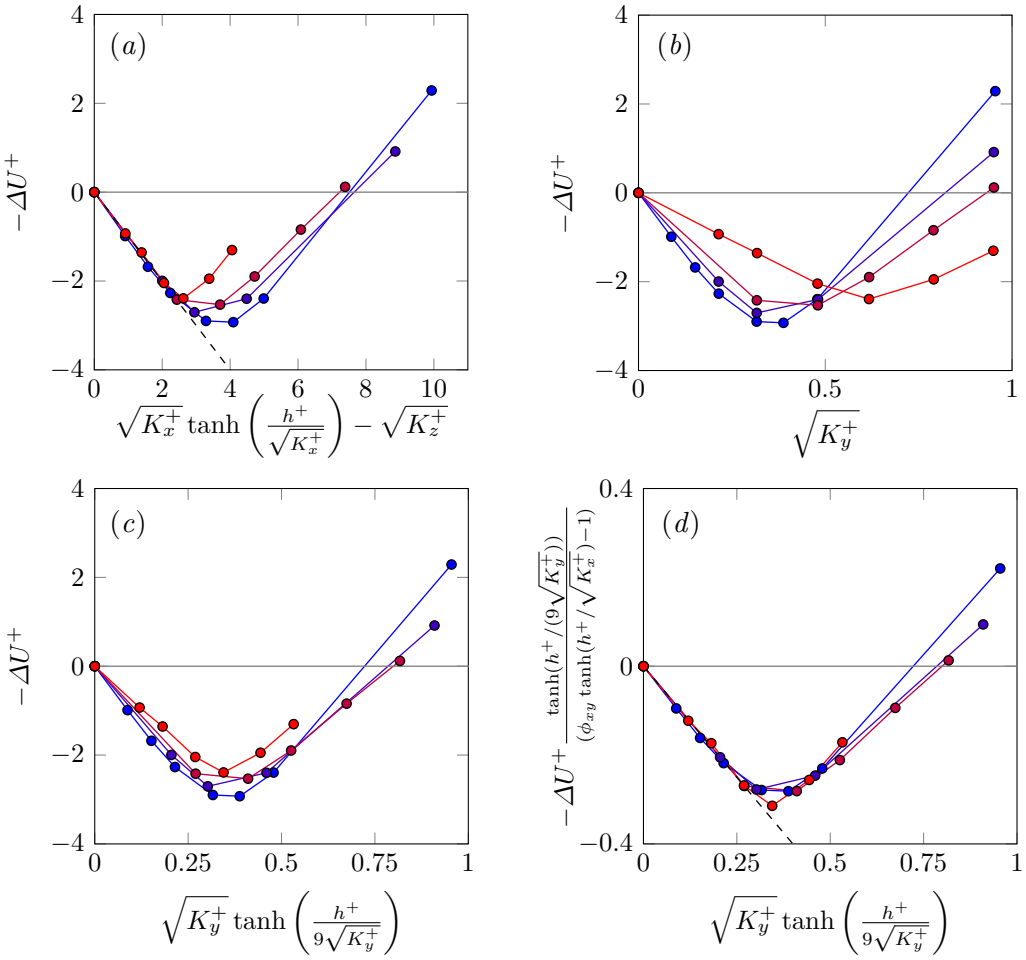

FIGURE 7.2 Drag reduction curves for substrates with the same permeabilities but different substrate thickness. From blue to red, representing decreasing thickness, cases C1-C7, C′1-C′7, C″1-C″7, and C‴1-C‴7, corresponding to $h/\sqrt{K_x} = 8.8$, 1.5, 1.0, and 0.5. ΔU^+ is represented versus (a) its theoretical value in the linear regime; (b) the wall-normal permeability lengthscale, $\sqrt{K_y^+}$; (c) the fitted permeability lengthscale for the breakdown $\sqrt{K'^+_{Br}}$. (d) ΔU^+, reduced with its predicted linear slope, versus $\sqrt{K'^+_{Br}}$. In (a) and (d), – – –, theoretical prediction $\Delta U^+ = \sqrt{K_x^+}\tanh(h^+/\sqrt{K_x^+}) - \sqrt{K_z^+}$.

and that the optimum value is still $\sqrt{K'^+_{Br}} \approx 0.38$, as in figure 7.1. All the curves can be once more collapsed by reducing ΔU^+ with its predicted slope in the linear regime and expressing the Reynolds number in terms of $\sqrt{K'^+_{Br}}$, as is done in panel (d). This suggests that the optimum performance for shallow substrates can also be predicted and would be $\Delta U^+_{max} \approx 0.8 \times 0.38 \times [\phi_{xy}\tanh(h/\sqrt{K_x}) - \phi_{zy}]/\tanh(h/9\sqrt{K_y})$. Note, however, that ΔU^+_{max} decreases slightly as the substrate depth is reduced, as can be appreciated in panel (a), and that even if there is a delay in the critical $\sqrt{K_y^+}$ in absolute terms, as observed in panel (b), any gain in the relative width of the 'drag bucket' region – the near-optimal range – is insignificant, as is clear from panel (d).

7.3 Flow statistics

To explore the underlying mechanisms for the behaviour observed in the drag reduction curves, let us focus on a fixed substrate configuration, that is on one of the curves in figure 7.1. Let us take the one with the anisotropy ratio $\phi_{xy} \approx 11.4$, that is, simulations C1-C7. This configuration has been chosen arbitrarily. The general trend is unchanged for the other two substrate configurations, $\phi_{xy} \approx 3.6$ and 5.5, and, for completeness, the corresponding data can be found in appendix F. To illustrate how the overlying turbulence is modified at different points along the drag reduction curve, figure 7.3 shows instantaneous realisations of u, v and p in an x-z plane immediately above the substrate-channel interface. For small $\sqrt{K_y^+}$, the flow field resembles that observed over a smooth wall. This is shown in panels (a-c) and (d-f), where the u-field displays the signature of near-wall streaks, and the v-field that of quasi-streamwise vortices. As $\sqrt{K_y^+}$ increases beyond the linear regime, the flow begins to be altered, as shown in panels (g-l). Some spanwise coherence emerges, becoming more prevalent for larger $\sqrt{K_y^+}$. Eventually, the flow becomes strongly spanwise-coherent and no trace of the near-wall cycle remains, as shown for a drag-increasing case in panels (m-o).

To assess quantitatively to what extent turbulence differs from that over smooth walls, we first focus on the one-point statistics resulting from the DNSs, portrayed in figures 7.4 and 7.6. The former shows the mean velocity profiles. In panel (a) the results are represented with the origin for the wall-normal height at the substrate-channel interface, $y^+ = 0$, as is typically done in the literature. In this representation, the non-zero slip velocity at the interface, U_{slip}^+, is apparent at $y^+ = 0$, while far away from the wall the adverse effect of ℓ_T^+ and the 'roughness-like' shape of the profile, that is the deviation from a smooth-wall-like shape, combine with U_{slip}^+ to yield the net velocity offset. In this framework, the effect of ℓ_T^+ and the deviation from the shape of a smooth-wall profile cannot be easily disentangled.

If the velocity profiles are represented with the origin for the wall-normal height at $y^+ = -\ell_T^+$ and if turbulence remained smooth-wall-like, the profiles could then be expected to be like those for smooth walls, save for the offset given by equation (3.7). Subtracting that offset would then give a collapse of all the velocity profiles, and any deviation can then be separately attributed to modifications in the turbulence (García-Mayoral *et al.*, 2019). In figure 7.4(b), the profiles are portrayed with the origin at $y^+ = -\ell_T^+$ and with the offset subtracted from the velocities. For cases C1-C3, which lie in the linear regime, the resulting collapse is indeed good, but beyond this regime the profiles deviate from the smooth-wall behaviour increasingly. Let us note that defining u_τ at $y^+ = -\ell_T^+$ implies that the wall-normal gradient of the mean profile at the interface is no longer necessarily $dU^+/dy^+|_{y^+=0} = 1$. This is because the stresses at that height in viscous units sum slightly less than one, and more specifically, because a non-zero transpiration gives rise to a Reynolds stress at the interface, so the viscous stress is no longer the only contribution to the total. As a result, U_{slip}^+ and ℓ_x^+ do not strictly have equal values and cannot be used interchangeably. For small

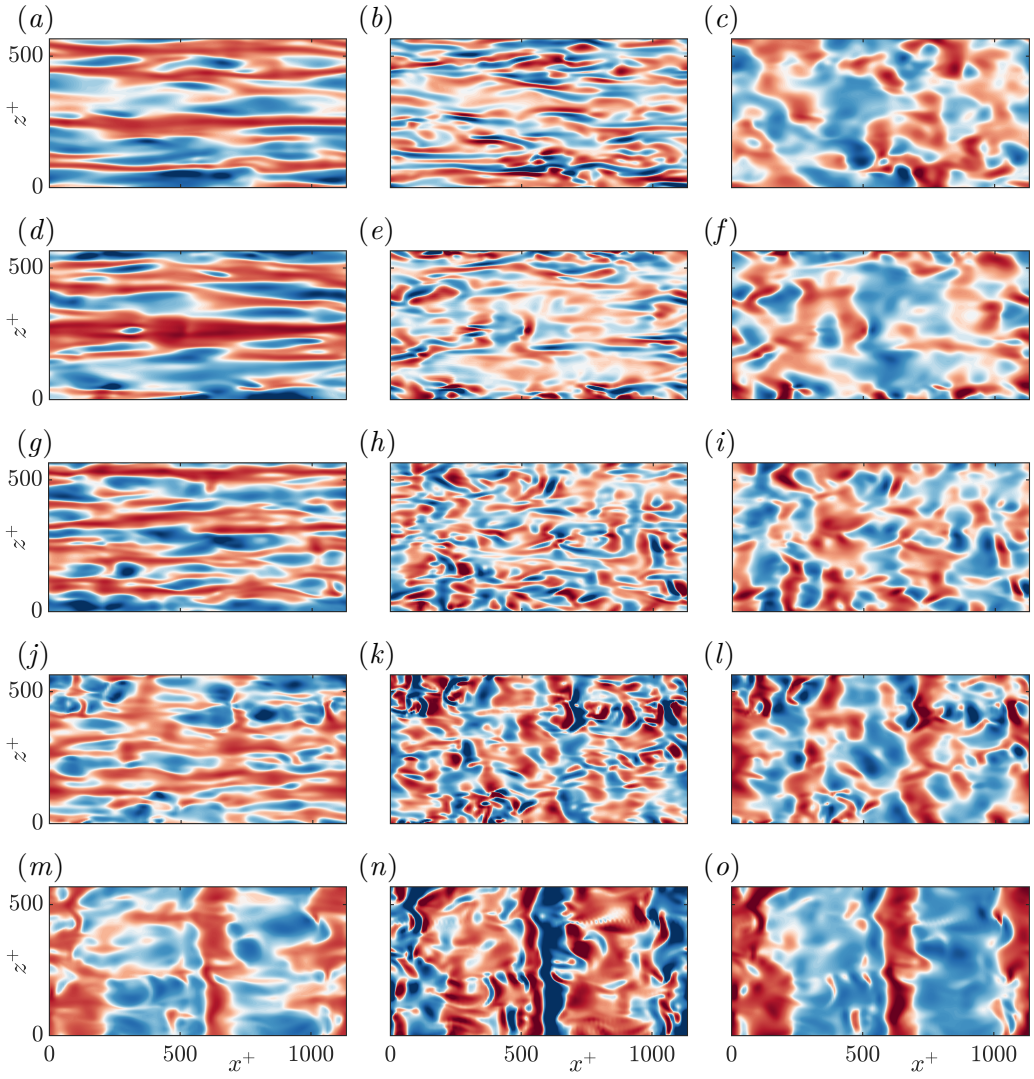

FIGURE 7.3 Instantaneous realisations of u^+, v^+ and p^+ for a smooth channel and for substrates with $\phi_{xy} \approx 11.4$ at a x-z plane $y^+ + \ell_T^+ \approx 2.5$. From left to right the columns are u^+, v^+ and p^+. From top to bottom, representing increasing permeabilities, (a-c) smooth wall, (d-f) case C2, (e-g) case C4, (h-j) case C6 and (m-o) case C7. In all cases, red to blue corresponds to $(2.2 + \sqrt{K_x^+}/2)[-1, 1]$ for u^+, $(0.08 + 2/3\sqrt{K_y^+})[-1, 1]$ for v^+ and $(5 + 5\sqrt[4]{K_y^+})[-1, 1]$ for p^+.

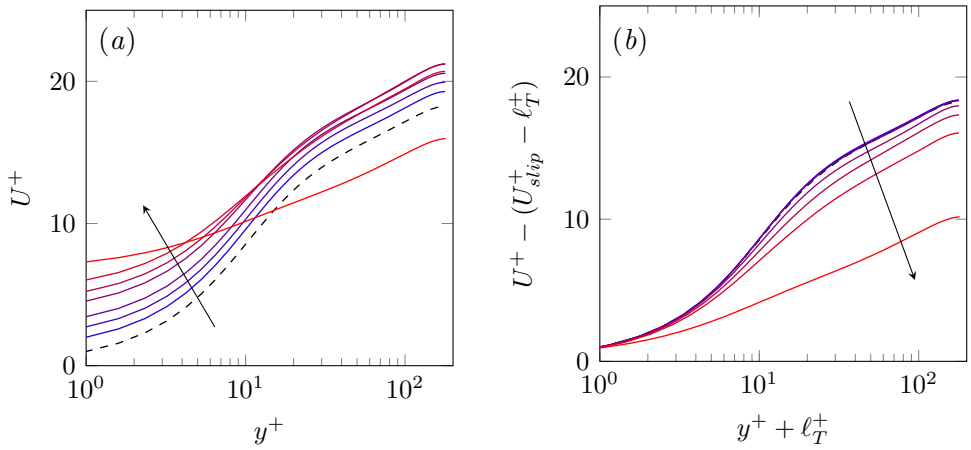

FIGURE 7.4 Mean velocity profiles for a substrate configuration with $\phi_{xy} \approx 11.4$. Permeabilities in viscous units increase in the direction of the arrow and from blue to red, which correspond to cases C1-C7. (a) Profiles scaled with u_τ measured at the interface plane, $y^+ = 0$. (b) Profiles shifted by the linearly extrapolated virtual origin of turbulence, $\ell^+_T = \sqrt{K^+_z}$, and scaled with the corresponding u_τ at $y = -\ell_T$, where the value at the origin, i.e. the offset predicted from the linear theory, $\Delta U^+ = U^+_{slip} - \ell^+_T$, has been subtracted. Black-dashed lines represent the smooth-channel case.

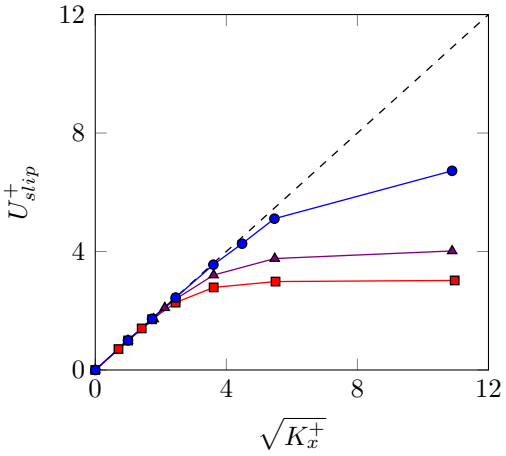

FIGURE 7.5 Slip velocity at the substrate-channel interface, U^+_{slip}, versus the slip length $\ell^+_x = \sqrt{K^+_x}$ for the three substrate configurations, —●—, $\phi_{xy} \approx 11.4$; —▲—, $\phi_{xy} \approx 5.5$; —■—, $\phi_{xy} \approx 3.6$. The symbols correspond to DNS cases listed in table 7.1 and the dashed line to $U^+_{slip} = \sqrt{K^+_x}$.

values of $\sqrt{K^+_y}$, the Reynolds stress at the substrate-channel interface is negligible, so this effect is small and $U^+_{slip} \approx \ell^+_x$. This is the case for the substrates lying on the linear regime. However, as $\sqrt{K^+_y}$ increases, the Reynolds stress at the interface ceases to be negligible, and $U^+_{slip} = dU^+/dy^+|_{y^+=0}\, \ell^+_x < \ell^+_x$. This discrepancy between U^+_{slip} and $\ell^+_x \approx \sqrt{K^+_x}$ for the substrates under consideration is shown in figure 7.5. The effect is small for the substrate of simulations C1-C7, but is significant for the substrates of B1-B7 and A1-A8, with results

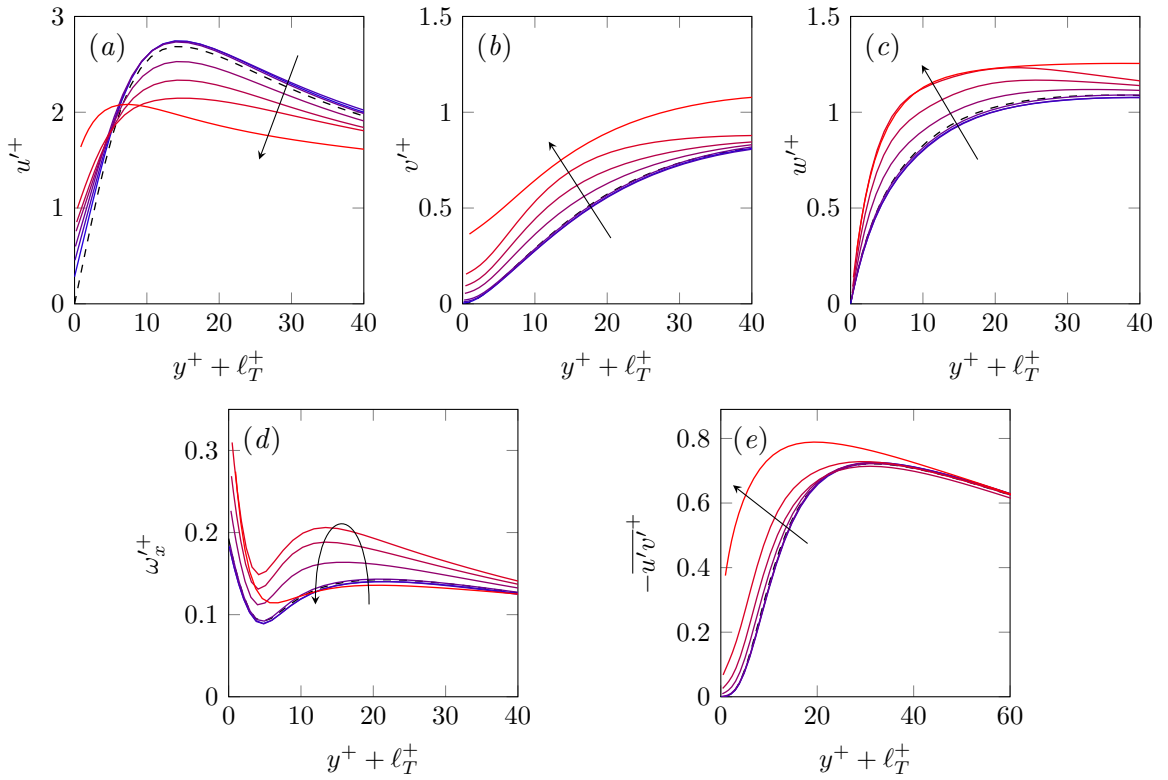

FIGURE 7.6 One-point turbulent statistics for a substrate configuration with $\phi_{xy} \approx 11.4$. Permeabilities in viscous units increase in the direction of the arrow and from blue to red, which correspond to cases C1-C7 scaled with the corresponding u_τ at $y = -\ell_T = -\sqrt{K_z}$, the linearly extrapolated virtual origin for turbulence. Black-dashed lines represent the smooth-channel case. Rms fluctuations of (a) the streamwise velocity, (b) the wall-normal velocity, (c) the spanwise velocity, and (d) the streamwise vorticity. (e) Reynolds stress.

portrayed in appendix F. The effect is particularly intense for the latter substrate, which reaches $\sqrt{K_y^+} \approx 3$ and experiences significant transpiration. Although U_{slip}^+ and ℓ_x^+ represent essentially the same concept, the quantitative effect of the streamwise slip is carried more accurately by U_{slip}^+, so the latter has been used for the velocity offset in figure 7.6(b). This explains why in chapter 4 we also subtracted the offset $U_{slip} - \ell_T^+$ to the mean velocity profiles. Notice that this effect is negligible in slip-only simulations or other idealised surfaces where zero transpiration is assumed (Fairhall *et al.*, 2019). Suga *et al.* (2010) measured experimentally the slip velocity for isotropic substrates with different $\sqrt{K_x^+}$, and their results are similar to those shown in figure 7.5 (cf. figure 4(b) in Suga *et al.* (2010)). Their results also accounted for the pressure driven flow within the substrates, which would include the extra slip velocity from Darcy's contribution discussed in section 6.4. However, for the mild pressure gradients considered, the slip velocity due to the overlying shear, $\sim \sqrt{K_x} dU/dy$, is significantly larger than that due to the pressure gradient, which justifies the similarity with the present results.

The observations on the agreement or deviation from smooth-wall data in the mean velocity profiles extend also to the rms velocity fluctuations and streamwise vorticity, as well as the Reynolds shear stress, portrayed in figures 7.6(*a*-*e*). For the cases in the linear regime, the agreement with smooth-wall data is good. The only difference is a small deviation in the profile of u'^+ in the region immediately above the interface, which was also observed in the simulations with $\ell_v^+ = 0$ in chapter 3 and the profiles for complex surfaces in chapter 4. As previously mentioned, this deviation is caused by the streamwise velocity effectively tending to zero at $y^+ = -\ell_U^+$, which is below the reference height $y^+ = -\ell_T^+$, and essentially does not alter near-wall dynamics, as observed for the slip-only simulations in chapter 3. Beyond the linear regime, the fluctuations of the streamwise velocity decrease in intensity, while those of the transverse components increase. For rough surfaces, this is often associated with a decreased anisotropy of the fluctuating velocity (Orlandi & Leonardi, 2006). The Reynolds stress behaves analogously, and the rms streamwise vorticity also becomes more intense, but experiences a significant drop for the final case, C7. The snapshots of figure 7.3 could suggest that this is caused by the eventual annihilation of the quasi-streamwise vortices of the near-wall cycle, as the spanwise-coherent structures become prevalent.

In the models proposed in chapter 6, the streamwise, spanwise and wall-normal permeabilities have separate effects. These models capture leading-order features, but in equations (2.3) the effect of the three permeabilities is coupled. This manifests in the DNS results and, although the coupled effects are secondary, they become increasingly important for large permeabilities.

The leading-order effect of the substrate on the overlying turbulence is, as discussed above, set by the transverse permeabilities. Although in the present study they are equal, it could be expected that $\sqrt{K_z^+}$ governed the virtual-origin effect, while $\sqrt{K_y^+}$ governed the onset of spanwise-coherent dynamics. However, once $\sqrt{K_y^+}$ becomes sufficiently large, $\sqrt{K_x^+}$ plays a secondary role by indirectly modulating the transpiration. Quantitatively, this influence is embedded in equations (2.3). In essence, the wall-normal flow that penetrates into the substrate is in a first instance impeded by $\sqrt{K_y^+}$, but from continuity it eventually needs to traverse the substrate tangentially, being then impeded by $\sqrt{K_x^+}$, before it leaves through the interface elsewhere. Thus, a large $\sqrt{K_x^+}$ amplifies the transpiration effect of $\sqrt{K_y^+}$ or, rather, a small $\sqrt{K_x^+}$ limits it. This can be observed by comparing the three substrates studied at roughly equal values of $\sqrt{K_y^+}$. As they have different anisotropy ratios, for the same $\sqrt{K_y^+}$ they have different $\sqrt{K_x^+}$. Examples are shown in figure 7.7. The values $\sqrt{K_y^+} \approx 0.2$, 0.4 and 1.0 have been chosen to observe the secondary effect of $\sqrt{K_x^+}$ in the linear regime, near the optimum drag reduction, and in the fully degraded regime, respectively. In the first case, the effect of $\sqrt{K_x^+}$ is negligible. The only effect is essentially that of $\sqrt{K_z^+}$ setting the virtual origin, and all the one-point statistics show good agreement with smooth wall data. The effect is still small near the optimum, for $\sqrt{K_y^+} \approx 0.4$, but the modulation by $\sqrt{K_x^+}$ begins to manifest, amplifying the effects of $\sqrt{K_y^+}$ already discussed above, such as the decreased

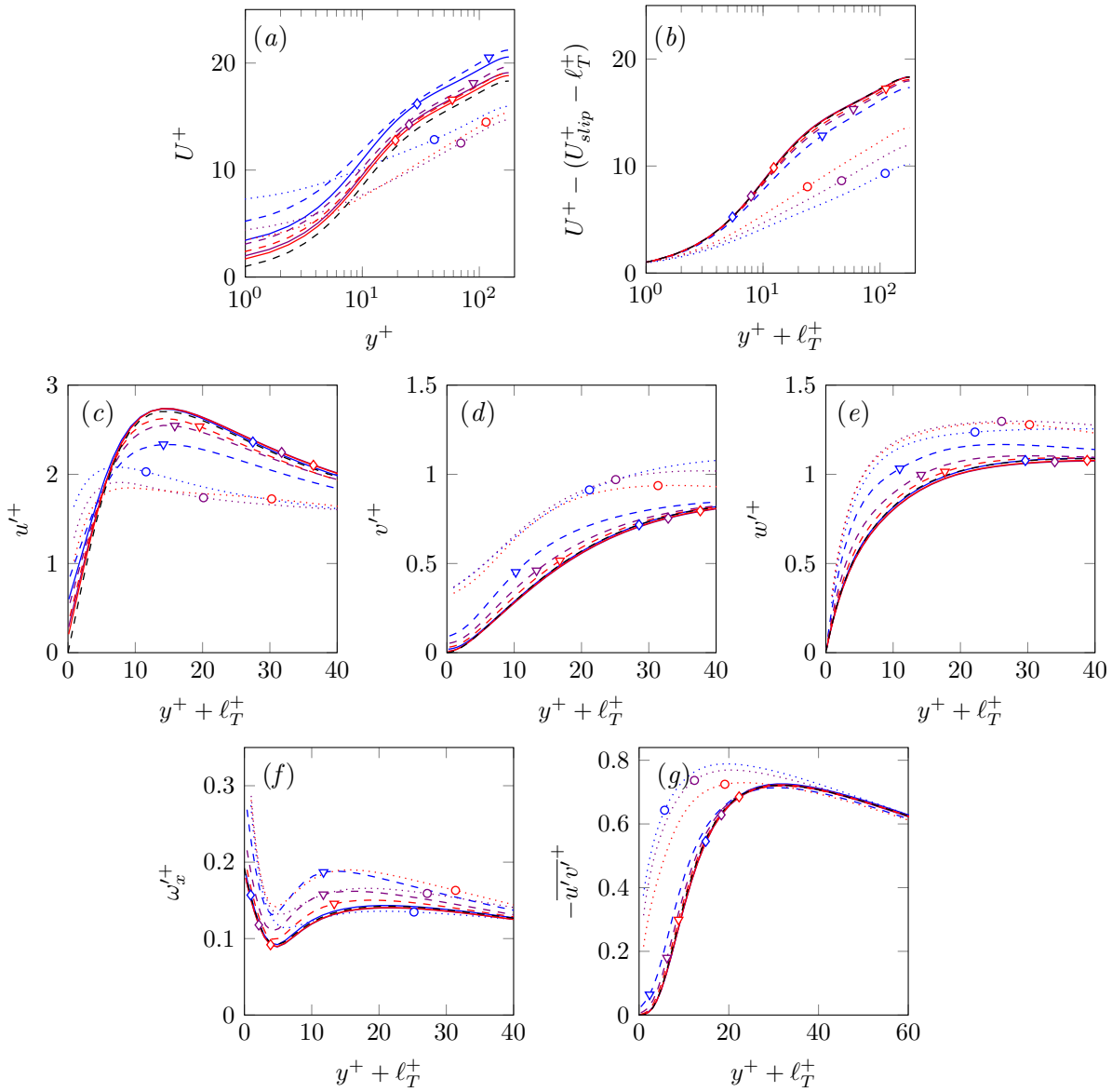

FIGURE 7.7 Turbulent statistics for different permeable substrates. Each symbol indicates cases with approximately the same $\sqrt{K_y^+}$ and $\sqrt{K_z^+}$. —◇—, cases A1, B1 and C3, with $\sqrt{K_y^+} \approx 0.2$; - -▽- -, cases A3, B3 and C5, with $\sqrt{K_y^+} \approx 0.4$; ··○··, cases A6, B6 and C7, with $\sqrt{K_y^+} \approx 1.0$. The colours represent substrate configurations with a fixed ϕ_{xy}: red, $\phi_{xy} \approx 3.6$; purple, $\phi_{xy} \approx 5.5$; blue, $\phi_{xy} \approx 11.4$. Black lines correspond to the smooth-channel case. Variables are scaled with the corresponding u_τ at $y = -\sqrt{K_z}$, the linearly extrapolated virtual origin for turbulence. (a) Mean velocity profiles, (b) mean velocity profiles shifted as in figure 7.4(a). (c), (d) and (e) streamwise, wall-normal and spanwise rms velocity fluctuations. (f) Streamwise vorticity rms fluctuations. (g) Reynolds stress.

anisotropy of the velocity fluctuations. Nevertheless, the Reynolds stress curve, and thus the shape of the mean velocity profile, remain close to those in the linear regime and for smooth walls. In the fully-degraded regime, $\sqrt{K_y^+} \approx 1.0$, the modulating effect of $\sqrt{K_x^+}$ becomes stronger and results in a further degradation of the Reynolds stress, the mean profile and the

drag. The near-wall cycle is severely disrupted in this regime, and the main effect of $\sqrt{K_x^+}$ on the velocity fluctuations is on u'^+ near the wall, directly through the increased streamwise slip.

In turn, $\sqrt{K_y^+}$ also has a secondary effect on the streamwise slip, through the non-zero Reynolds stress at the interface discussed above. Figure 7.5 illustrates how, for the same $\sqrt{K_x^+}$, which governs U_{slip}^+ to leading-order, substrates with larger $\sqrt{K_y^+}$ have a smaller slip velocity.

While the analysis of the one-point statistics reveals variations in average intensities at different heights, it cannot provide information on whether those variations are caused by contributions from lengthscales that are not active over smooth walls, or from a change in the intensity of the typical lengthscales of canonical wall turbulence. To investigate this, we analyse the spectral energy distribution of the fluctuating velocities.

As an example, spectral density maps of u^2, v^2, w^2 and uv are represented at a height of roughly 15 wall units above the virtual origin for turbulence in figure 7.8. For substrates in the linear regime, such as C2 in panels (*a*-*d*), the agreement in spectral distribution with smooth-wall flows is excellent, as it was for the rms values, further supporting the idea that near-wall turbulence remains essentially canonical. For substrate C4, which is just past the linear regime and has a near-optimum $\sqrt{K_y^+} \approx 0.32$, differences begin to appear in the spectral distributions, like additional energy at slightly shorter streamwise wavelengths, but most notably the emergence of a spectral region with high v^2 for large spanwise wavelengths, $\lambda_z^+ \approx 200-\infty$ and streamwise wavelengths $\lambda_x^+ \approx 100-200$. This feature is consistent with the onset of spanwise-coherent structures observed in figure 7.3, and was also observed previously for riblets and connected to the presence of Kelvin-Helmholtz-like rollers (García-Mayoral & Jiménez, 2011). The linear stability analysis in chapter 5 showed that the wavelength of the spanwise-coherent rollers, λ_x^+, scales in viscous units. In particular, the wavelength is set by the height where the second derivative of the mean flow, d^2U/dy^2, concentrates, which is analogous to the mixing layer thickness of free-shear flows. For small permeabilities, where the near-wall cycle still prevails, as in the present cases, the near-wall peak of d^2U/dy^2 scales in viscous units, and hence the wavelength also scales in viscous units. Although this cannot be determined from the present simulations, since they are conducted at essentially the same Reynolds number, it was verified by García-Mayoral & Jiménez (2012) for riblets. As the permeabilities increase, the near-wall cycle is destroyed and the near-wall peak in d^2U/dy^2 ceases to exist, leaving δ as the only available scale. The wavelength of the rollers scales then with δ, as suggested in Jiménez *et al.* (2001) and Breugem *et al.* (2006) and thoroughly reported by Kuwata & Suga (2017) and Suga *et al.* (2018). The new spectral region observed for case C4 becomes more intense for cases C6 and C7. For C6, which lies in the degraded regime but still yields a net reduction in drag, energy appears in wavelengths as short as $\lambda_x^+ \approx 50$, and the spanwise-coherent region spans a wider set of streamwise wavelengths, $\lambda_x^+ \approx 60-350$, although there is still a trace of the spectral densities of smooth-wall flow

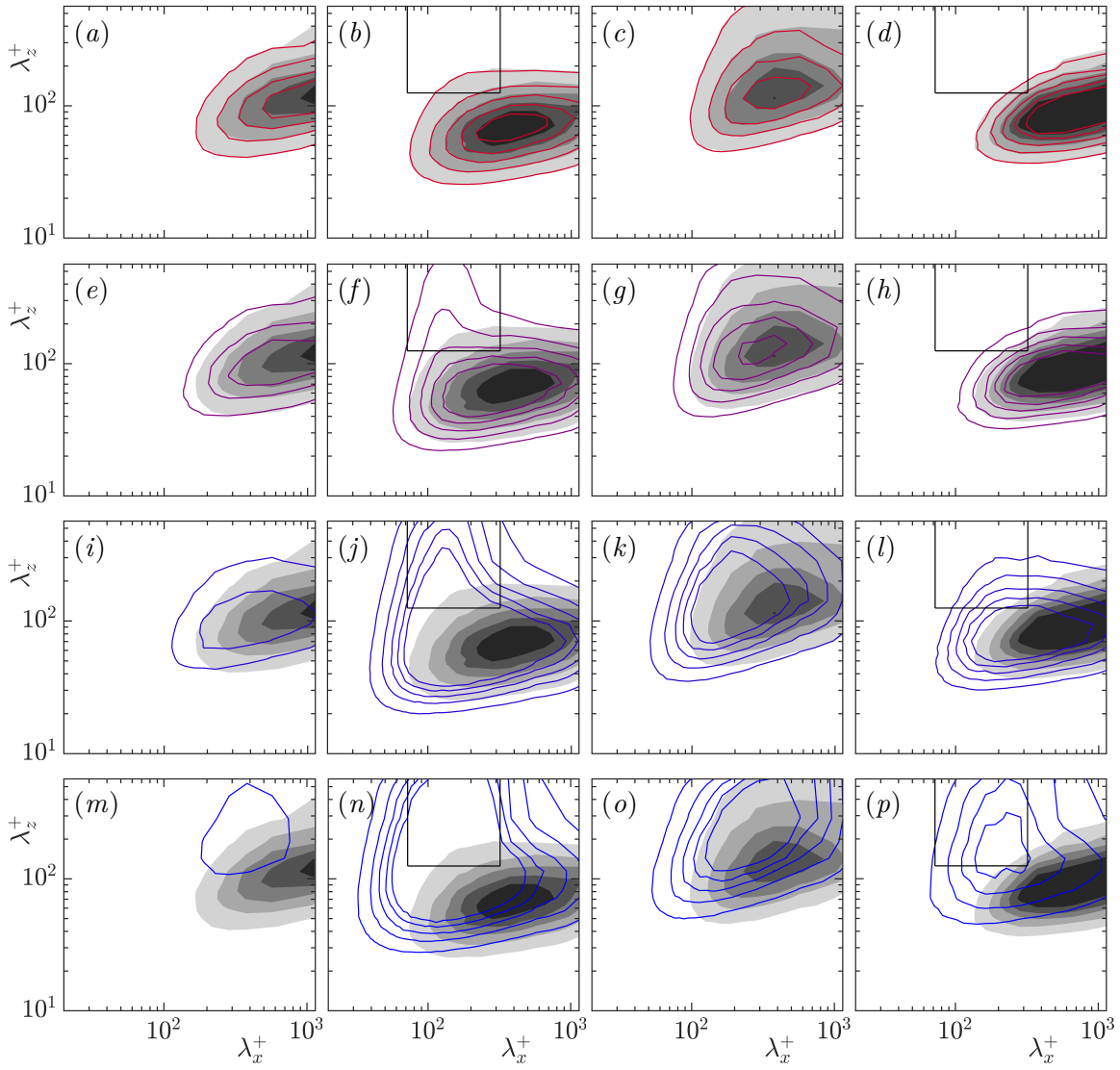

FIGURE 7.8 Premultiplied two-dimensional spectral densities for a substrate configuration with $\phi_{xy} \approx 11.4$ at a plane $y^+ + \ell_T^+ \approx 15.5$. First column, $k_x k_z E_{uu}$; second column, $k_x k_z E_{vv}$; third column, $k_x k_z E_{ww}$; fourth column, $k_x k_z E_{uv}$; with contour increments 0.3241, 0.0092, 0.0404 and 0.0239 in wall units, respectively. Shaded, smooth channel. Red contours, permeable cases: (*a-d*) case C2, (*e-h*) case C4, (*i-l*) case C6, and (*m-p*) case C7. The box indicates the region of the spectrum considered in section 7.4.

for long wavelengths, $\lambda_x^+ \gtrsim 500$, specially for v^2 and w^2. For case C7, which gives a net drag increase, any residual trace of the spectral distribution for smooth-wall turbulence has disappeared, and the range $\lambda_x^+ \approx 60 - 350$ becomes dominant in v^2.

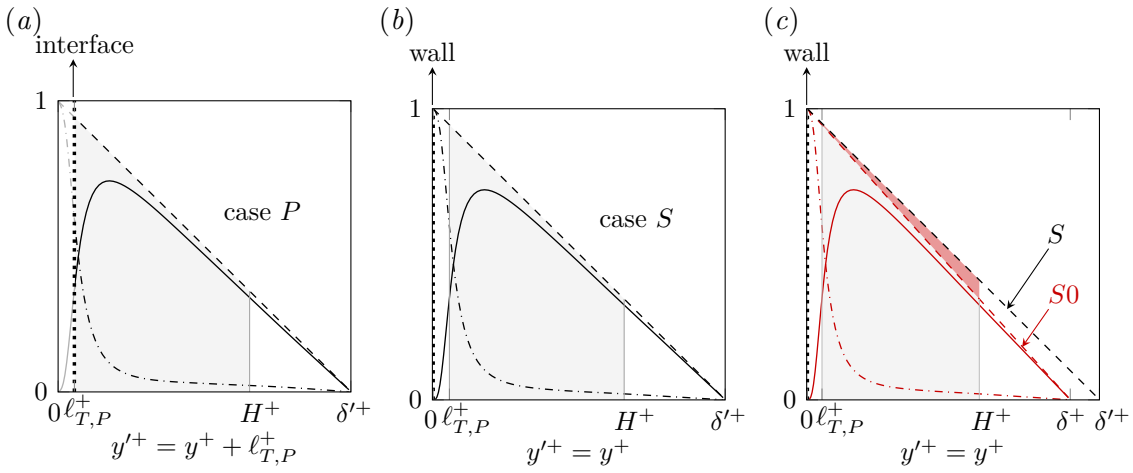

FIGURE 7.9 Sketch of stress curves taking the virtual origin of turbulence as reference. – · –, viscous stress dU^+/dy^+; ——, $\overline{u'v'}^+$; – – –, total stress. (a) Permeable case at a friction Reynolds number $\delta'^+ = \delta^+ + \ell^+_{T,P}$. ($b$) Smooth-wall case at the same friction Reynolds number δ'^+. (c) Smooth-wall case at a different friction Reynolds number, δ^+. The vertical black-dotted line indicates the substrate-channel interface in the permeable case and the wall in the smooth cases. The grey shaded area represents the integrated region in equation (7.4). The red shaded area in (c) shows the difference in the integrated area due to the difference in the friction Reynolds number.

7.4 Contributions to ΔU^+

The degradation of the drag reduction curves in figure 7.1 and the lack of collapse of the mean velocity profiles in figure 7.4(b) show that there is an additional contribution to ΔU^+ beyond the virtual-origins effect predicted in chapter 6. To investigate this, we obtain an expression for ΔU^+ by integrating the mean streamwise momentum equation for a permeable channel and comparing it with that for a smooth channel. This procedure follows closely MacDonald *et al.* (2016), Abderrahaman-Elena *et al.* (2019) and Fairhall *et al.* (2019), and is similar to that followed by García-Mayoral & Jiménez (2011). The streamwise momentum equation is averaged in time and in the streamwise and spanwise directions, and integrated in the wall-normal direction,

$$-\overline{u'v'}^+ + \frac{dU^+}{dy^+} = \frac{\delta'^+ - y'^+}{\delta'^+}, \tag{7.2}$$

where the virtual origin of turbulence is taken as the reference for the wall-normal coordinate, i.e. $y'^+ = y^+ + \ell^+_T$, and it is also the height where u_τ is measured. The effective half-channel height or the effective friction Reynolds number is then $\delta'^+ = \delta^+ + \ell^+_T$, as previously defined. In equation (7.2), $\overline{u'v'}^+$ is the Reynolds stress, dU^+/dy^+ the viscous stress and the right-hand side represents the total stress. These three terms are represented in figure 7.9(a).

Integrating again between two heights, the viscous stress term gives the velocity U^+ at those two heights, which can be compared to the corresponding equation for a smooth channel

to obtain an expression for ΔU^+. The upper integration limit is then taken at an arbitrary height in the logarithmic region, $y'^+ = H^+$, so that the difference in U^+ yields ΔU^+. For the lower limit, we set it at $y'^+ = \ell^+_{T,P}$, where $\ell^+_{T,P}$ refers to the virtual origin of turbulence for the permeable case, since for that layout equation (7.2) is defined only above that height. Integrating equation (7.2) from $y'^+ = \ell^+_{T,P}$, to an arbitrary height in the logarithmic region, $y'^+ = H^+$, yields

$$\int_{\ell^+_{T,P}}^{H^+} -\overline{u'v'}^+ dy'^+ + U^+(H^+) - U^+(\ell^+_{T,P}) = H^+ - \ell^+_{T,P} - \frac{H^{+2} - \ell^{+2}_{T,P}}{2\delta'^+}. \tag{7.3}$$

This equation applies not only to a permeable channel, but also to a smooth channel at the same Reynolds number, δ'^+, as depicted in figure 7.9(b). Note that for a smooth channel $y'^+ = y^+$, since the origin of turbulence is at the wall, but the lower integration limit can still be set at some height above the wall, $y'^+ = \ell^+_{T,P}$, with $\ell^+_{T,P}$ referring to the origin of the permeable case being compared.

Subtracting equation (7.3) for the permeable case and for the smooth channel, the resulting expression for ΔU^+ is,

$$\begin{aligned}\Delta U^+ &= U^+_P(H^+) - U^+_S(H^+) \\ &= \underbrace{U^+_P(\ell^+_{T,P})}_{U^+_{slip}} - U^+_S(\ell^+_{T,P}) \underbrace{- \int_{\ell^+_{T,P}}^{H^+} \left[\left(-\overline{u'v'}^+_P\right) - \left(-\overline{u'v'}^+_S\right)\right] dy'^+}_{\mathcal{T}_{uv}},\end{aligned} \tag{7.4}$$

where subscript 'P' denotes the permeable channel, and subscript 'S' the reference smooth channel at the same friction Reynolds number δ'^+. Equation (7.4) shows that ΔU^+, defined as the difference in U^+ between a permeable and smooth channel measured at the same distance from their respective origins of turbulence, consists of the sum of three terms.

The first term, is the slip velocity of the permeable case at the substrate-channel interface, U^+_{slip}. This is a drag-reducing term, and for the cases lying in the linear regime it can be approximated to the virtual origin of the mean flow, ℓ^+_U, since $dU^+_P/dy^+|_{y'^+=\ell^+_{T,P}} \approx 1$. The second term, $U^+_S(\ell^+_{T,P})$, is the mean velocity of the smooth channel measured at $y'^+ = \ell^+_{T,P}$. It is a drag-increasing term, and if $\ell^+_{T,P} \lesssim 5$, it can be accurately approximated as $U^+_S(\ell^+_{T,P}) \approx \ell^+_{T,P}$. This is essentially the same as the spanwise protrusion height of Luchini *et al.* (1991) and Luchini (1996), and the spanwise slip of superhydrophobic surfaces (Min & Kim, 2004; Busse & Sandham, 2012). The offset between these terms is then $U^+_{slip} - U_S(\ell^+_{T,P}) \approx \ell^+_U - \ell^+_{T,P}$ and represents the virtual-origin effect discussed throughout this thesis. Note, however, that the exact contribution to ΔU^+ involves velocities and not virtual origins as pointed out before. The contribution of the offset between these two terms to ΔU^+ is shown in figure 7.10,

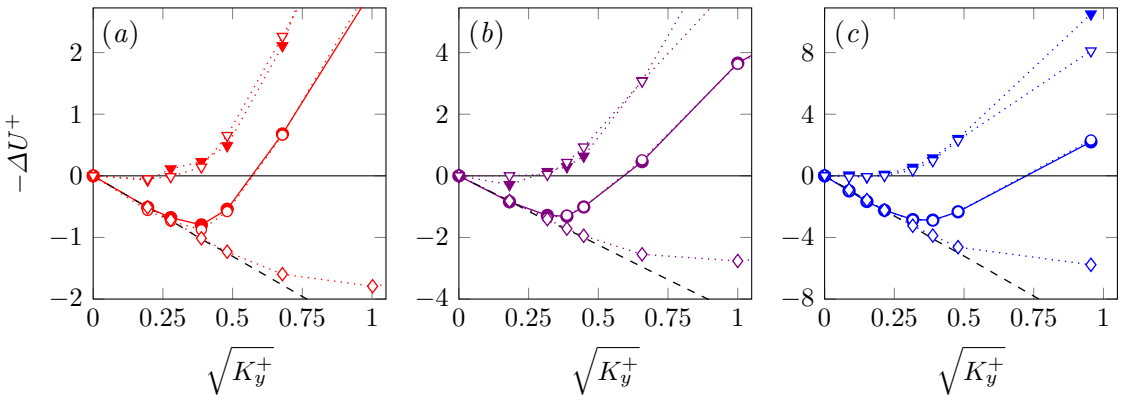

FIGURE 7.10 Different contributions to ΔU^+ as a function of $\sqrt{K_y^+}$ for (a) substrates A1-A8, with $\phi_{xy} \approx 3.6$, (b) substrates B1-B7, with $\phi_{xy} \approx 5.5$ and (c) substrates C1-C7, with $\phi_{xy} \approx 11.4$. –●–, ΔU^+ measured from the DNSs (same as in table 7.1); ··◇··, contribution from the virtual-origin effect, $U^+_{slip} - U^+_S(\ell^+_T)$; ··▽··, contribution from the additional Reynolds stress, $\mathcal{T}_{uv}$; ··▼··, contribution from the additional Reynolds stress restricted to the spectral window $\lambda_x^+ \approx 70 - 320$ and $\lambda_z^+ \gtrsim 120$; ··○··, ΔU^+ calculated from equation (7.4), as a sum of the contributions from the virtual-origin effect and the additional Reynolds stress. – – –, equation (6.7).

where we can appreciate that the virtual origin approximation $\ell_U^+ - \ell_T^+$ is valid not only in the linear regime, but even slightly beyond the optimum.

The third term, $\mathcal{T}_{uv}$, represents the additional Reynolds stress induced by the permeable substrate. It is a drag-increasing term and its contribution to ΔU^+ is also shown in figure 7.10. For the substrates lying in the linear regime, the Reynolds stress is smooth-wall-like, except for the displacement ℓ_T^+ towards the interface, and the term $\mathcal{T}_{uv}$ is therefore zero. The contribution of this term begins to be significant at the breakdown $\sqrt{K_y^+}|_{opt}$, and increases with $\sqrt{K_y^+}$ in the degraded region. An increase in Reynolds stress is therefore related to the degradation of the drag-reducing behaviour of permeable substrates.

The spectral energy distribution of the wall-normal velocity in figure 7.8 shows the appearance of a new spectral region for large spanwise wavelengths centred around $\lambda_x^+ \approx 150$, which is associated to the large spanwise coherent structures observed in figure 7.3. To explore whether the additional Reynolds stress accounted for by $\mathcal{T}_{uv}$ is due to the energy accumulated in this spectral region, we define a spectral box with $\lambda_x^+ \approx 70 - 320$ and $\lambda_z^+ \gtrsim 120$, as that depicted in figure 7.8, and quantify its contribution to the additional Reynolds stress, as in García-Mayoral & Jiménez (2011). The values are also included in figure 7.10, showing a close agreement with the whole $\mathcal{T}_{uv}$. This suggests that the new spanwise-coherent structures are indeed responsible for the degradation of the drag, as it was also observed for riblets in García-Mayoral & Jiménez (2011). In essence, these structures increase the turbulence mixing, increasing the local Reynolds stress and the global drag.

Note that equation (7.4) compares a permeable channel with a smooth one at the same friction Reynolds number. Often, however, a reference smooth channel at exactly the same

Reynolds number is not available. This is, for instance, the case for the simulations presented in this paper, where all the permeable cases are compared to the same smooth channel at a slightly different friction Reynolds number. When the Reynolds numbers match exactly, the total stress, and thus the Reynolds stress, collapse sufficiently far away from the surface, as they approach zero-value at the centre of the channel. The contribution $\mathcal{T}_{uv}$ can then be entirely ascribed to wall effects, that is to the presence of the substrate. If the Reynolds numbers differ, however, there may be a significant contribution to $\mathcal{T}_{uv}$ far from the surface, which is a Reynolds-number effect, rather than a direct effect of the surface. The same effect appears when comparing smooth channels at different friction Reynolds numbers, as illustrated in figure 7.9(c). To quantify this effect, we compare the smooth channel at Reynolds number δ'^{+}, used for equation (7.4) and represented by a subscript 'S', with another at a different Reynolds number δ^{+}, represented by a subscript '$S0$'. Subtracting the two integrated mean streamwise momentum equations, the universality of the near-wall mean velocity profile over smooth walls gives $U_S^+(\ell_{T,P}^+) = U_{S0}^+(\ell_{T,P}^+)$ and $U_S^+(H^+) = U_{S0}^+(H^+)$, yielding

$$\mathcal{T}_{Re} = -\int_{\ell_{T,P}^+}^{H^+} \left[\left(-\overline{u'v'}_S^+\right) - \left(-\overline{u'v'}_{S0}^+\right)\right] dy'^{+} = \frac{H^{+2} - \ell_{T,P}^{+2}}{2}\left(\frac{1}{\delta'^{+}} - \frac{1}{\delta^{+}}\right). \tag{7.5}$$

When the break-up of equation (7.4) is applied to DNS results from a complex surface, P in our case, and a smooth wall at a different Reynolds number, $S0$, the integral of the difference in Reynolds stresses would include both the surface and the Reynolds number effects. These, however, can be easily separated as

$$\begin{aligned}
&-\int_{\ell_{T,P}^+}^{H^+} \left[\left(-\overline{u'v'}_P^+\right) - \left(-\overline{u'v'}_{S0}^+\right)\right] dy'^{+} = \\
&-\int_{\ell_{T,P}^+}^{H^+} \left[\left(-\overline{u'v'}_P^+\right) - \left(-\overline{u'v'}_S^+\right)\right] dy'^{+} - \int_{\ell_{T,P}^+}^{H^+} \left[\left(-\overline{u'v'}_S^+\right) - \left(-\overline{u'v'}_{S0}^+\right)\right] dy'^{+} \\
&= \mathcal{T}_{uv} + \mathcal{T}_{Re}.
\end{aligned} \tag{7.6}$$

Note that, from equation (7.5), $\mathcal{T}_{Re}$ can be easily calculated *a priori* as the area of the trapezoid formed between the total stress lines for δ^+ and δ'^+, as highlighted in figure 7.9(c). $\mathcal{T}_{uv}$ can subsequently be obtained by subtracting $\mathcal{T}_{Re}$ from the integral of the difference in Reynolds stresses of cases P and $S0$, as given by equation (7.6), so that it only includes the effect of the surface. This has been the procedure used to obtain the results shown in figure 7.10, even though for the small values of ℓ_T^+ considered, the Reynolds number effect, $\mathcal{T}_{Re}$, is negligible.

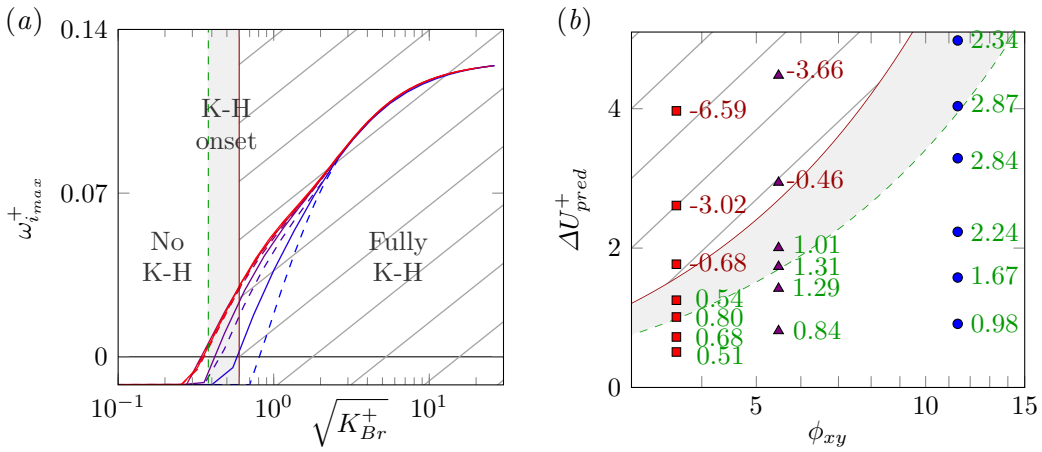

FIGURE 7.11 (*a*) Amplification of the most unstable mode versus $\sqrt{K^+_{Br}}$, as in figure 6.1, but with the threshold values for the onset of Kelvin-Helmholtz-like instability adjusted to $\sqrt{K^+_{Br}} \approx \sqrt{K^+_y} = 0.38 - 0.6$. (*b*) Predicted values of ΔU^+ from the linear theory of equation (6.7) versus the anisotropy ratio ϕ_{xy}, as in figure 6.2(*b*), but with the adjusted thresholds for the degraded region. The green line corresponds approximately to the optimum ΔU^+ ($\sqrt{K^+_y}|_{opt} \approx 0.38$); the red line corresponds approximately to zero ΔU^+ ($\sqrt{K^+_y}|_{\Delta U^+=0} \approx 0.6$). The symbols represent the DNS cases studied and the values next to them are the actual ΔU^+ measured from the DNSs. Cases beyond $\Delta U^+_{pred} > 5$ are not displayed.

7.5 Adjustment of the theoretical models

In chapter 6, we presented theoretical models to estimate the drag-reducing behaviour for anisotropic permeable substrates, a linear drag-reduction model for small permeabilities given by equation (6.4) and a threshold for the degradation of this linear regime based on the onset of Kelvin-Helmholtz rollers. The information obtained from the present DNSs can be used to assess the validity of these models, and if necessary adjust them, so that more accurate predictions can be made.

The drag reduction curves in figure 7.1 show that the linear regime is accurately represented by the offset between the virtual origins of the mean flow and that of turbulence, $\sqrt{K^+_x} - \sqrt{K^+_z}$, as predicted by equation (6.4). As discussed above, ΔU^+ in this regime would be more precisely given by the difference $U^+_{slip} - U^+_S(\ell^+_T)$, but the differences between $\sqrt{K^+_x}$ and U^+_{slip}, and between $\sqrt{K^+_z}$ and $U^+_S(\ell^+_T)$ only become significant for larger permeabilities – beyond the linear regime, as shown in figure 7.10.

The DNS results and the discussion in section 7.4 also support the idea that the degradation of the drag-reducing behaviour is caused by the formation of spanwise-coherent structures. These are generally associated to a Kelvin-Helmholtz-like instability, as discussed in chapter 6. In that chapter, we predicted that the onset of these structures was governed by $\sqrt{K^+_y}$, the leading order term of $\sqrt{K^+_{Br}}$ from equation (6.5), as shown in figure 6.1. From this figure, we estimated an *a priori* threshold for the onset of Kelvin-Helmholtz-like rollers in the range

$\sqrt{K_{Br}^+} \approx \sqrt{K_y^+} \approx 1 - 2.2$, beyond which equation (6.4) would no longer be valid. The drag reduction curves in figure 7.1(c), however, show that the degradation sets in for lower values of $\sqrt{K_y^+}$ than initially hypothesised. The optimum value of ΔU^+ occurs at $\sqrt{K_y^+}|_{opt} \approx 0.38$, after which performance degrades, and drag becomes greater than that for smooth walls for $\sqrt{K_y^+}|_{\Delta U^+=0} \approx 0.6$. Adjusting figure 6.1 to account for these observed values, we obtain figure 7.11(a), which shows that the onset occurs as soon as the predicted amplification of the instability becomes positive.

In chapter 6, combining the equation for the linear regime with the limiting values of $\sqrt{K_y^+}$, allowed us to design the parameter space for realisable drag reduction shown in figure 6.2(b), which later served to select the DNS cases studied in this chapter. Using the limiting values of $\sqrt{K_y^+}$ observed in the DNSs ($\sqrt{K_y^+} \approx 0.38 - 0.6$), the adjusted prediction map for ΔU^+ is shown in figure 7.11(b), where the actual values of ΔU^+ measured from DNSs are also shown. This figure illustrates how the theoretical predictions compare to the actual results obtained from DNS. In the linear regime, ΔU^+ is well predicted by the theory. At the optimum ΔU^+ line, $\sqrt{K_y^+} \approx 0.38$, the exact value of ΔU^+ is given by equation (7.1), that is, it is roughly 80% of the linear-regime prediction. Beyond this line, the performance degrades, and for the line $\sqrt{K_y^+} \approx 0.6$, the drag reduction is fully negated. Assuming that this behaviour holds for substrates with anisotropy ratios different to those studied in this work, figure 7.11(b), which essentially contains the same information of figure 7.2(d), can be used to estimate their performance.

Chapter 8

Conclusions and scope for future work

This thesis has investigated the effect that surface textures in general have on the overlying turbulent flow, with a focus on anisotropic permeable substrates and their ability to reduce skin-friction drag.

When the surface texture is small compared to the overying turbulent structures, the overlying turbulent flow does not perceive the detail of the texture, but a homogenised effect and the velocity components may appear to vanish at different heights. Luchini *et al.* (1991) and Jiménez (1994) noted that, for small surface textures, their effect on the flow can be reduced to a different virtual origin perceived by the mean flow and the overlying turbulence. The origin of turbulence can be interpreted as the equivalent, no-slip wall perceived by the quasi-streamwise vortices of the near-wall cycle, which, immediately above the surface, induce primarily a spanwise flow. Based on this, Luchini *et al.* (1991) proposed that, when the texture size is vanishingly small, the virtual origin of turbulence is that imposed by a spanwise homogeneous shear. Thus, to achieve drag reduction a surface texture should offer more resistance to the spanwise flow than to the streamwise mean flow. Luchini's model, however, neglects the effect of wall-normal transpiration, which can be significant for the drag.

In the first part of the thesis, we generalised Luchini's virtual-origin theory for drag reduction and explored its applicability to a variety of surfaces. This has led to two main conclusions. The first is that the effect of a textured surface in the flow can be reduced to a different virtual origin perceived by the mean flow and the overlying turbulence, confirming Luchini's original idea. The origin of turbulence, however, is not determined by the origin of the spanwise velocity alone, but by the origins perceived by the spanwise and wall-normal velocities. We showed that the near-wall cycle and the turbulence dynamics remain smooth-wall-like, save for the shift of the apparent origin to the origin perceived by turbulence, $y^+ = -\ell_T^+$. This height sets therefore the height origin for textured surfaces, which means that the friction velocity should be measured at that height, and it should be also the position

of the reference smooth wall for comparison. The only change in the mean velocity profile is then a shift by its value at the origin of turbulence, $\Delta U^+ = \ell_U^+ - \ell_T^+$, where ℓ_U^+ and ℓ_T^+ are the depths of the virtual origins of the mean flow and turbulence, respectively. The second conclusion from this first part is that the change in drag for different complex surfaces can be expressed in the framework of this unifying theory based on virtual origins. We showed that small surface textures can be effectively modelled using Robin boundary conditions for the three velocities without conducting computationally expensive, texture-resolved simulations. However, as the texture size is increased, the linear theory of virtual origins eventually breaks down, since additional drag-increasing mechanisms set in that change the overlying turbulent flow.

Further investigations should be conducted on the effect of virtual origins. More simulations need to be run to confirm the current findings and validate the preliminary expression derived to predict the origin of turbulence, ℓ_T^+. Additionally, the range of validity of the Robin boundary conditions for the three velocities should also be explored. This work is being carried out at present in our group (Ibrahim & García-Mayoral, 2019). The additional simulations conducted confirm that the flow is indeed characterised by two virtual origins, ℓ_U^+ and ℓ_T^+, with ΔU^+ being equal to their difference, and that the virtual origin of turbulence predicted by expression (3.9) is in good agreement with DNS results.

We have shown in this thesis that the effect of complex surfaces that lie in the linear regime can be modelled in terms of slip lengths (ℓ_x^+, ℓ_y^+ and ℓ_z^+), using homogeneous Robin boundary conditions. These slip lengths, or alternatively their respective virtual origins ℓ_u^+, ℓ_v^+ and ℓ_w^+, can, in turn, be used to predict the origins ℓ_U^+ and ℓ_T^+. These slip lengths can in theory be related to the geometry of the surface texture, without running computationally expensive, texture-resolved simulations to obtain them. Some work exists in the literature on this area, but further work is still needed. For instance, the slip lengths can be obtained by running computationally inexpensive Stokes or laminar simulations with a single texture unit, but for certain textures, simple expressions could also be defined, relating the geometrical parameters of the surface to the slip lengths they generate, such as those presented in chapter 6 for permeable substrates. On this note, it would be interesting to explore how the parameter that governs the breakdown for riblets, that is, the square root of the groove cross-section $\ell_g^+ = \sqrt{A_g^+}$, relates to the virtual origin of turbulence.

In any event, the virtual-origin theory is only capable of predicting the behaviour of surface textures in the linear regime. It cannot capture its breakdown, which is critical for practical application, as it provides the optimum performance that a given surface can achieve. With the ultimate aim of also modelling this breakdown regime, we raise the question of whether, for certain surfaces, the current virtual-origin model can be extended to capture that optimum. For anisotropic permeable substrates, the preliminary work that we performed in chapter 4 to model these instabilities have provided mixed results, and additional, more refined models should be investigated. For instance, the dependence of the wall-normal

velocity on the streamwise shear could also be considered. This opens a new research path to develop models that are able to capture the breakdown mechanisms and the departure from the linear regime for different complex surfaces. For surfaces for which the granularity of the texture is relevant for the breakdown mechanism, such as for the superhydrophobic posts of Seo *et al.* (2018) or the deep transverse grooves of MacDonald *et al.* (2018), models that discriminate between wavelengths and excite only certain modes could be investigated.

Based on the understanding gained from the virtual-origin theory, in the second part of the thesis we have studied anisotropic permeable substrates. We showed that streamwise-preferential substrates can reduce drag. The resulting drag reduction curves for different substrate configurations (i.e. different anisotropy ratios) is similar to the classic curves for riblets (Walsh & Lindemann, 1984). For small permeabilities the curves exhibit a linear drag reduction regime, where ΔU^+ increases linearly with the permeability lengthscale in wall units. This is followed by a degradation of performance, which eventually leads to an increase of drag.

We have demonstrated that the linear regime of small permeabilities, is captured well by the virtual-origin theory, which for permeable substrates gives $\Delta U^+ \approx \sqrt{K_x^+} - \sqrt{K_z^+}$, with $\sqrt{K_x^+}$ and $\sqrt{K_z^+}$ being the permeability lengthscales in the streamwise and spanwise directions. As permeabilities increase, the linear regime eventually breaks down. We found that the breakdown is essentially governed by the wall-normal permeability, K_y^+, and occurs for $\sqrt{K_y^+} \approx 0.38$, independently of the substrate anisotropy. The breakdown can be attributed to the appearance of spanwise-coherent structures, associated to a Kelvin-Helmholtz-like instability. We showed that a linear stability analysis can be used to capture the formation of Kelvin-Helmholtz-like instabilities and hence the breakdown of the linear regime. The viscous effects on the linear stability analysis have little effect on the results, which suggests that only the pressure/wall-normal velocity coupling at the substrate/free-flow interface is the relevant condition to capture the instability.

The models that we have developed based on the virtual-origin theory and linear stability analysis provide design guidelines to produce a drag-reducing permeable substrate and give quantitative estimates as to how much drag reduction could be expected, given by equation (7.1). This work is a first step towards a deeper understanding of the ability of anisotropic permeable substrates to reduce skin friction drag. This preliminary evidence suggests that streamwise-preferential permeable substrates can provide a performance benefit significantly better than riblets. For the substrate configurations considered, the largest drag reduction observed is $\approx 20 - 25\%$ at a friction Reynolds number $\delta^+ = 180$, which is at least twice that obtained for the riblets studied by Bechert *et al.* (1997). Further work is however required to confirm the present results and gain a better understanding on the effect that these substrates have on the overlying flow.

The Brinkman model that we used to characterise the permeable substrates has limitations. This have been widely discussed in the specialised literature (Lévy, 1983; Le Bars & Worster, 2006; Auriault, 2009; Bottaro, 2019), but there are still some open questions. For instance, it is unclear whether continuous or jump conditions should be imposed at the substrate/free-flow interface, or how the effective viscosity, $\tilde{\nu}$, relates to the parameters of the substrate. Conducting DNSs that fully resolve the microstructure of the permeable substrates would determine the range of validity of the current models, and would allow us to gain full understanding on the effect that these substrates have on the overlying turbulence.

References

Abderrahaman-Elena, N., Fairhall, C. T. & García-Mayoral, R. 2019 Modulation of near-wall turbulence in the transitionally rough regime. *Accepted in J. Fluid Mech.* **865**, 1042–1071.

Abderrahaman-Elena, N. & García-Mayoral, R. 2017 Analysis of anisotropic permeable surfaces for turbulent drag reduction. *Phys. Rev. Fluids* **2**, 114609.

Air & Cosmos International 2017 Lufthansa technik, airbus achieve 'shark skin' breakthrough. http://www.aircosmosinternational.com/lufthansa-technik-airbus-achieve-shark-skin-breakthrough-96051, [Online: accessed 16-October-2018].

Airbus 2018 Biomimicry: engineering in nature's style. https://www.airbus.com/newsroom/news/en/2018/01/biomimicry--engineering-in-nature-s-style.html, [Online: accessed 7-March-2019].

del Álamo, J. C. & Jiménez, J. 2006 Linear energy amplification in turbulent channels. *J. Fluid Mech.* **559**, 205–213.

Auriault, J. L. 2009 On the domain of validity of Brinkman's equation. *Transp. Porous Media* **79** (2), 215–223.

Bae, H. J., Lozano-Durán, A., Bose, S. T. & Moin, P. 2018 Turbulence intensities in large-eddy simulation of wall-bounded flows. *Phys. Rev. E* **3**, 014610.

Barkley, D. 2006 Linear analysis of the cylinder wake mean flow. *Europhys. Lett.* **75** (5), 750–756.

Battiato, I. 2012 Self-similarity in coupled Brinkman/Navier-Stokes flows. *J. Fluid Mech.* **699**, 94–114.

Battiato, I. 2014 Effective medium theory for drag-reducing micro-patterned surfaces in turbulent flows. *Eur. Phys. J. E* **37**, 19.

Beavers, G. S. & Joseph, D. D. 1967 Boundary conditions at a naturally permeable wall. *J. Fluid Mech.* **30** (1), 197–207.

Bechert, D. W. & Bartenwerfer, M. 1989 The viscous flow on surfaces with longitudinal ribs. *J. Fluid Mech.* **206**, 105–129.

Bechert, D. W., Bruse, M., Hage, W., van der Hoeven, J. G. T. & Hoppe, G. 1997 Experiments on drag-reducing surfaces and their optimization with an adjustable geometry. *J. Fluid Mech.* **338**, 59–87.

Beneddine, S., Sipp, D., Arnault, A., Dandois, J. & Lesshafft, L. 2016 Conditions for validity of mean flow stability analysis. *J. Fluid Mech.* **798**, 485–504.

Blackwelder, R. F. & Eckelmann, H. 1979 Streamwise vortices associated with the bursting phenomenon. *J. Fluid Mech.* **94** (3), 577–594.

Bottaro, A. 2019 Flow over natural or engineered surfaces: an adjoint homogenization perspective. *Submitted to J. Fluid Mech.* personal communication.

Breugem, W. P. & Boersma, B. J. 2005 Direct numerical simulations of turbulent flow over a permeable wall using a direct and a continuum approach. *Phys. Fluids* **17**, 025103.

Breugem, W. P., Boersma, B. J. & Uittenbogaard, R. E. 2006 The influence of wall permeability on turbulent channel flow. *J. Fluid Mech.* **562**, 35–72.

Brinkman, H. C. 1947 A calculation of the viscous force exerted by a flowing fluid on a dense swarm of particles. *Appl. Sci. Res.* **A1**, 27–34.

Busse, A. & Sandham, N. D. 2012 Influence of an anisotropic slip-length boundary condition on turbulent channel flow. *Phys. Fluids* **24**, 055111.

Canuto, C., Hussaini, M. Y., Quarteroni, A. M. & Zang, T. A. 1988 *Spectral methods in Fluid Dynamics*. Springer-Verlag, Berlin, Heidelberg.

Cess, R. D. 1958 A survey of the literature on heat transfer in turbulent tube flow. Report 8-0529-r24. Westinghouse Research.

Chang, M. 2006 Thermal convection in superposed fluid and porous layers subjected to a plane Poiseuille flow. *Phys. Fluids* **18**, 035104.

Choi, H., Moin, P. & Kim, J. 1994 Active turbulence control for drag reduction in wall-bounded flows. *J. Fluid Mech.* **262**, 75–110.

Clauser, F. H. 1956 The turbulent boundary layer. *Adv. App. Mech.* **4**, 1–51.

Cossu, C., Pujals, G. & Depardon, S. 2009 Optimal transient growth and very large–scale structures in turbulent boundary layers. *J. Fluid Mech.* **619**, 79–94.

Darcy, H. 1856 *Les fontaines publiques de la ville de Dijon*. Victor Dalmont, Paris.

Davit, Y., Bell, C. G., Byrne, H., Chapman, L. A. C., Kimpton, L. S., Lang, G. E., Leonard, K. H. L., Oliver, J. M., Pearson, N. C., Shipley, R. J., Waters, S. L., Whiteley, J. P., Wood, B. D. & Quintard, M. 2013 Homogenization via formal multiscale asymptotics and volume averaging: How do the two techniques compare? *Intl J. Numer. Meth. Fluids* **62**, 178–206.

Dawkins, P. T., Dunbar, S. R. & Douglass, R. W. 1998 The origin and nature of spurious eigenvalues in the spectral tau method. *J. Comput. Phys.* **147**, 441–462.

Deepu, P., Anand, P. & Basu, S. 2015 Stability of Poiseuille flow in a fluid overlying an anisotropic and inhomogeneous porous layer. *Phys. Rev. E* **92**, 023009.

Dupont, S., Gosselin, F., Py, C., De Langre, E., Hemon, P. & Brunet, Y. 2010 Modelling waving crops using large-eddy simulation: comparison with experiments and a linear stability analysis. *J. Fluid Mech.* **652**, 5–44.

Efstathiou, C. & Luhar, M. 2018 Mean turbulence statistics in boundary layers over high-porosity foams. *J. Fluid Mech.* **841**, 351–379.

Encinar, M. P., García-Mayoral, R. & Jiménez, J. 2014 Scaling of velocity fluctuations in off-wall boundary conditions for turbulent flows. *J. Phys. Conf. Ser.* **506**, 012002.

Eurostat statistics 2018 Greenhouse gas emission statistics. https://ec.europa.eu/eurostat/statistics-explained/index.php/Greenhouse_gas_emission_statistics_-_air_emissions_accounts, [Online; accessed 16-October-2018].

Fairhall, C. T. 2019 The influence of superhydrophobic surfaces on near-wall turbulence. PhD thesis, University of Cambridge.

Fairhall, C. T., Abderrahaman-Elena, N. & García-Mayoral, R. 2019 The effect of slip and surface texture on turbulence over superhydrophobic surfaces. *J. Fluid Mech.* **861**, 88–118.

Fairhall, C. T. & García-Mayoral, R. 2018 Spectral analysis of slip-length model for turbulence over textured superhydrophobic surfaces. *Flow Turb. Combust.* **100** (4), 961–978.

Ferziger, J. H. & Perić, M. 2002 *Computational methods for fluid dynamics*, 3rd edn. Springer.

Finnigan, J. 2000 Turbulence in plant canopies. *Annu. Rev. Fluid Mech.* **32**, 519–571.

Forchheimer, P. 1901 Wasserbewegung durch boden. *Z. Ver. Deutsch. Ing.* **45**, 1782–1788.

Frohnapfel, B., Hasegawa, Y. & Quadrio, M. 2012 Money versus time: evaluation of flow control in terms of energy consumption and convenience. *J. Fluid Mech.* **700**, 406–418.

Fukagata, K., Kasagi, N. & Koumoutsakos, P. 2006 A theoretical prediction of friction drag reduction in turbulent flow by superhydrophobic surfaces. *Phys. Fluids* **18**, 051703.

García-Mayoral, R. 2011 The interaction of riblets with wall-bounded turbulence. PhD thesis, Universidad Politécnica de Madrid.

García-Mayoral, R., Gómez-de-Segura, G. & Fairhall, C. T. 2019 The control of near-wall turbulence through surface texturing. *Fluid Dyn. Res.* **51** (1), 011410.

García-Mayoral, R. & Jiménez, J. 2011 Drag reduction by riblets. *Phil. Trans. R. Soc. A* **369**, 1412–1427.

García-Mayoral, R. & Jiménez, J. 2011 Hydrodynamic stability and breakdown of the viscous regime over riblets. *J. Fluid Mech.* **678**, 317–347.

García-Mayoral, R. & Jiménez, J. 2012 Scaling of turbulent structures in riblet channels up to $Re_\tau \approx 550$. *Phys. Fluids* **24**, 105101.

Gatti, D. & Quadrio, M. 2016 Reynolds-number dependence of turbulent skin-friction drag reduction induced by spanwise forcing. *J. Fluid Mech.* **802**, 553–582.

Ghisalberti, M. 2009 Obstructed shear flows: similarities across systems and scales. *J. Fluid Mech.* **641**, 51–61.

Gómez-de-Segura, G., Fairhall, C. T., MacDonald, M., Chung, D. & García-Mayoral, R. 2018*a* Manipulation of near-wall turbulence by surface slip and permeability. *J. Phys. Conf. Ser.* **1001**, 012011.

Gómez-de-Segura, G., Sharma, A. & García-Mayoral, R. 2018*b* Turbulent drag reduction using anisotropic permeable substrates. *Flow Turb. Combust.* **100** (4), 995–1014.

Gómez-de-Segura, G., Sharma, A. & García-Mayoral, R. 2018*c* Virtual origins in turbulent flows over complex surfaces. *2018 Proc. CTR Summer Program* pp. 277–286.

Gudmundsson, K. & Colonius, T. 2011 Instability wave models for the near-field fluctuations of turbulent jets. *J. Fluid Mech.* **689**, 97–128.

Hahn, S., Je, J. & Choi, H. 2002 Direct numerical simulation of turbulent channel flow with permeable walls. *J. Fluid Mech.* **450**, 259–285.

Hill, A. A. & Straughan, B. 2009 Poiseuille flow in a fluid overlying a highly porous material. *Adv. Water Res.* **32**, 1609–1614.

Hoyas, S. & Jiménez, J. 2006 Scaling of the velocity fluctuations in turbulent channels up to $Re_\tau = 2003$. *Phys. Fluids* **18**, 011702.

Hoyas, S. & Jiménez, J. 2008 Reynolds number effects on the Reynolds-stress budgets in turbulent channels. *Phys. Fluids* **20**, 101511.

IATA 2016 Iata forecasts passenger demand to double over 20 years. http://www.iata.org/pressroom/pr/Pages/2016-10-18-02.aspx, [Online: accessed 16-October-2018].

Ibrahim, J. I. & García-Mayoral, R. 2019 A unified approach to the study of turbulence over smooth and drag-reducing surfaces. In *11th International Symposium on Turbulence and Shear Flow Phenomena*.

Illingworth, S. J., Monty, J. P. & Marusic, I. 2018 Estimating large-scale structures in wall turbulence using linear models. *J. Fluid Mech.* **842**, 146–162.

Itoh, M., Tamano, S., Iguchi, R., Yokota, K., Akino, N., Hino, R. & Kubo, S. 2006 Turbulent drag reduction by the seal fur surface. *Phys. Fluids* **18**, 065102.

Jäger, W. & Mikelić, A. 2000 On the interface boundary condition of Beavers, Joseph and Saffman. *SIAM J. Appl. Math.* **60** (4), 1111–1127.

James, D. F. & Davis, A. M. J. 2001 Flow at the interface of a model fibrous porous medium. *J. Fluid Mech.* **426**, 47–72.

Jeong, J. & Hussain, F. 1995 On the identification of a vortex. *J. Fluid Mech.* **285**, 69–94.

Jeong, J., Hussain, F., Schoppa, W. & Kim, J. 1997 Coherent structures near the wall in a turbulent channel flow. *J. Fluid Mech.* **332**, 185–214.

Jiménez, J. 1994 On the structure and control of near wall turbulence. *Phys. Fluids* **6**, 944.

Jiménez, J. 2004 *Turbulence and vortex dynamics*. https://torroja.dmt.upm.es/area_alumnos/Introduccion_a_la_turbulencia/apuntes.pdf.

Jiménez, J. 2012 Cascades in wall-bounded turbulence. *Annu. Rev. Fluid Mech.* **44** (1), 27–45.

Jiménez, J. 2013*a* How linear is wall-bounded turbulence? *Phys. Fluids* **25**, 110814.

Jiménez, J. 2013*b* Near-wall turbulence. *Phys. Fluids* **25**, 101302.

Jiménez, J. 2018 Coherent structures in wall-bounded turbulence. *J. Fluid Mech.* **842**, P1.

Jiménez, J. & Moin, P. 1991 The minimal flow unit in near-wall turbulence. *J. Fluid Mech.* **225**, 221–240.

Jiménez, J. & Pinelli, A. 1999 The autonomous cycle of near-wall turbulence. *J. Fluid Mech.* **389**, 335–359.

Jiménez, J., Uhlmann, M., Pinelli, A. & Kawahara, G. 2001 Turbulent shear flow over active and passive porous surfaces. *J. Fluid Mech.* **442**, 89–117.

Joseph, D. D., Nield, D. A. & Papanicolaou, G. 1982 Nonlinear equation governing flow in a saturated porous medium. *Water Resour. Res.* **18** (4), 1049–1052.

Kawahara, M., Uhlmann, M. & van Veen, L. 2012 The significance of simple invariant solutions in turbulent flows. *Annu. Rev. Fluid Mech.* **44**, 203–225.

Kim, J. & Moin, P. 1985 Application of a fractional-step method to incompressible Navier-Stokes equations. *J. Comput. Phys.* **59** (2), 308–323.

Kline, S. J., Reynolds, W. C., Schraub, F. A. & Runstadler, P. W. 1967 The structure of turbulent boundary layers. *J. Fluid Mech.* **30** (4), 741–773.

Kong, F. & Schetz, J. 1982 Turbulent boundary layer over porous surfaces with different surface geometries. In *20th Aerospace Sciences Meeting*.

Kuwata, Y & Suga, K 2016 Lattice Boltzmann direct numerical simulation of interface turbulence over porous and rough walls. *Intl J. Heat and Fluid Flow* **61**, 145–157.

Kuwata, Y & Suga, K 2017 Direct numerical simulation of turbulence over anisotropic porous media. *J. Fluid Mech.* **831**, 41–71.

Lācis, U. & Bagheri, S. 2017 A framework for computing effective boundary conditions at the interface between free fluid and a porous medium. *J. Fluid Mech.* **812**, 866–889.

Le, H. & Moin, P. 1991 An improvement of fractional step methods for the incompressible Navier-Stokes equations. *J. Comput. Phys.* **92**, 369–379.

Le Bars, M. & Worster, M. G. 2006 Interfacial conditions between a pure fluid and a porous medium: implications for binary alloy solidification. *J. Fluid Mech.* **550**, 149–173.

Lee, M. & Moser, R. D. 2015 Direct numerical simulation of turbulent channel flow up to $Re_\tau = 5200$. *J. Fluid Mech.* **774** (1), 395–415.

Lévy, T. 1983 Fluid flow through an array of fixed particles. *Int. J. of Eng. Sci.* **21** (1), 11–23.

Liu, Q. & Prosperetti, A. 2011 Pressure-driven flow in a channel with porous walls. *J. Fluid Mech.* **679**, 77–100.

Lozano-Durán, A., Flores, O. & Jiménez, J. 2012 The three-dimensional structure of momentum transfer in turbulent channels. *J. Fluid Mech.* **694**, 100–130.

Lozano-Durán, A. & Jiménez, J. 2014 Effect of the computational domain on direct numerical simulations of turbulent channels up to $Re_\tau = 4200$. *Phys. Fluids* **26**, 011702.

Luchini, P. 1996 Reducing the turbulent skin friction. *Comput. Methods Appl. Sci. - Proc. 3rd ECCOMAS CFD Conf.* pp. 466–470.

Luchini, P., Manzo, F. & Pozzi, A. 1991 Resistance of a grooved surface to parallel flow and cross-flow. *J. Fluid Mech.* **228**, 87–109.

Lundgren, T. S. 1972 Slow flow through stationary random beds and suspensions of spheres. *J. Fluid Mech.* **51** (02), 273–299.

MacDonald, M., Chan, L., Chung, D., Hutchins, N. & Ooi, A. 2016 Turbulent flow over transitionally rough surfaces with varying roughness densities. *J. Fluid Mech.* **804**, 130–161.

MacDonald, M., Ooi, A., García-Mayoral, R., Hutchins, N. & Chung, D. 2018 Direct numerical simulation of high aspect ratio spanwise-aligned bars. *J. Fluid Mech.* **843**, 126–155.

Manes, C., Poggi, D. & Ridolfi, L. 2011 Turbulent boundary layers over permeable walls: scaling and near-wall structure. *J. Fluid Mech.* **687**, 141–170.

Matsumura, Y. & Jackson, T. L. 2014 Numerical simulation of fluid flow through random packs of cylinders using immersed boundary method. *Phys. Fluids* **26**, 043602.

Min, T. & Kim, J. 2004 Effects of hydrophobic surface on skin-friction drag. *Phys. Fluids* **16** (7), L55.

Minale, M. 2014 Momentum transfer within a porous medium. II. Stress boundary condition. *Phys. Fluids* **26**, 123102.

Mittal, S. 2008 Global linear stability analysis of time-averaged flows. *Intl J. Numer. Meth. Fluids* **58** (1), 111–118.

Mizuno, Y. & Jiménez, J. 2013 Wall turbulence without walls. *J. Fluid Mech.* **723**, 429–455.

Moin, P. & Mahesh, K. 1998 Direct numerical simulation: a tool in turbulence research. *J. Fluid Mech.* **30**, 539–578.

Moser, R. D., Kim, J. & Mansour, N. N. 1999 Direct numerical simulation of turbulent channel flow up to $Re_\tau = 590$. *Phys. Fluids* **11** (4), 943–945.

Neale, G. & Nader, W. 1974 Practical Significance of Brinkman extension of Darcy's Law. *Can. J. Chem. Eng.* **52**, 475–478.

Ochoa-Tapia, J. A. & Whitaker, S. 1995*a* Momentum transfer at the boundary between a porous medium and a homogeneous fluid–I. Theoretical development. *Intl J. Heat and Mass Transf.* **38** (14), 2635–2646.

Ochoa-Tapia, J. Alberto & Whitaker, S. 1995*b* Momentum transfer at the boundary between a porous medium and a homogeneous fluid–II. Comparison with experiment. *Intl J. Heat and Mass Transf.* **38** (14), 2647–2655.

Orlandi, P & Jiménez, J. 1994 On the generation of turbulent wall friction. *Phys. Fluids* **6** (12), 634–641.

Orlandi, P. & Leonardi, S. 2006 DNS of turbulent channel flows with two- and three-dimensional roughness. *J. Turb.* **7**, N73.

Orszag, S. A. 1971 On the Elimination of Aliasing in Finite-Difference Schemes by Filtering High-Wavenumber Components. *J. Atmos. Sci.* **28** (6), 1074.

Perot, J. B. 1993 An analysis of the fractional step method. *J. Comput. Phys.* **108**, 51–58.

Perot, J. B. 1995 Comments on the fractional step method. *J. Comput. Phys.* **121**, 190–195.

Pujals, G., García-Villalba, M., Cossu, C. & Depardon, S. 2009 A note on optimal transient growth in turbulent channel flows. *Phys. Fluids* **21**, 015109.

Py, C., De Langre, E. & Moulia, A. 2006 A frequency lock-in mechanism in the interaction between wind and crop canopies. *J. Fluid Mech.* **568**, 425–449.

Quadrio, M., Frohnapfel, B. & Hasegawa, Y. 2016 Does the choice of the forcing term affect flow statistics in DNS of turbulent channel flow? *Euro. J. Mech. B/Fluids* **500**, 286–293.

Raupach, M. R., Finnigan, J. J. & Brunei, Y. 1996 Coherent eddies and turbulence in vegetation canopies: the mixing-layer analogy. *Bound.-Lay. Meteorol.* **78** (3-4), 351–382.

Reynolds, W. C. & Hussain, A. K. M. F. 1972 The mechanics of an organized wave in turbulent shear flow. Part 3. Theoretical models and comparisons with experiments. *J. Fluid Mech.* **54**, 263–288.

Reynolds, W. C. & Tiederman, W. G. 1967 Stability of turbulent channel flow, with application to Malkus's theory. *J. Fluid Mech.* **27** (2), 253–272.

Rosti, M. E., Brandt, L. & Pinelli, A. 2018 Turbulent channel flow over an anisotropic porous wall – Drag increase and reduction. *J. Fluid Mech.* **842**, 381–394.

Rosti, M. E., Cortelezzi, L. & Quadrio, M. 2015 Direct numerical simulation of turbulent channel flow over porous walls. *J. Fluid Mech.* **784**, 396–442.

Rothstein, J. P. 2010 Slip on superhydrophobic surfaces. *Annu. Rev. Fluid Mech.* **42**, 89–109.

Saffman, P. G. 1971 On the boundary condition at the surface of a porous medium. *Stud. Applied Math.* **50** (2), 93–101.

Sangani, A. & Behl, S. 1989 The planar singular solutions of Stokes and Laplace equations and their application to transport processes near porous surfaces. *Phys. Fluids A* **1**, 21–37.

Sanmiguel Vila, C. & Flores, O. 2018 Wall-based identification of coherent structures in wall-bounded turbulence. *J. Phys. Conf. Ser.* **1001**, 012007.

Schmid, P. J. & Henningson, D. S. 2000 *Stability and transition in shear flows*. Springer, New York.

Schoppa, W. & Hussain, F. 2002 Coherent structure generation in near-wall turbulence. *J. Fluid Mech.* **453**, 57–108.

Seo, J., García-Mayoral, R. & Mani, A. 2015 Pressure fluctuations and interfacial robustness in turbulent flows over superhydrophobic surfaces. *J. Fluid Mech.* **783**, 448–473.

Seo, J., Garcia-Mayoral, R. & Mani, A. 2018 Turbulent flows over superhydrophobic surfaces: flow-induced capillary waves, and robustness of air–water interfaces. *J. Fluid Mech.* **835**, 45–85.

Seo, J. & Mani, A. 2016 On the scaling of the slip velocity in turbulent flows over superhydrophobic surfaces. *Phys. Fluids* **28**, 025110.

Seo, J. & Mani, A. 2018 Effect of texture randomization on the slip and interfacial robustness in turbulent flows over superhydrophobic surfaces. *Phys. Rev. Fluids* **3**, 044601.

Sharma, A. & García-Mayoral, R. 2019 Turbulent flows over dense canopies. *Submitted to J. Fluid Mech.* personal communication.

Simens, M. P. 2008 The study and control of wall bounded flows. PhD thesis, Universidad Politécnica de Madrid.

Sipp, D. & Lebedev, A. 2007 Global stability of base and mean flows: a general approach and its applications to cylinder and open cavity flows. *J. Fluid Mech.* **593**, 333–358.

Smith, C. R. & Metzler, S. P. 1983 The characteristics of low speed streaks in the near low region of a turbulent boundary layer. *J. Fluid Mech.* **129**, 27–54.

Spalart, P. R. 1988 Direct simulation of a turbulent boundary layer up to $R_\theta = 1410$. *J. Fluid Mech.* **187**, 61–98.

Spalart, P. R. & McLean, J. D. 2011 Drag reduction: enticing turbulence, and then an industry. *Phil. Trans. R. Soc. A* **369**, 1556–1569.

Suga, K., Matsumura, Y., Ashitaka, Y., Tominaga, S. & Kaneda, M. 2010 Effects of wall permeability on turbulence. *Intl J. Heat and Fluid Flow* **31** (6), 1–21.

Suga, K., Nakagawa, Y. & Kaneda, M. 2017 Spanwise turbulence structure over permeable walls. *J. Fluid Mech.* **822**, 186–201.

Suga, K., Okazaki, Y., Ho, U. & Kuwata, Y. 2018 Anisotropic wall permeability effects on turbulent channel flows. *J. Fluid Mech.* **855**, 983–1016.

Swearingen, J. D. & Blackwelder, R. F. 1987 The growth and breakdown of steamwise vortices in the presence of a wall. *J. Fluid Mech.* **182**, 255–290.

Tam, C. K. W. 1969 The drag on a cloud of spherical particles in low Reynolds number flow. *J. Fluid Mech.* **38** (3), 537–546.

Taylor, G. I. 1971 A model for boundary condition of a porous material. Part 1. *J. Fluid Mech.* **49** (2), 310–326.

Tennekes, H. & Lumley, J. L. 1972 *A first course in turbulence*. MIT Press.

Tilton, N. & Cortelezzi, L. 2008 Linear stability analysis of pressure-driven flows in channels with porous walls. *J. Fluid Mech.* **604**, 411–445.

Turton, S. E., Tuckerman, L. S. & Barkley, D. 2015 Prediction of frequencies in thermosolutal convection from mean flows. *Phys. Rev. E* **91**, 043009.

Vafai, K. & Kim, S. J. 1990 Fluid mechanics of the interface region between a porous medium and a fluid layer - an exact solution. *Intl J. Heat and Fluid Flow* **11** (3), 254–256.

Valdés-Parada, F. J., Aguilar-Madera, C. G., Ochoa-Tapia, J. A. & Goyeau, B. 2013 Velocity and stress jump conditions between a porous medium and a fluid. *Adv. Water Res.* **62**, 327–339.

Walsh, M. J. & Lindemann, A. M. 1984 Optimization and application of riblets for turbulent drag reduction. *AIAA Pap.* **84**, 0347.

Whitaker, S. 1986 Flow in porous media I: a theoretical derivation of Darcy's law. *Transp. Porous Media* **1**, 3–25.

Whitaker, S. 1996 The Forchheimer equation: a theoretical development. *Transp. Porous Media* **25**, 27–61.

Wilkinson, S. 1983 Influence of wall permeability on turbulent boundary-layer properties. In *21st Aerospace Sciences Meeting* (ed. USA Reno).

Ybert, C., Barentin, C., Cottin-Bizonne, C., Joseph, P. & Bocquet, L. 2007 Achieving large slip with superhydrophobic surfaces: Scaling laws for generic geometries. *Phys. Fluids* **19**, 123601.

Zagni, A. F. E. & Smith, K. V. H. 1976 Channel flow over permeable beds of graded spheres. *J. Hydraul. Res.* **102** (2), 207–222.

Zampogna, G. A. & Bottaro, A. 2016 Fluid flow over and through a regular bundle of rigid fibres. *J. Fluid Mech.* **792**, 5–35.

Zhang, Q. & Prosperetti, A. 2009 Pressure-driven flow in a two-dimensional channel with porous walls. *J. Fluid Mech.* **631**, 1–21.

Appendix A

Analytical solution of Brinkman's equation

The flow within the porous medium is approximated using Brinkman's equation (2.1), where K_x, K_y and K_z are the principal directions of the permeability tensor and are considered to be different. Together with the continuity equation, the system of equations is

$$\nu\left(\frac{\partial^2 u}{\partial x^2}+\frac{\partial^2 u}{\partial y^2}+\frac{\partial^2 u}{\partial z^2}\right)-\frac{\nu}{K_x}u-\frac{\partial p}{\partial x}=0, \tag{A.1a}$$

$$\nu\left(\frac{\partial^2 v}{\partial x^2}+\frac{\partial^2 v}{\partial y^2}+\frac{\partial^2 v}{\partial z^2}\right)-\frac{\nu}{K_y}v-\frac{\partial p}{\partial y}=0, \tag{A.1b}$$

$$\nu\left(\frac{\partial^2 w}{\partial x^2}+\frac{\partial^2 w}{\partial y^2}+\frac{\partial^2 w}{\partial z^2}\right)-\frac{\nu}{K_z}w-\frac{\partial p}{\partial z}=0, \tag{A.1c}$$

$$\frac{\partial u}{\partial x}+\frac{\partial v}{\partial y}+\frac{\partial w}{\partial z}=0, \tag{A.1d}$$

which can be solved analytically. Here we restrict ourselves to the permeable substrate at the bottom of the channel, which extends from $y=-h$ to $y=0$ and we neglect the influence of a mean pressure gradient within the substrate, as discussed in section 6.4.

In order to solve equation (A.1), we reduce this system of partial differential equation (PDE) with three dependent variables into a single equation with a single dependent variable. We start by taking the divergence of the Brinkman equation (A.1a)-(A.1c) and use the continuity equation (A.1d) to simplify, which yields

$$\frac{1}{K_x}\frac{\partial u}{\partial x}+\frac{1}{K_y}\frac{\partial v}{\partial y}+\frac{1}{K_z}\frac{\partial w}{\partial z}+\frac{1}{\nu}\nabla^2 p=0. \tag{A.2}$$

We then take the y-derivative of equation (A.2) and replace $\partial p/\partial y$ from equation (A.1b) to eliminate the pressure term. Using continuity again to remove the terms in w, the following PDE is obtained

$$\frac{\partial^2 u}{\partial x \partial y}\left(\frac{1}{K_x}-\frac{1}{K_z}\right)-\frac{1}{K_y}\left(\frac{\partial^2 v}{\partial x^2}+\frac{\partial^2 v}{\partial z^2}\right)-\frac{1}{K_z}\frac{\partial^2 v}{\partial y^2}+\nabla^4 v=0, \tag{A.3}$$

which has terms in v and u alone. To remove u, we take the y-derivative of equation (A.1a) and subtract the x-derivative of (A.1b). The obtained expression is then differentiated with respect to x, yielding

$$\left(\nabla^2-\frac{1}{K_x}\right)\frac{\partial^2 u}{\partial x \partial y}-\left(\nabla^2-\frac{1}{K_y}\right)\frac{\partial^2 v}{\partial x^2}=0. \tag{A.4}$$

Substituting for $\partial^2 u/\partial x \partial y$ from equation (A.3), a single equation for v is obtained. This equation can be solved by expanding in Fourier series along x and z, so that $v(x,y,z)=\hat{v}(y)\mathrm{e}^{i\alpha_x x}\mathrm{e}^{i\alpha_z z}$, where α_x and α_z are the wavenumbers, i the imaginary unit, $i=\sqrt{-1}$, and the hat indicates variables in Fourier space. Differentiating in x and z becomes then multiplying by $i\alpha_x$ and $i\alpha_z$, respectively, leading to the following ordinary differential equation (ODE)

$$\begin{aligned}&\left\{D^6+D^4\left[-3\alpha^2-\frac{1}{K_x}-\frac{1}{K_z}\right]+D^2\left[\frac{1}{K_y}\alpha^2+\left(2\alpha^2+\frac{1}{K_z}\right)\left(\alpha^2+\frac{1}{K_x}\right)+\alpha^4-\right.\right.\\&\left.\left.\alpha_x^2\left(\frac{1}{K_x}-\frac{1}{K_z}\right)\right]+\left[\left(\alpha^2+\frac{1}{K_y}\right)\left(-\alpha^2\left(\alpha^2+\frac{1}{K_x}\right)+\alpha_x^2\left(\frac{1}{K_x}-\frac{1}{K_z}\right)\right)\right]\right\}\hat{v}=0,\end{aligned} \tag{A.5}$$

where $D\equiv\partial/\partial y$ and $\alpha^2=\alpha_x^2+\alpha_z^2$. This is a sixth order equation, where all the derivatives are even, and the corresponding characteristic equation, obtained by substituting $D^i\hat{v}$ with r^i $(i=\{0,2,4,6\})$, is a bicubic equation

$$a_3 r^6+a_2 r^4+a_1 r^2+a_0=0, \tag{A.6}$$

where the coefficients

$$\begin{cases}a_3=1,\\ a_2=-3\alpha^2-\dfrac{1}{K_x}-\dfrac{1}{K_z},\\ a_1=\dfrac{1}{K_y}\alpha^2+\left(2\alpha^2+\dfrac{1}{K_z}\right)\left(\alpha^2+\dfrac{1}{K_x}\right)+\alpha^4-\alpha_x^2\left(\dfrac{1}{K_x}-\dfrac{1}{K_z}\right),\\ a_0=\left(\alpha^2+\dfrac{1}{K_y}\right)\left(-\alpha^2\left(\alpha^2+\dfrac{1}{K_x}\right)+\alpha_x^2\left(\dfrac{1}{K_x}-\dfrac{1}{K_z}\right)\right).\end{cases}$$

This equation can be reduced to a cubic equation and then solved algebraically. If the discriminant of equation (A.6) is non-zero, i.e. $\Delta = 18a_3a_2a_1a_0 - 4a_2^3a_0 + a_2^2a_1^2 - 4a_3a_1^3 - 27a_3^2a_0^2 \neq 0$, there are 6 different roots. The roots of the original equation (A.6) are denoted as $\pm r_1$, $\pm r_2$ and $\pm r_3$ and the general solution for $\hat{v}$ is then

$$\hat{v}(y) = A\mathrm{e}^{+r_1 y} + B\mathrm{e}^{-r_1 y} + C\mathrm{e}^{+r_2 y} + D\mathrm{e}^{-r_2 y} + E\mathrm{e}^{+r_3 y} + F\mathrm{e}^{-r_3 y}. \tag{A.7}$$

The constants A, B, C, D, E and F are determined once the boundary conditions are imposed and are a function of the geometry and the wavenumbers, α_x and α_z. Similar expressions for the pressure and the streamwise and spanwise velocities can be obtained by substitutions into equations (A.1b), (A.3), and the continuity equation (A.1d), respectively,

$$\begin{aligned}\hat{p}(y) = \nu\Big[r_1\left(A\mathrm{e}^{+r_1 y} - B\mathrm{e}^{-r_1 y}\right) + r_2\left(C\mathrm{e}^{+r_2 y} - D\mathrm{e}^{-r_2 y}\right) + r_3\left(E\mathrm{e}^{+r_3 y} - F\mathrm{e}^{-r_3 y}\right)\Big] \\ - \nu\left(\alpha^2 + \frac{1}{K_y}\right)\Big[\frac{1}{r_1}\left(A\mathrm{e}^{+r_1 y} - B\mathrm{e}^{-r_1 y}\right) + \frac{1}{r_2}\left(C\mathrm{e}^{+r_2 y} - D\mathrm{e}^{-r_2 y}\right) + \\ \frac{1}{r_3}\left(E\mathrm{e}^{+r_3 y} - F\mathrm{e}^{-r_3 y}\right)\Big],\end{aligned} \tag{A.8}$$

$$\begin{aligned}\hat{u}(y) = i\frac{1}{1/K_x - 1/K_z}\frac{\alpha^2}{\alpha_x}\left(\frac{1}{K_y} + \alpha^2\right)\Big[\frac{A}{r_1}\mathrm{e}^{+r_1 y} - \frac{B}{r_1}\mathrm{e}^{-r_1 y} + \frac{C}{r_2}\mathrm{e}^{+r_2 y} - \frac{D}{r_2}\mathrm{e}^{-r_2 y} \\ + \frac{E}{r_3}\mathrm{e}^{+r_3 y} - \frac{F}{r_3}\mathrm{e}^{-r_3 y}\Big] - i\frac{1}{1/K_x - 1/K_z}\frac{1}{\alpha_x}\left(\frac{1}{K_z} + 2\alpha^2\right)\Big[Ar_1\mathrm{e}^{+r_1 y} \\ - Br_1\mathrm{e}^{-r_1 y} + Cr_2\mathrm{e}^{+r_2 y} - Dr_2\mathrm{e}^{-r_2 y} + Er_3\mathrm{e}^{+r_3 y} - Fr_3\mathrm{e}^{-r_3 y}\Big] \\ + i\frac{1}{1/K_x - 1/K_z}\frac{1}{\alpha_x}\Big[Ar_1^3\mathrm{e}^{+r_1 y} - Br_1^3\mathrm{e}^{-r_1 y} + Cr_2^3\mathrm{e}^{+r_2 y} - Dr_2^3\mathrm{e}^{-r_2 y} + Er_3^3\mathrm{e}^{+r_3 y} - Fr_3^3\mathrm{e}^{-r_3 y}\Big],\end{aligned} \tag{A.9}$$

$$\hat{w}(y) = -\frac{\alpha_x}{\alpha_z}\hat{u} + i\frac{1}{\alpha_z}\frac{d\hat{v}}{dy}. \tag{A.10}$$

To obtain A, B, C, D, E and F, the boundary conditions need to be considered. The permeable substrate is delimited by an impermeable solid wall at the bottom, where no-slip and impermeability conditions are imposed, and by the free channel flow at the top, where continuity of the normal and tangential stresses holds, together with the continuity of the three velocity components. The boundary conditions at the substrate-channel interface have already been introduced in equation (2.2). Expanding these boundary conditions in Fourier space, and assuming $\tilde{\nu} \approx \nu$, the continuity of the normal and tangential stresses at the

interface simplifies to the continuity of pressure and wall-normal shear ($d\hat{u}/dy$ and $d\hat{w}/dy$), respectively. Thus, the boundary conditions for the permeable substrates are

$$\hat{u} = \hat{w} = \hat{v} = 0 \quad \text{at} \quad y = -h, \quad \text{and} \tag{A.11a}$$

$$\left.\frac{d\hat{u}}{dy}\right|_{y=0^-} = \left.\frac{d\hat{u}}{dy}\right|_{y=0^+}, \quad \left.\frac{d\hat{w}}{dy}\right|_{y=0^-} = \left.\frac{d\hat{w}}{dy}\right|_{y=0^+}, \quad \hat{p}|_{y=0^-} = \hat{p}|_{y=0^+} \quad \text{at} \quad y = 0, \tag{A.11b}$$

where, at $y = 0$, the plus and minus signs correspond to the fluid and substrate sides of the interface, respectively.

By applying the above boundary conditions to equations (A.7), (A.9), (A.10) and (A.8), the particular solution at the substrate-channel interface is

$$\hat{u}|_{y=0^-} = \mathcal{C}_{uu}(\alpha_x, \alpha_z)\left.\frac{d\hat{u}}{dy}\right|_{y=0^+} + \mathcal{C}_{uw}(\alpha_x, \alpha_z)\left.\frac{d\hat{w}}{dy}\right|_{y=0^+} + \mathcal{C}_{up}(\alpha_x, \alpha_z)\hat{p}|_{y=0^+}, \tag{A.12a}$$

$$\hat{w}|_{y=0^-} = \mathcal{C}_{wu}(\alpha_x, \alpha_z)\left.\frac{d\hat{u}}{dy}\right|_{y=0^+} + \mathcal{C}_{ww}(\alpha_x, \alpha_z)\left.\frac{d\hat{w}}{dy}\right|_{y=0^+} + \mathcal{C}_{wp}(\alpha_x, \alpha_z)\hat{p}|_{y=0^+}, \tag{A.12b}$$

$$\hat{v}|_{y=0^-} = \mathcal{C}_{vu}(\alpha_x, \alpha_z)\left.\frac{d\hat{u}}{dy}\right|_{y=0^+} + \mathcal{C}_{vw}(\alpha_x, \alpha_z)\left.\frac{d\hat{w}}{dy}\right|_{y=0^+} + \mathcal{C}_{vp}(\alpha_x, \alpha_z)\hat{p}|_{y=0^+}, \tag{A.12c}$$

where the coefficients $\mathcal{C}_{ij}(\alpha_x, \alpha_z)$ are a function of the wavenumbers, α_x and α_z, and of the geometry of the substrate, i.e. K_x, K_y, K_z and h. An equivalent analysis can be carried out for the upper permeable substrate. Considering the symmetry properties for each variable yields

$$\hat{u}|_{y=(2\delta)^+} = -\mathcal{C}_{uu}(\alpha_x, \alpha_z)\left.\frac{d\hat{u}}{dy}\right|_{y=(2\delta)^-} - \mathcal{C}_{uw}(\alpha_x, \alpha_z)\left.\frac{d\hat{w}}{dy}\right|_{y=(2\delta)^-} + \mathcal{C}_{up}(\alpha_x, \alpha_z)\hat{p}|_{y=(2\delta)^-}, \tag{A.13a}$$

$$\hat{w}|_{y=(2\delta)^+} = -\mathcal{C}_{wu}(\alpha_x, \alpha_z)\left.\frac{d\hat{u}}{dy}\right|_{y=(2\delta)^-} - \mathcal{C}_{ww}(\alpha_x, \alpha_z)\left.\frac{d\hat{w}}{dy}\right|_{y=(2\delta)^-} + \mathcal{C}_{wp}(\alpha_x, \alpha_z)\hat{p}|_{y=(2\delta)^-}, \tag{A.13b}$$

$$\hat{v}|_{y=(2\delta)^+} = \mathcal{C}_{vu}(\alpha_x, \alpha_z)\left.\frac{d\hat{u}}{dy}\right|_{y=(2\delta)^-} + \mathcal{C}_{vw}(\alpha_x, \alpha_z)\left.\frac{d\hat{w}}{dy}\right|_{y=(2\delta)^-} - \mathcal{C}_{vp}(\alpha_x, \alpha_z)\hat{p}|_{y=(2\delta)^-}. \tag{A.13c}$$

When $\alpha_x = 0$ or $\alpha_z = 0$, Brinkman's equation simplifies and so does its solution. These cases are solved separately in sections A.1, A.2 and A.3.

A.1 Modes $\alpha_x \neq 0$, $\alpha_z = 0$

When $\alpha_z = 0$, the z-derivatives become zero and the Brinkman equation for w, i.e. equation (A.1c), decouples from the other two. The original system of equations simplifies then to

$$\nu\left(\frac{\partial^2 u}{\partial x^2} + \frac{\partial^2 u}{\partial y^2}\right) - \frac{\nu}{K_x}u - \frac{\partial p}{\partial x} = 0, \tag{A.14a}$$

$$\nu\left(\frac{\partial^2 v}{\partial x^2} + \frac{\partial^2 v}{\partial y^2}\right) - \frac{\nu}{K_y}v - \frac{\partial p}{\partial y} = 0, \tag{A.14b}$$

$$\left(\frac{\partial^2 w}{\partial x^2} + \frac{\partial^2 w}{\partial y^2}\right) - \frac{1}{K_z}w = 0, \tag{A.14c}$$

$$\frac{\partial u}{\partial x} + \frac{\partial v}{\partial y} = 0. \tag{A.14d}$$

The velocities u and v can be solved with a procedure similar to that described above, while w can be solved separately.

Taking the two-dimensional divergence of equations (A.14a) and (A.14b) in the (x, y) plane and using continuity yields

$$\left(\frac{1}{K_y} - \frac{1}{K_x}\right)\frac{\partial v}{\partial y} + \frac{1}{\nu}\nabla^2_{xy} p = 0. \tag{A.15}$$

Taking the y-derivative of equation (A.14b) and substituting $\partial v/\partial y$ from (A.15) yields an equation in p alone. Taking the Fourier transform in x leads to

$$\left\{D^4 + \left[-2\alpha_x^2 - \frac{1}{K_x}\right]D^2 + \alpha_x^2\left[\alpha_x^2 + \frac{1}{K_y}\right]\right\}\hat{p} = 0. \tag{A.16}$$

The corresponding characteristic equation is biquadratic,

$$m^4 + m^2\left(-2\alpha_x^2 - \frac{1}{K_x}\right) + \left(\alpha_x^4 + \frac{\alpha_x^2}{K_y}\right) = 0. \tag{A.17}$$

Rewriting (A.17) as a second order equation, the roots of the characteristic equation are

$$\pm m_1 = \pm\sqrt{\frac{1 + 2\alpha_x^2 K_x + \sqrt{4\alpha_x^2 K_x\left(1 - \frac{K_x}{K_y}\right) + 1}}{2K_x}},$$

$$\pm m_2 = \pm\sqrt{\frac{1 + 2\alpha_x^2 K_x - \sqrt{4\alpha_x^2 K_x\left(1 - \frac{K_x}{K_y}\right) + 1}}{2K_x}}.$$

Except for the case in which $m_1 = m_2$, i.e. $\frac{K_x}{K_y} = 1 + 1/(4\alpha_x^2 K_x)$, the expression for $\hat{p}$ becomes:

$$\hat{p}(y) = A'\mathrm{e}^{m_1 y} + B'\mathrm{e}^{-m_1 y} + C'\mathrm{e}^{m_2 y} + D'\mathrm{e}^{-m_2 y}, \tag{A.18}$$

where A', B', C' and D' depend on the wavenumber α_x and the geometrical properties of the permeable medium, K_x and K_y, and are determined by imposing the boundary conditions – impermeability and no slip conditions at $y = -h$, and continuity of pressure and $d\hat{u}/dy$ at $y = 0$. The general solutions for $\hat{u}$ and $\hat{v}$ are obtained by appropriate substitutions from equations (A.14d) and (A.15), respectively, which yields

$$\hat{u} = -\frac{i}{\alpha_x \nu \left(\frac{1}{K_y} - \frac{1}{K_x}\right)} \Big[\left(m_1^2 - \alpha_x^2\right) \left(A e^{m_1 y} + B e^{-m_1 y}\right) + \left(m_2^2 - \alpha_x^2\right) \left(C e^{m_2 y} + D e^{-m_2 y}\right) \Big], \tag{A.19}$$

$$\hat{v} = -\frac{1}{\nu \left(\frac{1}{K_y} - \frac{1}{K_x}\right)} \left[\left(m_1 - \frac{\alpha_x^2}{m_1}\right) \left(A e^{m_1 y} - B e^{-m_1 y}\right) + \left(m_2 - \frac{\alpha_x^2}{m_2}\right) \left(C e^{m_2 y} - D e^{-m_2 y}\right) \right]. \tag{A.20}$$

As before, imposing the boundary conditions to equations (A.18), (A.19) and (A.20), impermeability and no-slip condition at the bottom limit, and continuity of tangential and normal stresses at the substrate-channel interface, the solution for $\hat{u}$ and $\hat{v}$ is obtained. Taking the solution at $y = 0$, the streamwise and wall-normal velocities at the interface are reduced to the following form

$$\hat{u}|_{y=0^-} \equiv \mathcal{C}_{up}(\alpha_x, 0)\hat{p}|_{y=0^+} + \mathcal{C}_{uu}(\alpha_x, 0)\frac{d\hat{u}}{dy}\bigg|_{y=0^+}, \tag{A.21a}$$

$$\hat{v}|_{y=0^-} \equiv \mathcal{C}_{vp}(\alpha_x, 0)\hat{p}|_{y=0^+} + \mathcal{C}_{vu}(\alpha_x, 0)\frac{d\hat{u}}{dy}\bigg|_{y=0^+}. \tag{A.21b}$$

Comparing to the general expressions in (A.12), the coefficients $\mathcal{C}_{uw}(\alpha_x, 0)$ and $\mathcal{C}_{vw}(\alpha_x, 0)$ are zero, which was expected, as there is no coupling between $\hat{w}$, and the other two velocities, $\hat{u}$ and $\hat{v}$, for modes $(\alpha_x, 0)$. Similar interface conditions can also be obtained for the upper substrate. By symmetry,

$$\hat{u}|_{y=(2\delta)^+} \equiv \mathcal{C}_{up}\hat{p}|_{y=(2\delta)^-} - \mathcal{C}_{uu}\frac{d\hat{u}}{dy}\bigg|_{y=(2\delta)^-}. \tag{A.22a}$$

$$\hat{v}|_{y=(2\delta)^+} \equiv -\mathcal{C}_{vp}\hat{p}|_{y=(2\delta)^-} + \mathcal{C}_{vu}\frac{d\hat{u}}{dy}\bigg|_{y=(2\delta)^-}, \tag{A.22b}$$

In contrast, solving equation (A.14c) for $\hat{w}$ is straightforward. Expanding it as a Fourier series gives

$$\frac{\partial^2 \hat{w}}{\partial y^2} - \left(\alpha_x^2 + \frac{1}{K_z}\right)\hat{w} = 0, \tag{A.23}$$

whose solution is

$$\hat{w} = E'_{x0} \mathrm{e}^{y/L_w} + F'_{x0} \mathrm{e}^{-y/L_w}, \tag{A.24}$$

where $L_w = 1/\sqrt{\alpha_x^2 + 1/K_z}$. Applying now the boundary conditions for $\hat{w}$, $\hat{w} = 0$ at the impermeable wall and continuity of $d\hat{w}/dy$ at the interface, leads to

$$\hat{w} = L_w \frac{\mathrm{e}^{(y+h)/L_w} - \mathrm{e}^{-(y+h)/L_w}}{\mathrm{e}^{h/L_w} + \mathrm{e}^{-h/L_w}} \left.\frac{d\hat{w}}{dy}\right|_{y=0^+}. \tag{A.25}$$

Comparing to the expressions presented in (A.12), $\mathcal{C}_{ww}(\alpha_x, 0)$ is the proportionality term in equation (A.25) between $\hat{w}$ and its gradient, whereas $\mathcal{C}_{wu}(\alpha_x, 0) = \mathcal{C}_{wp}(\alpha_x, 0) = 0$. Hence, in this case the nine coefficients presented for the general interface conditions (A.12) are reduced to only five.

A.2 Modes $\alpha_x = 0$, $\alpha_z \neq 0$

In this case, Brinkman's equation for u decouples from the other two. For cases with the same permeability in y and z directions, $K_z = K_y$, the solution simplifies to

$$\left(\frac{\partial^2 u}{\partial y^2} + \frac{\partial^2 u}{\partial z^2}\right) - \frac{1}{K_x} u = 0, \tag{A.26a}$$

$$\nu\left(\frac{\partial^2 v}{\partial y^2} + \frac{\partial^2 v}{\partial z^2}\right) - \frac{\nu}{K_y} v - \frac{\partial p}{\partial y} = 0, \tag{A.26b}$$

$$\nu\left(\frac{\partial^2 w}{\partial y^2} + \frac{\partial^2 w}{\partial z^2}\right) - \frac{\nu}{K_y} w - \frac{\partial p}{\partial z} = 0, \tag{A.26c}$$

$$\frac{\partial v}{\partial y} + \frac{\partial w}{\partial z} = 0. \tag{A.26d}$$

Taking the two-dimensional divergence of equations (A.26b) and (A.26c) in the (y, z) plane leads to a Laplace equation for the pressure. We then take the Fourier transform with respect to z (i.e. $p(y, z) = \hat{p}(y)\mathrm{e}^{i\alpha_z z}$) to get

$$\hat{p}(y) = A'' \mathrm{e}^{\alpha_z y} + B'' \mathrm{e}^{-\alpha_z y}. \tag{A.27}$$

The general expressions for $\hat{v}$ and $\hat{w}$ can then be derived from the equations (A.26b) and (A.26d), respectively, as a function of constants A'' and B'' and two new constants C'' and D''. These constants are obtained by applying the boundary conditions for $\hat{p}$, $\hat{v}$ and $\hat{w}$ from (A.11).

The streamwise velocity is solved similarly to w in section A.1. We take the Fourier transform of equation (A.26a) in z, which gives

$$\frac{\partial^2 \hat{u}}{\partial y^2} - \left(\alpha_z^2 + \frac{1}{K_x}\right)\hat{u} = 0. \tag{A.28}$$

The solution, after applying the boundary conditions for $\hat{u}$, is

$$\hat{u} = L_u \frac{\mathrm{e}^{(y+h)/L_u} - \mathrm{e}^{-(y+h)/L_u}}{\mathrm{e}^{h/L_u} + \mathrm{e}^{-h/L_u}} \left.\frac{d\hat{u}}{dy}\right|_{y=0^+}, \tag{A.29}$$

where $L_u = 1/\sqrt{\alpha_z^2 + 1/K_x}$. The proportionality coefficient relating $\hat{u}$ with its gradient is the coefficient $\mathcal{C}_{uu}(0, \alpha_z)$, i.e.

$$\mathcal{C}_{uu}(0, \alpha_z) = L_u \frac{\mathrm{e}^{(y+h)/L_u} - \mathrm{e}^{-(y+h)/L_u}}{\mathrm{e}^{h/L_u} + \mathrm{e}^{-h/L_u}}, \tag{A.30}$$

and $\mathcal{C}_{up}(0, \alpha_z) = \mathcal{C}_{uw}(0, \alpha_z) = \mathcal{C}_{wu}(0, \alpha_z) = \mathcal{C}_{vu}(0, \alpha_z) = 0$.

A.3 Mode $\alpha_x = 0$, $\alpha_z = 0$

Although the coefficients for the mean can be directly obtained from the expressions derived in sections A.1 and A.2, this case deserves further discussion. When $\alpha_x = \alpha_z = 0$, the equations for u, v and w decouple from each other and the velocities for mode zero become

$$\hat{u} = \sqrt{K_x} \frac{\mathrm{e}^{(y+h)/\sqrt{K_x}} - \mathrm{e}^{-(y+h)/\sqrt{K_x}}}{\mathrm{e}^{h/\sqrt{K_x}} + \mathrm{e}^{-h/\sqrt{K_x}}} \left.\frac{d\hat{u}}{dy}\right|_{y=0^+}, \tag{A.31a}$$

$$\hat{w} = \sqrt{K_z} \frac{\mathrm{e}^{(y+h)/\sqrt{K_z}} - \mathrm{e}^{-(y+h)/\sqrt{K_z}}}{\mathrm{e}^{h/\sqrt{K_z}} + \mathrm{e}^{-h/\sqrt{K_z}}} \left.\frac{d\hat{w}}{dy}\right|_{y=0^+}, \tag{A.31b}$$

$$\hat{v} = 0. \tag{A.31c}$$

Equations (A.31a) and (A.31b) are obtained from equations (A.25) and (A.29) for $\alpha_z = 0$ and $\alpha_x = 0$, respectively, while equation (A.31c) is obtained from continuity, after applying the boundary condition that $\hat{v} = 0$ at $y = 0$. Comparing the particular at $y = 0$ to the general boundary conditions introduced in equation (A.12), we have

$$\hat{u}|_{y=0} = \sqrt{K_x} \tanh\left(\frac{h}{\sqrt{K_x}}\right) \left.\frac{d\hat{u}}{dy}\right|_{y=0^+} = \mathcal{C}_{uu}(0,0) \left.\frac{d\hat{u}}{dy}\right|_{y=0^+}, \tag{A.32a}$$

$$\hat{w}|_{y=0} = \sqrt{K_z} \tanh\left(\frac{h}{\sqrt{K_z}}\right) \left.\frac{d\hat{w}}{dy}\right|_{y=0^+} = \mathcal{C}_{ww}(0,0) \left.\frac{d\hat{w}}{dy}\right|_{y=0^+}, \tag{A.32b}$$

$$\hat{v}|_{y=0} = 0, \tag{A.32c}$$

where all the coefficients from equation (A.12) are zero except for $\mathcal{C}_{uu}$ and $\mathcal{C}_{ww}$, which relate the tangential velocities to their wall-normal gradient. These are the mean slip lengths ℓ_x^+ and ℓ_z^+ derived by Abderrahaman-Elena & García-Mayoral (2017).

Appendix B

Analytical solution of Stokes equation

One of the techniques used in chapter 3 to model the effect of virtual origins is Stokes model. We assume that the flow between the virtual walls and the boundaries of the channel can be modelled as a Stokes flow, which can be solved analytically. Together with the continuity equation, the system of equations to solve is

$$\left(\frac{\partial^2 u}{\partial x^2}+\frac{\partial^2 u}{\partial y^2}+\frac{\partial^2 u}{\partial z^2}\right)-\frac{1}{\nu}\frac{\partial p}{\partial x}=0, \tag{B.1a}$$

$$\left(\frac{\partial^2 v}{\partial x^2}+\frac{\partial^2 v}{\partial y^2}+\frac{\partial^2 v}{\partial z^2}\right)-\frac{1}{\nu}\frac{\partial p}{\partial y}=0, \tag{B.1b}$$

$$\left(\frac{\partial^2 w}{\partial x^2}+\frac{\partial^2 w}{\partial y^2}+\frac{\partial^2 w}{\partial z^2}\right)-\frac{1}{\nu}\frac{\partial p}{\partial z}=0, \tag{B.1c}$$

$$\frac{\partial u}{\partial x}+\frac{\partial v}{\partial y}+\frac{\partial w}{\partial z}=0. \tag{B.1d}$$

Here we restrict ourselves to the bottom boundary of the channel. The above system is then solved between the virtual wall, which is located at $y=-\ell$, and the plane where the boundary conditions are applied, located at $y=0$. The procedure followed to solve equation (B.1) is similar to that detailed in appendix A for the solution of Brinkman's equation, although simpler. As with Brinkman's equation, we start by taking the divergence of the Stokes equation (B.1a)-(B.1c) and use the continuity equation (B.1d) to simplify, which yields the Laplace equation for the pressure,

$$\nabla^2 p=0. \tag{B.2}$$

The problem is solved by expanding in Fourier series along x and z, so for equation (B.2) $p(x,y,z) = \hat{p}(y)\mathrm{e}^{i\alpha_x x}\mathrm{e}^{i\alpha_z z}$. The roots of the corresponding characteristic equation are $\pm r = \pm\sqrt{\alpha_x^2+\alpha_z^2}$. The general solution for $\hat{p}$ is then

$$\hat{p}(y) = A_S \mathrm{e}^{+ry} + B_S \mathrm{e}^{-ry}, \tag{B.3}$$

where the constants A_S and B_S are determined once the boundary conditions are imposed. Similar expressions for the three velocity components can be obtained. Using the expression for the pressure (B.3) in equation (B.1a) and (B.1b), yields

$$\hat{v}(y) = \left(C_S + \frac{y}{2\nu}A_S\right)\mathrm{e}^{+ry} + \left(D_S + \frac{y}{2\nu}B_S\right)\mathrm{e}^{-ry}, \tag{B.4}$$

$$\hat{u}(y) = \left(E_S + i\frac{\alpha_x y}{2\nu\sqrt{\alpha_x^2+\alpha_z^2}}A_S\right)\mathrm{e}^{+ry} + \left(F_S - i\frac{\alpha_x y}{2\nu\sqrt{\alpha_x^2+\alpha_z^2}}B_S\right)\mathrm{e}^{-ry}, \tag{B.5}$$

and from continuity

$$\hat{w}(y) = -\frac{\alpha_x}{\alpha_z}\hat{u} + i\frac{1}{\alpha_z}\frac{d\hat{v}}{dy}. \tag{B.6}$$

To obtain A_S, B_S, C_S, D_S, E_S and F_S, the boundary conditions need to be considered. This system is solved as a response to the overlying tangential shear, $d\hat{u}/dy$ and $d\hat{w}/dy$, and the pressure, $\hat{p}$, at the reference plane $y = 0$; and with no-slip and impermeability conditions at the virtual wall, $y = -\ell$. Thus, the boundary conditions are

$$\hat{u} = \hat{w} = \hat{v} = 0 \quad \text{at} \quad y = -\ell, \quad \text{and} \tag{B.7a}$$

$$\left.\frac{d\hat{u}}{dy}\right|_{y=0^-} = \left.\frac{d\hat{u}}{dy}\right|_{y=0^+}, \quad \left.\frac{d\hat{w}}{dy}\right|_{y=0^-} = \left.\frac{d\hat{w}}{dy}\right|_{y=0^+}, \quad \hat{p}|_{y=0^-} = \hat{p}|_{y=0^+} \quad \text{at} \quad y = 0, \tag{B.7b}$$

where, at $y = 0$, the plus and minus signs correspond to the sides immediately above and below the reference plane, respectively.

By applying the above boundary conditions to equations (B.3), (B.4), (B.5) and (B.6), the particular the solution at the reference plane $y = 0$ is

$$\hat{u}|_{y=0} = \mathcal{C}_{S,uu}\left.\frac{d\hat{u}}{dy}\right|_{y=0^+} + \mathcal{C}_{S,uw}\left.\frac{d\hat{w}}{dy}\right|_{y=0^+} + \mathcal{C}_{S,up}\hat{p}|_{y=0^+}, \tag{B.8a}$$

$$\hat{w}|_{y=0} = \mathcal{C}_{S,wu}\left.\frac{d\hat{u}}{dy}\right|_{y=0^+} + \mathcal{C}_{S,ww}\left.\frac{d\hat{w}}{dy}\right|_{y=0^+} + \mathcal{C}_{S,wp}\hat{p}|_{y=0^+}, \tag{B.8b}$$

$$\hat{v}|_{y=0} = \mathcal{C}_{S,vu}\left.\frac{d\hat{u}}{dy}\right|_{y=0^+} + \mathcal{C}_{S,vw}\left.\frac{d\hat{w}}{dy}\right|_{y=0^+} + \mathcal{C}_{S,vp}\hat{p}|_{y=0^+}, \tag{B.8c}$$

where the coefficients $\mathcal{C}_{S,ij}$ are a function of the wavenumbers, α_x and α_z, and of the depth of the virtual origin, ℓ. An equivalent analysis can be carried out for the upper boundary, which considering the symmetry properties for each variable, yields

$$\hat{u}|_{y=(2\delta)} = -\mathcal{C}_{S,uu}\frac{d\hat{u}}{dy}\bigg|_{y=(2\delta)^-} - \mathcal{C}_{S,uw}\frac{d\hat{w}}{dy}\bigg|_{y=(2\delta)^-} + \mathcal{C}_{S,up}\hat{p}|_{y=(2\delta)^-}\,, \tag{B.9a}$$

$$\hat{w}|_{y=(2\delta)} = -\mathcal{C}_{S,wu}\frac{d\hat{u}}{dy}\bigg|_{y=(2\delta)^-} - \mathcal{C}_{S,ww}\frac{d\hat{w}}{dy}\bigg|_{y=(2\delta)^-} + \mathcal{C}_{S,wp}\hat{p}|_{y=(2\delta)^-}\,, \tag{B.9b}$$

$$\hat{v}|_{y=(2\delta)} = \mathcal{C}_{S,vu}\frac{d\hat{u}}{dy}\bigg|_{y=(2\delta)^-} + \mathcal{C}_{S,vw}\frac{d\hat{w}}{dy}\bigg|_{y=(2\delta)^-} - \mathcal{C}_{S,vp}\hat{p}|_{y=(2\delta)^-}\,. \tag{B.9c}$$

Appendix C

Mean velocity profile for linear stability analysis

Following Reynolds & Tiederman (1967), the equations for the turbulent mean velocity profile, $U(y)$, assumed parallel, are obtained by decomposing the flow as the sum of a mean and a fluctuation, $(u, 0) = (U(y) + u', v')$ and averaging in x, which yields

$$\frac{d}{dy}\left(\overline{u'v'}\right) = -\frac{\partial P}{\partial x} + \nu\frac{d^2U}{dy^2}, \tag{C.1a}$$

$$\frac{d\overline{v'^2}}{dy} = -\frac{\partial P}{\partial y}. \tag{C.1b}$$

The Reynolds stress is modelled using the analytical expression derived by Cess (1958), which uses a y-dependent eddy viscosity. Namely, the molecular plus eddy viscosity, referred to as $\nu_T(y)$, is

$$\nu_T = \frac{\nu}{2}\left[1 + \frac{\kappa^2\delta^{+2}}{9}\left(2\eta - \eta^2\right)^2\left(3 - 4\eta + 2\eta^2\right)^2\left(1 - \exp\left(\frac{-\eta\delta^+}{A}\right)\right)^2\right]^{1/2} + \frac{\nu}{2}, \tag{C.2}$$

where $\eta = y/\delta$ is the wall-normal coordinate normalised with the half-channel height and δ^+ is the friction Reynolds number based on the friction velocity and the half-channel height, i.e $\delta^+ = u_\tau\delta/\nu$. Equation (C.1a) becomes then

$$\frac{dP}{dx} = +\frac{d}{dy}\left[\nu_T\frac{dU}{dy}\right]. \tag{C.3}$$

It follows from equation (C.1b) that the streamwise mean pressure gradient is independent of y, so we can replace it by $dP/dx = -u_\tau^2/\delta$. Integrating equation (C.3) twice and using the boundary conditions $U(y = 0) = U_{slip}$ and $dU/dy(y = \delta) = 0$, the mean velocity profile is

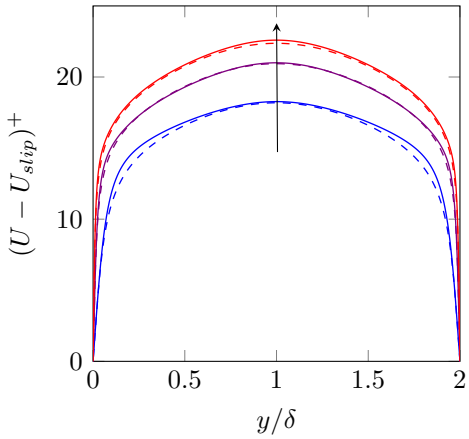

FIGURE C.1 – – –, Cess mean profiles obtained from the empirical expression (C.4) with $A = 25.4$ and $\kappa = 0.426$; ——, profiles from direct numerical simulations from Lee & Moser (2015) for three different Reynolds numbers. From blue to red $\delta^+ = 180$, 550 and 1000.

$$U(y) = U_{slip} + u_\tau^2 \int_0^y \frac{1 - y_1/\delta}{\nu_T(y_1/\delta)} \, \mathrm{d}y_1, \tag{C.4}$$

where U_{slip} denotes the slip velocity at the substrate-channel interface and is specified once the flow within the permeable substrate is solved. The values of the two parameters κ and A in equation (C.2) are taken equal to those used by Hoyas & Jiménez (2006) ($A = 25.4$ and $\kappa = 0.426$), which have been fitted to DNS results for $\delta^+ = 2000$, and are kept constant for different Reynolds numbers. In figure C.1, the analytical profiles obtained from equation (C.4) are compared to those obtained from DNSs at three Reynolds numbers $\delta^+ = 180$, 550 and 1000. This mean profile has been widely used in the literature for a linear stability analysis, as in Reynolds & Hussain (1972), Jiménez *et al.* (2001) del Álamo & Jiménez (2006), Pujals *et al.* (2009), Cossu *et al.* (2009), García-Mayoral & Jiménez (2011) or Abderrahaman-Elena & García-Mayoral (2017).

Appendix D

Analytical solution of Darcy's equation

In this appendix we solve the two-dimensional Darcy equation within the permeable channel. The particular solution at the substrate-channel interface will serve as boundary conditions for Rayleigh's equation within the channel in chapter 5.

Together with the continuity equation, the system of equations to solve is

$$\frac{\nu}{K_x}u + \frac{\partial p}{\partial x} = 0, \tag{D.1a}$$

$$\frac{\nu}{K_y}v + \frac{\partial p}{\partial y} = 0, \tag{D.1b}$$

$$\frac{\partial u}{\partial x} + \frac{\partial v}{\partial y} = 0. \tag{D.1c}$$

These equations can be solved with a procedure similar to that described for Brinkman's equation in appendix A. We restrict ourselves to the substrate at the bottom boundary of the channel, which extends between $y = -h$ and $y = 0$. Firstly, taking the two-dimensional divergence of equations (D.1a) and (D.1b) and using continuity yields

$$\left(\frac{1}{K_y} - \frac{1}{K_x}\right)\frac{\partial v}{\partial y} + \frac{1}{\nu}\nabla^2_{xy}p = 0. \tag{D.2}$$

Taking then the y-derivative of equation (D.1b) and substituting $\partial v/\partial y$ from (D.2) yields an equation in p alone, which after a Fourier transform in x leads to

$$\left(D^2 - \alpha_x^2\frac{K_x}{K_y}\right)\hat{p} = 0, \tag{D.3}$$

where as before $D \equiv d/dy$. From equation (D.3), the roots of the corresponding characteristic equation are $r_D = \pm\alpha_x\sqrt{K_x/K_y}$ and the expression for $\hat{p}$ becomes,

$$\hat{p}(y) = A_D \mathrm{e}^{r_D y} + B_D \mathrm{e}^{-r_D y}. \tag{D.4}$$

Using equation (D.1b), the expression for $\hat{v}$ is then

$$\hat{v}(y) = -\frac{\alpha_x}{\nu}\sqrt{K_x K_y}\left(A_D \mathrm{e}^{r_D y} - B_D \mathrm{e}^{-r_D y}\right), \tag{D.5}$$

where A_D and B_D depend on the wavenumber α_x and the geometrical properties of the permeable medium, K_x and K_y. These coefficients are determined by imposing the boundary conditions. Note that for the inviscid stability analysis, only the continuity of the wall-normal velocity at the substrate-channel interface is imposed, so $\hat{v}$ within the bottom substrate is solved by imposing the impermeability condition at $y = -h$ and continuity of pressure at $y = 0$. That is, the boundary conditions are

$$\hat{v} = 0 \quad \text{at} \quad y = -h, \quad \text{and} \tag{D.6a}$$

$$\hat{p}|_{y=0^-} = \hat{p}|_{y=0^+} \quad \text{at} \quad y = 0, \tag{D.6b}$$

where, at $y = 0$, the plus and minus signs correspond to the fluid and substrate sides of the interface, respectively. By applying these boundary conditions to equations (D.4) and (D.5), and taking the solution at the substrate-channel interface, the wall-normal velocity at $y = 0$ is

$$\hat{v}|_{y=0} = -\frac{\alpha_x}{\nu}\sqrt{K_x K_y}\tanh\left(\alpha_x h\sqrt{\frac{K_x}{K_y}}\right)\hat{p}|_{y=0^+} = \mathcal{C}_{Darcy}\hat{p}|_{y=0^+}. \tag{D.7}$$

This equation, together with its symmetric for the substrate at the top boundary of the channel, constitutes the boundary condition for the inviscid stability analysis in chapter 5 when the substrates are poorly-connected, as used by Abderrahaman-Elena & García-Mayoral (2017).

Appendix E

Order of magnitude analysis for the flow in the channel region and within the permeable substrate

In this appendix an order of magnitude analysis for the channel region and the permeable substrate is carried out to evaluate if there is any term in the governing equations that can be neglected and still capture properly the behaviour of the instabilities involved.

E.1 Channel flow

From previous studies of turbulent flows over riblets (García-Mayoral & Jiménez, 2011) and permeable substrates (Breugem *et al.*, 2006; Abderrahaman-Elena & García-Mayoral, 2017), the appearance of the aforementioned spanwise-coherent rollers is expected. These rollers have a height of the order of 15 wall units and a streamwise wavelength of the order of 100 wall units.

Let us assume that the wavelength $\lambda = 2\pi/\alpha$ is the characteristic lengthscale of the flow in streamwise direction, while the shear-layer length, is that in the wall-normal direction. From Cess mean velocity profile (Cess, 1958), the shear-layer length is $y_c^+ \approx 9$, i.e. $\mathcal{O}[10]$. In addition, u_c is the characteristic velocity for streamwise velocity fluctuation, v_c for the wall-normal velocity and $10u_\tau$ for the mean velocity, since in a turbulent boundary layer this is the order of magnitude of the mean velocity at $y^+ = 10$, where the Kelvin-Helmholtz rollers develop.

We start by estimating the terms for the longitudinal linearised momentum equation (equation 5.1b). From continuity, we get that $v_c \sim u_c y_c/\lambda$, so that the two components of the convective terms are of the same order. Referring all the terms with respect to the convective ones, yields

$$\underbrace{\frac{\partial u'}{\partial t}}_{\substack{\frac{u_c}{t_c} \\ | \\ \frac{\lambda}{10u_\tau}\frac{1}{t_c}}} + \underbrace{U\frac{\partial u'}{\partial x} + v'\frac{dU}{dy}}_{\substack{\frac{10u_\tau u_c}{\lambda} + \frac{v_c 10u_\tau}{y_c} \\ | \\ O[1]}} = - \underbrace{\frac{\partial p'}{\partial x}}_{\substack{\frac{p_c}{\lambda} \\ | \\ \frac{p_c}{10u_\tau v_c}\frac{\lambda}{y_c}}} + \underbrace{\frac{\partial}{\partial x}\left(2\nu_T\frac{\partial u'}{\partial x}\right) + \frac{\partial}{\partial y}\left(\nu_T\left(\frac{\partial u'}{\partial y} + \frac{\partial v'}{\partial x}\right)\right)}_{\substack{\cancel{\frac{\nu u_c}{\lambda^2}} + \frac{\nu u_c}{y_c^2} \\ | \\ \frac{\nu}{10u_\tau y_c}\frac{\lambda}{y_c}}}.$$

From previous work (García-Mayoral & Jiménez, 2011; Abderrahaman-Elena & García-Mayoral, 2017) we know that the wavelengths we are interested in are of the order of 100 wall units, and taking $y_c^+ \sim \mathcal{O}[10]$, the ratio between convective and viscous terms is $\mathcal{O}[1/10]$, since

$$\frac{\text{viscous terms}}{\text{convective terms}} \approx \frac{1}{10}\frac{\nu}{u_\tau y_c}\frac{\lambda}{y_c} = \frac{1}{10}\frac{1}{y_c^+}\frac{\lambda^+}{y_c^+} \approx \frac{1}{10}\frac{1}{10}\frac{100}{10} = \frac{1}{10}. \tag{E.1}$$

The viscous terms in the longitudinal momentum equation are thus negligible compared to the convective ones and an inviscid stability analysis would therefore suffice. An equivalent analysis can be carried out for the momentum equation in y.

E.2 Permeable substrate

Although as a first approximation the viscous terms in the channel could be neglected, the same cannot be said about the viscous terms inside the permeable substrate. This will be proved by *reduction to absurdity*. That is, we seek to demonstrate that the viscous terms within the permeable layer need to be retained by showing that an inconsistency is reached from its denial.

Let us assume that the Brinkman term in equation (2.1) is negligible. The Darcy term is then balanced by the pressure terms. As in the previous section, the characteristic magnitudes for the pressure, and the streamwise and wall-normal velocity fluctuations are p_c, u_c and v_c, respectively. The wavelength $\lambda^+ = 2\pi/\alpha^+ \in [20 - 100]$ is the characteristic lengthscale of the flow in x, and the penetration depth L_p is that in the wall-normal direction. The penetration depth is defined as the height below the free-fluid/substrate interface where the overlying flow penetrates and is discussed in detail in section 5.2. In this analysis, we will assume that the thickness of the substrate is sufficiently large so that the overlying flow does not perceive its effect and it does not set any lengthscale of the problem. Particularly, we assume that $h^+ \gg \sqrt{K_x^+}, \sqrt{K_y^+}$.

By estimating the order of magnitude of the terms for the streamwise Brinkman equation and referring them to the Darcy term, we obtain

$$\underbrace{-\frac{\nu}{K_x}u'}_{\substack{\frac{\nu u_c}{K_x}\\ |\\ O[1]}} \underbrace{-\frac{\partial p'}{\partial x}}_{\substack{\frac{p_c}{\lambda}\\ |\\ \frac{p_c\lambda}{\nu u_c}\frac{K_x}{\lambda^2}}} \underbrace{+\nu\frac{\partial^2 u'}{\partial x^2}}_{\substack{\frac{\nu u_c}{\lambda^2}\\ |\\ \frac{K_x}{\lambda^2}}} \underbrace{+\nu\frac{\partial^2 u'}{\partial y^2}}_{\substack{\frac{\nu u_c}{L_p^2}\\ |\\ \frac{K_x}{L_p^2}}} = 0.$$

If the viscous terms are negligible, the following conditions need to be satisfied

$$\begin{cases} \dfrac{K_x}{\lambda^2} \ll 1 & \Rightarrow \quad K_x \ll \lambda^2, \\ \dfrac{K_x}{L_p^2} \ll 1 & \Rightarrow \quad K_x \ll L_p^2, \end{cases}$$

while the pressure fluctuations verify

$$p_c \sim \frac{\nu u_c}{\lambda}\frac{\lambda^2}{K_x}. \tag{E.2}$$

Equivalently, for the wall-normal component of Brinkman's equation, we obtain

$$\underbrace{-\frac{\nu}{K_y}v'}_{\substack{\frac{\nu v_c}{K_y}\\ |\\ O[1]}} \underbrace{-\frac{\partial p'}{\partial y}}_{\substack{\frac{p_c}{L_p}\\ |\\ \frac{p_c L_p}{\nu v_c}\frac{K_y}{L_p^2}}} \underbrace{+\nu\frac{\partial^2 v'}{\partial x^2}}_{\substack{\frac{\nu v_c}{\lambda^2}\\ |\\ \frac{K_y}{\lambda^2}}} \underbrace{+\nu\frac{\partial^2 v'}{\partial y^2}}_{\substack{\frac{\nu u_c}{L_p^2}\\ |\\ \frac{K_y}{L_p^2}}} = 0.$$

Here there are two possibilities: the pressure term can be either of the same order of magnitude as the Darcy term or greater than the Darcy term.

Darcy term balanced by the pressure term

In the first case, we proceed as for the streamwise Brinkman equation. After referring all the terms to the Darcy term, the following conditions need to be satisfied so that the viscous terms can be neglected

$$\begin{cases} \dfrac{K_y}{\lambda^2} \ll 1 & \Rightarrow \quad K_y \ll \lambda^2, \\ \dfrac{K_y}{L_p^2} \ll 1 & \Rightarrow \quad K_y \ll L_p^2. \end{cases}$$

In addition, the pressure terms are balanced by the Darcy term. By using the order of magnitude for p_c obtained from above (equation E.2) and $v_c \sim u_c \delta_{Br}/\lambda$ from the continuity equation, we obtain

$$\frac{\text{pressure terms}}{\text{Darcy terms}} \sim \frac{p_c L_p}{\nu v_c} \frac{K_y}{L_p^2} \sim \frac{\lambda^2}{L_p^2} \frac{K_y}{K_x} \sim O[1]. \tag{E.3}$$

From this, there are two different branches depending on whether K_x is greater of less than K_y. For $K_x \ll K_y$, summing up all the conditions, the orders of magnitude that must be satisfied to neglect the Brinkman terms are as follows

$$\begin{array}{ccccccc} \underbrace{K_x^+} & \ll & \underbrace{K_y^+} & \ll & \underbrace{\left(\lambda^+\right)^2} & \ll & \underbrace{\left(L_p^+\right)^2}, \\ | & & | & & | & & | \\ \ldots & & [1-500] & & \left[(20)^2-(100)^2\right] & & ? \end{array} \tag{E.4}$$

An order of magnitude for L_p can be obtained from section 5.2.1, where $L_p^2 \sim \lambda^2/(4\pi^2) K_y/K_x$, and hence expression (E.4) is only satisfied for certain anisotropy ratios, $K_x/K_y < 1/(4\pi^2)$ specifically.

For $K_x \gg K_y$, on the other hand, the necessary conditions are

$$\begin{array}{ccccccc} \underbrace{K_y^+} & \ll & \underbrace{K_x^+} & \ll & \underbrace{\left(L_p^+\right)^2} & \ll & \underbrace{\left(\lambda^+\right)^2} \\ | & & | & & | & & | \\ \ldots & & [1-500] & & ? & & \left[(20)^2-(100)^2\right] \end{array} \tag{E.5}$$

For this to be true, there must be at least a jump of two orders of magnitudes between K_x^+ and λ^{+2}, which is not satisfied for the whole range of λ^+, showing that the Brinkman term cannot be neglected. From section 5.2.1, assuming that $\alpha\sqrt{K_y} < 1$ and $\alpha^2 K_x \gtrsim 1$, the penetration depth L_p when $K_x \gg K_y$ is of the order of $L_p^2 \sim \lambda\sqrt{K_y}/\pi$. In this case, L_p^{+2} would be of the same order of magnitude or smaller than K_x, contradicting the necessary conditions in expression E.5 to neglect the viscous terms. Therefore, the absence of viscous terms may incorrectly determine the behaviour of the instabilities, which is indeed the case, as it can be shown in section 5.2.

Pressure term dominant

If the pressure term in the wall-normal Brinkman equation is dominant, the equation reduces to

$$\frac{\partial p'}{\partial y} = 0 \tag{E.6}$$

In this case, comparing the pressure terms to the two viscous terms, we obtain

$$\frac{\lambda^2}{K_x}\frac{\lambda^2}{L_p^2} \gg 1 \qquad \text{and} \qquad \frac{\lambda^2}{K_x} \gg 1,$$

which, given that $\lambda^2/K_x \gg 1$ from the streamwise Brinkman equation, these conditions are generally satisfied whatever the relation between λ and L_p is. The wavelength λ could even be smaller than L_p, as long as $\lambda^2/K_x \gg L_p^2/\lambda^2$.

On the other hand, the pressure term needs to be greater than the Darcy term, which yields

$$\frac{\text{pressure terms}}{\text{Darcy terms}} \sim \frac{p_c L_p}{\nu v_c}\frac{K_y}{L_p^2} \sim \frac{\lambda^2}{L_p^2}\frac{K_y}{K_x} \gg 1 \tag{E.7}$$

and the necessary conditions in this case also differ depending on the anisotropy ratio K_x/K_y. For $K_x \gg K_y$, condition (E.7) translates into $\lambda^2 >>> L_p^2$, where the anisotropy ratio must be $K_x/K_y \ll \lambda^2/L_p^2$. The sequence of the order of magnitudes of the parameters for $\partial p'/\partial y = 0$ is similar to that in expression (E.5), which is already shown not to be satisfied.

For $K_x \ll K_y$, expression (E.7) allows several different relations between λ and L_p. Grouping all the possible requirements for the Brinkman terms to be negligible, in this case, we obtain

$$\underbrace{K_x^+}_{\substack{| \\ \dots}} \ll \underbrace{K_y^+}_{\substack{| \\ [1-500]}} \qquad \text{and} \qquad K_x^+ << \begin{cases} \left(L_p^+\right)^2 << \left(\lambda^+\right)^2, & \text{or} \\ \left(L_p^+\right)^2 \sim \left(\lambda^+\right)^2, & \text{or} \\ \left(\lambda^+\right)^2 << \left(L_p^+\right)^2 & \left(\text{if } \dfrac{\lambda^2}{L_p^2} > \dfrac{K_x}{K_y} \quad \& \quad \dfrac{\lambda^2}{L_p^2} > \dfrac{K_x}{\lambda^2}\right), \end{cases} \tag{E.8}$$

which together with condition (E.4) covers almost the whole range of permeabilities and λ values. The Brinkman term can therefore be neglected when $K_x/K_y \ll 1$. This may be the reason why the behaviour of the Kelvin-Helmholtz instability for substrates with $K_x \ll K_y$ can be captured well with Darcy's equation, as suggested by the governing parameter of the instability found in sections 5.2 and 5.3.

Appendix F

Additional turbulence statistics for channel flows with permeable substrates with $\phi_{xy} \approx 3.6$ and $\phi_{xy} \approx 5.5$

In chapter 7 results for only the permeable substrate with $\phi_{xy} \approx 11.4$ are discussed. In this appendix, the flow statistics for the other two substrate configurations are presented. The mean velocity profiles for configurations with $\phi_{xy} \approx 5.5$ and $\phi_{xy} \approx 3.6$ are compiled in figure F.1.

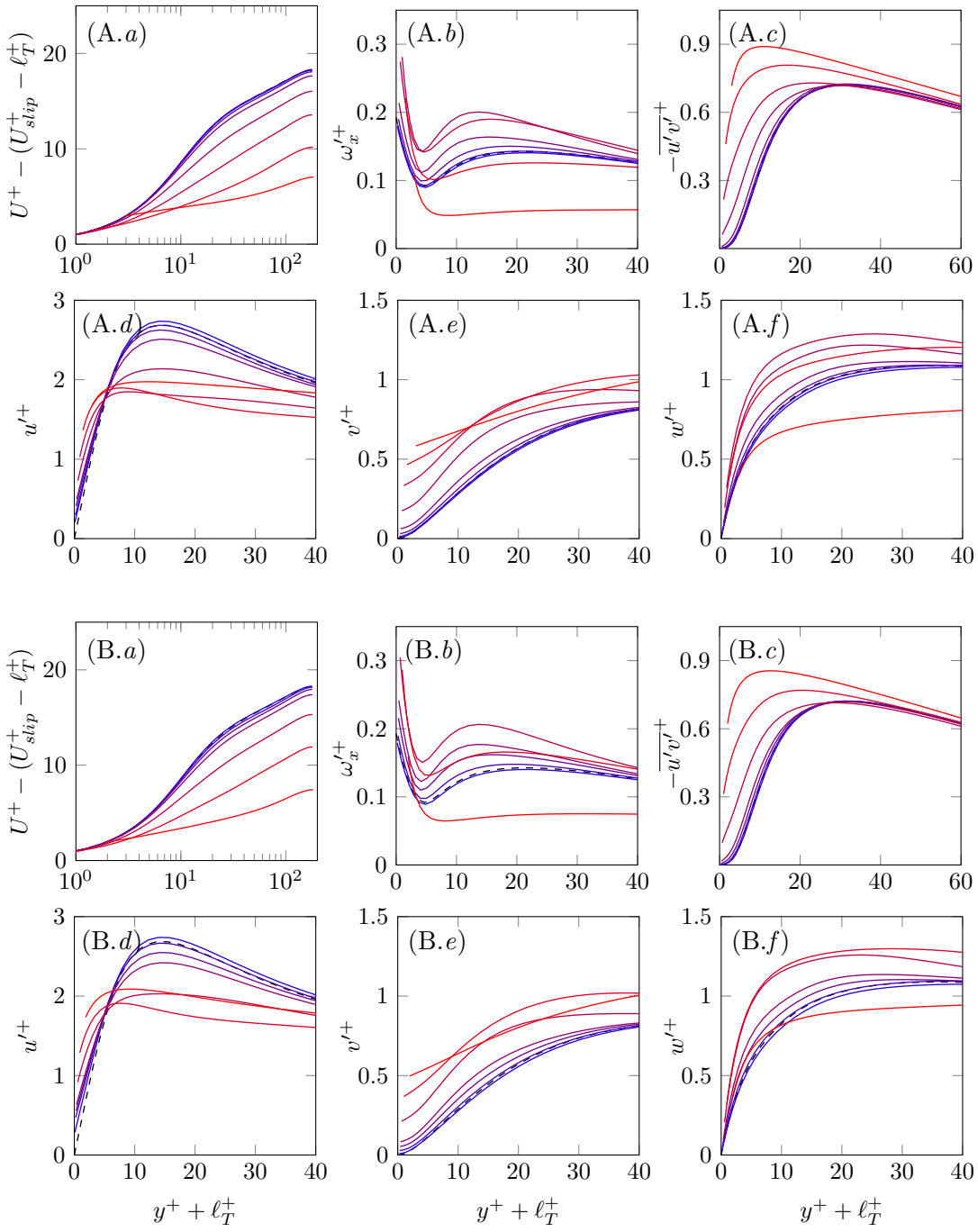

FIGURE F.1 One-point turbulent statistics for (A.*a*-A.*f*) a substrate configuration with $\phi_{xy} \approx 3.6$, which corresponds to cases A1-A8; (B.*a*-B.*f*) a substrate configuration with $\phi_{xy} \approx 5.5$, which corresponds to cases B1-B7. Permeability values increase from blue to red and profiles are scaled with the corresponding u_τ at $y = -\ell_T = -\sqrt{K_z}$, the linearly extrapolated virtual origin for turbulence. Black-dashed lines represent the smooth-channel case. (A.*a*, B.*a*) Mean velocity profiles shifted by ℓ^+_T and where the value at the origin, i.e. the offset predicted from the linear theory, $\Delta U^+ = U^+_{slip} - \ell^+_T$, has been subtracted. Rms fluctuations of (A.*b*, B.*b*) the streamwise velocity, (A.*c*, B.*c*) the wall-normal velocity, (A.*d*, B.*d*) the spanwise velocity, and (A.*e*, B.*e*) the streamwise vorticity. (A.*f*, B.*f*) Reynolds stress.